Metal Oxide-Hierarchical Porous Silica Nanocomposites Prepared by Nanoemulsion Templating and Integrative Synthesis

by

Manal Amin Abdel-Mogoud Hessien

A thesis

presented to the University of Waterloo

in fulfillment of the

thesis requirement for the degree of

Doctor of Philosophy

in

Chemistry–Nanotechnology

Waterloo, Ontario, Canada, 2012

Declaration

I hereby declare that I am the sole author of this thesis. This is a true copy of the thesis, including any required final revisions, as accepted by my examiners.

I understand that my thesis may be made electronically available to the public.

Abstract

Nanoemulsions are templates that have the potential to fill the gap between micellar systems and latex particles in the preparation of porous materials. A nanoemulsion can also be used as a carrier for uploading the desired materials inside the pore formed after the removal of the template. In this research, oil-in-water (O/W) nanoemulsions were prepared by means of a low-energy method based on a phase inversion composition (PIC) technique, using two nonionic surfactants (Tween 80 and Span 80), which can be mixed in order to adjust the hydrophilic-lipophilic balance (HLB). The influence of a number of parameters on the tunability and stability of such nanoemulsions was also studied. The effect of the simultaneous intercrossing of multifactors on droplet size was explored using a process-mixture design, and the size of the nanoemulsion oil droplets was measured by means of dynamic light scattering (DLS).

The nanoemulsions were combined with sol-gel method in order to prepare porous silica with a macroporosity in the 50 nm to 400 nm range. The results demonstrate that a precise synergy between the silica source and the nanoemulsions is essential for effective interactions and homogeneous structures. Depending on the nature of such interactions, a variety of materials were observed, from hollow particles to continuous gels. Changing the size of the oil droplet and the volume of the nanoemulsions produced silica with differing pore sizes and varying total pore volumes. The obtained hierarchical porous silica (HPS) were characterized using mercury porosimetry, small angle X-ray scattering (SAXS), nitrogen isotherms, Fourier transform infrared (FTIR) analysis, transmission electron microscopy (TEM), and scanning electron microscopy (SEM).

The parallel use of the oil vesicles as containers for the further synthesis of metal oxide is a novel method of internally functionalizing the silica. When hydrophobic metal precursors are dissolved into the oil phase before the preparation of the nanoemulsion, they are confined within the globular cavities of the silica. The thermal treatment applied to the material to burn the organics then leads to the final formation of metal oxide nanoparticles, which are larger than the porosity of the silica matrix but entrapped within the large cavities, producing a

"rattle-like" structure. This method was demonstrated through the synthesis of Fe_2O_3, Fe_3O_4, and Co_3O_4 nanoparticles, and the results showed that a rather large amount of metal oxide (up to a 60 wt.% of metal oxide in nanocomposites) be generated while still maintaining the nanometric size observed at lower concentrations. This method allows control of the type of metal oxide, the concentration of the metal oxide, and the pore size, which enables the creation of different types of nanocomposites. Metal oxide hierarchical porous silica (MHPS) nanocomposites were characterized based on nitrogen isotherms, TEM and SEM observations, FTIR analysis, X-ray diffraction (XRD), and Mossbauer spectroscopy. Magnetic measurements were also taken.

This new method, using the new templating objects, is a perfect illustration of the concept of "integrative synthesis," whereby the combination of building units and reactional mechanisms leads to complex structures as a result of true synergy among the elements during the reaction. In this case, the size of the nanoemulsion and the total water volume both contribute to the generation of distinctive architectures. In addition, the reaction of the metal oxide precursors within the cavities limits the extension of the final crystal size, but the surrounding solid matrix plays a role as well by keeping the particles apart. The final factor is that the reactive materials cannot leak from the silica because of the rattle-like structure, but the reagents can reach those particles through the porosity of the silica framework.

Acknowledgements

I want to express my gratitude to my supervisor, Professor Eric Prouzet, for his supervision, advice, continuous encouragement, and helpful discussions during this research. I also extend my appreciation and thanks to my advisory committee members for their valuable comments:

Professor Abdelhamid Sayari (University of Ottawa, Department of Chemistry)

Professor Flora Ng (University of Waterloo, Department of Chemical Engineering)

Professor Jean Duhamel (University of Waterloo, Department of Chemistry)

Professor Pavle Radovanovic (University of Waterloo, Department of Chemistry)

Professor Dmitriy Soldatov (University of Guelph, Department of Chemistry)

I am very grateful for my Egyptian supervisors, instructors, and friends at Cairo University and in the Department of Ceramics at the National Research Centre, in particular, Professors Nabil Ghoneim, Bahgat Algholy, Atef Othman and Mahmoud Zawra. I deeply appreciate your boundless support and confidence in me. I would like to thank especially the Ministry of Higher Education and Scientific Research for their sponsorship during my studies. To all my friends in Egypt, my friends at the University of Waterloo, my lab-mates and my friends in Waterloo, I would also like to say thank you so much for your constant encouragement.

Everything I have achieved while working toward this PhD degree I owe to those who have encouraged me so steadfastly from Egypt: my mother, for her continuous moral support and prayers for me and for all her love and affection, and my father for being the inspiration for my scientific vocation. Words fail to express my appreciation for my wonderful husband, Mohamed, whose dedication; love, emotional support, and compassion have lifted other loads from my shoulders so that I could focus on my academic pursuits during my studies and our amazing four-year life in Waterloo. I also owe my lovely children, Mariam, Shaza, and Ahmed, an enormous debt of gratitude for their patience.

My siblings Abeer, Hanan, and Mohamed contributed their endless love and unconditional moral support, always surprising me with their much-treasured phone calls. I am also very grateful to my dear mother-in-law for encouraging me and being patient while we were absent and for her understanding when I lost my father-in-law during this work and was not able to be near him.

Dedication

To my beloved Parents,

To my beloved husband ....Mohamed,

and my lovely children ...Mariam…Shaza…Ahmed,

To my sisters….Abeer ...Hanan,

and my brother ...Mohamed

Table of Contents

List of Figures

List of Tables

List of Abbreviations

DLS	Dynamic Light Scattering
EDAX	Energy Dispersive X-Ray Spectroscopy
HLB	Hydrophilic-Lipophilic Balance .
HPS	Hierarchical Porous Silica
HSSS	Hydrolyzed Sodium Silicate Solution
MHPS	Metal Oxide-Hierarchical Porous Silica
MNE	Metal Oleate-Nanoemulsion
NE	Nanoemulsion
O/W	Oil-In-Water Nanoemulsions
O-NE	Oil-In-Water Nanoemulsions
PIC	Phase Inversion Composition
PIT	Phase Inversion Temperature
S/O	Surfactant-To-Oil Ratio
SS	Sodium Silicate
W-NE	Wax/Oil-In-Water Nanoemulsion
XAS	X-Ray Absorption Spectroscopy
XMCD	X-Ray Magnetic Circular Dichroism

List of Symbols

d	density	g/cm^3
D_h	hydrodynamic diameter	nm
PV	pore volume	cc/g
SA	surface area	m^2/g
SR	surface roughness	------

Chapter 1
Introduction

1.1 Motivation

Silica as a stable and biocompatible material has attracted a great deal of interest, particularly with respect to the synthesis of porous silica, allowed by the high flexibility of the silica framework. Indeed, due to its good thermal stability, good abrasion resistance, electrical insulation properties, large surface area and good compatibility with numerous other materials (both organic and inorganic), porous silica has found wide application in the fields of adsorption, selective separation, catalysis, and sensing. Recent focus has also been on the exploration of porous silica for imaging, and as an inorganic carrier for enzyme immobilization.[1]

Porous materials are usually synthesized with the use of organic templates trapped within an inorganic framework, whereby the porosity is enhanced through the removal of the organic phase. The type of porous material is dependent on the size of the organic template, and a variety of such materials have thus far been synthesized. With single molecules, 0.2 nm–1.5 nm microporous to supermicroporous, crystallized or amorphous molecular sieves can be obtained including the large family of natural or synthetic zeolites, aluminophosphates and gallophosphates.[2] A shift from single molecules to surfactant-based micellar assemblies enabled the formation of 2.0 nm–10.0 nm mesoporous materials, such as MCM-41, SBA-15, or MSU silica.[3-6]

On a larger scale, the use of colloidal particles or latex as templates allows the preparation of reverse opal-like structures, which have regular pores greater than 300 nm and provide specific photonic properties. However, no specific templates have been developed for the synthesis of porous materials that can fit within the intermediate size range (between 50 nm and 300 nm), in spite of the substantial benefits of such materials for extremely important applications in catalysis, chromatography, purification, or photonics. Therefore, oil-in-water nanoemulsions appear to be good candidates for such templates because their oil droplet size lies within the suitable range.[7] Nanoemulsions have been prepared by mechanical methods, but this process did not allow the nanoemulsions to be very stable. Since the use of the low-energy methods that led to much more stable objects, interest in these systems has been growing, as demonstrated by the still limited but increasing number of reports in the literature related to this topic.[8-10]

To realize nanoemulsions potential as templates in the synthesis of porous materials, additional criteria beyond the simple preparation of such nanoemulsions must be met. The templates must be as versatile as possible so that they can be adapted to suitable structures; they must be stable enough to withstand high concentrations without exhibiting any phase transition or Ostwald ripening, they must be rigid enough to resist the mechanical constraints created by the condensation of the inorganic framework, and their size must be adapted to enable the preparation of a full range of porous materials from a single composition. An ideal nanoemulsion would contain also groups of surface molecules that can interact with the inorganic precursors, which should contribute to a favorable interaction between the organic entities and the inorganic precursors. Previous work has demonstrated that the interaction between PEO chains and silica precursors is helpful in the synthesis of mesoporous silica with polyoxyethylene (PEO) nonionic surfactants.[11] Nanoemulsions are less stable than hard templates such as latex but are less expensive and more adaptive, and their ability to be filled with hydrophobic precursors opens the door to the integrated internal functionalization of the materials.

Nanoemulsion is formed of continuous and dispersed phases. Macroporous materials are prepared by using continuous phase to build a solid network around dispersed phase. Nanoparticles are prepared by doing reaction in dispersed phase. When two phases are used in reaction, functionalized porous nanocomposites are formed, as depicted in Figure 1.1.[12]

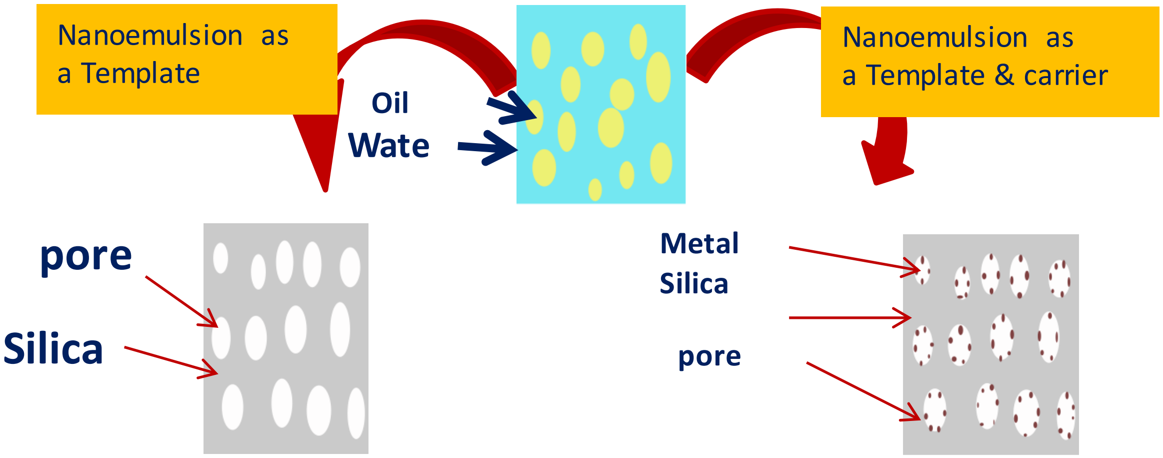

Figure 1.1: Schematic representation of reaction of an emulsion in the dispersed phase (using nanoemulsion as a template) for the preparation of porous materials and reaction in both phases (using nanoemulsion as a template and a carrier) for the preparation of composites, respectively.

1.2 Research Objectives

This research was driven by the following goals: 1) to control the preparation of a stable and tunable O/W nanoemulsion; 2) to apply the prepared nanoemulsion as a template for the creation of macroporous silica; 3) to apply the nanoemulsion as a carrier or nanoreactor for functional materials in order to add functionality to porous silica in a straightforward manner; 4) to develop a new template for filling the gap between a mesoporous structure and a macroporous structure; and 5) to functionalize magnetic, optical, and other materials within a silica matrix based on one-pot synthesis.

The specific steps required for the completion of this project were as follows. First, the individual factors that affect the size of the nanoemulsion as well as the interaction between different factors were studied experimentally. Second, a variety of nanoemulsions were applied as templates for the preparation of hierarchical porous silica using an inexpensive and environmentally friendly precursor for silica: sodium silicate. Third, the O/W nanoemulsion was integrated as a carrier and nanoreactor for hydrophobic functional materials as this carrier provides an easy method for applying functionality to porous silica to prepare metal oxide-hierarchical porous silica (MHPS) nanocomposites.

1.3 Outline of the Thesis

The thesis is divided into seven chapters. The first chapter introduces the work and explains the motivation behind it. The second chapter provides a comprehensive review of the literature related to the preparation of porous silica through the templating and functionalizing of silica.

The third chapter presents a study of single-parameter methods for controlling the size of the nanoemulsion droplets, and the fourth chapter includes the development of a process-mixture design model for controlling the size of the nanoemulsion droplets based on the simultaneous operation of multiple factors. These two chapters have been published previously in *Langmuir*.

The fifth chapter describes the use of the nanoemulsion as a template for the preparation of macroporous silica, and the sixth chapter explains how it can function as a template and, at the same time, as a carrier for the functional material. Parts of these two chapters have been published as a short communication in *ChemComm* and the complements of these two chapters will be submitted as a complete paper to the *Chemistry of Materials* journal. The seventh, and final, chapter includes the overall conclusions along with recommendations for further work.

1.4 Contributions

The research conducted for this thesis is expected to provide the following contributions. An enhanced understanding of nanoemulsions prepared with the use of phase inversion composition method is expected. A new system for the templating of porous inorganic materials is investigated. The synergy between soft matter and soft chemistry through the integration of nanoemulsions and the sol-gel chemistry of sodium silicate is demonstrated. The functionalization of porous silica with metal oxide through one-step synthesis using a nanemulsion as both a nanoreactor and a template is explored

Chapter 2

Literature Review

2.1 Overview

This chapter provides a review of the literature related to the integrative use of a nanoemulsion as a template for creating macroporosity within silica gel and as a nanoreactor for functionalizing the internal surface of macroporosity. Also included is reference to studies of porous materials, which are formed of a framework and pores: sol-gel is employed for building the framework, and the template is then used for the creation of the pores. Figure 2.1 outlines the contents of the chapter. The solid network, which must be prepared simultaneously with the pores, is usually produced by means of soft chemistry (sections 2.4–2 .6). The pores are formed by soft matter/template (sections 2.7 and 2.8). A process that is based on the combination of soft chemistry and soft matter is usually termed integrative synthesis (section 2.3). Emulsification mechanism and preparation methods for nanoemulsions are mentioned in Section 2.9 followed by strategies used to functionalize porous silica in Section 2.10 and using nanoemulsion as a nanoreactor in Section 2.11. Finally, metal oleate preparation as hydrophobic precursor for metal oxide nanoparticles

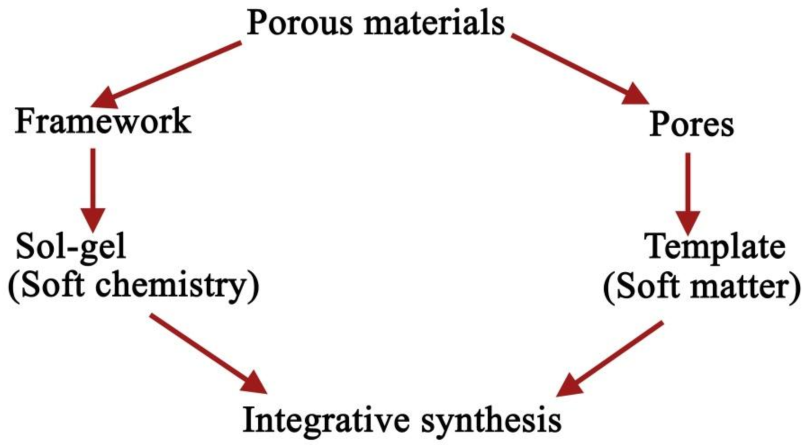

Figure 2.1: Outline of the contents of this chapter.

2.2 Porous Materials

Porous materials can be defined simply as nanostructured materials that contain cavities or channels, known as pores. The pores generate high specific surface areas and a rich surface chemistry. They can be either closed, in which case, they have no contact with the external surface, or open, when they do have contact. Depending on the number of openings to the external surface, open pores are categorized as cylindrical (two openings, either through or cross-linked) or blind (one opening). An ink-bottle pore is a special type of blind pore in which the opening is smaller than the pore size itself.[1-2,3]

According to the size of their pores, porous materials are ranked as microporous, mesoporous, or macroporous. Pore size is defined as the distance between the opposite walls of the pore. A micropore is a pore whose internal width is less than 2 nm, a mesopore has an internal width between 2 nm and 50 nm, and the internal width of a macropore is greater than 50 nm. A material that exhibits pores in the micro-range, the meso-range, and/or the macro-range is known as a hierarchical porous material.

Porous materials with single-size porosity have beneficial applications in the areas of adsorption, membranes, sensors, fuel cells, batteries, catalysis, and separation. However, hierarchical porous materials have recently attracted increased interest, especially for catalysis and separation, for which easy accessibility is a major requirement. In multimodal porosity, macroporosity prevents the blocking of the meso/micropores (by means of reagents and/or products) and facilitates diffusion (especially for large molecules or for viscous systems), and meso/macroporosity provides the high surface area required and selectivity with respect to size and shape.[4]

2.3 Integrative Synthesis

As mentioned, integrative synthesis refers to the integration of soft chemistry (chimie douce, or more specifically, sol-gel) and soft matter (complex fluids). The “soft” designation indicates the ability of materials to interact without disruption to their functions that form networks (soft chemistry) and patterning effects (soft matter). Integrative synthesis couples chemistry with processing and provides a method of synthesizing complex hierarchical objects. It is considered an interdisciplinary tool box[5] that has two main menus: soft chemistry, for building a framework with a choice of either inorganic or organic chemistry, and soft matter, for building patterns within the framework, for which the choices are micelles, liquid crystals, or emulsions. A variety of alternative names for integrative synthesis include integrative chemistry, the chemistry of shapes,[6-8] and overall length scale syntheses.[9]

The purpose of integrative synthesis is to provide not only shaping but also functionality. It is used for the preparation of hierarchical porous materials; however, the hierarchy is present not only in the final texture but also in the level of strength during shaping. At the microscopic scale, shaping is promoted through a strong covalent or iono-covalent chemical interaction. At the mesoscopic scale (either between a microscopic framework and mesoscopic pores or within a mesoscopic template). Organization at the macroscopic length scale is even weaker and still shaping is based on a weaker electrostatic or ionic interaction.

2.4 Soft Chemistry

Soft chemistry is related to the concept of "chimie douce" pioneered by J. Livage. It begins at the molecular level, which provides benefits for the design and engineering of nanomaterials. Soft chemistry is topotactic, in that the final product retains a memory of the structure of the precursor. Solids prepared at room temperature based on soft chemistry routes offer a rich surface chemistry.

Soft chemistry is also related to chemical reactions that can occur at room temperature, which means that this designation is not restricted to sol-gel chemistry but can be extended to include coordination chemistry, supramolecular chemistry, and polymer chemistry.[4, 10]

2.5 Sol-Gel Chemistry

Dispersed solid colloidal particles, known as sols, grow extensively or aggregate to make up a three-dimensional, open-network that can reach macroscopic dimensions, limited only by the size of the containers. Such a network is known as a gel. The continuous transformation of a sol to a gel constitutes the gelation process, and the abrupt change from the liquid to the solid stage is termed the sol-gel transition. A nanostructured solid network (gel) is formed in a liquid reaction medium (sol) as a result of the polymerization process. The driving reactions behind the sol-gel process are hydrolysis and condensation.

The sol-gel process is based on precursors such as a metal alkoxide $M\text{-}(OR)_n$, which is more popular than metal salts $M\text{-}X_n$, where M is a metal centre such as Ti, Zr, or Si; n is its oxidation state; and X and RO are leaving groups in the form of salts and alkoxides. The first step in the sol-gel process is the hydrolysis reaction, which involves the hydrolysis of the leaving group attached to a metal centre and leads to a hydroxyl-metal species. The hydrolysis causes the formation of a hydroxylated silica (silicic acid) species. By definition, hydrolysis is a chemical reaction in which the chemical bonds in a molecule are broken, and a water molecule enters to become part of the final product, commonly resulting in OH functional groups.

$$M\text{-}OR + H_2O \longrightarrow M\text{-}OH + R\text{-}OH \qquad (1)$$

An oligomer is formed by a condensation reaction in which two metal centres are bridged by means of an oxo bridge (2) or olation (3).

$$M\text{-}OH + XO\text{-}M \longrightarrow M\text{-}O\text{-}M + X\text{-}OH \qquad (2)$$

$$M\text{-}OH + XO\text{-}M \longrightarrow M\text{-}(OH)\text{-}M\text{-}OX \qquad (3)$$

An inorganic network is built from successive hydrolysis and condensation reactions. The relative contribution of each reaction strongly affects the structure, connectivity, and morphology of the network. The network structure formed, ranging from branched to compact, is strongly dependent on the reaction conditions, such as the pH, catalysis, reaction time, water content, metal concentration, and solvent.[11-16]

2.6 Sol-Gel Chemistry of Sodium Silicate

Kistler was the first to produce a silica aerogel using sodium silicate Na_2SiO_3 (water glass). Silica aerogel is characterized by a disordered mesoporosity with an average pore size of 20 nm to 40 nm and a microporosity of 2 nm, with a rather high surface area from 250 m^2/g to 800 m^2/g and a skeletal density of about 2 g/cm^3.[17-18]

The nomenclature used with respect to the sol-gel of sodium silicate differs slightly from that used for a sol-gel of alkoxide. No real hydrolysis step takes place in the formation of water glass but only the neutralization of sodium silicate to form silicic acid. The neutralization of the sodium silicate is achieved simply by means of the partial protonation of $Si\text{-}O^-$ centres replacing sodium ions, as in the first reaction shown in Figure 2.2. [17]

The condensation reaction rate differs depending on the pH. If the pH is less than 4 (acidic conditions), the predominant species is silicic acid oligomers (meta-silicic acid (H_2SiO_3) or ortho-silicic acid (H_4SiO_4)), which tend to form ring-like structures with 3–6 Si atoms. The condensation rate at this pH is still very low due to the dissolution of the larger silica species because of competition for the protonation oxide. If the pH is higher than 10 (basic conditions), the condensation is very slow due to the electrostatic repulsion within the predominant species (SiO_3^{2-}) at this pH. If the pH is between 4 and 10, silica gel may form either through a single step or through a two-step reaction.[17]

The single-step reaction occurs through the addition of acid catalyst to the sodium silicate at pH = 12 until the final pH reaches the range of 5–9, at which point the silica gel is formed. This process is also called acid catalysis or a neutralization reaction.[17]

The first step in the two-step reaction is the replacement of the sodium ion with a proton through the use of an ion exchange resin. This process results in the formation of silicic acid at a pH of about 2, so this step is considered the acid catalysis step. The second step is the base catalysis, which entails the addition of a Lewis base (F^-) or a Bronsted base (OH^-) to the silicic acid, resulting in the formation of the silica gel. The two-step reaction is also known as the acid-base catalysis reaction.[17]

Sierra et al. prepared a silica gel using the two-step reaction but without employing an ion exchange resin.[19] The purpose of using an ion exchange resin is to decrease the pH of the sodium silicate from about 12 to a pH of about 2 through the replacement of the sodium ions with protons. This goal can be achieved through the addition of sodium silicate to very acidified water so that the acidified sodium silicate solution contains sodium silicate in an acidified hydrolyzed form. The gelling can then be induced through the addition of the base catalyst. Both the Si concentration and the pH are among the main factors that affect the nanostructuration of the gel, the effect on the nanostructure appears on the primary particle size, the pore size distribution, and the fractality.

At this stage, the silica gel formed is called a hydrogel or a wet gel because it contains a large proportion of water. Silica hydrogels are aged for a period so that the inorganic silica framework can be mechanically reinforced. The entire aging process includes two mechanisms: syneresis and/or Ostwald ripening, both of which modify the water in the pores of the silica wet gel.

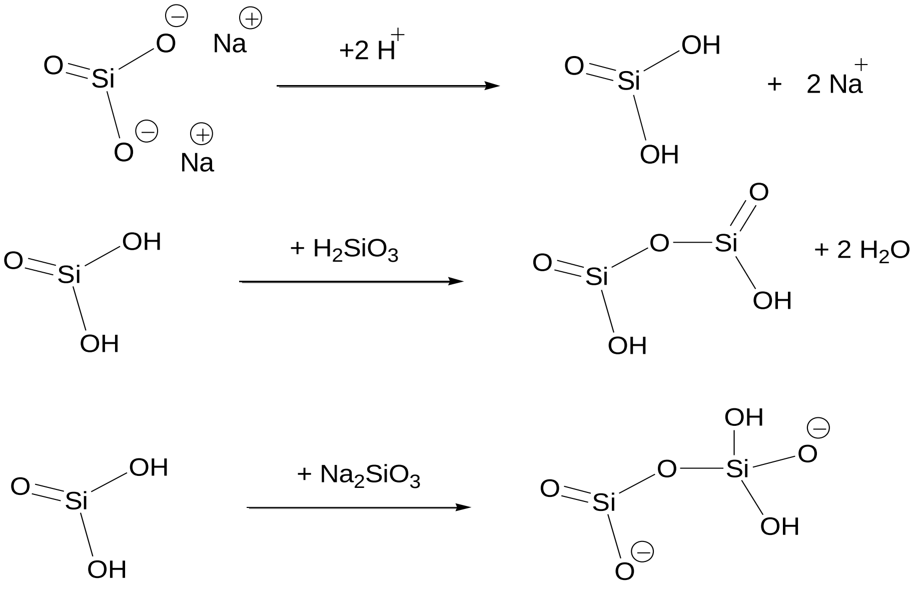

Figure 2.2: Acidification of a sodium silicate molecule to produce silicic acid and its reaction with another molecule of (a) silicic acid or (b) sodium silicate.[17]

The next step is to dry the silica wet gel so that the water entrapped in the pores of the wet gel evaporates. Three main routes are commonly used for the drying step. Normal evaporation drying involves the capillary stresses that inevitably occur whenever gas-liquid menisci appear at the pore boundaries. Capillary stress causes the formation of dried fragments of gels rather than monolithic gels, which explains why it is important to use drying techniques that do not involve capillary stresses or a gas-liquid transformation. Freeze-drying entails by-passing the triple point by first transforming the water into ice and then transforming the ice directly into vapor. Supercritical drying, which necessitates the bypassing of the critical point of CO_2, results in the formation of a monolithic gel. However, supercritical drying is both time-consuming and costly.[20]

2.7 Templating

As previously explained, integrative synthesis is a combination of soft chemistry and soft matter. Soft matter includes complex fluids such as micelles and emulsions. Because a solid template such as latex is used to create macroporous materials, templating rather than soft matter is the general name used in this thesis.

The dictionary definition of a template is “a shaped piece of rigid material used as a pattern for processes such as cutting out, shaping, or drilling; i.e. something that serves as a model for others to copy”.[46] In chemistry, templating is the procedure by which a template is integrated within a framework in order to generate an entire continuous range of nanocomposites: organic, inorganic, or hybrid.

A template may be either an endotemplate or an exotemplate. Endotemplate is the term used when the template is occluded in the growing framework. Examples of an endotemplate are micelles, liquid crystals, and latex. Exotemplate denotes the use of a scaffold (material with structural pores) as the template. Another material grows within the structural pores of the scaffold, resulting in a porous material. An example of an exotemplate is a silica monolith used for preparing a carbon replica. The work conducted for this thesis involved endotemplate rather than exotemplate.[21]

The term templating can be used interchangeably with nanocasting when the pore is a direct replica of the template (the size and shape of the templates appear to be correlated with the resulting pores). When the templating is so perfect that it creates the impression of a 1:1 correspondence between both the size and shape of the template and the size and shape of the pore that remains after the removal of the template, templating can be called nanocasting. In other cases in which a 1:1 correspondence is not proven after the template removal, naming the template based on the structure-directing agent or the organic additive is preferable.[21]

The mechanisms that govern templating are diverse; however, some fundamental conditions must be met in order for templating to occur. A favorable interaction between the surface of the template and the growing framework is required; otherwise, the template will not be incorporated within the framework, and phase separation will result. This interaction becomes more important as the size of the template decreases because the interface between the template and the framework expands. Another requirement is that the difference in density between the template and the framework must be comparable, or the template will settle or float on the solution that contains the framework. The template must also be both sufficiently stable and homogeneously dispersed in the solution that holds the growing framework.

There are two general pathways to prepare porous materials with templates: cooperative templating and true liquid crystal templating. The cooperative method is based on a cooperative interaction between the surfactant and the inorganic species by which an organic/inorganic composite is formed. The true liquid crystal templating depends on using a preformed surfactant liquid crystalline phase which is subsequently loaded with the precursor for the inorganic material. A schematic representation for the two pathways is shown in Figure 2.3.[22-23]

Templates create voids in a solid framework through the inclusion of the template species, which occupy a space around which the solid is formed. Then, when the template is later removed, the space is accessible and a pore can develop. The size of the void can range from the molecular scale, when a single molecule is used as a template for preparing microporous materials such as zeolites, to the mesoscopic scale, when aggregates of surfactants (micelles) or liquid crystals are used as a template for the fabrication of mesoporous materials such as SBA and MCM, to the macroscopic scale, when latex particles are used as a template for the creation of ordered macroporous materials such as inverse opals.

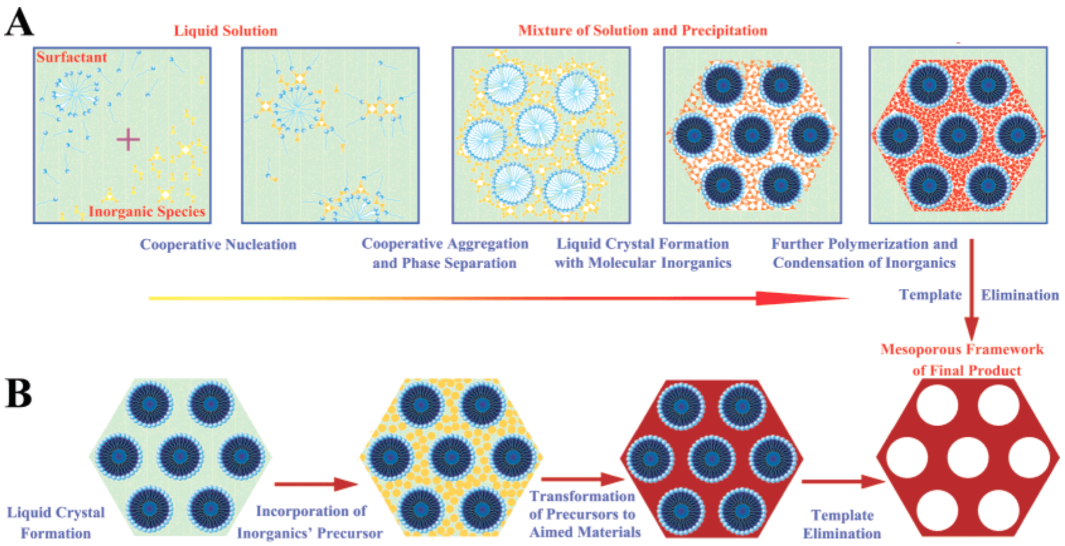

Figure 2.3: Different synthetic approaches for mesoporous: (A) cooperative surfactant self-assembly; (B) templating process using a "true" liquid-crystal. Reprinted with permission from Ref (22).

Templating procedures have been developed for the preparation of microporous and mesoporous materials. Ordered macroporous materials known as inverse opals are formulated using opal as a template either natural or synthetic opal. Synthetic opal, or colloidal crystal, is prepared through the packing of monodisperse spherical polymer or silica with a diameter of several hundred nanometers. This packing must be perfect because it affects the ordered nature of the subsequent macroporosity. This step is followed by infiltration as a means of depositing the framework around the opal and then removing the template, thus creating the ordered macroporous materials, as shown in Figure 2.4. This method of preparation is highly sensitive, especially if a photonic band gap material is required, and colloidal crystals are also expensive.

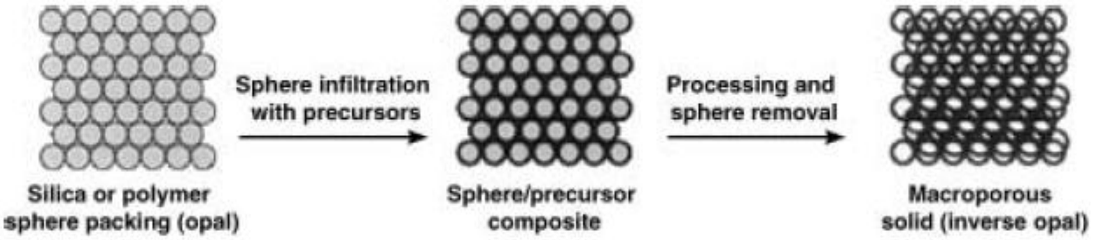

Figure 2.4: Schematic representation of the synthesis process for inverse opals, reprinted with permission from Ref (21).

2.8 Emulsion Templating

Emulsion templating is used for the preparation of macroporous organic and inorganic materials with a pore size of several micrometers. Work in emulsion templating was pioneered in 1996 by Schuth et al.[24] and in 1997 by Imhof et al.[25-30]

Schuth et al. used cooperative templating by mixing surfactant, water and mesitylene, and slow addition of TEOS while under stirring. Emulsion is formed during the stirring step. They prepared hollow spheres in the range of 50 µm with a mesoporous silica shell.[24]

Imhof et al. prepared isooctane-in-formamide emulsion stabilized by triblock copolymer and prepared by high energy homogenizer. They used the emulsion to prepare non-ordered macroporous materials. They then fractionated it so that polydispersity < 10%, to prepare ordered macroporous materials and a high oil volume larger than 55% to prepare inverse opal structure. They stated that emulsion templating is a general method to prepare such macroporous materials as macroporous silica, titania and zirconia; however, they put one limitation on this method: that the precursor must not destabilize the emulsion. They used metal alkoxide, which is compatible with oil-in-formamide emulsion.[31]

One year later, Imhof et al., [29] expanded the emulsion templating to include aqueous and non-aqueous sol-gel chemistry by using water-in-oil and oil-in-water emulsions rather than non-aqueous emulsion. The generalization of emulsion templating stems from the ease of finding a well-matched emulsion because emulsion can be made by using any two mutually insoluble liquids stabilized by suitable surfactants which is not involved in the templating. Most alkoxides are very reactive with water, so they cannot be used with water-in-oil emulsion. This challenge can be solved by using non-aqueous emulsions as Imhof did or by using metal salts resources with oil-in-water emulsion as the author of this thesis did. Imhof et al. prepared monoliths with a pore size in the range of 50 nm up to few microns.

Backove et al.[32-34] used Pickering emulsion (emulsion stabilized by solid particles instead of surfactant) to prepare macroporous materials. Particle-stabilized emulsion generates monodisperse droplets either water-in-oil or oil-in-water emulsions with droplet size ranging from few microns to 1 mm. Their porous materials have high porosity (>50%) that they called macrocellular foam because the authors started with a high internal phase emulsion (HIPE).

Schmidt-Winkel et al.[35-36] mentioned that microemulsion templates are easier to prepare by simply mixing the water, surfactant, oil, and a cosurfactant that leads to mesoporous materials with narrow pore size distributions without further processing. They also described how to prepare well-defined, adjustable, ultra-large pores of mesostructured cellular foams (MCFs) and how to engineer mesoporous systems for applications such as catalyst supports where mass transport is often limited by small pore openings.

Phadke et al. succeeded using an emulsion template to prepare titania containing mesopores and micropores. They prepared an oil/water emulsion using paraffin oil, water, and Span 80/Tween 80 by homogenizers. They managed to tune the oil droplet size from 30 nm to 1 µm by changing the volume of oil to between 10 % and 20 %.[37]

Examples of work done in emulsion templating are compared in Table 2.1. Both templating methods, cooperative templating and true liquid crystal, are used. Microemulsions with droplet size in the micron range are prepared by mixing, and nanoemulsions with droplet size less than 500 nm are prepared with high energy methods as homogenizers. Oil-in-water, water-in-oil and Pickering emulsions are used to template macroporous materials. Materials prepared by this method may be hollow spheres or macroporous monoliths. There is a missing research area related to using nanoemulsion prepared by low-energy methods, to templating by true liquid crystal method, to covering the missing range in 50-300 nm, and to using sodium silicate as inorganic precursor.

Table 2.1: Examples of work done in emulsion templating.

Author	**Templating method**	**Emulsion preparation**	**Emulsion type**	**Prouduct**
Schmidt-Winkel et al[35-36]	Cooperative	Mechanical stirring	-----------	Mesostructured cellular foams (MCFs)
Binks [38]	cooperative	High Energy method (homogenizer)	O/W and W/O pickering emulsion	Spherical interconnected pores, Bicontionus assembly of silica, Hollow spheres of silica
Stebe et al. [39]	True liquid crystal	Mechanical emulsion	Fluorinated emulsion	Silica with macropores (1-3 µm)
Landfester et al. [40]	cooperative	High Energy method (Ultrasonication)	W/O emulsion	Silica capsules with pore size of 150-600 nm
McGrath[41]	True liquid crystal	Mechanical blender	O/W emulsion	Hollow spheres with pores in micron range
Sambrook et al.[42]	True liquid crystal	Mechanical shearing	W/O emulsion	Hollow spheres with pores in micron range

Emulsion templating has significant advantages over the use of hard templates. The emulsion templating method is versatile in that it can be adapted to a variety of organic and inorganic systems and to numerous sphere or monolith shapes. Changing the concentration of the dispersed phase of the emulsion template also enables control of the porosity of the prepared materials, and varying the size of the emulsion droplets permits the manipulation of the pore size of the final materials. This tuning of the emulsion droplet is accomplished through modifications to the emulsification conditions. As well, because the emulsion droplets are deformable, they can withstand the stresses that occur during gelation and shrinkage.[29-30, 41, 43]

2.9 Nanoemulsions

An emulsion is composed of two immiscible liquids and surfactants: one liquid is dispersed, in the form of droplets, in a second liquid, and the interface between the droplets and the second liquid is stabilized by the surfactants. An emulsion can thus be considered a type of colloidal solution that contains a dispersed phase (external phase) covered by a layer of surfactants along with a continuous phase (internal phase) that surrounds the surfactant-stabilized dispersed phase.[44]

Emulsions are labelled according to their composition. In oil-in-water (O/W) emulsions, oil is the internal (dispersed) phase and water is the external (continuous) phase, while the opposite is the case with water-in-oil (W/O) emulsions. Increasing the number of components creates more complicated emulsion systems, such as O/W/O and W/O/W ternary emulsions.

2.9.1 Emulsification Mechanism

Three major steps are involved in the emulsification process: the breaking up of the droplets, the adsorption of the surfactants, and droplet collision. In the first step, a positive free energy change is associated with the breaking up of the droplets, which is an indication of a non-spontaneous process. The Gibbs free energy of the system during this step can be correlated with the change in the surface tension and the entropy:[45]

$$\Delta G = \Delta A \Upsilon - T\,\Delta S \qquad (4)$$

where G represents the free energy; Υ represents the surface tension, which is always positive; and S represents the entropy, also positive in this case. The quantity ΔA is associated with the change in the total area of the system when the droplets break up, and it can be further defined as follows:

$$\Delta A = A_2 - A_1 \quad (5)$$

where A_1 is the area of the larger droplets and A_2 is the area of the smaller droplets. Once the droplets have broken up, the value of A_2 is greater than that of A_1, making ΔA a positive number. As a result, ΔG is always positive, and this step of the emulsification process is thus a non-spontaneous process. The non-spontaneity of this step is caused by the creation of new surfaces (increase in area), which leads to an increase in the energy required in order to sustain them. Through agitation, the energy can be transmitted to the droplets in the internal phase from the surrounding external phase. Each formed droplet has an internal pressure (P) which is given by the following equation:

$$P = 2\gamma / R \quad (6)$$

where R is the radius of the droplet. This equation indicates the requirement for a higher level of input energy in order to create a smaller droplet size.

The second step of the emulsion mechanism involves the adsorption of the surfactants, which is crucial because it plays the most important role in the formation and stabilization of the emulsions. The adsorbed surfactants form a thick palisade layer that stabilizes the formed droplets by decreasing the interfacial tension. The surfactant layer creates a repulsive interaction in the form of electrostatic repulsion or steric hindrance, which prevents the coalescence of the droplets. It is worth noting here that nonionic surfactants have a specific property termed the hydrophilic-lipophilic balance (HLB). HLB values range from 0 to 20, with higher values indicating that the surfactant is more hydrophilic than lipophilic. The HLB value determines the type of emulsion formed: for HLB values less than 8, a W/O emulsion is the most likely result whereas higher HLB values often produce O/W emulsions.

In the third step, the destabilization of the droplets takes place through droplet collision. When droplets collide, four phenomena can occur: coalescence, breaking, flocculation, and creaming. These destabilization processes can be discussed with respect to the identity of the individual droplets, the reversibility of the process, the level of change, and the phase separation. Creaming takes place when two droplets approach each other without losing their identity, which occurs when the density differs between the two phases of the emulsion. A comparison of coalescence, breaking, and flocculation is summarized in Table 2.2.

Table 2.2: Comparison of coalescence, breaking, and flocculation

	Coalescence	**Breaking**	**Flocculation**
Identity of individual droplets	lost	lost	maintained
Reversibility of the process	irreversible	irreversible	reversible
Level of change	microscopic	macroscopic	microscopic
Phase separation	no	yes	no

2.9.2 Microemulsions and Nanoemulsions

The terms ‘‘microemulsions’’ and ‘‘nanoemulsions’’ are used interanchangably in the scientific literature. However, they are distinctly different types of colloidal dispersions: a microemulsion is thermodynamically stable, whereas a nanoemulsion is not. There is also different opinion about the upper particle size limits for nanoemulsions of 500 nm, 200 nm and 100 nm and it was not specified whether this limit is particle radius or particle diameter. Nanoemulsions are also known as miniemulsions, fine-dispersed emulsions, submicron emulsions.[44,46]

A microemulsion is a thermodynamically stable colloidal dispersion consisting of small spheroid particles of a dispersed phase dispersed within a continuous phase. Microemulsion is also referred to as droplet microemulsion or swollen micelle systems. A nanoemulsion is defined as a thermodynamically unstable colloidal dispersion consisting of two immiscible liquids, with one of the liquids being dispersed as small spherical droplets in the other liquid.

A thermodynamically stable microemulsion has a milky white appearance, as shown in Figure 2.5. An emulsion of this nature can be prepared using surfactants with concentrations higher than 20 wt%. A nanoemulsion appears transparent or translucent and can be produced with the addition of a smaller amount of surfactant than is required for a microemulsion. Unlike a microemulsion, a nanoemulsion is kinetically stable, resulting in long-term stability.[47]

A nanoemulsion indicates a pronounced stability in suspension due to the very small size: less than 500 nm. The stability of a nanoemulsion is the primary reason for its suitability for templating and as a nanoreactor. Rather than the thermodynamic stability of a microemulsion, a nanoemulsion has kinetic stability that can prevent phase separation for months and provide the ability to withstand the effects associated with temperature change and dilution.

Figure 2.5: Photograph of a nanoemulsion (left) and a macroemulsion (right) with droplet diameters of 35 nm and 1µm, respectively, Reprinted with permission from Ref (48).

2.9.3 Nanoemulsion Preparation Methods

Two main methods are used for preparing nanoemulsions: high-energy and low-energy.

2.9.3.1 High-Energy Methods

With high-energy methods, a high level of energy is used to break large droplets into smaller ones, and a large quantity of surfactant is required. The high-energy source might be ultrasound generators or high-pressure homogenizers. The formation of a nanoemulsion in this way is dependent on the quantity of the energy, the amount of the surfactant, and the nature of the components. A nanoemulsion prepared using high-energy methods is highly sensitive to any changes in composition.

When energy consumption is considered, the high-energy method compares unfavourably with the low-energy method. With the high-energy method, the amount of energy required increases with scaling up, an effect that does not occur with the low-energy method. As well, part of the energy is lost, especially with sonication, which dissipates a portion of the energy. From an application perspective, nanoemulsions prepared using the high-energy method are useful for generating polymeric nanoparticles, where the formulation parameters are directly controllable if any component is added that exceeds the formulation parameters, in which case destabilization can easily occur. Nanoemulsions prepared with the high-energy method are unsuitable for encapsulating fragile molecules such as peptides, proteins, or drugs, where degradation or activity loss during the processing is probable because of the high energy involved in the media.[46]

2.9.3.2 Low-Energy Methods

The phase inversion method is characterized by the use of small amounts of surfactants and a low-energy source and can be subdivided as either catastrophic inversion also known as Phase Inversion Composition (PIC) or as isothermal inversion reversible process or transitional inversion which is known as Phase Inversion Temperature (PIT) as shown in Figure 2.6.

Phase Inversion Composition (PIC) occurs when the water volume fraction is changed, as shown in Figure 2.6. This irreversible process is based on the mechanism depicted in Figure 2.7, whereby the rapid coalescence of the droplets is caused by the increasing water volume, which forces the droplets to form a bicontinuous phase. With even greater increases in the water volume, the bicontinuous phase breaks down into micro- or nano-droplets, depending on the other conditions in the emulsion.

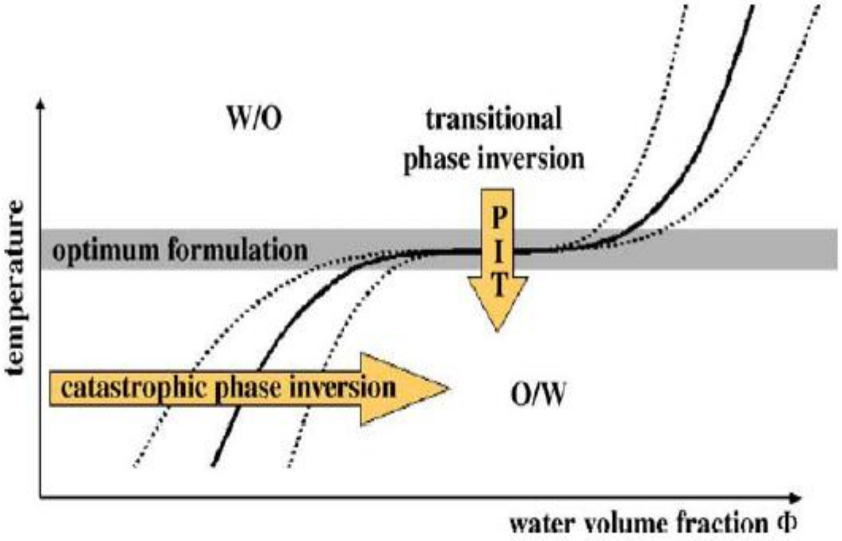

Figure 2.6: Schematic illustration of catastrophic phase inversion (Phase Inversion Composition) and transitional phase inversion, Reprinted with permission from Ref (48).

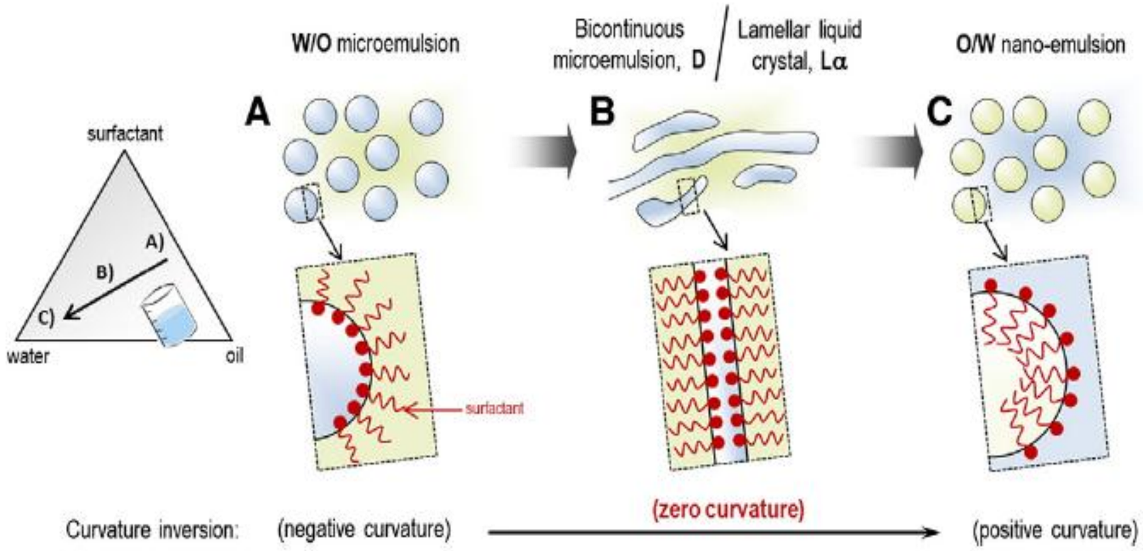

Figure 2.7: Schematic illustration of catastrophic phase inversion, Reprinted with permission from Ref (49).

Transitional inversion takes place when the temperature is changed, in which case it is then called a phase inversion temperature (PIT) process, or when the HLB is changed, which is called the isothermal inversion reversible process. The mechanism of transitional inversion processes is illustrated in Figure 2.8. During a transitional inversion, the temperature increases, and the hydrogen bonds that have formed between the nonionic surfactants and the water phase are broken down. As the hydrogen bonds break, the hydrophilicity decreases and the hydrodrophobicity increases, resulting in a change in temperature that affects the HLB. For example, as the temperature increases, the HLB of the surfactants also increases, forcing them to become more adsorbed in the oil phase. As a result, the curvature of the W/O interface gradually changes from positive to negative, forming O/W instead.

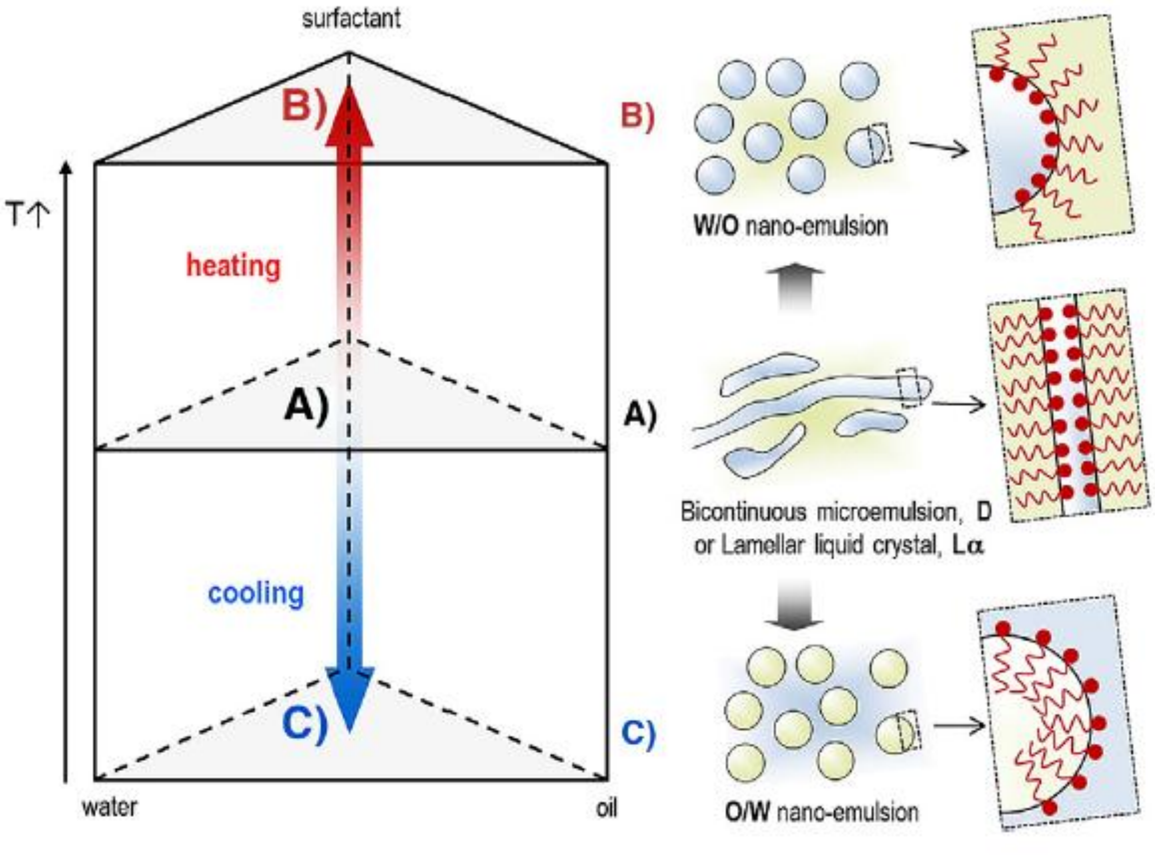

Figure 2.8: Schematic illustration of transitional phase inversion, Reprinted with permission from Ref. (49).

2.10 Functionalizing Porous Silica

A functional material is added to mesoporous silica to generate functionalized mesoporous silica which created new potential opportunities in materials sciences, catalysis and separation. Sanchez et al.[4, 50] reported an example for functionalizing mesoporous silica in which they integrated maghemite with mesoporous silica for use as a multifunctional device with twofold activity for the diagnosis and treatment of diseases. Magnetic materials are important for biomedical applications; however, they require a functional shell to allow them to be easily dispersed, to enhance their chemical stability, and to reduce their toxicity for use in imaging or therapy.

There are many possible pathways to modify porous materials when one wants to add to them a new function as schematically shown in Figure 2.9 [22] Generally, the functionalization methods are divided into direct synthesis or post synthesis, as depicted in Figure 2.10. The common factor between the two ways is that the modification is done through covalent linkage between the functional groups and the silica framework.

The direct synthesis methodology depends on condensing the functional material together with the silica precursor. Direct synthesis provides several advantages such as uniform distribution of the functional groups; short preparation time; and high dispersion and efficient immobilizing for large amounts of functional groups onto the mesoporous material surface. Therefore, mesoporous silica functionalized with organic groups can be obtained directly in one step, thus reducing the number of preparation processes and time.

The post-synthesis methodology was used to incorporate a wide variety of functional groups onto the surface of pre-synthesized mesoporous silica. Post-synthesis functionalization is limited by the density of Si-OH groups on the surface. However, grafting method tends to form more thermally stable silica networks and higher order than co-condensation.[51,52]

The direct synthesis and post-synthesis functionalization strategies are well established methods to functionalize mesoporous silica and can be also used to functionalize macroporous silica. Macroporous materials can be functionalized through adding functional material to template itself before synthesis. Examples of functionalizing macroporous materials are represented in the following paragraphs.

Z. Chen et al. prepared hollow silica spheres functionalized internally with Pd nanoparticles. Their process consisted of three steps; first, to adhere the Pd nanoparticles to the surface of carbon nanospheres ; second, to coat carbon nanospheres with a layer of mesoporous silica; and finally to calcine material to burn out carbon and surfactant.[53]

Cooper et al. prepared hierarchically porous composites containing site-isolated metal nanoparticles. They used polyacrylamide (PAM) beads as templates to induce hierarchical structure. They soaked PAM beads in aqueous acrylate stabilized golden nanoparticles (GNP) followed by soaking PAM/GNP in silica sol. The organic stabilizer at the surface of the nanoparticles was removed during the calcination process to result in the immobilization of naked metal nanoparticles in the porous inorganic oxide matrix which may be catalytically active for various chemical reactions.[54]

Dhainaut et al. prepared sulfonic hierarchical porous SBA-15 by post-synthesis grafting of sulfonic acid. They applied the prepared material as a catalyst for production of biodiesel from bulky plants oil and found that enhanced reactivity was observed. They explained the increased reactivity with the presence of macroporosity which induces better mass transport.[55]

Crippa et al. prepared TiO_2–SiO_2 composite materials with nanostructured TiO_2 particles grafted onto macroporous silica support. They wanted titania particles to be anchored on silica surface and not embedded into the silica matrix. They functionalized titania particles with different organic molecules so functionalized titania particles can easily interact with PEG onto the macropores of the silica matrix, as depicted in Figure 2.11.[56]

Despite the multitude of examples shown here, there is still a great potential of using the nanoemulsion technique for the internal functionalization of macroporous materials. Especially, the implementation of nanoemulsion as a carrier for the functional material precursors and/or nanoreactor to transform precursor to required functional material.

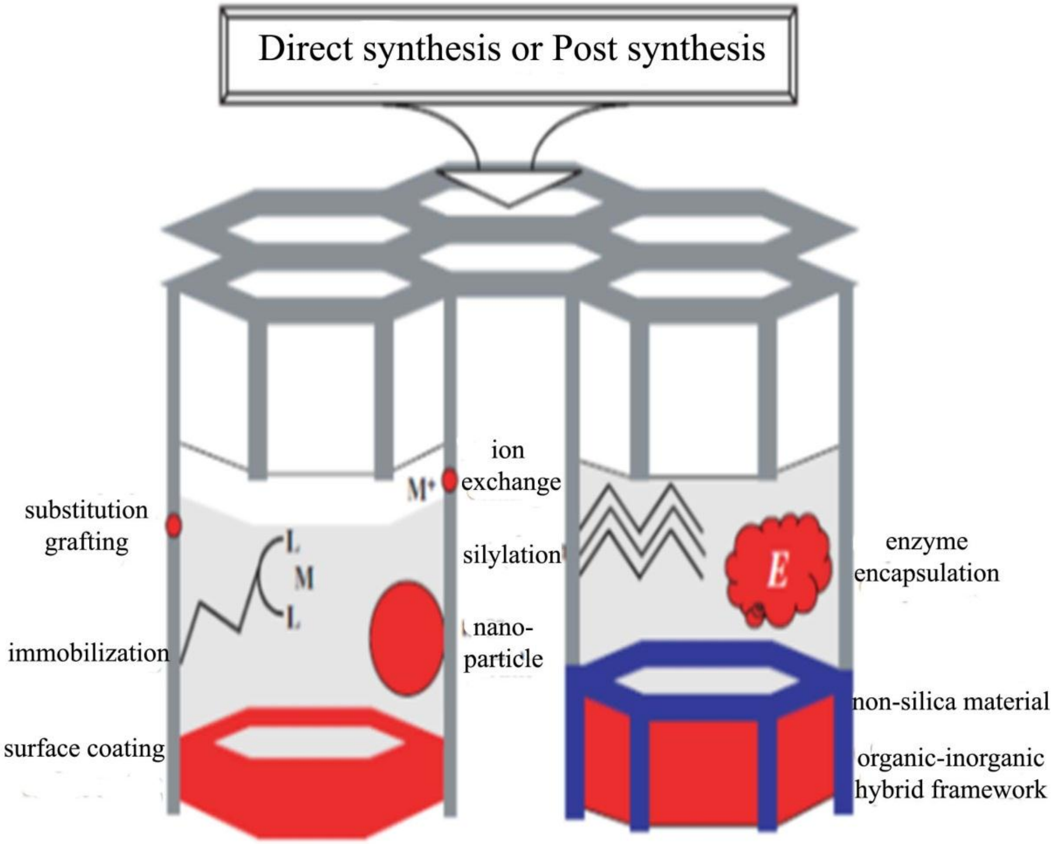

Figure 2.9: Schematic sketch of the various methods for the functionalization of porous material. There are many possible strategies and pathways to introduce novel functions in porous materials, Reprinted with permission from Ref. (22).

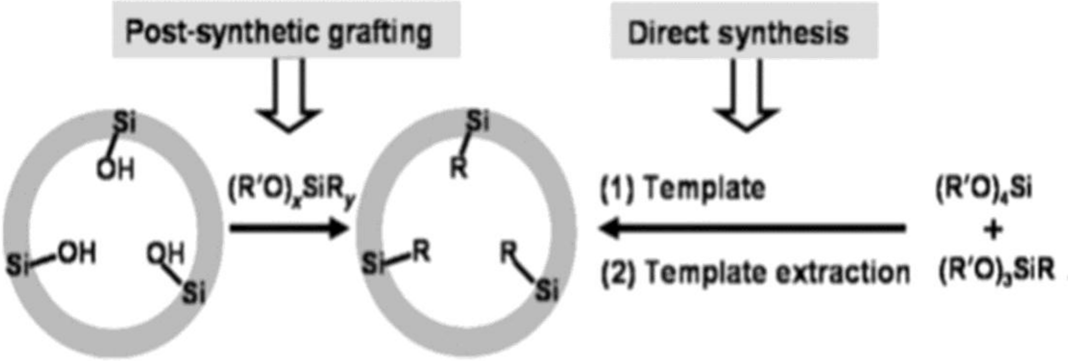

Figure 2.10: Synthesis of hybrid mesoporous materials containing organic groups that dangle into the channels, Reprinted with permission from Ref.(57).

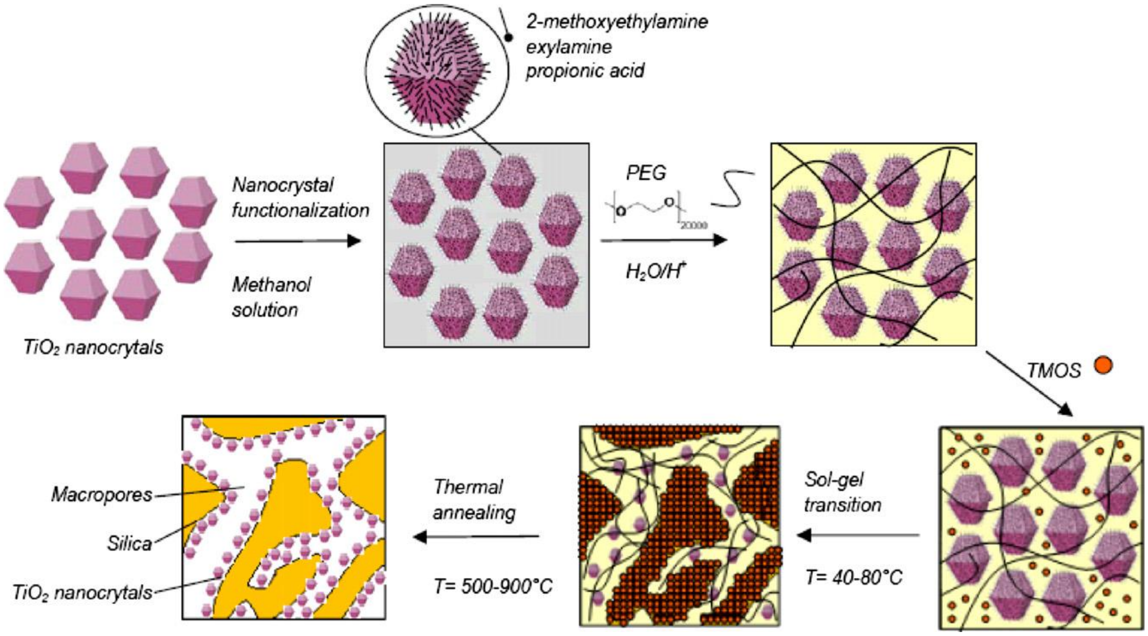

Figure 2.11: Preparation of titania nanocrystals anchored on macropores of silica matrix, Reprinted with permission from Ref (56).

2.11 Nanoparticles Prepared in Nanoemulsions

Nanoemulsions provide a unique reaction environment to prepare nanoparticles within the individual droplets of nanoemulsion (hundreds of nanometres). Nanoparticles, prepared within the restricted space of droplets, have some implications coming from the confinement of reaction within droplet. First, the final size of an individual nanoparticle is restricted to the amount of material available for the synthesis of one particle. Second, different types or hybrid nanoparticles can be prepared by multiple reactions conducted simultaneously within one droplet. Third, aggregation of crystals is limited by the number of crystals found in one droplet. Fourth, the crystal growth is limited by the surfactants on the surface of oil droplets. Fifth, the confinement can change the nucleation and crystallization behaviour and generate crystalline phases that are not thermodynamically stables.

Nanoemulsions can be considered as nanoreactors based on reactions that can be conducted in each droplet independently provided that the composition of the droplets does not change during reaction by merging droplets together. Using emulsion or nanoemulsion to prepare materials is more popular in polymer than inorganic materials as microemulsion-, emulsion-, and suspension polymerization. Also, emulsions and nanoemulsions are used in the encapsulation of drug.[58]

Few examples in the literature reported preparing inorganic nanoparticles within nanoemulsions. Landfester mentioned some of the possibilities of preparing inorganic nanoparticles within nanoemulsions as depicted in Figure. 2.12. Pink circles indicate reactions occurring in oil droplets of oil-in-water nanoemulsions and blue circles indicate reactions occurring in water droplets of water-in-oil nanoemulsions. Among the reactions that may take place in nanoemulsions are phase transition, precipitation, crystallization and sol-gel reactions. Han et al. fabricated indium nanoparticles by using molten indium and polyalphaolefin (PAO) oil. They prepared nanoemulsion by using ultrasounds and the average diameter of nanoparticle was about 30 nm as determined by TEM.[59]

Although the research using nanoemulsion as nanoreactor is promising, the author did not find any study which adequately covers the preparation of metal oxide starting with hydrophobic precursors by oil-in-water nanoemulsion.

2.12 Hydrophobic Precursors for Metal Oxide Nanoparticles

The process conditions required for the synthesis of monodisperse micrometre-sized particles are relatively well established, and similar principles could be applied to the synthesis of uniformly sized nanocrystals. The inhibition of additional nucleation during growth, in other words, the complete separation of nucleation and growth, is critical for the successful synthesis of monodisperse nanocrystals, for which a metal–surfactant complex would make an effective growth source. The research conducted for this thesis was not based on the use of toxic and expensive organometallic compounds such as iron pentacarbonyl. Instead, a metal oleate complex was prepared based on the reaction of inexpensive and environmentally friendly compounds: metal chlorides and sodium oleate, as shown in Figure 2.13. This process allows monodisperse nanocrystals to be obtained on an ultralarge scale of 40 g in a single reaction and without a further size-sorting process. When the multiple reactors are set up in parallel, multi-kilograms of monodisperse nanocrystals can be readily produced. The subsequent synthetic process is also environmentally friendly and economical because it uses non-toxic and inexpensive reagents such as metal chlorides. A third advantage is that the synthetic method is a generalized process suitable for synthesizing different kinds of monodisperse nanocrystals.[60]

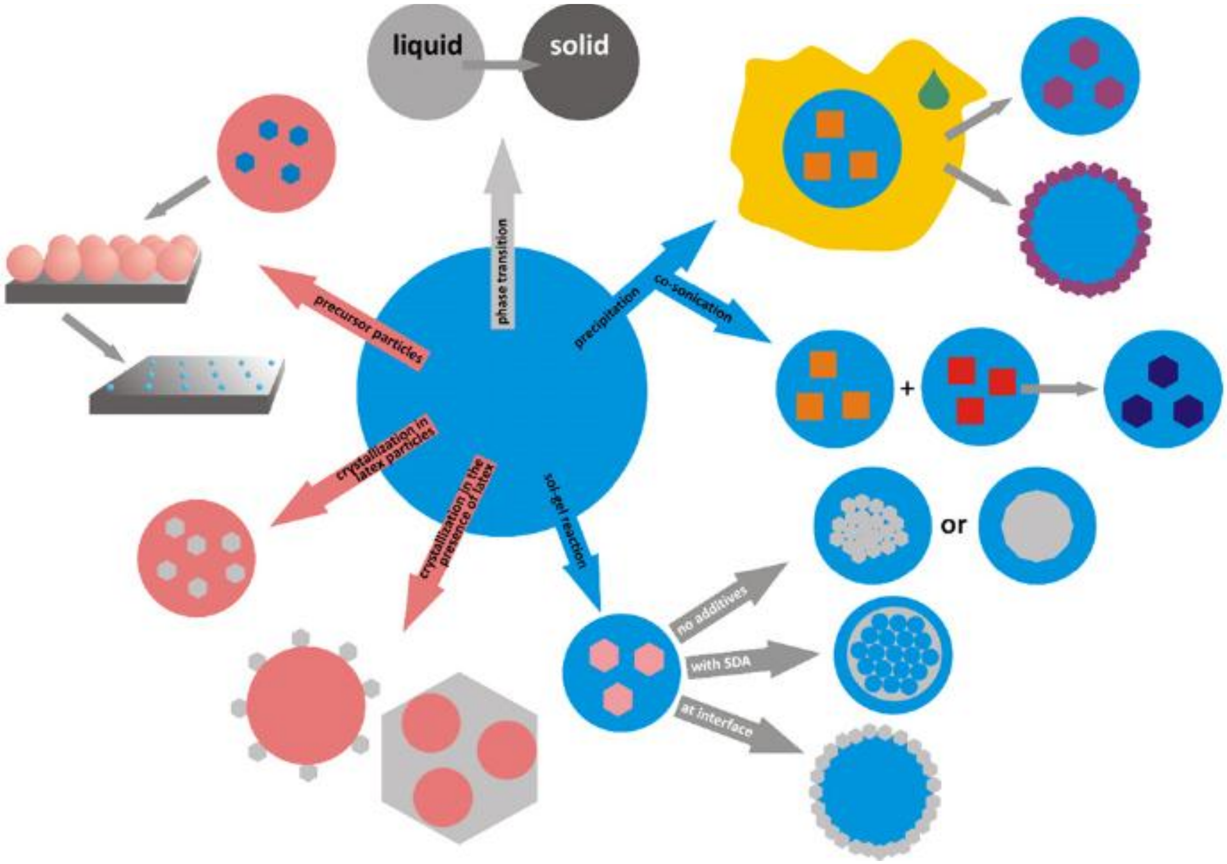

Figure 2.12: Schematic representation of the processes yielding inorganic nanoparticles within nanoemulsion, Reprinted with permission from Ref.(61)

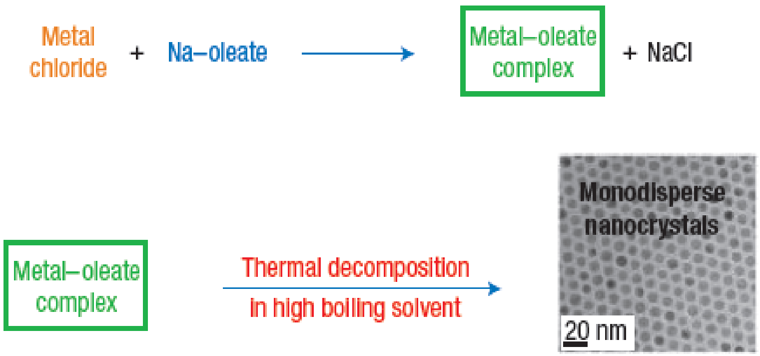

Figure 2.13: Metal oleate precursors were prepared from the reaction of metal chlorides and sodium oleate, Reprinted with permission from Ref. (60).

Chapter 3

Nanoemulsion: A Single-Parameter Study*

3.1 Overview

This chapter presents an analysis of the parameters that control both the stability and tunability of oil-in-water (O/W) nanoemulsions prepared according to the phase inversion composition (PIC) method. The nanoemulsions were prepared with Tween 80 and Span 80, two nonionic surfactants that can be mixed in order to adjust the hydrophilic-lipophilic balance (HLB). Nanoemulsions that are stable for several days can be obtained using this method, and they remain unchanged even at high concentrations. This research has identified the critical distances of the interactions that control the degree of freedom in the motion of the oil droplets. The diameter of these oil droplets can be adjusted to between 65 nm and 200 nm. Varying the parameters, including the temperature of preparation, the surfactant-to-oil ratio (S/O), and the HLB, allows control of the final size of the nanoemulsion droplets.

3.2 Introduction

The interest in oil-in-water nanoemulsions is demonstrated by the still limited, but increasing literature on this topic.[1-12] To the knowledge of the author, the first study on preparation of nanoemulsions with Tween 80 and Span 80 was reported by Liu et al., who prepared paraffin oil-in-water nanoemulsions by the phase inversion composition (PIC) method, a low-energy emulsification process. They reported the preparation of stable nanoemulsions with diameters ranging from 100 nm to 200 nm.[13] The surfactants used in their system are a combination of Span 80, a sorbitan monooleate with a low hydrophilic-lipophilic balance (HLB = 4.3), and Tween 80, an ethoxilated sorbitan monooelate ester with a high HLB (HLB = 15).

Reprinted with permission from Manal Hessien, Nigel Singh, ChonHoon Kim, and Eric Prouzet, "Stability and Tunability of O/W Nanoemulsions Prepared by Phase Inversion Composition" *Langmuir*, 2011, *27* (6), pp 2299–2307 Publication Date (Web): February 2, 2011 (Article) DOI: 10.1021/la104728r.

Because these two surfactants possess the same backbone structure as shown in Figure 3.1, they can mix easily, leading to a controlled change in the final HLB.

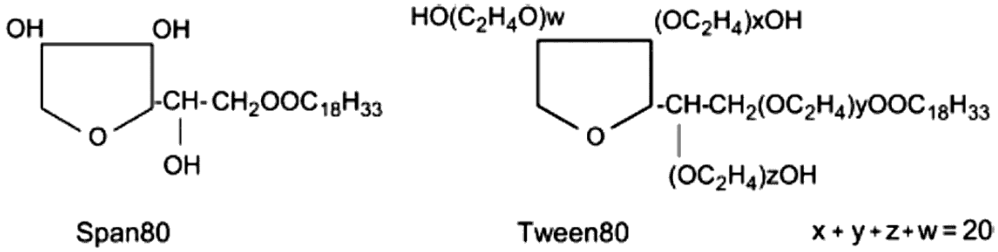

Figure 3.1: Molecular structure of Span 80 and Tween 80 surfactants.

Before any investigation of the synthesis of nanoemulsion-based porous materials was considered in this thesis, a complete study of the evolution and stability of nanoemulsions produced within a (Tween80:Span 80:paraffin oil:water) system was conducted to provide the required knowledge on the ways to use these systems, and on their stability as a function of different parameters (concentration, temperature) that could be modified during the future synthesis. Therefore, this study explored the influence of these parameters, and the results, which extend beyond those of previous analyses,[13] demonstrate the high stability of the nanoemulsions and how they evolve as a function of the synergy among the parameters.

Pey et al., using a mixture of nonionic Tween 20 and Span 20 surfactants, established that the oil droplet size decreases as the S/O ratio increases, and that this size exhibits a dependence on the percentage of Tween 20.[14] Fernandez et al. prepared microemulsions at 80 °C with a mixture of nonionic surfactants (Cremophor A6 and Cremophor A25) with a constant HLB and a preparation temperature. They found that increasing the surfactant concentration from 2.5 wt% to 10 wt% resulted in a change in the droplet profile from a bimodal at 10 μm and 0.6 μm to a single modal at 0.3 μm.[15] Liu et al. obtained also paraffin oil droplets with diameters as small as 100 nm from a mixture of Span 80 and Tween 80. They noticed that stable nanoemulsions with a droplet diameter of less than 200 nm were formed at 50 °C if both a critical S/O ratio and a specific value of the HLB were optimized.[13] The objective of this chapter was to study the parameters that can affect the stability and tunability of paraffin oil-in-water nanoemulsions. The understanding for the stability and tunability of nanoemulsion are essential before applying nanoemulsion as a template and/or nanoreactor.

3.3 Experimental Section

A number of experiments were conducted, with the goal of analyzing how varying the parameters affects the nanoemulsion produced. This section outlines the materials and methods that were used and explains how the samples were prepared for the analysis.

3.3.1 Materials

The oily phase used for the experiments was paraffin oil (d = 0.86 g/cm^3; Fluka). The emulsion was prepared with deionized water and stabilized using a mixture of two surfactants: sorbitan monooleate (Span 80, d = 1.08 g/cm^3, Mw = 428.6 g; Across) and polyoxyethylene (20) sorbitan monooleate (Tween 80, d = 0.994 g/cm^3, Mw =1,310 g; Sigma). All reagents were used as received without further purification.

3.3.2 Methods

Nanoemulsions were prepared by first dissolving the surfactants (Tween 80 and Span 80) into the paraffin oil, under gentle magnetic stirring for 15 min. Since the formation of these nanoemulsions is based on a W/O to O/W phase inversion, any trials that proceeded in a different addition order failed to produce stable nanoemulsions (Figure 3.2). The PIC mechanism was described as resulting from a curvature inversion created by the transition from the initial water-in-oil (W/O) structure to the final O/W nanoemulsion, as the amount of water, initially small, becomes progressively larger, as previously shown in Figure 2.9.[15-16] The critical step in the formation of O/W nanoemulsions by PIC is this phase transition, which explains why the addition of water to oil leads to nanoemulsions, whereas the addition of oil to water does not. This transition from W/O to O/W proceeds via an intermediate bicontinuous phase whose characteristic distance, which is dependent on the surfactant/oil (S/O) ratio, controls the final oil droplet size.

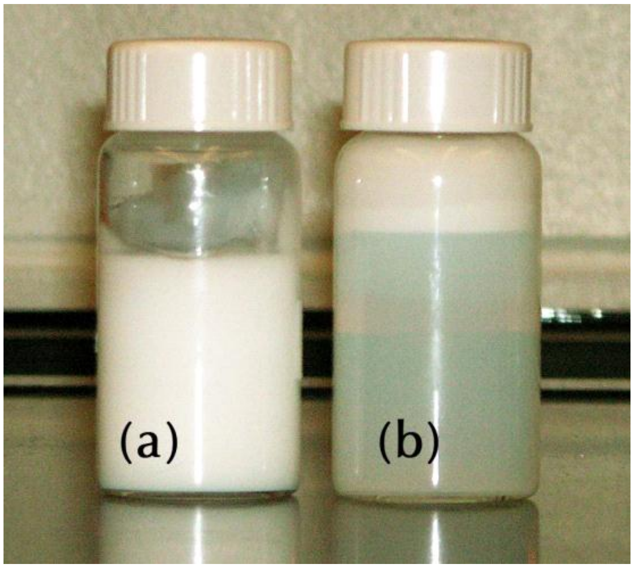

Figure 3.2: Structure of the nanoemulsion as a function of the sequence of addition of the components: (a) Tween and Span added into paraffin oil, and water added into the oil phase; (b) Tween dissolved first in water and Span80 dissolved in paraffin oil, and the aqueous solution then added into the oil phase. The first method leads to a stable nanoemulsion and the second method undergoes a rapid phase separation.

The required amount of water was added drop by drop to the mixture of oil and surfactant under slow magnetic stirring (60 rpm). Both the agitation speed and the addition rate were kept constant for all samples. For samples prepared at temperatures between 5 °C and 80 °C, the temperature of both the oil-surfactant mixture and the water were first adjusted separately to the required temperature in a cooling/heating bath before being mixed according to the above process. Varying the (Span 80:Tween 80) ratio enabled different HLBs to be achieved, depending on the amount of each surfactant, based on the following relationship:

$$\mathrm{HLB}_{\mathrm{mix}} = \mathrm{HLB}_{\mathrm{T}} * T\,\% + \mathrm{HLB}_{\mathrm{S}} * S\,\% = 15 * T\,\% + 4.3 * S\,\% \qquad (1)$$

where $\mathrm{HLB}_{\mathrm{T}}$ is the HLB for Tween 80 (15), T % is the mass percentage of Tween 80, $\mathrm{HLB}_{\mathrm{S}}$ is the HLB for Span 80 (4.3), and S % is the percentage by weight of Span 80. The size of the nanoemulsion droplets was studied through dynamic light scattering (DLS) (Vasco, from Cordouan Technologies). This system allowed for a determination of the diffusion coefficient of the emulsion droplets, even in very concentrated systems, from which the hydrodynamic diameter was deduced based on the Stokes-Einstein equation:

$$D = (k_B T) / (3\pi \eta D_h) \qquad (2)$$

where D is the diffusion coefficient, η is the viscosity of the emulsion, T is the temperature, k_B is the Boltzmann constant, and D_h is the hydrodynamic diameter.

A 60 mW monomode red laser (λ = 658 nm) dynamic light scattering (DLS) with variable intensity was used to obtain the measurements, which were carried out at a variety of temperatures (from 25 °C to 70 °C) with the detector set at 135 °C. The correlation parameters were adapted for each sample (sampling time x number of channels) in order to collect the whole autocorrelation curve. The accuracy and reproducibility of the results were checked by running several measurements with different recording times. Most of the autocorrelation curves were fitted with a single-size cumulant model, the lack of polydispersity being checked in parallel with Padé-Laplace fits.[17-18]

3.3.2.1 Samples for the analysis of temperature and dilution

A nanoemulsion (HLB = 11.6) was prepared with the following mass composition: 2.25 g Span 80, 4.77 g Tween 80, 20.0 g paraffin oil, and 73.0 g water. The measurements were carried out at temperatures between 25 °C and 70 °C, with temperature steps of 5 °C, and with the nanoemulsion being diluted (in mass) by a (nanoemulsion :dilution water) ratio varying from 1:1 to 1:500. Additional samples with lower water content were also prepared as a means of extending the study range. Their composition is listed in Table A.1 (Appendix A).

3.3.2.2 Samples for the analysis of the surfactant/oil weight ratio (S/O) and HLB

A first series of analyses were carried out with nanoemulsions prepared with the same HLB = 11.6, and an S/O ratio varying from 0.2 to 1.0. The samples are listed in Table A.2. To avoid any interdroplet interaction that could hamper the free motion of nanoemulsions, all samples were diluted before measurement with a nanoemulsion:water dilution of 1:1,000. A second series of analyses were run with samples prepared with different HLBs, as listed in Table A.3.

Previous studies referred to a relationship between the HLB and the S/O was based on previous results indicating that nanoemulsions prepared at different temperatures (30 °C, 40 °C, and 50 °C) exhibit a stability domain that depends on their HLB (11.3, 10.7, and 10.2, respectively) and that different oil droplet diameters are obtained (240 nm, 200 nm, and 150 nm, respectively).[6] A possible relationship between the HLB and the nanoemulsion size was extrapolated from these results:

$$HLB_{mix} = 8.4 + 0.012D_h \qquad (3)$$

Therefore, different nanoemulsions were prepared with different S/O ratios and different HLB_{mix} values based on equation (3). The value of HLB_{mix} was calculated from an evaluation of the diameter D_i, based on the volume (or mass of oil Q_i) and surface S_i of the oil droplets, which depends on the S/O ratio. Derivation of equation (4) is in Appendix A.

$$S_1 / S_2 = Q_1 / Q_2 = (n_1 / n_2)\,(D_1/D_2)^2 = D_2 / D_1 \qquad (4)$$

Because the goal of this study was to evaluate whether a steady change in D_h could result from a change in the HLB, a first approximation was based on the assumption that variations in the Tween 80:Span 80 ratio have no effect on the surface coverage. Although this initial assumption was not fully confirmed by the following analyses, those results do not drastically affect the conclusions that can be drawn from this analysis. Previous experimental values were used as a starting point, [6,15] with D_1 = 240 nm, S_1 = 5 wt%, and oil = 20 wt%, and the value of a droplet with a diameter D_2 was estimated when the amount of surfactant S_2 is modified (i.e., S/O) based on equation (4), and the value of the HLB is changed by altering the Tween 80:Span 80 balance according to equation (3).

3.3.2.3 Samples for the analysis of the influence of the preparation temperature

Three series of nanoemulsions (HLB = 11.6) with S/O ratios equal to 0.25, 0.5, and 1.0 were prepared at temperatures ranging between 5 °C and 80 °C, as listed in Tables A.4 and A.5. All DLS analyses were carried out at 25 °C, and the samples were diluted based on a dilution ratio of 1:2000 after the existence of a nanoemulsion had been confirmed from an examination of the pristine preparation.

3.4 Results and Discussion

3.4.1 Influence of Concentration and Temperature of Analysis on Stability of Nanoemulsion

3.4.1.1 Concentration

DLS provides information about the diffusion coefficient D of the scattering objects, from which the size is deduced via the Stokes-Einstein formula. Any factor that could modify the diffusion coefficient could therefore be translated into an apparent size variation, and any interaction that could hinder the free motion of the scattering objects will have a correspondingly strong effect on D and consequently on D_h. The initial aim of this research was to explore the limit of stability of the nanoemulsion structure as the concentration increases because such a property has extremely important consequences for the further use of these nanoemulsions as templates. The evolution of the hydrodynamic diameter D_h (respectively the diffusion coefficient D) as a function of the dilution ratio is shown in Figure 3.3 (respectively Figure A.1). The D_h (respectively D) decreases (respectively increases) drastically as the dilution ratio increases, until a constant value of D_h = 250 nm is finally reached for a dilution ratio greater than 1:50. This dilution is the threshold beyond which no interaction between oil droplets is observed. It results in constant values for the diffusion coefficients beyond this dilution ratio (Figure A.1), hence the correct “real” value of D_h.

The actual hydrodynamic diameter of the nanoemulsion prepared for this study is concluded to be 250 nm, and a dilution ratio $\geq$ 100 was established as the requirement for a correct determination. In subsequent analyses, all measurements were carried out with dilutions equal to 1:1000 or 1:2000 to ensure that no interaction between the oil droplets could disturb the final D_h value.

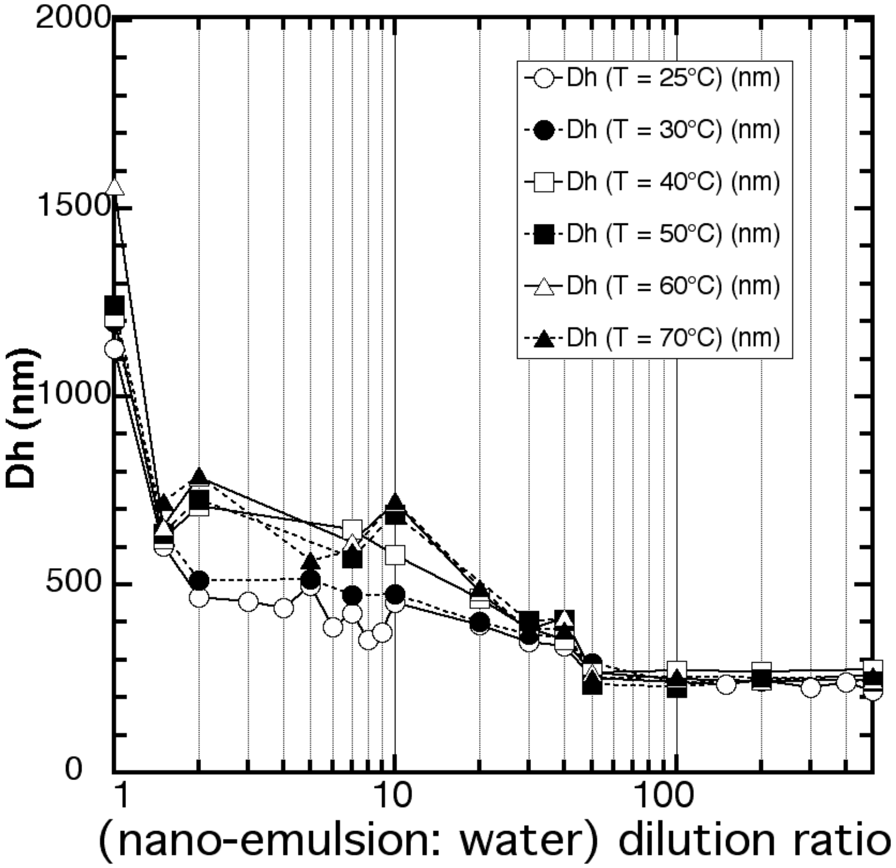

Figure 3.3: For different analysis temperatures, the evolution of the apparent hydrodynamic diameter D_h of the nanoemulsion as a function of the dilution ratio.

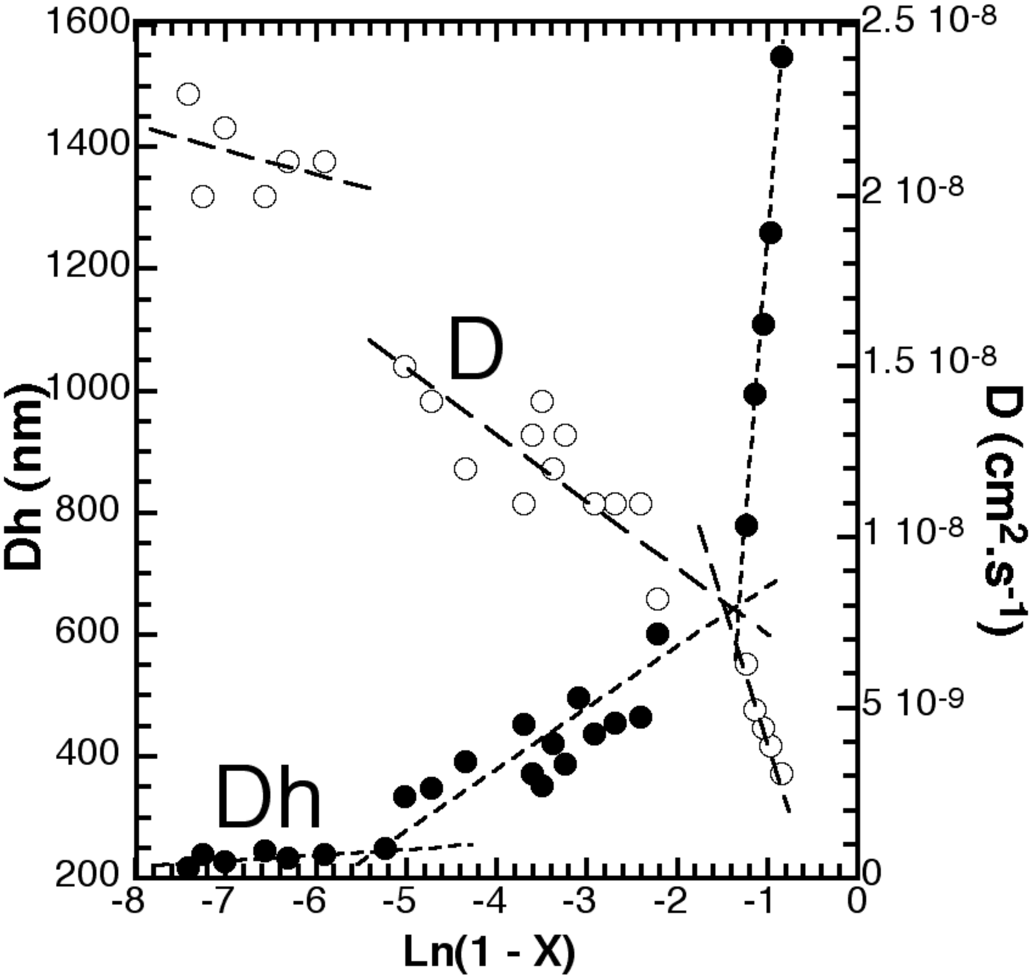

Figure 3.4: Evolution at 25 °C of the apparent hydrodynamic diameter D_h (●) and the diffusion coefficient (○) as a function of Ln(1-X), where X is the water content of the nanoemulsions after dilution. The dashed lines are provided as a visual aid.

This analysis also demonstrates that the nanoemulsion remains surprisingly stable even at high concentrations even though the size deduced from D is wrong, the autocorrelation function can still be fitted with a single size (Cumulant) model (see Figures A.2 to A.4, in Appendix A), which reveals that no polydispersity is observed. In addition, the ability to observe mobile objects that scatters, even at high concentration reveals the lack of transition from moving oil droplets to a static bicontinuous phase. The stability of the nanoemulsion was further investigated through the preparation of samples with additional concentrations (Table A.1, in Appendix A). These values are reported as a function of Ln(1 - X) ($0 < X < 1$)

with X being the total water amount (in mass) (Table A.6, in Appendix A). The choice of this variable allowed the description of the influence of dilution on DLS parameters to be more precise, especially at high values of dilution. Figure 3.4 displays the evolution of the D_h and the D as a function of Ln(1-X).

Three domains can be clearly identified. At higher dilutions (small Ln(1-X)), the value of D_h is constant and corresponds to the actual diameter (D_h = 250 nm). This domain extends from the highest dilution down to a 1:50 dilution (X = 0.9947, ln(1 - X) = -5.24). A second region that displays a steady increase in the apparent hydrodynamic diameter and a parallel decrease in the diffusion coefficient is defined for $0.74 < X < 0.9947$. The final domain, characterized by a sharp increase in the hydrodynamic diameter and a parallel decrease in the diffusion coefficient, can be observed for $X < 0.74$. This three-step evolution of the mobility of the nanoemulsion as a function of increasing concentration (decreasing water content) demonstrates an increasing interaction between the objects, leading first ($0.9947 < X < 0.74$) to a limited hampering of mobility, followed by a significant restraint in mobility when the water content by weight decreases to less than 0.74.

3.4.1.2 Temperature of Analysis

The samples previously tested were also used in order to determine the possible influence of the temperature on the stability and structure of the nanoemulsion. In Figure 3.5, the measurements of D_h obtained for three dilutions and recorded at different temperatures between 30 and 70 °C are reported. Only the results that correspond to dilutions high enough to prevent any interaction between the nanoemulsion droplets are reported as the Brownian motion should affect the diffusion coefficient of nanoemulsions at higher concentrations. These results clearly demonstrate that, once it has been formed, the size of the nanoemulsion is independent of the temperature of the nanoemulsion itself. On the other hand, the effect of the temperature during the preparation of nanoemulsions is much more substantial and an important parameter in the final structure of oil droplets as will be discussed in subsequent sections.

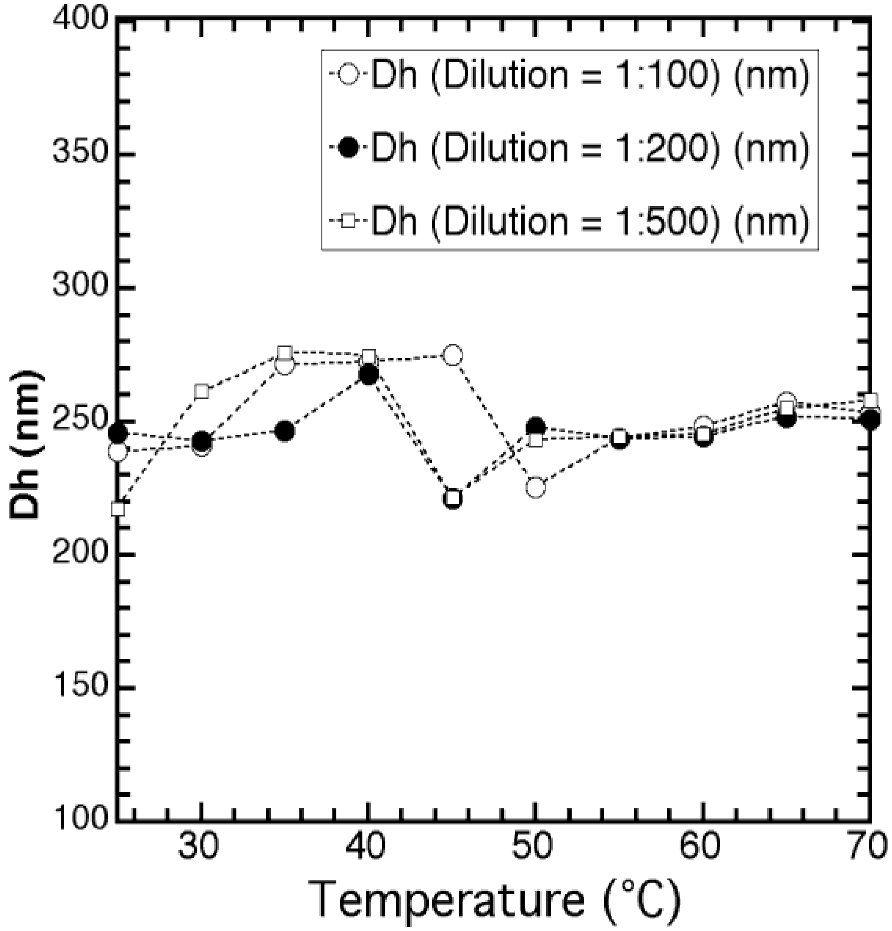

Figure 3.5: Evolution at different analysis temperatures of measurements for the apparent hydrodynamic diameter D_h of the nanoemulsion as a function of the dilution ratio.

3.4.1.3 Stability of Nanoemulsions

Because the stability of nanoemulsions is an important parameter with respect to the use of these systems as templates, the limits of stability of the nanoemulsions were explored as a function of the water fraction adjusted either by dilution or by the preparation of more concentrated nanoemulsions (Tables A.1 and A.6, in Appendix A). DLS confirms the stability of these nanoemulsions and the motion of isolated objects is still detected at high concentration. This stability is confirmed based on the single-size fit for all DLS measurements, which indicates the absence of aggregation or partial merging as the water content is reduced (Figures A.2 to 4, in Appendix A).

Nevertheless, the DLS results show that the diffusion coefficient D becomes constant only beyond a critical (nanoemulsion: dilution water) ratio of 1:100 (Figure A.1, in Appendix A) and that it corresponds to a hydrodynamic diameter D_h of 250 nm (Figure 3.3). The low D (respectively D_h) values (respectively high values) at dilution ratios lower than 1:50 do not correspond to a change in the nanoemulsion size but to an increasing steric cluttering that hinders the free motion of the oil droplets, leading to a decrease in the diffusion coefficient from which D_h is calculated. Beyond the experiments done, this observation demonstrates that careful attention must be given to DLS analyses for these systems with respect to the level of dilution required for correct measurements which could explain some discrepancy observed in the literature.

The results of the D and the D_h values as a function of the water content X (Figure 3.4) and the observation of three domains reveals an increasing interaction between the objects initially allowed to move freely (high dilution; zone I: $0.9947 < X$), then partially restrained (medium dilution; zone II: $0.74 < X < 0.9947$), and finally with severely hampered mobility (high concentration; zone III: $X < 0.74$). These observations can be related to the average water distance between two oil droplets, as a function of the water content (Figure 3.6).

Water distance between two oil droplets is calculated as follows. Example of a calculation for a sample with the following composition: Water = 73 g, oil = 20 g, Tween80 = 4.77 g, Span80 = 2.25g with density equal to 1.0, 0.86, 0.994, and 1.08, respectively. The total volume of this sample is equal to 103.48 cm^3 ($1.03X10^{23}$ nm^3). The hydrodynamic diameter (D_h) of an oil droplet is 250 nm, and its volume is $V = \pi D_h^3/6 = 8.18X10^6$ nm^3. As the total oil volume is 23.26 cm^3 = $23.26X10^{21}$ nm^3, the number of oil droplets in this composition, with 20 g of oil, is equal to $23.26X10^{21}/8.18X10^6=2.84X10^{15}$. The whole volume can be divided among the oil droplets by assigning a cubic cell to each oil droplet. The volume of one cubic cell is equal to $1.03X10^{23}/2.84X10^{15} = 36.3X10^6 nm^3$.The length of this cube (l) is equal to 330 nm, and the water thickness is equal to 330-250 = 80 nm. The length l corresponds to the diameter of a sphere made of the oil droplet (D_h = 250 nm) plus a water shell of 40 nm. Hence, in this example, the water distance between two oil droplets is equal to 80 nm.

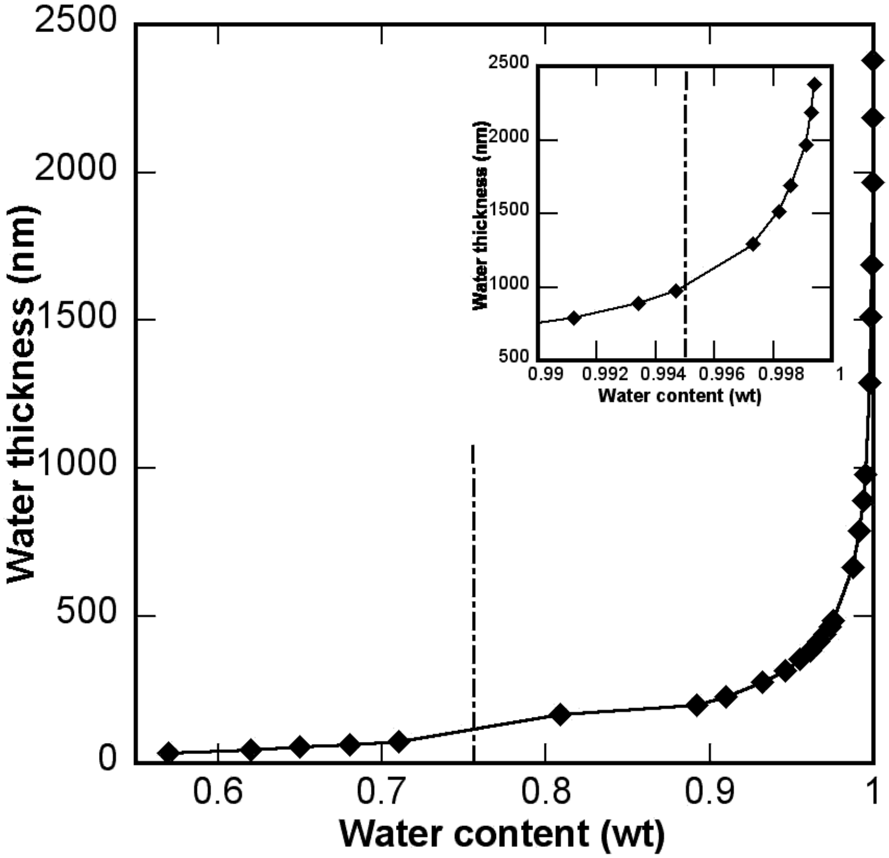

Figure 3.6: Variation of the water thickness separating two nanoemulsion droplets as a function of the water content. The vertical dashed lines correspond to the breaks in the evolution of the diffusion coefficient measured by DLS.

It can be deduced from this analysis that the oil droplets can move freely only if the water thickness between two droplets is greater than 1.0 μm (X > 0.9947) (Figure 3.6, inset), which corresponds to a water shell thickness of 500 nm around each oil droplet. Below this value, the nanoemulsion motion is progressively hindered down to a water content of X = 0.74. This value corresponds to a water thickness of 120 nm (Figure 3.6), that is, a water shell thickness of 60 nm around each droplet (Figure 3.7).

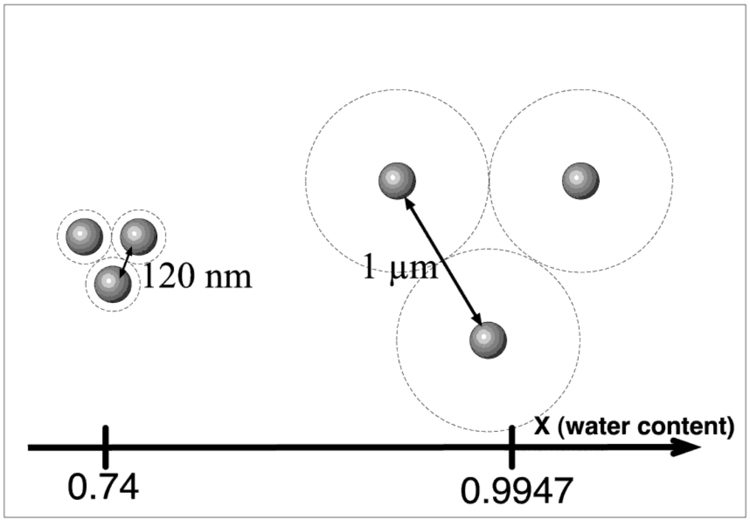

Figure 3.7: Characteristic distances in the nanoemulsion (droplet diameter = 250 nm), as a function of the water content, deduced from results displayed in Figure 3.6.

For X < 0.74, the diffusion coefficient D decreases extremely rapidly as a result of oil droplets coming into close contact. As previously observed, these oil droplets are extremely stable because they do not merge even when the water content becomes so small that the whole nanoemulsion is almost gelled.

This stability was also demonstrated by the DLS analyses carried out at different temperatures (Figures 3.5), which do not reveal any change in the structure or size of the oil droplets. This finding confirms that, unlike methods based on mechanical emulsification, low-energy emulsion methods such as the PIC process lead to a very stable structure resulting from a fine physical-chemical balance. These nanoemulsions are stable for several days, especially when they are stored in a diluted form, whereas nanoemulsions prepared by high-energy mechanical mixing are very often stable only for a period of two hours up to two days.[19]

At this stage, nanoemulsion is prepared by PIC method and its stability is confirmed under different concentrations/dilutions and under different temperatures of measurements. It is worth noting that after about 30 months, nanoemulsions are still homogenous with one phase as can be seen by naked eye. Beyond the stability of nanoemulsion, it is important to better understand how the oil droplet size can be tuned which will in turn change the pore size when using nanoemulsion as a template. Tunability of oil droplet size is achieved by changing S/O weight ratio, HLB and temperature of preparation.

3.4.2 Influence of the Surfactant/Oil Weight Ratio (S/O) and HLB

The size of the oil droplet is supposed to be the result of the balance between the total oil volume and the maximum coverage surface that can be created by the surfactant heads to embed this oil. As the surfactant molecules cover the surface of the oil droplet, it would be expected that increasing the surfactant-to-oil ratio would induce a shrinking of the oil droplet, as a result of the parallel increase of the total coverage surface, provided that all other parameters remain constant.

A first series of samples was prepared with different S/O ratios and a constant HLB_{mx} = 11.6 (Table A.2). DLS measurements were recorded at 25 °C with a 1:1000 dilution ratio. The size of the nanoemulsion decreased as expected, and increasing the S/O ratio from 0.2 to 0.5 leads to the decrease of the D_h from 155 nm to 135 nm ((●) in Figure 3.8).

A second series of samples were prepared with different S/O ratios but with an HLB_{mix} (□) varied from 12 to 9.4 based on equations (3) and (4). Compared with the previous samples, a variation in the D_h (■) toward smaller sizes can be observed, the D_h becoming equal to 150 nm at HLB = 11.3 instead of 155 nm at HLB=11.6 for constant S/O = 0.25 for both samples. This value of D_h still decreases from about 175 nm down to 105 nm as the S/O ratio increased from 0.2 to 0.5, but surprisingly, D_h increases again as S/O values become larger than 0.5. This analysis confirms the relevance of the S/O ratio to size control, but the increasing D_h above S/O = 0.5 appears to be quite contradictory to the single influence of that parameter alone. Both the S/O ratio and the HLB_{mix} seem to have a combined influence on variations in the D_h.

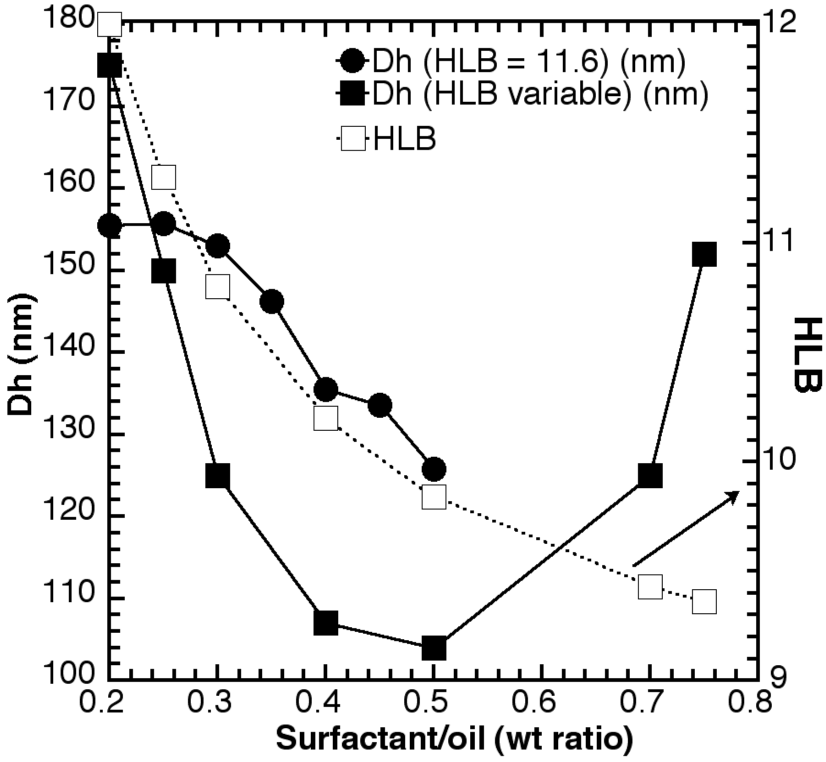

Figure 3.8: Evolution of the hydrodynamic diameter D_h measured at 25 °C, as a function of the surfactant/oil weight ratio: (●) for a constant HLB $_{mix}$ and (□) for an HLB $_{mix}$ varied according to the (□) curve.

3.4.3 Influence of the Temperature of Preparation

Samples were prepared at temperatures between 5 °C and 80 °C with the S/O ratio equal to 0.25, 0.5, and 1.0 but all DLS measurements were recorded at 25 °C (Figure 3.9). As the temperature of the preparation increases, it can be observed that the size of the nanoemulsion drops down, this effect being limited above 60 °C. This trend is more significant for the highest S/O values: for S/O = 0.25, the D_h decreases from 195 nm (10 °C) to 170 nm (60 °C) with a 13 % shrinkage; for S/O = 0.5, the D_h decreases from 160 nm (10 °C) down to 95 nm (70 °C), with a 40 % shrinkage; and for S/O = 1.0, the D_h decreases from 117 nm (10 °C) to 57 nm (60 °C), with a 51 % reduction. These results confirm that the temperature of the preparation has a drastic effect on the size of the nanoemulsion droplets and that these systems remain stable even after the system has been cooled to room temperature. In Figure

3.9, by increasing the S/O ratio from 0.25 to 1 it is always combined with a decrease in D_h keeping the temperature of preparation constant.

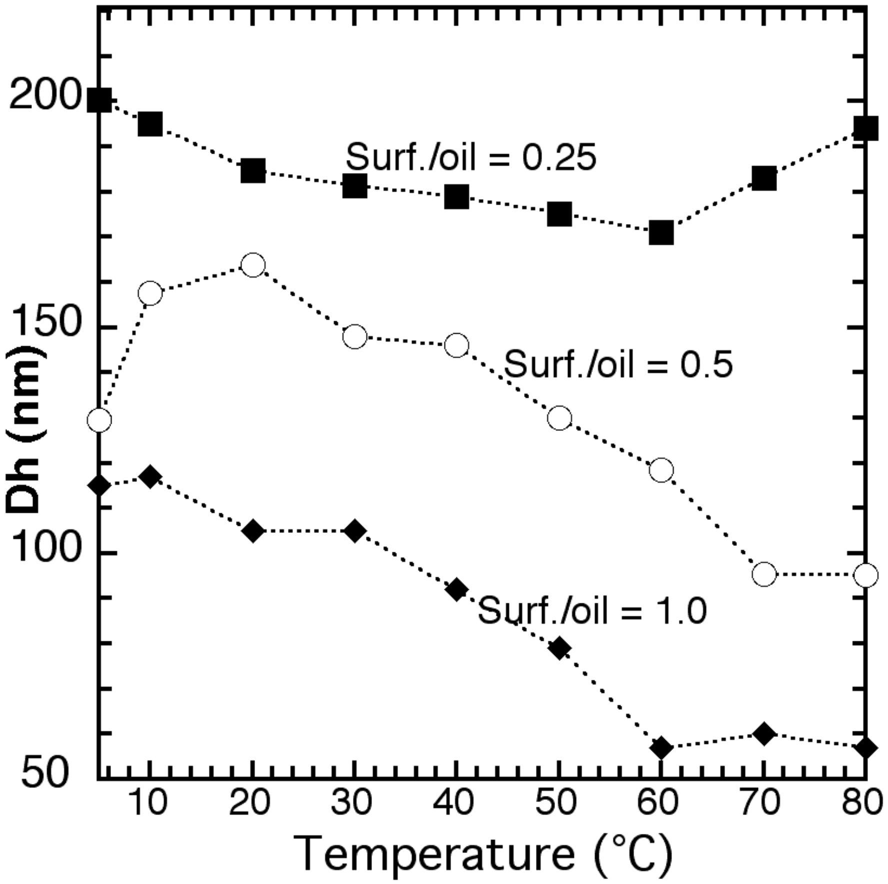

Figure 3.9: Evolution of the hydrodynamic diameter D_h measured at 25 °C, as a function of the temperature of preparation of the nanoemulsions, for different surfactant-to-oil weight ratios: (■) 0.25, (○) 0.5, and (♦) 1.0 (HLB = 11.6).

3.4.4 Tunability of the Nanoemulsions

As mentioned before, the size of the nanoemulsion droplets can be theoretically modified if the correct balance between the total surface of the oil droplets and their size is determined, the total oil volume being constant. Different methods can be employed in order to achieve this balance, the obvious method being simply to increase the S/O ratio. The analyses (Figures 3.8 and 3.9) conducted for the research presented in this work confirm this evolution, and the achievement of this balance can be assigned to the higher concentration of surfactant that allows for the formation of a larger surface of oil droplets while the overall oil volume remains constant. This condition can be achieved only through the creation of smaller droplets.[11, 20-21] However, this effect is limited, and it can be observed (Figure 3.8) that reducing in parallel the HLB according to equation (3) is more important.

Once the nanoemulsions have been prepared, their size remains independent of any further temperature fluctuation, but the initial temperature of preparation has an enormous influence on the final droplet size (Figure 3.9). This phenomenon can be explained by the increasing hydrophobicity of nonionic surfactants (here, Tween 80 since Span 80 is already hydrophobic as proved by its low HLB) resulting from the increase in the preparation temperature. Without specific information about the actual structure of the bicontinuous phase, it can be assumed that Tween 80 becomes more hydrophobic and shifts progressively from the O/W interface into the oil phase, a shift that should modify the structure of the intermediate bicontinuous phase, leading to smaller droplets. However, this single parameter does not fully explain the evolution of the D_h as a function of the preparation temperature when the S/O ratio varies (Figure 3.9). This reduction in size can be observed to reach a limit when the temperature increases (60 °C for S/O = 1.0 and 70 °C for S/O = 0.5), and an increase can even be observed for S/O = 0.25. It is most probable that a full understanding of this evolution could be acquired by a close analysis of the intermediate bicontinuous phase, which should be investigated based on other analyses, especially by means of ultra-small angle X-ray scattering.

It was also observed that decreasing the HLB_{mix} by increasing the Span 80 over Tween 80 ratio leads also to a reduction in the oil droplet size (Figure 3.8). This result seems somewhat counter intuitive because Span 80 is characterized by its small molecular area (0.46 nm^2), compared to Tween 80 (2.48 nm^2).[10] It would be expected that decreasing the HLB_{mix} by adding a higher proportion of Span would lead to a smaller equivalent surface and hence a larger droplet size, provided that the S/O ratio remains constant. However, the HLB_{mix} is defined by weight, rather than molar proportions (equation (1)), and decreasing the HLB_{mix} by increasing the proportion of Span 80 is not based on a one-to-one molecule exchange. Moreover, it results in a dramatic increasing of the number of moles of Span 80 because the molar weight of Span 80 is only 0.32 times that of Tween 80, as demonstrated by the calculation of the number of molecules of surfactants required for changing the HLB, and the resulting effect on the total surfactant surface area of decreasing the HLB from 12 to 9.4 by adapting the weight percentage in surfactant, results in a drastic increasing of the number of Span 80 molecules which results finally into a higher surface of surfactant heads, despite the fact that the head of Span is smaller than that of Tween (Figure 3.10). These results confirm that the actual effect of decreasing the HLB_{mix} results primarily in a larger surface coverage, and that there is no direct physicochemical influence of the HLB itself.

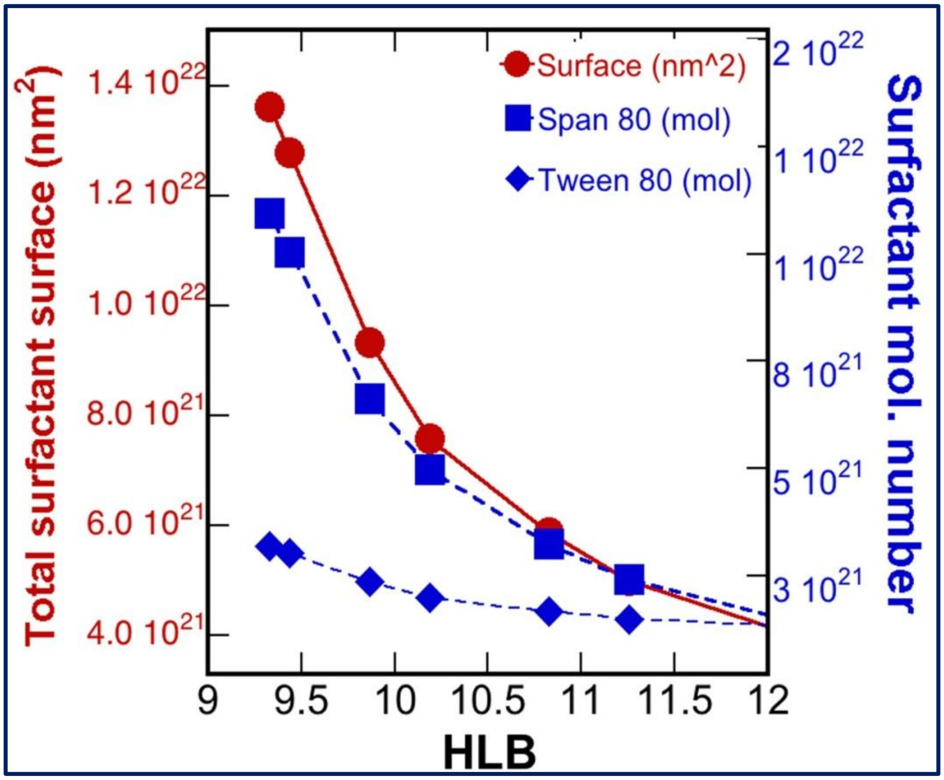

Figure 3.10: Evolution of the total surface of surfactant area, and the number of moles of surfactant (calculated from Table A.3) as a function of the HLB.

3.5 Summary

For both fundamental and applied development, researchers have begun to focus on nanoemulsions prepared with the low-energy emulsification method. The work conducted in this thesis has permitted the identification of the characteristic parameters that govern both the stability and tunability of nanoemulsions prepared with a combination of nonionic surfactants.

First, even at high concentrations, these systems are very stable, and no phase separation is observed for long time. Moreover, unlike nanoemulsions prepared by mechanical processes, these systems are stable over a period of weeks, especially when they are diluted. It must also be noted that interactions between the oil droplets occur even at rather high dilutions, and that DLS analyses must eliminate these interactions by providing an appropriate dilution. These nanoemulsions, once prepared, are not modified by temperatures within the 25 °C to 80 °C range. The tunability of these systems is controlled by a number of parameters: Surfactant-to-oil ratio, hydrophobic-lipophilic balance and temperature of preparation. Increasing surfactant-to-oil ratio from 0.25 to 1 is accompanied with a decrease in droplet diameter from 180 nm to 60 nm, keeping all the other parameters constant. By changing the temperature of preparation from 5 °C to 80 °C is associated with a decline in oil droplet size from 115 nm to 60 nm. Decreasing HLB from 12 to 9.8 is complemented with a drop in hydrodynamic diameter from 180 nm to 105 nm.

These systems are complex, and their structure depends on the close cross-interaction of parameters whose actual influence has yet to be determined. For example, both HLB and the temperature of preparation have an effect on the size of oil droplet; however, the temperature also has an effect on the HLB itself. As presented in Chapter 4, the application of an experimental design in order to study the interactions among the HLB, the temperature, and the surfactant-to-oil ratio is therefore important.

Chapter 4

Nanoemulsion: Experimental Design Study*

4.1 Overview

The parameters examined in Chapter 3 were discussed independently, but the entire stability of these nanoemulsions, and their tunability, results from a combination of all of the parameters. The process-mixture design method combines a mixture design with process design in order to describe the cross-links between parameters such as composition (mixture design, represented by a phase diagram), temperature of preparation, and hydrophilic lipophilic balance (HLB) (axis of the diagram). A number of parameters, among them the temperature of preparation, the surfactant-to-oil (S/O) ratio, and the HLB, allow the control of the final size of the nanoemulsions. These parameters can have conflicting effects on the oil droplet size, making size-design based on single parameter analysis, difficult. Therefore, the process-mixture design is a good choice because it permits the inclusion of cross-interactions into the final definition of preparation parameters for a given size of nanoemulsion. The hydrodynamic diameter D_h was chosen as a response for this study. Oil droplets of the nanoemulsion can be adjusted to between 65 nm and 400 nm by governing, either singly or collectively, a variety of factors, including the S/O ratio, the HLB, and the temperature of preparation.

Adapted with permission from Manal Hessien, Nigel Singh, ChonHoon Kim, and Eric Prouzet, “Stability and Tunability of O/W Nanoemulsions Prepared by Phase Inversion Composition” Langmuir, 2011, 27 (6), pp 2299–2307 Publication Date (Web): February 2, 2011 (Article) DOI: 10.1021/la104728r.

4.2 Introduction

Nanoemulsions are thermodynamically unstable but kinetically stable. This thermodynamic instability is the reason for the dependence of the final properties of nanoemulsions on all conditions involved during their preparation, including preparation conditions or formulation compositions. For this reason, traditional experimentation has been the method of studying nanoemulsions, but these experiments are time consuming because only one parameter at a time is changed while all other conditions are kept constant. Moreover, this type of experimentation assumes that the variables under investigation do not interact, i.e., do not affect one another, which is less than satisfactory. To overcome the drawbacks associated with traditional experimentation, and after the initial study reported in Chapter 3 that allowed us to clearly point out the meaningful parameters and how they act, an experimental design was used for optimizing the nanoemulsion preparation.[1]

Using a mixture of Span 80 and Tween 80, Liu et al. obtained paraffin oil droplets with diameters as small as 100 nm.[2] They noticed that stable nanoemulsions with a droplet diameter below 200 nm were formed at 50 °C if both a critical surfactant-to-oil ratio and a specific value of the HLB were optimized, but they did not explore this observation any further. Actually, to the author knowledge, no study has considered the complex and intersecting influence of all parameters (surfactant content, surfactant-to-oil ratio, HLB, preparation temperature) and proposed a full description of these systems. A few reports have partially addressed this problem by using methods such as factorial design, but they focused more on process parameters such as the addition rate versus stirring rate, and the surfactant-to-oil ratio versus the percentage of surfactant.[3] The work conducted for this thesis employed a more sophisticated method based on a process-mixture experimental design.[4,5] This method enabled an exploration of the combined influence of different chemical (components proportions, HLB) and physical (temperature of preparation) parameters on the final stability and tunability of these nanoemulsions, as a function of the actual phase diagram.

The objective of this chapter was to apply an Experimental Design to develop robust, reliable statistical models that can be used to construct the operating window (based on the input variables and required properties) and to perform response surface optimization for the design of paraffin oil-in-water nanoemulsion.

A three-component mixture design of the experiment was chosen for the study. The input variables are the proportion (in weight percentage) of the components: paraffin oil, surfactant mixture, and water. The response variable in this study is the hydrodynamic diameter of the oil droplet. The levels of all process variables (i.e. variables not related to the component proportions such as the components' properties and processing variables) should be kept as constant as possible. Mixture design is represented by simplex coordinate system which is a sided figure with q vertices in q-1 dimensions. The mixture design for a three-component mixture is presented in Figure 4.1.[6]

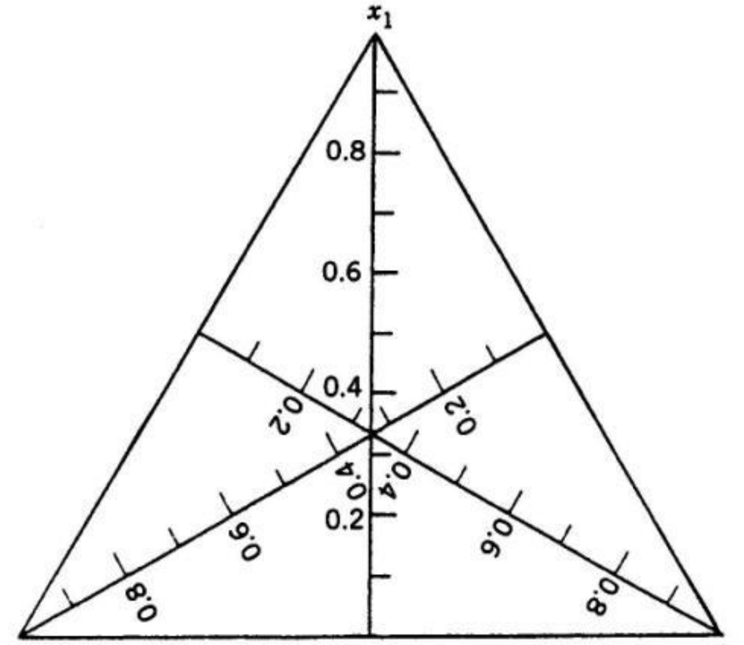

Figure 4.1: Simplex coordinate system for a three-component mixture.

Oil droplet size of nanoemulsion is not affected by composition only but also with variables rather than components (oil, water and surfactant) such as temperature and HLB. Process-

Mixture design is the experimental design used to follow both mixture and process effects on oil droplet size. This design combines the standard mixture design with factorial or fractional factorial design for process variables as illustrated in Figure 4.2.[6]

Mixture and process-mixture experimental design methodology have been applied to develop response surface models that can be used to correlate the input properties of nanoemulsions (composition and processing) to the hydrodynamic diameter of oil droplets of nanoemulsion. The models obtained can then be inverted to predict the hydrodynamic diameter of nanoemulsion at compositions and under processing parameters within the range applied.

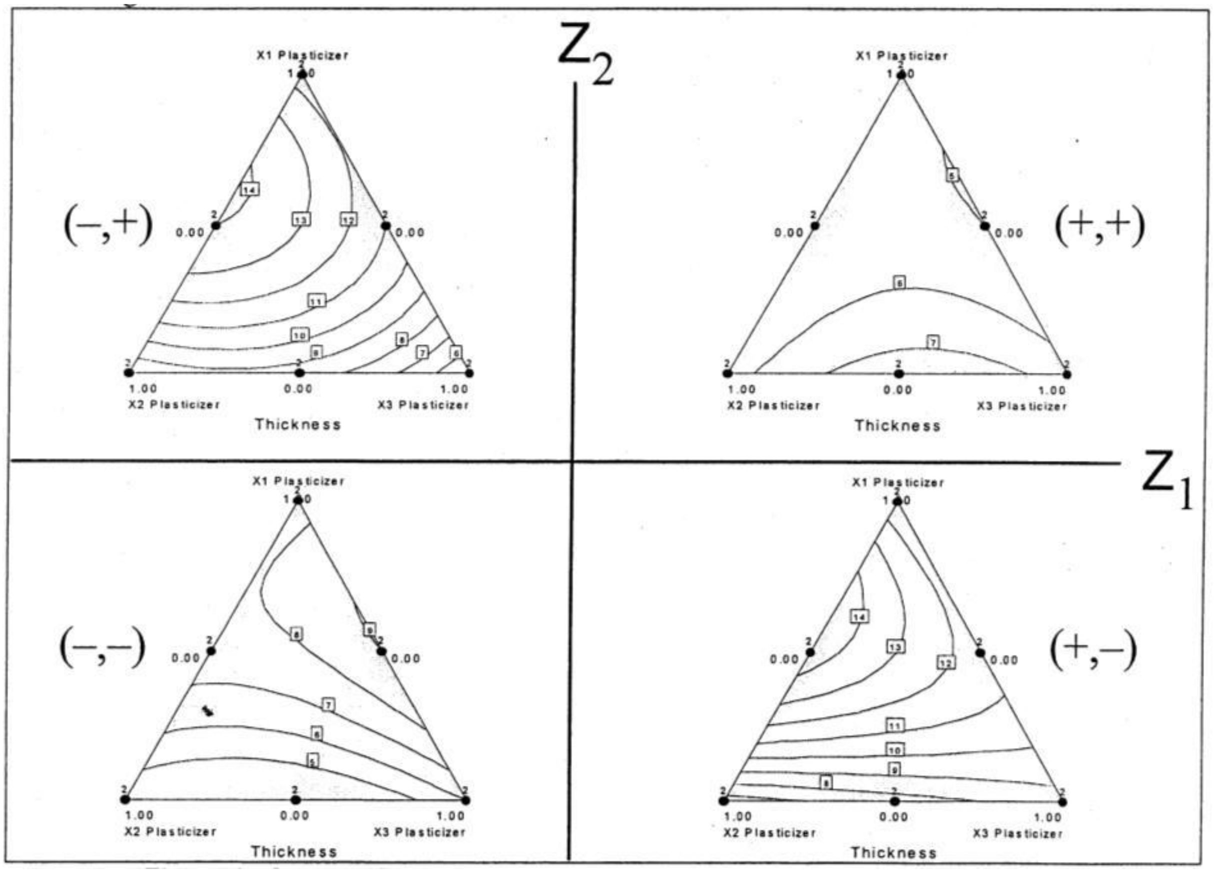

Figure 4.2: A process-mixture designs with a three-component mixture design and a 2X2 factorial design of process variables Z_1 and Z_2.

4.3 Experimental Design

The samples used in this chapter were prepared by the Phase Inversion Composition (PIC) method and the hydrodynamic diameter (D_h) of the oil droplets were measured by using dynamic light scattering (DLS) on highly diluted samples (as discussed in Chapter 3 that the dilution of the original nanoemulsion does not modify the size of the oil droplet).

The compositions of the samples were defined within a (water:oil:surfactant) ternary diagram. The lowest and highest levels of weight concentrations were chosen to fit within the expected domain of existence of the nanoemulsions: $0.45 < \text{water} < 0.85$; $0.10 < \text{oil} < 0.40$; $0.05 < \text{surfactant} < 0.15$ (Figure 4.3). Twelve samples of nine compositions were prepared, the central composition being replicated four times (Figure 4.3). The effects of the HLB and the preparation temperature were studied through the definition of five sets of samples (Table B.1, in Appendix B). All samples of the same set were prepared on the same day in a random order defined by the program. Samples were left to rest overnight, and on the second day of preparation, 1:2000 diluted samples were prepared for dynamic light scattering (DLS) measurements. The results were entered into the Design-Expert program, which used the DLS values to create a model that would enable the calculation of the equations linking the different parameters to the final nanoemulsion size.

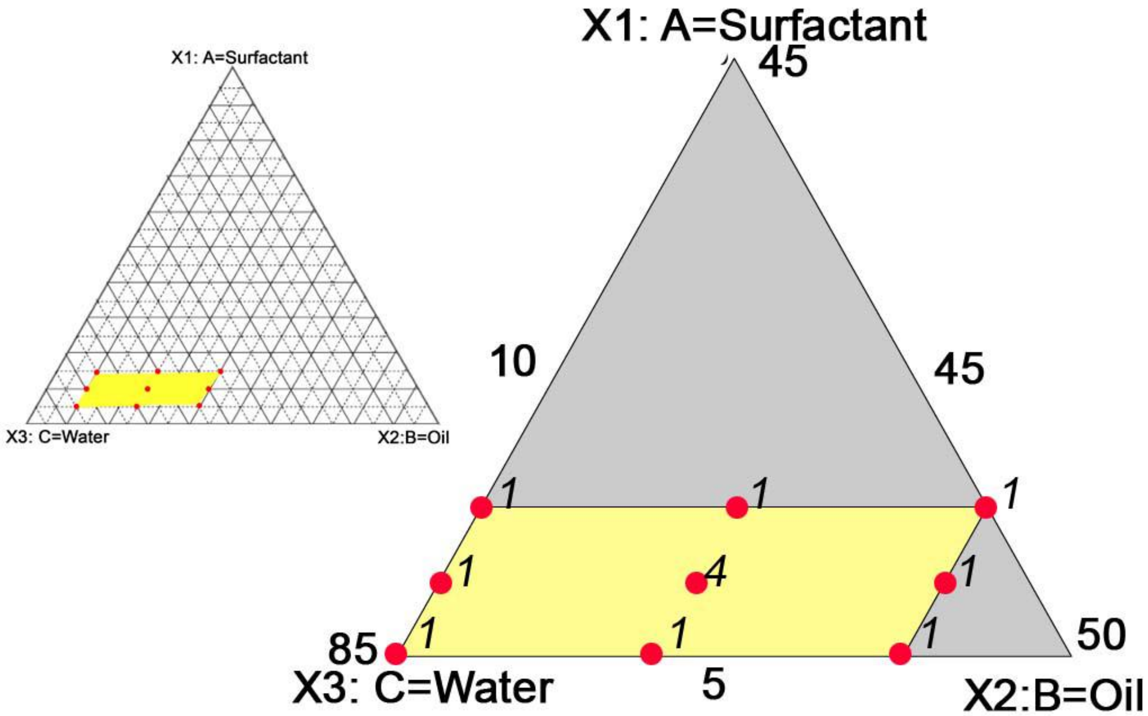

Figure 4.3: Domain of definition of the experimental design within the ternary (surfactant/oil/water) phase diagram of the nanoemulsion. The proportions of Tween 80 and Span 80 were defined according to the appropriate HLB. Left: full phase diagram displaying the domain of study; right: reduced phase diagram used for the experimental design. The numbers refer to the amount of each sample prepared for each composition, based on the experimental design requirements.

The experimental design was used as a means of studying the parallel influence of all of the parameters. The Design-Expert program V.8.0.4 (Stat-Ease Inc.) was used to define the optimum number of experiments according to the limits selected for this study. Design Expert Software was used to generate, to construct and to evaluate the properties of the proposed set of design points. The software was used firstly to determine the number of experiments required; Secondly, to define the data points on the phase diagram and thirdly to map the evolution of hydrodynamic diameter of oil droplet size (D_h) within the phase diagram, from the experimental data collected by DLS measurement. The D_h values were entered into software then evaluation for the models were conducted. The choice among various fitting models used to describe the response variations for all design points was based on the value of two statistical parameters: high R^2 and low Prob(F).

The significance of the regression model was tested using the "Prob (F)" statistics test, which tests the full model against a model with no variables, and with the estimate of the dependent variable being the mean of the values of the dependent variable. The benefit of using Prob (F) is the fact that it incorporates the probability that the null hypothesis for the full model is true (i.e., that all of the regression coefficients are zero). For example, if Prob (F) has a value of 0.01, then there is 1 chance over 100 that all of the regression parameters are zero. This low value implies that at least some of the regression parameters are nonzero and that the regression equation does have validity in fitting the data (i.e., the independent variables are not purely random with respect to the dependent variable). In general, a term that has a probability value less than 0.05 is considered significant with respect to the regression model and a probability value greater than 0.10 is generally regarded as insignificant.

4.4 Results and Discussion

The parameters (composition, preparation temperature, and HLB) that had been studied independently, in the previous chapter, were combined in this chapter. These combined analyses were carried out through experimental design, with the sample compositions defined according to Table B.2. (Appendix B).

4.4.1 Process-Mixture Design Model

Figure 4.4 shows the 2D response surface map (2D-RSM) of the process-mixture design which combines 5 mixture designs, each represented with a phase diagram, and a process design represented with HLB on the x-axis and temperature on the y-axis. The 2D-RSP describes the variations in the hydrodynamic diameter (D_h, nm) as a function of the different components (oil, surfactant, and water) at three different HLBs based on the respective proportions of Tween 80 and Span 80 and on three different temperatures of preparation (50 °C, 60 °C, and 70 °C) (Table B.3). The 3D response surface maps of the process-mixture design are displayed in Figure 4.5.

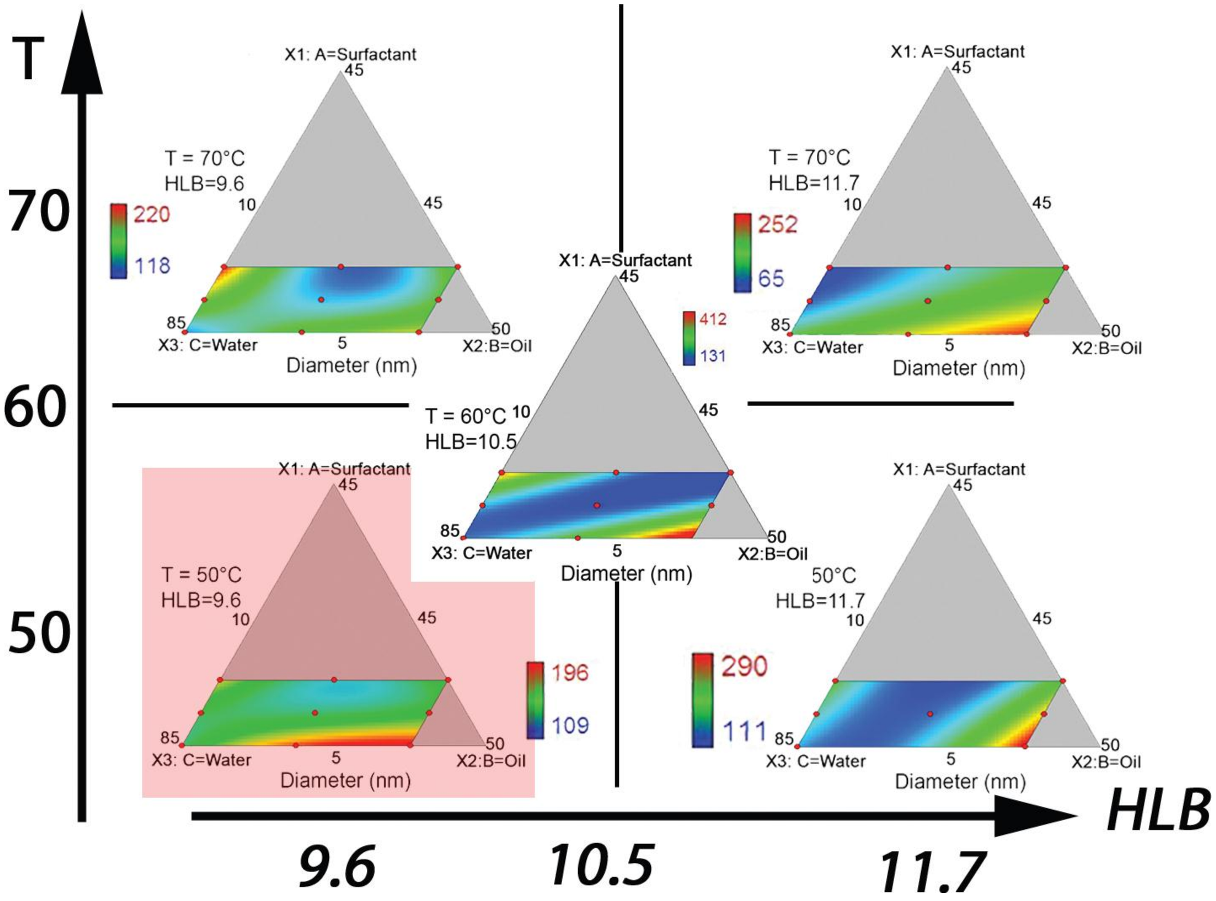

Figure 4.4: 2D response surface map for the hydrodynamic diameter D_h deduced from the experimental design, for samples prepared at different temperatures (50 °C, 60 °C, and 70 °C) and different HLBs (9.6, 10.5, and 11.7). The response surface map for (T = 50 °C, HLB = 9.6) is statistically insignificant.

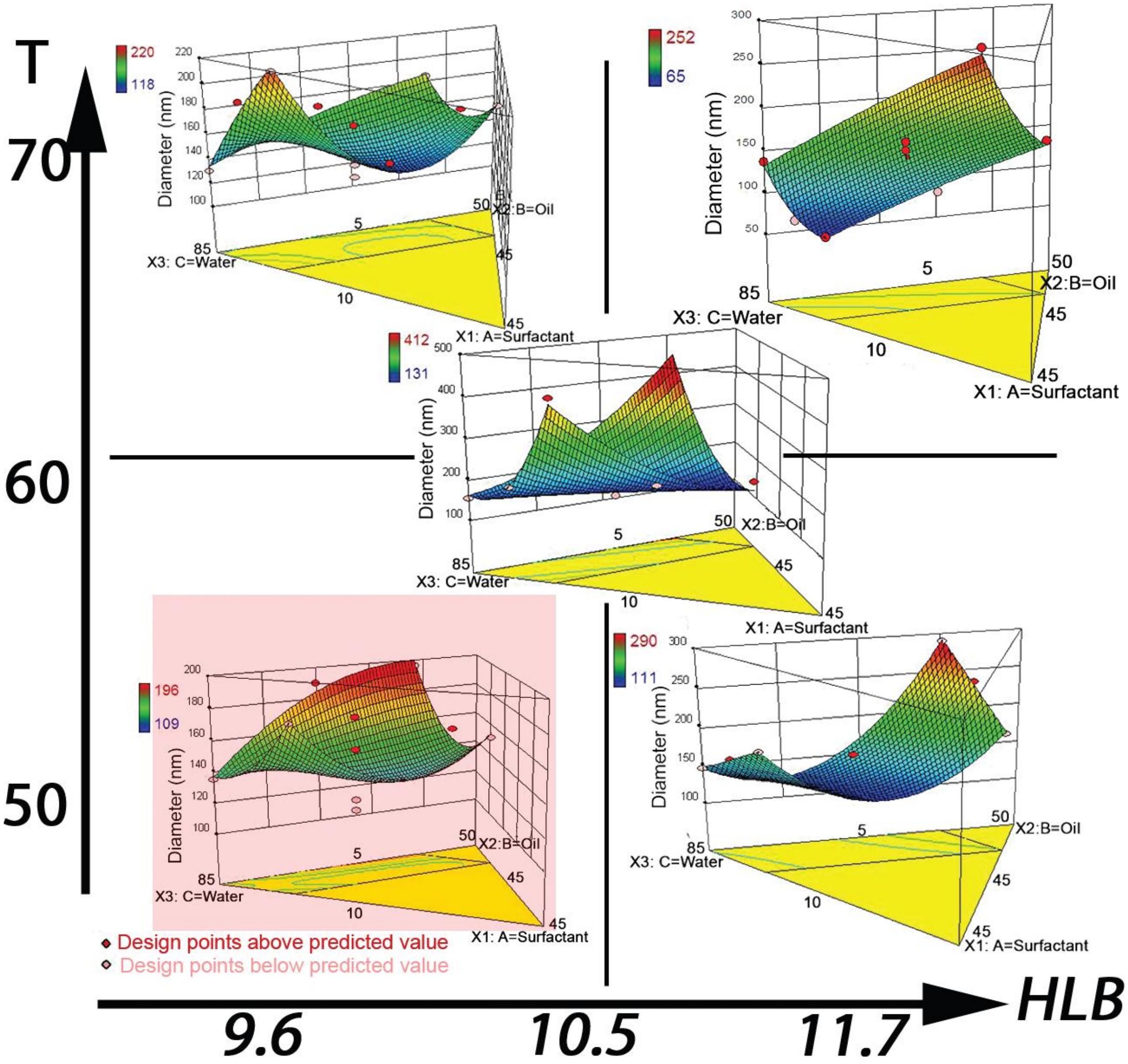

Figure 4.5: 3D response surface map superimposed over the phase diagram for the hydrodynamic diameter D_h deduced from the experimental design, for samples prepared at different temperatures (50 °C, 60 °C, and 70 °C) and different HLBs (9.6, 10.5, and 11.7). The response surface map for (T = 50 °C, HLB = 9.6) is statistically insignificant.

A process design is indicated by parameters rather than composition: the HLB and the temperature of preparation on the x-axis and the y-axis, respectively. Each process parameter is tested for three different values of temperatures 50 °C, 60 °C, and 70 °C and HLB of 9.6, 10.5, and 11.7. A mixture design is represented by a phase diagram of the three components of the nanoemulsion: oil, surfactants, and water. Generally, these figures provide an idea of the way the oil droplet size can be tuned between 65 nm and 400 nm through changes in either the process parameters or the composition. These results show that the size of these nanoemulsions depends not only on the composition but also on additional parameters such as the HLB or the temperature of preparation. A discussion on the origin of the influence of these parameters follows. The process-mixture design shows the importance of experimental design in covering a wide range of results with conducting a selected number of experiments. If nanoemulsion with specific size is required, with a quick look at the surface map, it is easy to determine the temperature, HLB and the composition required to prepare specific droplet size.

The results of the samples prepared at 50 °C with an HLB of 9.6 (set 1) could not be used because, for these samples, the statistical validity of the surface response model deduced from the experimental data was not statistically significant, as illustrated by the discrepancy between the experimental points and the surface (Figure 4.5) and as proven based on the high Prob (F) parameter (Table B.4).

4.4.2 Mixture Design Models

Comparing the mixture design models for each set by looking for the phase diagrams in 3D-RSM one can find that the mixture design models for set nos. 4 (50 °C, HLB = 11.7) and 3 (60 °C,HLB = 10) are quite similar, with D_h exhibiting a minimum along the whole study domain at the center of the response surface, and two maxima, one close to the highest oil concentrations and the other at highest surfactant content. For the set no. 2 (70 °C, HLB = 9.6), the whole response surface is rather flat, fluctuating between 118 and 220 nm, and the minimum has shifted toward the top middle of the study zone. Finally, the variation of D_h for the set no. 5 (70 °C, HLB = 11.7) presents a quasi linear decrease from the highest oil content to the water-surfactant rich domain, with a variation from 250 to 65 nm. These results show that the oil droplet size of these nanoemulsion, depend not only on the process variables, but also on the composition as one can see in the four phase diagrams, hydrodynamic diameter of oil droplet is changing with changing composition within the same phase diagram at the same process variables.

4.4.3 Mutiparameters Effect

For the sake of simplicity, the effects of the parameters on the hydrodynamic diameter were described one by one. The hydrodynamic diameter D_h was calculated from the equations deduced from the experimental design points (Figure 4.4 and Table B.4), for different HLBs and preparation temperatures. The calculated D_h values were used to draw Figures 4.6 – 4.9. These curves are plotted as a function of the oil:surfactant weight ratio (O/S), which is more pertinent for the present analysis than is the S/O ratio. Each figure has two curves: (a) presents the evolution of D_h for iso-concentrations of the surfactant, that is, the lines parallel to the base of the analysis area illustrated in Figure 4.4, and (b) describes the evolution of D_h for iso-concentrations in the oil, that is, the lines parallel to the left side of the analysis area illustrated in Figure 4.4.

O/W nanoemulsions prepared by the PIC method are obtained through a progressive addition of water, starting from an initial W/O system, to the final formation of the O/W nanoemulsion, via an intermediate bicontinuous mesophase.[7,8,3] The intermediate mesophase corresponds to a critical volume of water required for the phase inversion, this critical volume being dependent on the components (oil and surfactant). The curves displayed in Figure 4.6 demonstrate that the oil droplets that were formed, once the critical water amount has been added, remain unchanged whatever the further addition of water, and that the critical parameter is the oil/surfactant ratio (resp. surfactant/oil) that must remain roughly equal to 2.5 (resp. 0.4) for this preparation temperature and HLB. When this ratio varies with either an oil content increase, or a surfactant content increase (Figures 4.4 and 4.5), the value of D_h begins to increase, as illustrated by the evolution of D_h for iso-concentrations in surfactant (Figure

4.6.a), that is, lines parallel to the base of the analysis area, and in oil (Figure 4.6.b), that is, lines parallel to the right side of the analysis area.

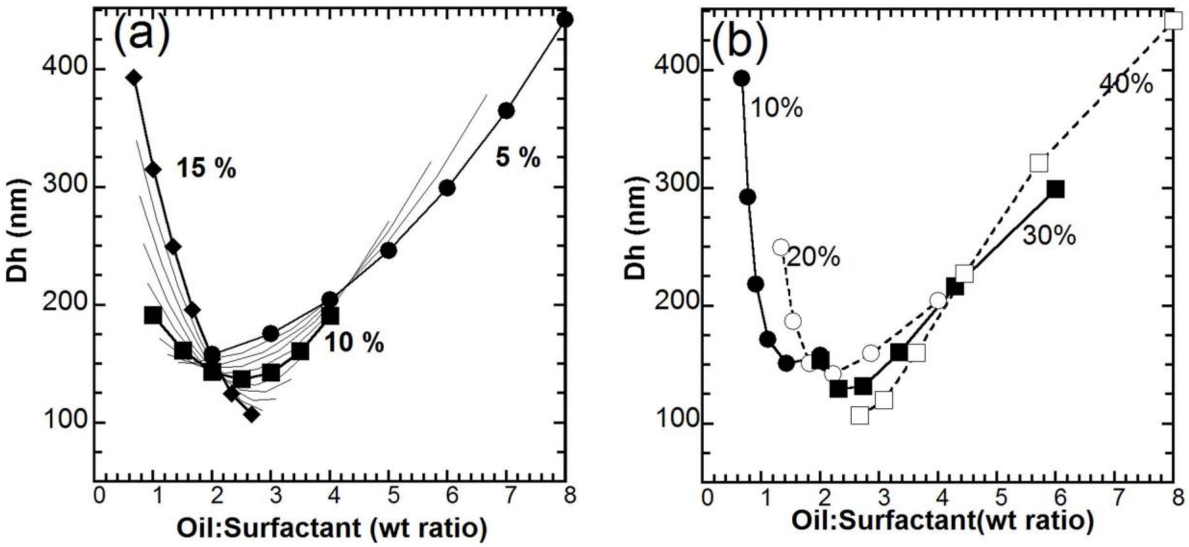

Figure 4.6: Evolution of the hydrodynamic diameter (D_h) as a function of the oil : surfactant weight ratio, for the (T = 60 °C, HLB = 10.5) samples and for different values of (a) surfactant wt.% (♦ = 15 wt.%, ■ = 10 wt.% and ● = 5 wt.%) the lines between these symbols are for in-between wt.% and (b) oil wt.% (● = 10 wt.%, ○ = 20 wt.%, ■ = 30 wt% and □ = 40 wt.%).

In Figure 4.6(a), the value of D_h increases progressively as O/S increases behind critical O/S concentration, which corresponds to a parallel increase of the oil/water ratio, since the surfactant percentage is constant. This progressive increasing of D_h finds its origin in the progressive decrease of the water content. The study area was obviously selected in an area of stability of the nanoemulsion, but increasing the oil/water ratio will shift the system closer to the critical water amount required to achieve well-defined nanoemulsions. It is still above the critical minimal value required to obtain the W/O to O/W transition, but it results in larger oil droplets. On this other side, reducing O/S below 2.5, that is, increasing the amount of surfactant for a given volume of oil (Figure 4.6.b) will create an excess of surfactant, compared with the optimum value (O/S = 2.5) for the available oil volume. The initial spherical droplets should evolve toward ellipsoidal or rod-like objects as observed for the spherical to rod-like transition of pure surfactant micelles, interpreted by the single angle DLS measurement as an increase of D_h.

Figure 4.7 shows the results of set no. 4 (50 °C, HLB = 11.7) which when compared to Figure 4.6 (set no. 3, T = 60 °C, HLB = 10.6) corresponds to a higher hydrophilicity (lower temperature of preparation) that is expected to lead to a higher droplet size and a higher total droplet surface (higher HLB) that is expected to lead to a smaller droplet size. As a result of these two opposite trends, the same response surface as for set no. 3 was observed, but the region of minimum for D_h is larger and expanded to the left side of the study area.

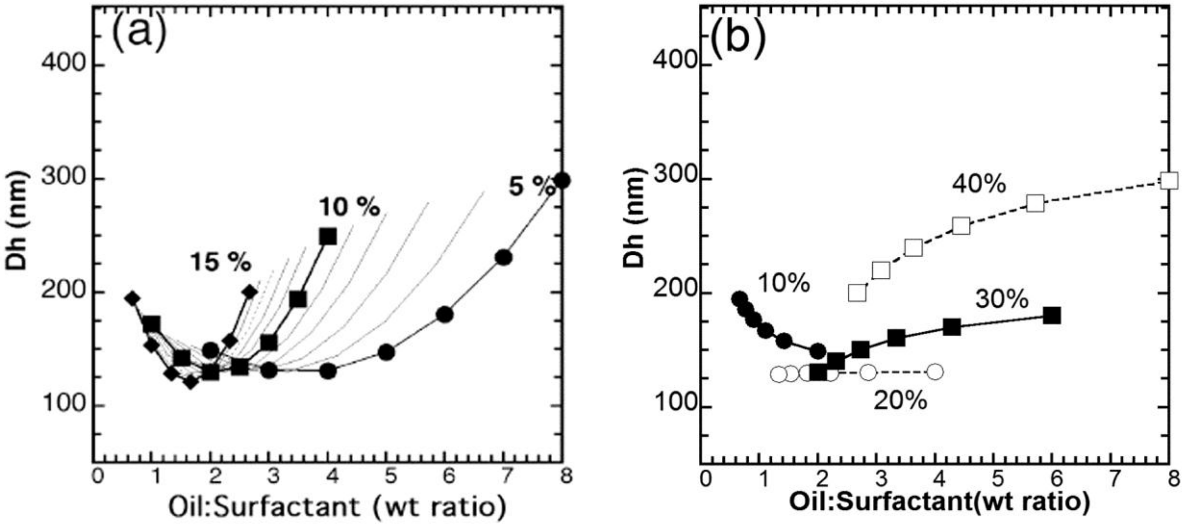

Figure 4.7: Evolution of the hydrodynamic diameter D_h as a function of the oil:surfactant weight ratio, for the (T = 50 °C, HLB = 11.6) samples, for different values of (a) surfactant wt.% (♦ = 15 wt.%, ■ = 10 wt.% and ● = 5 wt.%) the lines between these symbols are for in-between wt.% and (b) oil wt.% (● = 10 wt.%, ○ = 20 wt.%, ■ = 30 wt% and □ = 40 wt.%).

Compared with set no. 3, set no. 2 (70 °C, HLB = 9.6) exhibits a higher hydrophobicity that leads to smaller sizes and lower HLB that leads to larger sizes. Here again, the opposite influence of these parameters gives a constant value of D_h, marked by a rather flat response surface (Figure 4.8) with (D_h taking values between 120 nm and 200 nm) 120 nm <D_h < 200 nm as soon as the oil:surfactant ratio becomes greater than 1. For this set again, it is demonstrated that increasing the surfactant concentration (O/S < 1) leads to an increase in D_h.

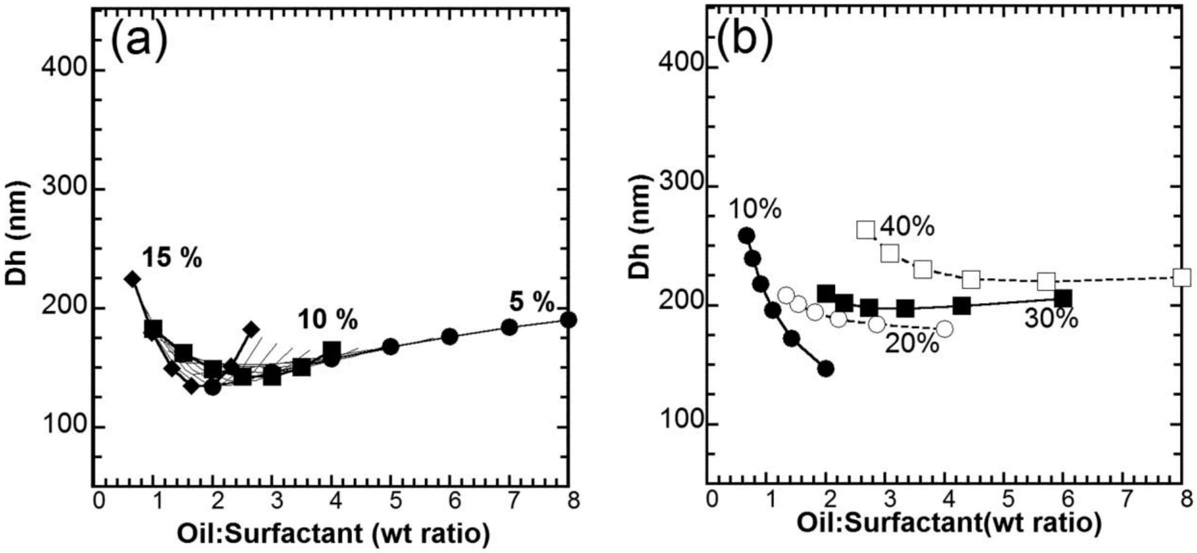

Figure 4.8: : Evolution of the hydrodynamic diameter D_h as a function of the oil:surfactant weight ratio, for the (T = 70 °C, HLB = 9.6) samples, for different values of (a) surfactant wt.% (♦ = 15 wt.%, ■ = 10 wt.% and ● = 5 wt.%) the lines between these symbols are for in-between wt.% and (b) oil wt.% (● = 10 wt.%, ○ = 20 wt.%, ■ = 30 wt% and □ = 40 wt.%).

Finally, the set no. 5 (70 °C, HLB = 11.7) combines two factors that must lead to a size reduction of the oil droplets. This trend is confirmed with the lowest sizes obtained (D_h = 65 nm). It seems surprising to observe a totally different shape (flat surface) with a minimum size obtained for the highest volumes of the surfactant content, that is, the smallest O/S ratio (Figure 4.9). However, this can be well understood in the light of the previous results: the expected optimum O/S ratio as observed in set no. 3 is certainly shifted toward lower values, and only the right part of the curve is illustrated in sets nos. 3 and 2. These analyses confirm that a full understanding of the complex behavior of these nanoemulsions and benefit from multiparameter analyses allowed by experimental design.

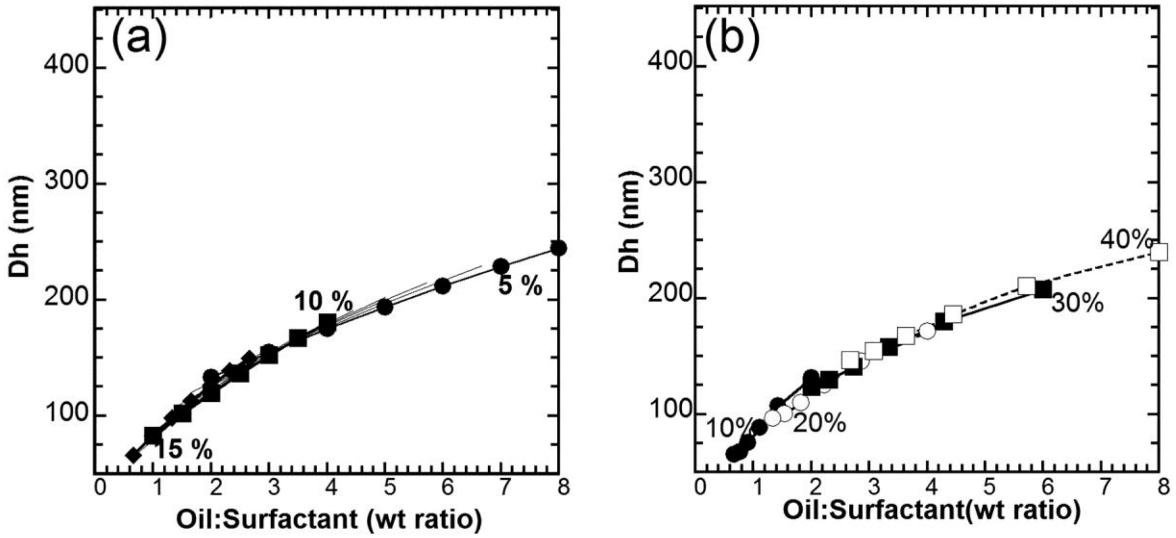

Figure 4.9: Evolution of the hydrodynamic diameter D_h as a function of the oil:surfactant weight ratio, for the (T = 70 °C, HLB = 11.6) samples, for different values of (a) surfactant wt.% (♦ = 15 wt.%, ■ = 10 wt.% and ● = 5 wt.%) the lines between these symbols are for in-between wt.% and (b) oil wt.% (● = 10 wt.%, ○ = 20 wt.%, ■ = 30 wt% and □ = 40 wt.%).

4.5 Summary

This experimental work illustrates the importance of using a process-mixture experimental design in order to incorporate an accurate consideration of the cross-interactions in these complex systems. The surfactant/oil ratio is a parameter that can help to reduce the oil droplet size but the size control depends also on other parameters and an optimum must be found within the phase diagram, once the temperature of the preparation and the HLB have been defined. The temperature of preparation has a major influence and its origin should be found in the control of the hydrophobic/hydrophilic balance of the Tween 80 during the formation of the intermediate bicontinuous phase. Oil droplets of the nanoemulsion can be tuned to between 65 nm and 400 nm by controlling, either singly or collectively, a variety of factors, including the S/O ratio, the HLB, and the temperature of preparation. Further than the stability and tunability of nanoemulsion discussed in chapter 3 and 4, it is important to know how the integration of nanoemulsion as a template to prepare macroporous materials will proceed.

Chapter 5

Hierarchical Porous Silica*

5.1 Overview

Hierarchical porous silica (HPS) was prepared by using an oil-in-water (O/W) nanoemulsion as a template which was prepared by phase inversion composition (PIC) method. In this chapter, it is demonstrated how nanoemulsions can be used as structure-directing agents and how they can be integrated within a silica matrix by means of integrative synthesis (Figure 5.1). Low-cost sodium silicate was used as the silica precursor, with no additional templating agent. First, the appropriate conditions for the integration of nanoemulsion with sodium silicate were examined followed by characterization of the resulting HPS with SEM, Hg porosimetry, N_2 adsorptin isotherm, FTIR, SAXS. Hierarchical porous silica (HPS) materials have a large pore volume (~ 1.5 cc/g in average),a high surface area (~ 240 m^2/g in average), a high porosity (58%-93%) and average surface roughness of 2.55. The microstructure of HPS can be tuned between hollow spheres and macroporous materials.

5.2 Introduction

Since the discovery of mesostructured silica,[1,2] soft matter has been used as a structure-directing agent in numerous studies. Micellar objects have been demonstrated to be suitable templating agents in many systems;[3] however, despite some reported findings, the resulting pore size is usually limited to 30 nm at most.[4,5] At the other end of the template size spectrum, latex provides very well ordered structures, creating materials with reverse opal-like structures and pore sizes in the micrometer range.

---

*Partially adapted Hessien, M.; Leone, P.; Suchaud, M.; Lebeau, B.; Nouali, H.; Guari, Y.; Prouzet, E., Nanocrystalline iron oxide synthesised within Hierarchical Porous Silica prepared by nanoemulsion templating. *Chem Commun (Camb)* **2012,** *48* (80), 10022-4.

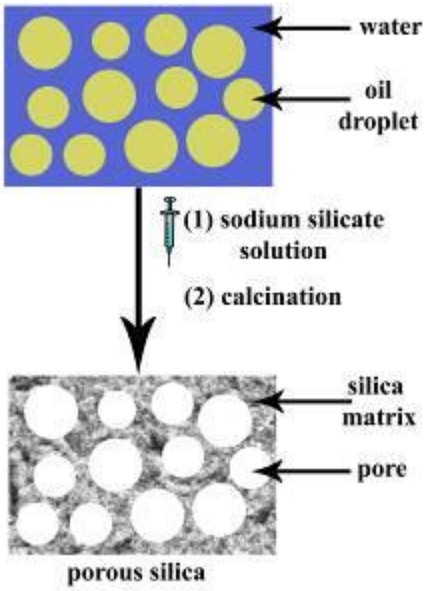

Figure 5.1: Integrative synthesis of hierarchical porous silica through the integration of nanoemulsion templating and the sol-gel chemistry of sodium silicate.

It appears that there are not so many templating objects with a size ranging between the micelle and latex categories. The latex can be prepared in a reduced size however, it is already expensive and decreasing size is more expensive. Therefore, nanoemulsions appear to be the suitable candidates for filling this gap, since their size can range from smaller values than those obtained with latex, and for a cost that is tremendously lower. Oil-in-water (O/W) nanoemulsions differ from microemulsions mostly by their size[6,7] and show substantial potential as new templates for materials with pores in the 50 nm–300 nm range. Until recently, and despite major efforts in the preparation of nanoemulsions by high energy processes, their main drawback was their intrinsic instability. This drawback was overcomed by using low-energy methods such as phase inversion temperature (PIT) or phase inversion composition (PIC), that produce very stable objects,[8] and allow for a fine control of the oil droplet size to be tuned to between 50 nm and 300 nm.[9]

Compared with latex, nanoemulsions are obviously more fragile and subject to facile destabilization if the surrounding physico-chemical parameters are not controlled. Their use as potential templates around which some solid framework could grow, the droplets are exposed to mechanical stress that could also destroy the original droplets used as templates. However and still compared with latex, nanoemulsions offer two major advantages: (i) their lower cost and the ability to control oil droplet size, and (ii) their potential for the integration of additional reagents within the oil droplets, with the opportunity to create functional materials with a hierarchical structure. Initial work in this area was conducted by Imhof et al., who developed a number of hollow or porous materials using emulsions.[10-15] Today, a whole range of materials have been synthesized using emulsions as templating objects,[16-20] but only a few of the research studies reported in the literature have examined the use of O/W nanoemulsions prepared by low-energy method as templating objects, and the author has been unable to discover any that explore the particular synthesis of porous silica from sodium silicate.[21]

5.3 Experimental Section

5.3.1 Materials

All chemicals were used as received, without further purification: paraffin oil (d = 0.86 g/cm^3) (Fluka); paraffin wax (ASTM D 127, Aldrich); sorbitan monooleate (Span 80™, d = 1.08, Mw = 428.6 g) (Across) and polyoxyethylene (20) sorbitan monooleate (Tween 80™, d = 0.994, Mw = 1,310 g) (Sigma); sodium silicate solution (reagent grade, ~10.6 % Na_2O and ~26.5 % SiO_2, d = 1.39) (Sigma-Aldrich); HCl (37 %, Sigma-Aldrich); and ammonium hydroxide (28 %–30 %, d = 0.9 g/cm^3, 14 M).

5.3.2 Methods

5.3.2.1 Preparation of the Hydrolyzed Sodium Silicate Solution (HSSS)

For all samples, the silica source was obtained from the dispersion of 11.12 g of sodium silicate solution in 70 g of a (0.7 M) HCl aqueous solution. The sodium silicate was added dropwise with a constant stirring during the addition. The final pH of the hydrolyzed sodium silicate solution was about 2. Aliquots of this mother solution were then used for the other preparations.

5.3.2.2 Synthesis of the Hierarchical Porous Silica (HPS)

The general synthesis process is illustrated in Figure 5.2. The O/W nanoemulsion was prepared using the PIC technique, as described in detail in Chapter 3, and the compositions of the nanoemulsions used are listed in Tables C.2 and C.4 in Appendix C, along with the criteria for making a selection, Table C3 in Appendix C Prior acidification of the nanoemulsion to pH 2 is required in order to avoid the quick condensation of the silica when the hydrolyzed sodium silicate solution is added. The solution of sodium silicate was added gradually to acidic nanoemulsion, with slow magnetic stirring. The opposite process (adding the nanoemulsion to the silicate) also proved to be effective for producing the same final structure. The resulting solution was mixed for 2 min, after which ammonia was added drop by drop until gelling occurred. The gels were left to age for one week before being freeze dried and calcined at 500 °C under air for 2 h, in order to burn off the paraffin oil and surfactants and open up the porosity. The resulting powder was dispersed into deionized water and centrifuged at 5,000 rpm for 15 min in order to remove the sodium chloride, generated during the preparation. The washing procedure was repeated until all of the sodium chloride had been washed out, as verified using the silver nitrate method. After being washed, the samples were dried again at 75 °C.

Figure 5.2: Preparation of the nanoemulsion/silica hydrogel.

Nine series of HPS samples were prepared: five of them O-*y*-HPS-*x*, which were prepared with different oil-in-water nanoemulsions (O-*y*-NE), and four of them W-*y*-HPS-*x*, which were prepared with different wax/oil-in-water nanoemulsions (W-*y*-NE). Details of the composition of the hierarchical porous silica are listed in Table C.5and 6 (Appendix C).

O-*y*-HPS-*x* represents the HPS prepared with a paraffin oil nanoemulsion (O), where *y* refers to the sample number of the oil nanoemulsion (O-*y*-NE), and *x* indicates the vol.% of the nanoemulsion to the hydrolyzed sodium silicate solution (HSSS). W-*y*-HPS-*x* represents the HPS prepared with a paraffin oil/wax nanoemulsion (W-*y*-NE), where *y* refers to the sample number of the wax/oil nanoemulsion (W-*y*-NE), and *x* indicates the vol.% of the nanoemulsion to the HSSS.

5.3.3 Characterization Methods

5.3.3.1 Mercury Porosimetry

The porosity of the silica powder samples was analyzed using mercury intrusion porosimetry (Micrometrics, Autopore IV) equipment. This apparatus enables one to change the pressure between 2.6.10^{-6} MPa and 400 MPa. Prior to the measurement, the silica powders were degassed at 150 °C in a vacuum (100 Pa) for about 12 h. Approximately 40 mg of dried silica powder were introduced into the low-pressure chamber (2.6.X 10^{-6} MPa–0.2 MPa) of the penetrometer. During the first stage, the cell was vacuum sealed and filled with mercury. The penetrometer containing the silica powder and the mercury was then placed in the high-pressure chamber (0.2 MPa–333 MPa). During the second stage, pressure was applied in order to force the mercury to diffuse into the porous sample. As the intrusion occurs, the mercury level in the stem varies based on the Washburn equation:[22]

$$P\, r = -2\sigma\cos\theta \qquad (1)$$

where P is the applied pressure, r is the radius of the pore, σ is the interfacial tension, and θ is the contact angle (for mercury σ = 485 mN/m and θ = 130°). The mercury porosimetry measurements were done in collaboration with Bénédicte LeBeau, and Habiba Nouali; (University de Haute Alsace).

5.3.3.2 Scanning Electron Microscope

Scanning electron microscope (SEM) images on gold-coated samples were collected with an LEO FSEM 1530, operating at 5 kV. Metal oxide-silica samples were also prepared for transmission electron microscopy (TEM) analysis using extractive replicas of ultramicrotomy techniques deposited onto copper grids. The TEM measurements were carried out at 100 kV with a JEOL 1200 EXII microscope.

5.3.3.3 Small Angle X-ray Scattering

Small-angle x-ray scattering (SAXS) analysis can probe the electron density fluctuations in the pores within the matrix. Scattering patterns are reported as a function of the scattering wave vector q (nm^{-1}), and q is related to the d-spacing according to Bragg's law given in Equation (2).

$$d=2\pi/q \tag{2}$$

SAXS measurements were carried out using the SAXSess system (Anton Paar), with a 2.2 kW copper anode ($\lambda = 1.54$ angstrom) and the SAXSquant and OptiQuant software.

Surface roughness can be extracted by plotting the scattering profile on the log(I)-log(q) scale. The linear behavior indicates that the SAXS profiles follow power law $I(q) \sim q^{-\alpha}$, where α is the fractal exponent. The value of α indicates which type of fractal is found: volume or surface.

5.3.3.4 Nitrogen Adsorption/Desorption Isotherms (N_2 Isotherm)

Nitrogen isotherms were measured at 77 K according to standard procedures that require the sample to be first dried at 150 °C for 10 h, prior to the measurements. In order to calculate surface roughness from isotherms, the experimental adsorption isotherm is modified according to

$$\Theta = k\,[\log(Po/P)]^{-\nu} \qquad (3)$$

where $\nu = 3 - Ds$, Θ is the relative adsorption calculated by normalizing the curve with the highest adsorption value, k is a constant and Ds is the surface fractal dimension. An easy way to obtain Ds is to convert Equation (3) according to

$$\log(\Theta) = \log(k) - \nu \log(\log(Po/P)) \qquad (4)$$

ν is obtained directly, hence Ds, as the slope of the line. Ds must vary between 2 (flat surface) and 3, with the increases beyond 2 corresponding to an increasing roughness. The pressure range that must be used for this model corresponds to multilayer coverage where the gas adsorption probes the actual surface before pore condensation ($0.05 < P/Po < 0.3$).

5..3.3.5 Fourier Transform Infrared Spectroscopy

FT-IR spectra were recorded from 400 to 4,000 cm^{-1} (16 scans, 0.2 cm^{-1}) by transmission with a Brucker Tensor 27 spectrometer (OPUS program). Absorption was adjusted by mixing the samples with KBr (Fisher Scientific).

5.3.3.6 Transmission Electron Microscope

Transmission electron microscope (TEM) samples were prepared using extractive replicas of ultramicrotomy techniques for deposits on copper grids. TEM measurements were observed at 100 KV with a JEOL 1200 EXII microscope. These measurements were conducted in collaboration with Yannick Guari, in Montpellier University.

5.4 Results and Discussion

5.4.1 Influence of Precursor Acidity on the Final Structure

The successful integration of the nanoemulsion with the sodium silicate solution is dependent on an accurate determination of the conditions conducive to integration. The synthesis parameters that result in an adequate sol-gel reaction, whereby both the solution of hydrolyzed sodium silicate and the nanoemulsion are mixed, were therefore defined.

5.4.1.1 Sodium Silicate at pH ~ 10 and a Neutral Nanoemulsion

The addition of sodium silicate to the aqueous phase of the nanoemulsion induces a rise in pH (to pH = 13) that destabilizes the entire system (Figure 5.3.a) with a white top layer and a transparent solution in the bottom. Surprisingly, when the pH of this biphasic solution was adjusted to less than 10, a homogeneous and stable solution was recovered (Figure 5.3.b). The possibility of using this stable and homogeneous nanoemulsion/silica solution as a precursor of porous silica was explored. It was noticed that this solution, if left at rest, managed to gel over time after several days, but this mechanism was boosted up by the addition of a basic catalyst, as explained in the following.

In the course of the experimental work that explored this new domain for porous materials, the potential interest of the initial biphasic solution was not noticed, until the final writing. As a result, we did not carry out a complete analysis of this system and our observation is for the moment based on hypotheses that are summarized hereafter.

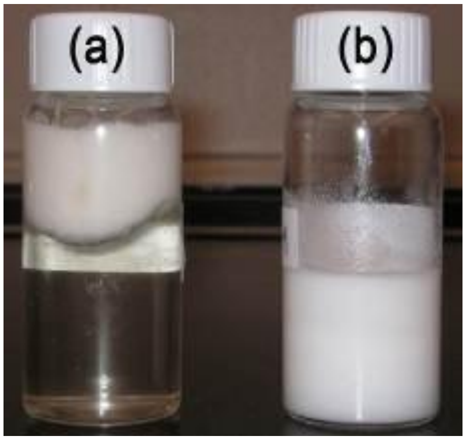

Figure 5.3: Photograph showing (a) separated nanoemulsion/sodium silicate materials with pH = 13 and (b) homogenous nanoemulsion/silica materials with pH ~ 10.

First, a superficial observation would lead to the conclusion that the addition of the basic sodium silicate results in to a complete destruction of the nanoemulsion with the oil phase on the top and water at the bottom. However, this explanation does not stand since a slight variation of pH down to 10, gives back a homogeneous solution, as a proof that the initial oil droplets remained untouched. Hence, it is assumed that the addition of silicate species combined with a high pH, favors the interaction between these species and the surface of the nanoemulsion. This surface is made of the PEO groups of the Tween 80 molecules and hydroxo-groups from Span 80, these latter being not able to actually interact (and Span 80 is highly hydrophobic). Before a full study that will be carried out after the present work, a possible mechanism can be postulated: silicate species interact with the PEO groups (probably via the oxygen atoms, as demonstrated for MSU mesoporous silica), and reduce the hydrophilic interaction with the water molecules. This interaction modifies the actual HLB of these nanoemulsions and creates hydrophobic entities that will migrate to the top of the vial as they contain oil. Being able to reduce the interaction of silicate with PEO by reducing the pH (hence by adding protons that could favor the creation of hydrogen bonds between water molecules and PEO), will increase the hydrophilicity of these objects and takes back the silica/nanoemulsion to a homogeneous system. As usual, some important results are identified during the final writing, and this observation, under the light of our whole study that allowed us to improve our knowledge of such systems, will lead to deeper analysis in the future.

The sample with a homogeneous structure (Figure 5.3.b) was calcined at 500 °C, then observed by SEM. Figure 5.4 shows that the material has a sponge-like macroporous structure after calcination, which results from the nanoemulsion, but the silica skeleton does not display the "memory" of the initial oil droplets, which could have merged and lead to this bicontinuous structure (silica and porosity) during the slow gelling step.

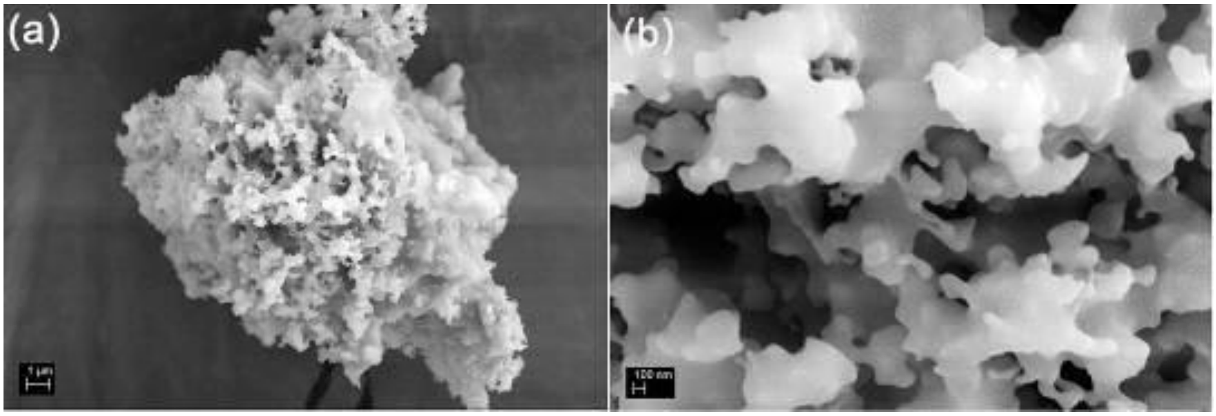

Figure 5.4: SEM micrographs of silica prepared with a neutral nanoemulsion and sodium silicate solution, with pH ~ 10 adjusted after mixing (Figure 5.3 (b)).

This porous structure, however, is obviously far from the perfect inverse replica of the nanoemulsion that was in mind initially. The visual observation of the homogeneous sample (Figure 5.3.b) and its white color let us think that objects large enough to scatter light, exist in the solution at basic pH (pH 10). This is in line with the initial observation at higher pH (pH 13) (Figure 5.3.a) as explained above. It can be postulated that there is still a strong interaction between the sodium silicate and the nanoemulsion, which could prevent the silica to gel and embed the oil droplets within.

Based on this observation, the sodium silicate solution was acidified to pH = 2 with dilute HCl before it was mixed with the nanoemulsion, and an initial transparent solution was obtained. The adjustment of pH of the sodium silicate prevents the disturbance of the nanoemulsion and, at the same time, induces the neutralization of the sodium silicate. As a result, the sodium silicate solution was added to the nanoemulsion in a molecular state, with almost no interaction with the nanoemulsion droplets. In this way, the sodium silicate forms a silica hydrogel that entraps the oil droplets and generates macroporosity after calcination. It appears from this observation that a future study should explore more in-depth the influence of the initial pH on the final material structure.

5.4.1.2 Hydrolyzed Sodium Silicate Solution (HSSS) at pH ~ 2 and a Neutral Nanoemulsion

The sodium silicate solution was acidified to pH 2 in order to place the silicate in a domain characterized by a high hydrolysis rate but with a low level of condensation. The O/W nanoemulsion (NE) was initially prepared with a neutral pH (5–6). When the acidic sodium silicate solution was added to the neutral nanoemulsion, the formation of a white suspension could be observed. Ammonia was added in order to produce a gel, and after the reaction of the silicate was complete, SEM observations of the final material were obtained. The images reveal the presence of a heterogeneous population with large well-defined, dense particles, attributable to the reaction, along with some minor fluffy aggregates, ascribable to the final reaction of the sodium silicate resulting from the addition of the ammonia, Figure 5.5, details of compositions of these samples are listed in Table C7 (Appendix C).

A closer observation of these low density aggregates reveals that they are made of hollow particles with an egg-shell structure (Figure 5.5.c-f). This thin silica shell that formed around the oil droplets show that the reaction took place where the silicate acidified at pH 2 (low condensation rate) could interact with an area of higher pH (higher condensation rate), that is, the vicinity of the nanoemulsion (pH 5–7). After the addition of ammonia, the whole structure gels and links the initial egg shells. The synthesis of the silica gel through the base catalysis (addition of the ammonia) of the acidified sodium silicate solution (pH 2) combined with a neutral nanoemulsion, results in the disordered mesoporous structures that can be observed in the SEM images (Figures 5.5(e) and 5.5(f)). Compositions of two samples are mentioned in Table C.5.

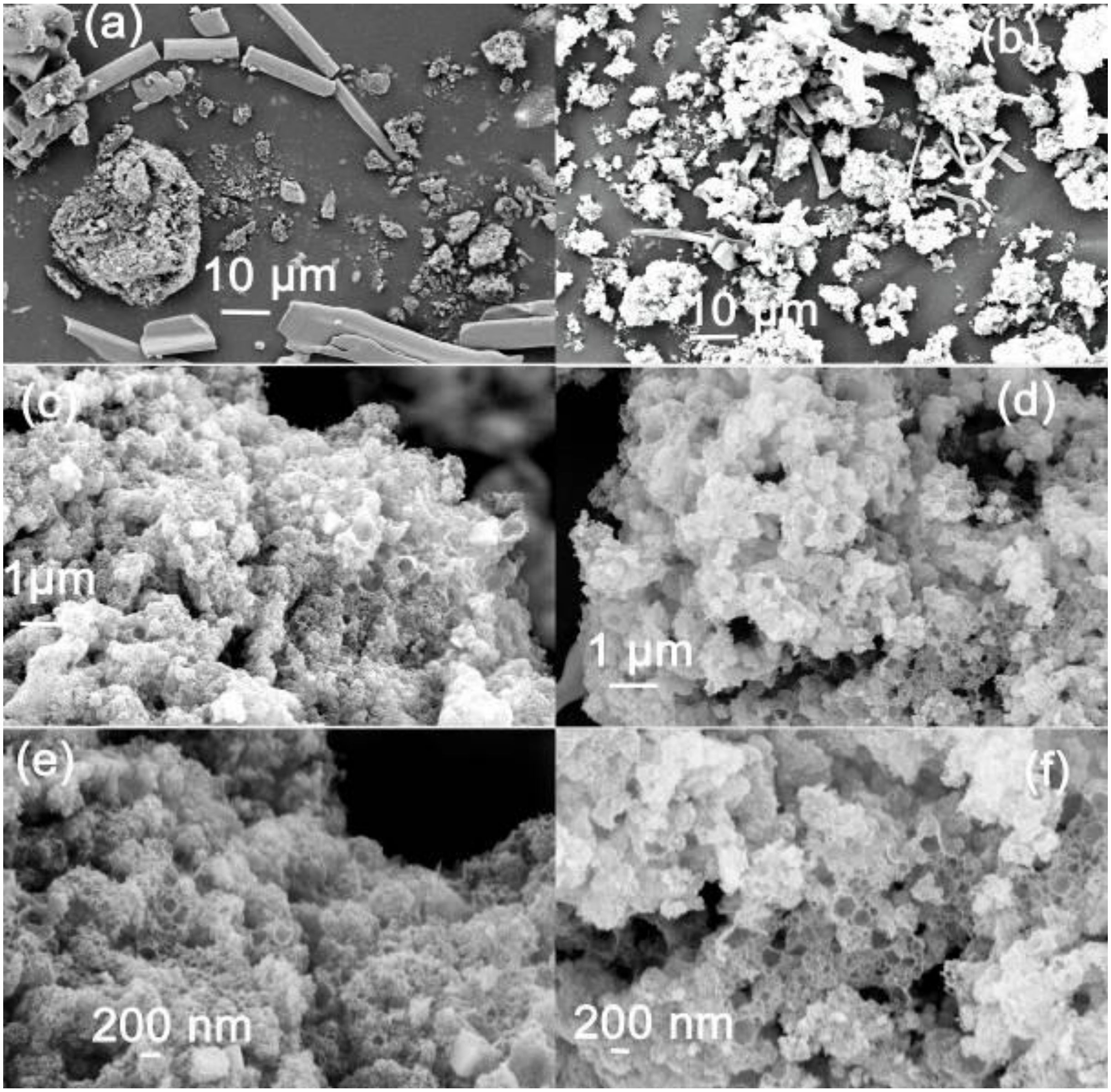

Figure 5.5: SEM micrographs of silica prepared with a pH 2 sodium silicate solution and a neutral nanoemulsion: (a), (c), and (e) with NE/HSSS vol.% = 18 ; (b), (d), and (f) with NE/SS = 50 .

5.4.1.3 Both Hydrolyzed Sodium Silicate Solution (HSSS) and Nanoemulsion at pH ~ 2

To prevent initial reaction between the acidic sodium silicate and the neutral nanoemulsion, a similar acidification process entailing the addition of dilute HCl was applied to the nanoemulsion in order to bring its pH down to 2. In that case, no reaction between the sodium silicate solution and the nanoemulsion was observed, and the condensation of the silica was initiated only after the addition of the ammonia.

As a result of a silica condensation controlled only by the addition of ammonia, a final monolithic porous structure was obtained (Figure 5.6) in place of particles observed previously (Figure 5.5). With the lack of reaction due to equal pH levels of the nanoemulsion and the sodium silicate solution, the oil droplets could be distributed homogeneously within the mixture of the nanoemulsion and the sodium silicate solution. As a result, the further addition of ammonia induces the silica condensation in a homogeneous system where the silica framework confines the oil droplets during the reaction.

Compared with the previous examples, this synthesis allowed one to obtain a better control over the reaction and the kinetics and induce the silica condensation "on demand", instead as a result of a complete or partial spontaneous reaction. Hence, a more deeply study to investigate the parameters of the synthesis starting with both precursors (sodium silicate and nanoemulsion) acidified at pH 2.is represented. However, keeping in mind that the other methods offer promising developments regarding the final structure that could be achieved, the present work was focused on the process used to remove any kinetic factor.

Figures 5.6(e) and 5.6(f) clearly show the mesoporous structure of the silica matrix, which results from the selection of conditions conducive to the formation of the silica, in contrast with the dense structure of the silica matrix observable in Figure 5.4(b) produced when the sodium silicate was not in a hydrolyzed state. To obtain an integrating synthesis of the sodium silicate solution and the nanoemulsion, both should have a pH of 2, with ammonia as the catalyst that induces the condensation of the silicate.

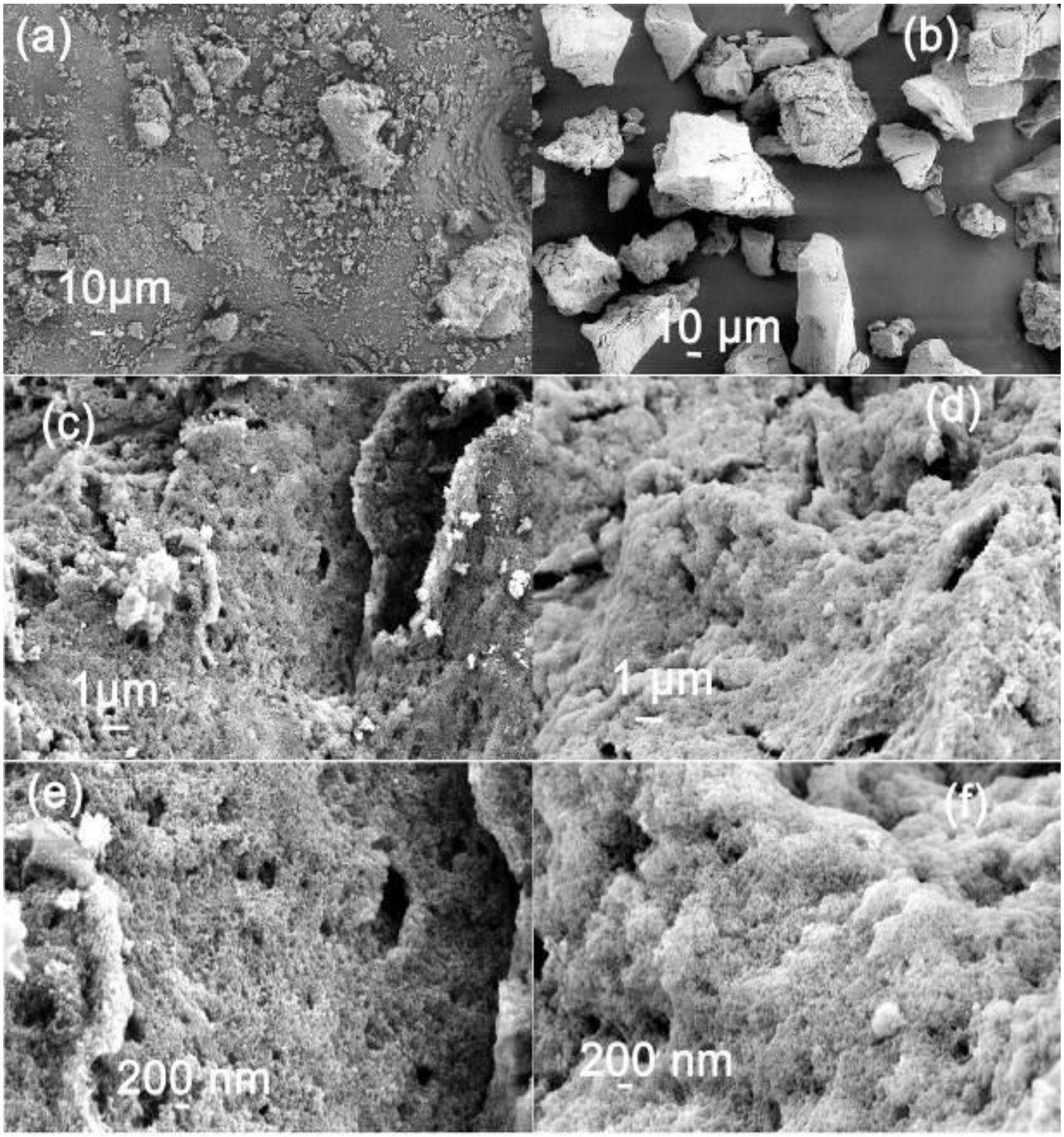

Figure 5.6: SEM micrographs for O-2-HPS-2.5 (a, c, e) and O-2-HPS-50 (b, d, f).

5.4.2 Influence of Ammonia

Once the pH had been adjusted for both the NE (Nanoemulsion) and the HSSS (Hydrolyzed Sodium Silicate Solution), they were mixed, and the condensation of the silica was induced through the basic catalysis resulting from the addition of a sufficient amount of ammonia.

When the amount of ammonia was low, the reaction took approximately 30 min and produced a white powder (Figure 5.7.a). As the volume of ammonia was increased, the reaction time decreased, and above a critical amount of catalyst, a gel was obtained (Figure 5.7.b).

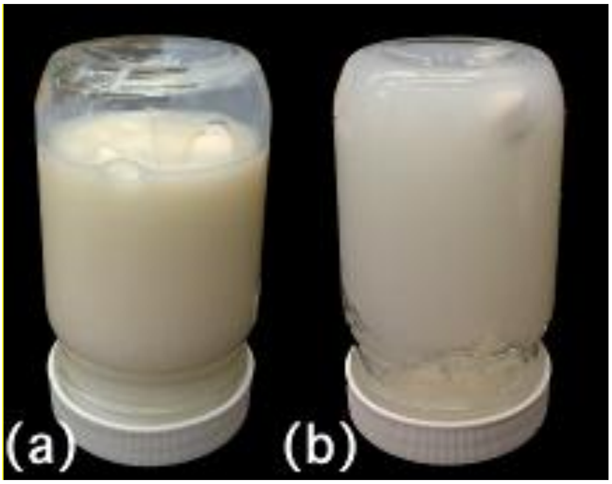

Figure 5.7: Comparison of NE:HSSS syntheses with different amounts of ammonia: (a) a small amount, resulting in a powder; (b) a large amount, resulting in a gel (photographs of one-year-old samples).

The volume of ammonia was indeed critical for the production of the final silica gel required so that the nanoemulsion is successfully entrapped within the inorganic structure. This critical value was checked through the preparation of a series of NE/HSSS solutions, beginning with a fixed amount of HSSS, followed by the addition of varying amounts of NE, with the final NE:HSSS vol.% equals to 2.5, 25, 50, 100, and 200. For each NE:HSSS ratio, a series of samples were prepared to which different volumes of ammonia were added: between 0.0 mL and 1.0 ml. The samples were left to react until a white precipitate appeared, or until the gelling was complete (the parameter for gelling was the ability to put the vial upside down as illustrated in Figure 5.7.b). This reaction took several minutes, depending on the amount of ammonia.

Figure 5.8 displays the link between the volume of ammonia (Figure 5.8.a) or its final molarity (Figure 5.8.b), with the formation of a powder (blue) or gel (green), as a function of the NE to HSSS volume ratio. For all of the NE:HSSS ratios, a minimum amount of ammonia is required to obtain the formation of a gel. For the most concentrated solutions (NE:HSSS <

50 vol.%), this volume is fairly constant and equal to 0.1 mL (Figure 5.8.a). Above this threshold (as the system becomes more diluted), an increasing volume of ammonia is required to achieve gelling, up to 0.6 mL for the NE:HSSS = 200 vol.%.

These raw values were converted in terms of the molarity of the ammonia in order to take into account the dilution effect resulting from the increasing amount of NE. As expected, a similar but less significant trend can be seen, as first proof of the importance of the dilution parameter with respect to gel formation: for NE:HSSS $\leq$ 50 vol.%, the slight increase in the ammonia volume observed in Figure 5.8.a, was only the result of dilution, whereas higher dilutions require a more basic medium to achieve the gel formation (Figure 5.8.b).

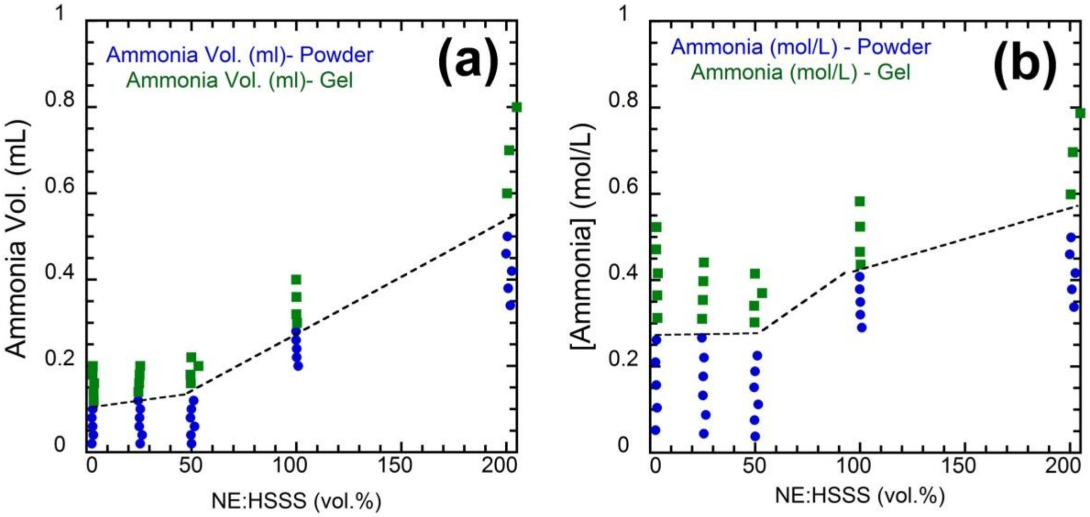

Figure 5.8: Evolution of the amount of ammonia required in order to create a shift from a silica powder (blue dots) to a silica gel (green squares), reported (a) as the volume and (b) as the concentration of ammonia as a function of the vol.% of the nanoemulsion in the hydrolyzed sodium silicate solution. The dashed lines are provided as a visual aid.

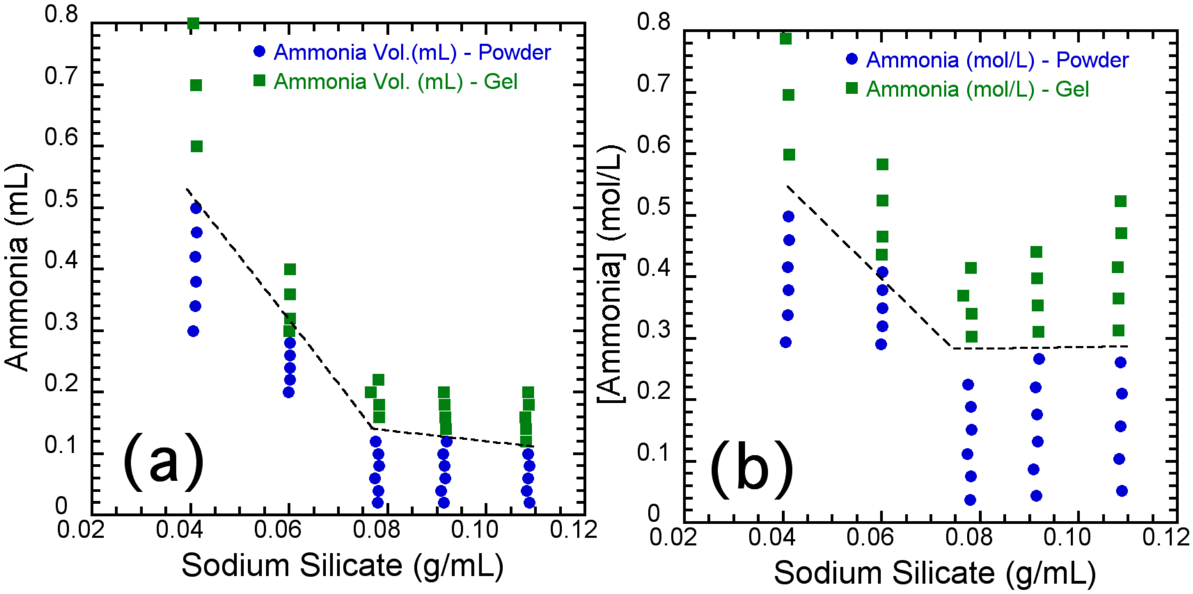

Figure 5.9: Evolution of the amount of ammonia required in order to create a shift from a silica powder (blue dots) to a silica gel (green squares), reported (a) as the volume and (b) as the concentration of ammonia as a function of the concentration of the sodium silicate. The dashed lines are provided as a visual aid. (the volume change resulting from the addition of ammonia is neglected).

High concentrations of sodium silicate (SS) correspond to low NE:HSSS ratios. At high concentrations of SS, the gel appeared once a 0.3 mol.L^{-1} concentration of ammonia had been reached.(Figure 5.9 (b)) This finding clearly indicates that the formation of the gel with high concentrations of SS (resp. low NE:SS ratio) depends only on the concentration of the catalyst. As the SS concentration decreases (resp. NE:SS increases), a higher concentration of the catalyst is required for the gel to form. The limit at 0.07 g.L^{-1} of the SS (resp. NE:HSSS > 50 wt%) delineates the boundary between a system in which the silica framework can percolate once the required catalyst has been added (high concentrations of SS) and a system in which an additional chemical driving force must be provided in order to counteract the effects of the dilution of the SS solution.

SEM observations of the calcined silica resulting either from the gel, or from the powder obtained with the NE (NE:HSSS = 50 vol.%) enabled to characterize the structural differences resulting from the powder or gel formation (Figure 5.10). The influence of the nanoemulsion on the final structure was determined by a comparison with a silica gel obtained with the same conditions of concentration and pH, except that no NE was present. The silica resulting from the use of the sodium silicate alone (Figures 5.10.a and b) exhibits the expected fluffy structure produced when the silica condenses.

When the reaction occurs after the addition of the NE but with an amount of ammonia that does not produce the gel, a disordered structure can be observed in the particles (Figure 5.10.c and d), which is quite similar to that observed with pure silicate. This points out to the fact that the formation of a powder does not allow for a complete insertion of the NE droplets in the silica framework. On the contrary, if a gel was produced, the whole NE remains within the silica structure and contributes to generate a continuous porous structure with cavities that can be assigned to the initial oil droplets (Figures 5.10.e and h). At this stage, the required conditions for successful integration between nanoemulsion and sol-gel of sodium silicate are defined and hereinafter acidified NE (pH ~2); hydrolyzed sodium silicate solution (pH~2); and with the addition of required ammonia to induce gelling are always used. The resulting structure is called Hierarchical Porous Silica (HPS) which is characterized using SEM, Hg porosimetry, FTIR, N_2 isotherm and SAXS.

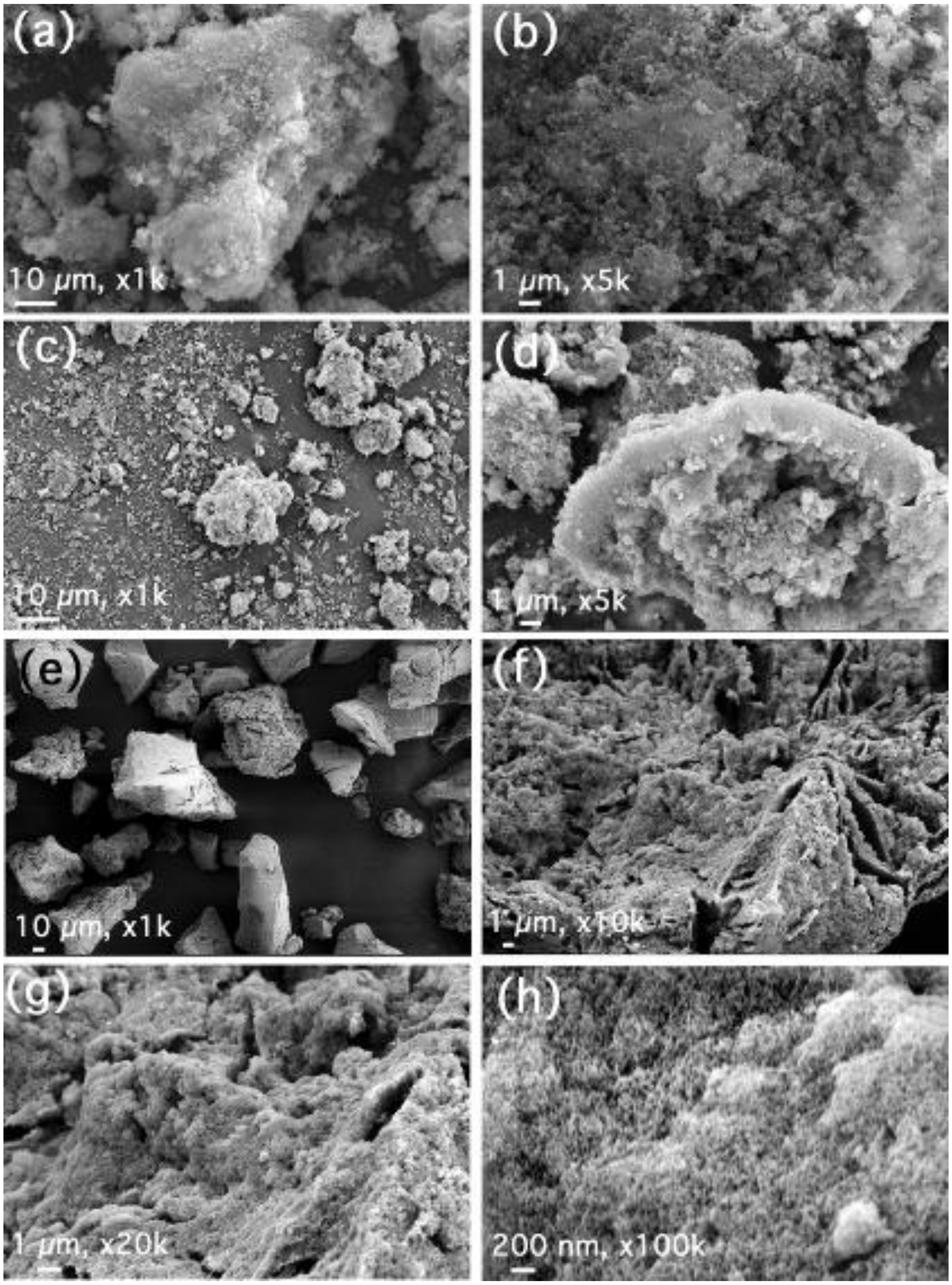

Figure 5.10: SEM micrographs of (a) and (b) pure silica gel, (c) and (d) a powder obtained with NE:HSSS = 50 vol.%, and (e) to (h) a gel obtained with NE:HSSS = 50 vol.%. All samples were observed after calcination.

5.4.3 Characterization of Hierarchical Porous Silica Prepared with an Oil Nanoemulsion (O-*y*-HPS-*x*)

The oil droplets are obviously expected to be deeply disturbed by the mechanical constraints that result from the silica condensation and gel syneresis. Therefore, the synthesis of HPS and the resulting structures were studied, by comparing two types of nanoemulsion. For the first type, the initial system is made of pure (liquid) paraffin oil, and for the second one, a mixture of paraffin oil and wax were used in order to prepare the nanoemulsion at a temperature where the organic phase is liquid, before it was added to the sodium silicate at room temperature, where the oil/wax droplets have frozen. The structural characterizations that were carried out on the final silica, prepared with the "oil" or the "wax" route are reported

5.4.4 Effects of the Nanoemulsion Volume on the Microstructure

The resulting templated materials are characterized by SEM, which shows how macropores are embedded in the silica matrix as a result of trapping the initial oil droplets of nanoemulsion in the silica matrix during condensation, as shown in Figure 5.11. These three photos are for hierarchical porous silica (O-*1*-HPS-*x*) with different volume of nanoemulsion increasing from 25 to 50 to 100. Figure 5.11(a) shows some macropores distributed within a silica matrix for HPS prepared with 25 vol.%; more macropores are distributed in a silica matrix with 50 vol.% (Figure 5.11(b)) and increasing numbers of macropores are distributed in HPS with 100 vol.% of nanoemulsion (Figure 5.11(c)). In this set of samples, as increasing nanoemulsion volume ratio added to a constant volume of sodium silicate solutions results in more numerous macropores. However, this is not the case with other sets of samples.

Figure 5.12 shows SEM photos for hierarchical porous silica (O-*3*-HPS-*x*) prepared with x = 2.5, 25, and 50. For O-*3*-HPS-*2.5*, the structure is continuous, with macropores trapped inside the mesoporous silica matrix. For O-*3*-HPS-*25*, the structure appears as agglomerated hollow spheres with a moderate thickness for the silica shell. For O-*3*-HPS-*50*, the structure resembles that of O-*3*-HPS-*25* but with a thin thickness for the silica shell. Higher magnification for the same set of samples is mentioned in Figure C.1 (Appendix C).

Increasing the volume of the nanoemulsion (x) changes the structure from that of a macroporous matrix to that of agglomerated hollow sphere, and increasing the emulsion volume thins silica shell. The agglomeration of hollow spheres is caused by condensation of unreacted silica precursor on the surface of isolated spheres when they come closer to each other in the later stages f the reaction, as observed by Schacht et al. [23]

To follow up the change in silica shell thickness, Figure 5.13 shows how the thickness of the silica shell should vary according to the volume of nanoemulsion added. These data are the result of theoretical calculations described in Appendix C. For a hierarchical porous silica (O-*3*-HPS-x) series prepared with a nanoemulsion of oil droplet diameter = 65nm, the silica shell is about 85 nm, 20 nm and 15nm for nanoemulsion volume 2.5%, 25% and 50%, respectively. The silica shell, for O-*3*-HPS-*2.5,* is thick enough that a shell of separate droplets merges to form a continuous structure, trapping the pores inside as depicted in Figure 5.12(a). On the other hand, for O-*3*-HPS-*25,* the shell is so thin (~ 20 nm) that the shells cannot merge, thus leading to the formation of hollow spheres as depicted in Figure 5.12(b). For higher nanoemulsion vol.%, O-*3*-HPS-*50,* agglomerated hollow spheres are observed but with thinner shell (~ 15 nm) as depicted in Figure 5.11(c). It is worth noting here that an increasing nanoemulsion volume is inevitably combined with an increasing total amount of water in the reaction media leading to decreasing silica concentration. Therefore, as the nanoemulsion volume increases, the silica concentration decreases.

This change in microstructure from macroporous material to hollow spheres can be attributed to a change in templating behavior from volume templating (macroporous structure) to surface templating (hollow spheres), as summarized in Figure 5.14 and data of this figure are in Table C9 in Appendix C. These observations are consistent with the findings of Fournier et al.[24] and Stein et al.[25] Fournier et al.[24] observed that hollow spheres are produced when the silica precursor concentration is lowered so that individual oil droplets are silicified rather than formed into a continuous network as is necessary for the macroporous materials. Stein et al.[25] differentiate between surface templating and volume templating depending on interaction between spheres and precursors. If interaction is strong, the surface template is achieved rather than volume template, which is formed if interaction is weak. It is obvious that the present study, which aimed to explore the dimensions of the research field, could not address all the mechanistic details, which will have to be explored in the future. However, the observations regarding the pH-induced interactions between the nanoemulsion and the silica precursors, as well as the different structure observed (see Paragraph 4, this Chapter), give clues on the occurrence of similar interactions in our systems.

The theoretical calculations represented in Figure 5.13 show that the change from macroporous materials to hollow spheres should be observed in the three series mentioned. However, comparing SEM photos for O-*1*-HPS-*x* (Figure 5.11) with SEM photos for O-*3*-HPS-*x* (Figure 5.12) shows that the effect of increasing the nanoemulsion volume is not always the same. Deeper understanding of the differences between the two sets is required.

Two sets of samples (O-*1*-HPS-*x*) and (O-*3*-HPS-*x*) were prepared from nanoemulsion (O-*1*-NE) and (O-*3*-NE), the detail compositions of nanoemulsion are mentioned in Table C2. (Appendix C). The two nanoemulsions have the same oil (10 g) and the same surfactant over oil ratio (1.5). They differ in their preparation temperature (60 °C and 70 °C) and HLB (10.5 and 11.7), which results in different oil droplet diameters (400 nm and 65 nm), respectively for (O-*1*-NE) and (O-*3*-NE). The question that arises now is how the change in the droplet size causes the microstructure of the resulting templated silica to change from macroporous materials to hollow spheres.

The oil droplet size can be expressed in terms of the oil/water interfacial area (m^2) created which can be calculated by knowing oil droplet diameter and oil content in each nanoemulsion. In this study, the concentration of sodium silicate was kept constant at 14.5 g sodium silicate in 88 g of water (pH = 2) and the volume of nanoemulsion added varied. The change in nanoemulsion volume is accompanied by adding extra water and oil droplets. The calculated interfacial oil/water area (m^2) and the calculated sodium silicate concentration/interfacial area ($g/L.m^2$) are represented in Figure 5.15 and the details of calculation are in Table C1 (Appendix C)

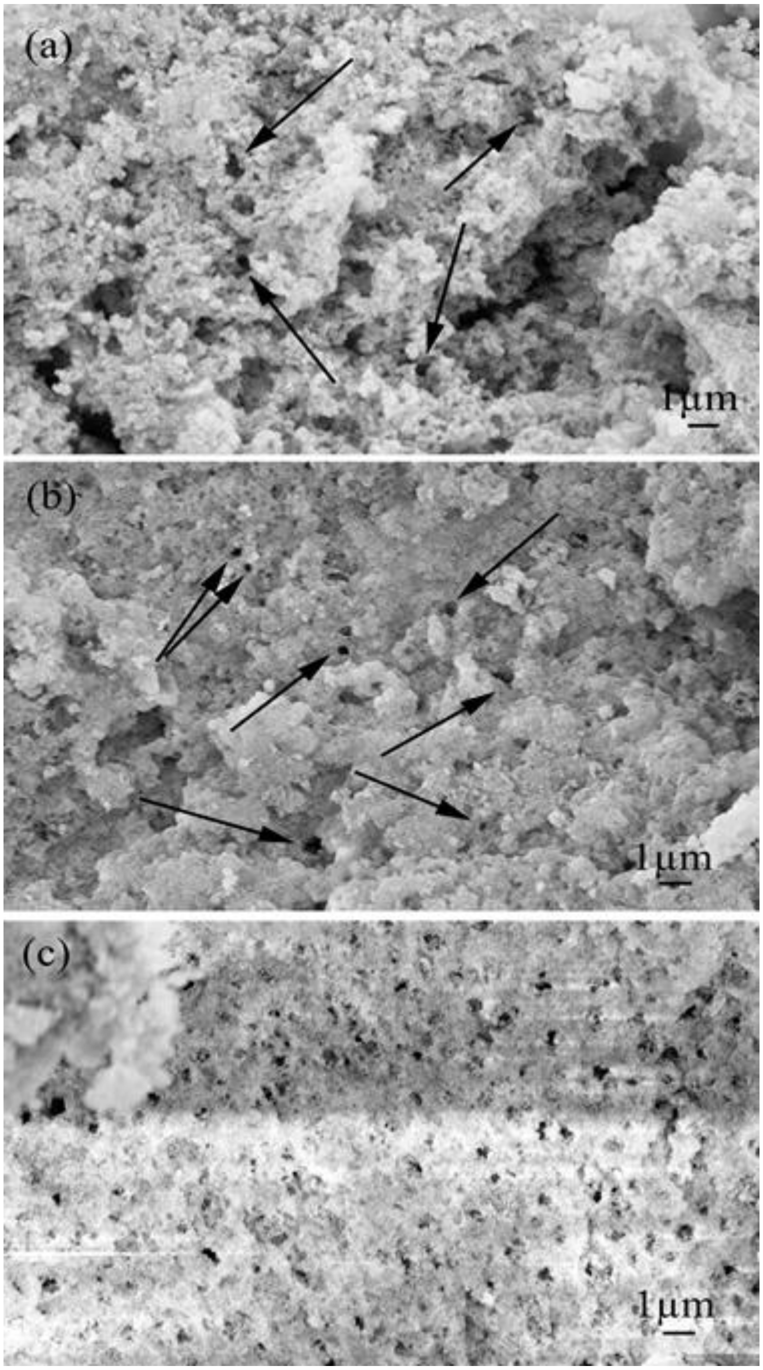

Figure 5.11: **SEM images of hierarchical porous silica O-1-HPS-*x* samples prepared with (a) *x* = 25 , (b) *x* = 50 and (c) *x* = 100. Black arrow indicates some of the macropores.**

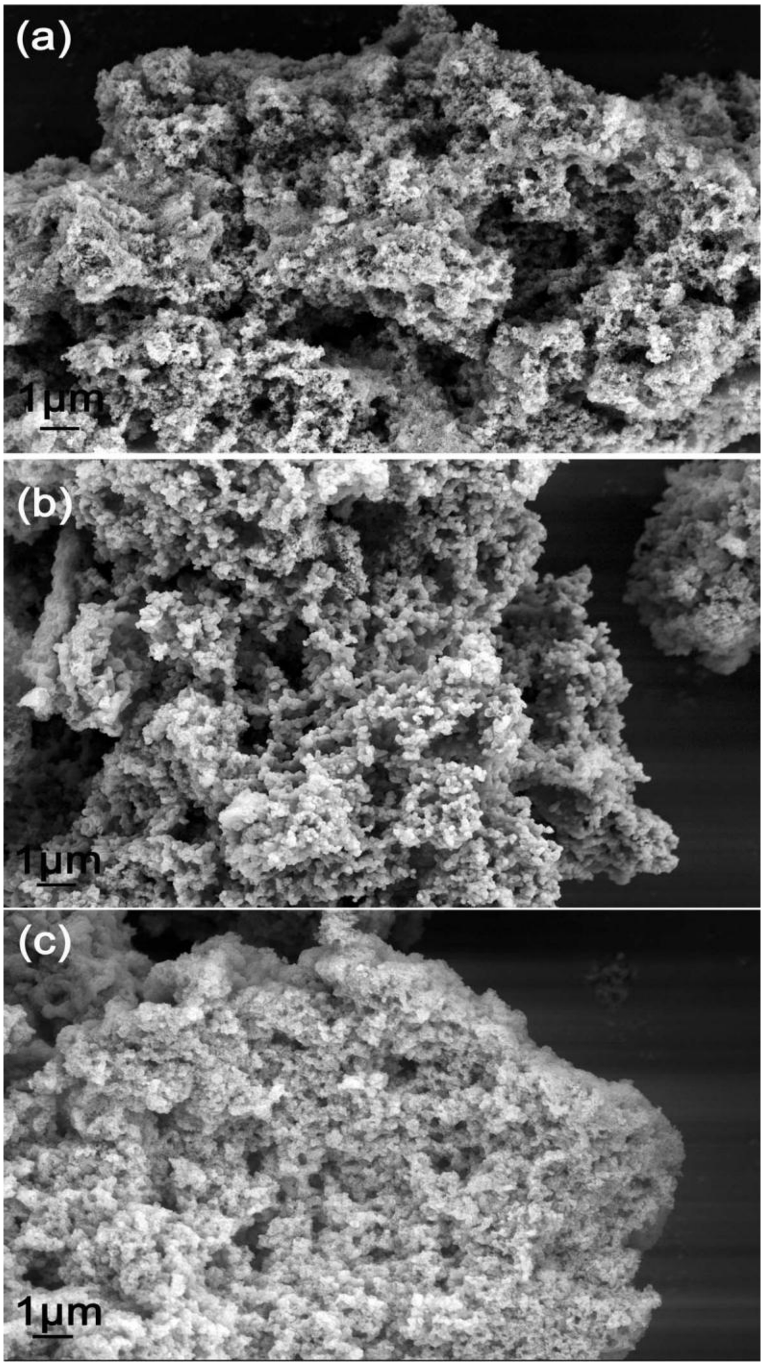

Figure 5.12: SEM images of hierarchical porous silica (O-*3*-HPS-*x*) samples prepared with *x* = 2.5 (a), 25 (b) , and 50 (c).

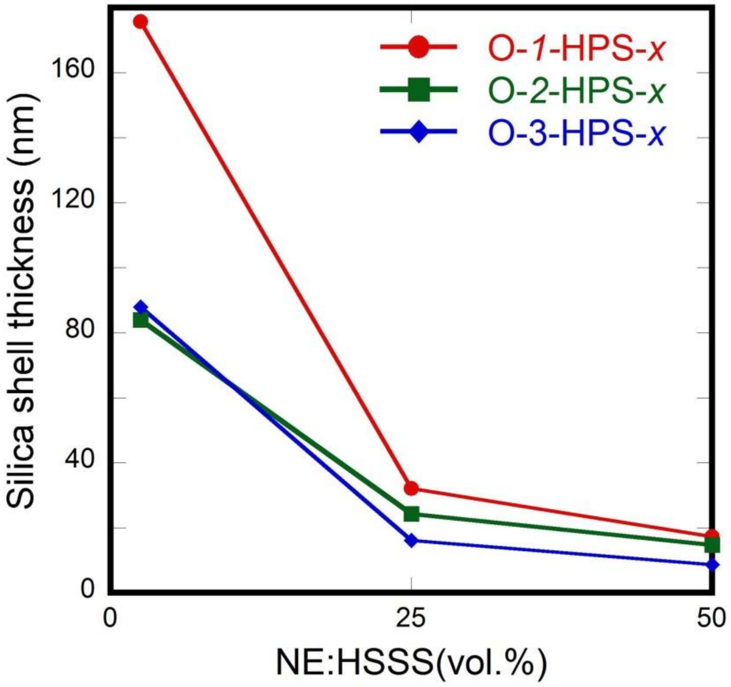

Figure 5.13: Effects of the volume of the nanoemulsion on the thickness of the silica shell

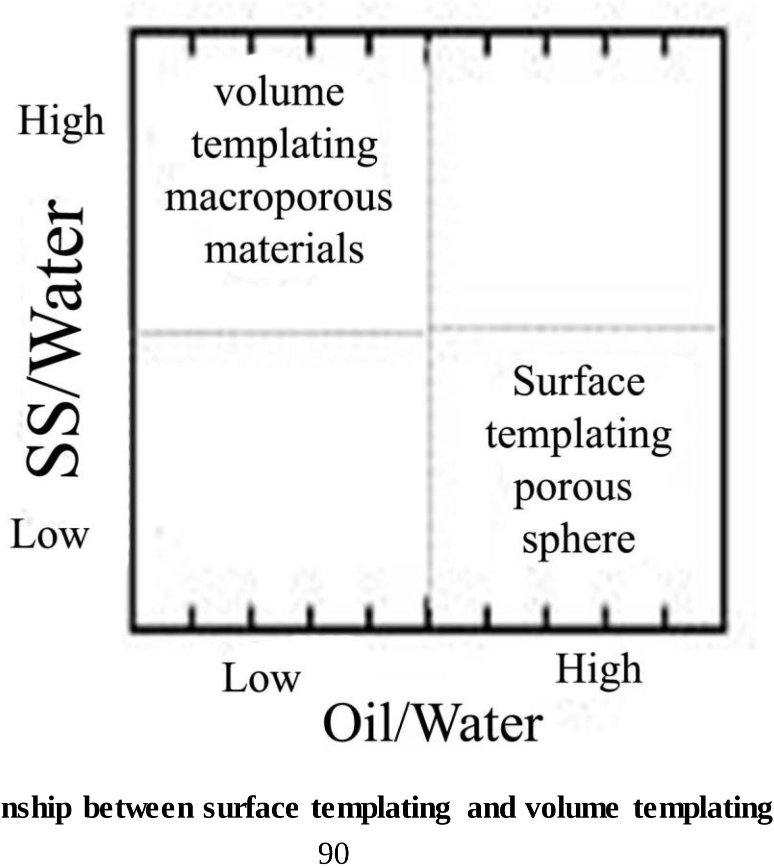

Figure 5.14: Relationship between surface templating and volume templating.

In Figure 5.15 (a), within each series (O-*y*-HPS-*x*) oil/water interfacial area is increased by increasing the nanoemulsion volume used. As an example, in the series O-*1*-HPS-*x* the interfacial area increases from 3.7 to 72 m^2 by increasing the nanoemulsion volume from 2.5% to 50%. The interfacial area is increasing in the first three series because of oil droplet diameter decreases from 400 nm, 200 nm, to 65 nm for O-*1*-HPS-*x*, O-*2*-HPS-*x* and O-*3*-HPS-*x* respectively while the oil mass was kept constant (10 g). For the series O-*4*-HPS-*x* and O-*5*-HPS-*x*, the interfacial area increases because of increasing oil mass from 25 g to 40 g. The interfacial area can be tuned between 3.7 m^2 to 760 m^2 and this is one of the advantages of nanoemulsion templating where it can be adjusted to easily control the interfacial area used in the reaction.

The silica concentration/interfacial area is depicted in Figure 5.15 (b). The silica concentration was kept constant in all the samples and the interfacial area is the variable which results in the change of silica concentration/interfacial area from 44 ($g/L.m^2$) to 0.16 ($g/L.m^2$). Figure 5.16 shows SEM for hierarchical porous silica (HPS) with different silica concentration/interfacial area. It seems that there is a critical silica concentration/interfacial area (0.7 – 0.6 $g/L.m^2$) where hollow spheres start to form

It is worth noting that there are two crystal growth processes: homogenous nucleation and heterogeneous nucleation. When nucleation happens within bulk solution with the formation of new interface between solution and solid phases, it is homogenous and it needs additional surface energy. When nucleation happens on existing nuclei or interface, it is heterogeneous nucleation which requires less energy. This is one reason for starting nucleation of silica at oil/water interface and the second one is that this interface is rich in surfactants which makes condensation of silica favourable. Hence, for silica concentration less than 0.6 ($g/L.m^2$), silica condensation is mostly heterogeneous and takes place at oil/water interface resulting in hollow spheres as in Figure 5.16(d,e). When silica concentration is higher than critical concentration, silica condensation is performed by both types of nucleation, meaning that heterogeneous nucleation is working at interface while homogenous nucleation is working in the bulk as a result of high silica concentration and low interface area as shown in Figure

5.16(a, b, c).[26-28]Either macroporous or hollow spheres silica is formed, both structure proved that NE is a suitable template to create macroporosity

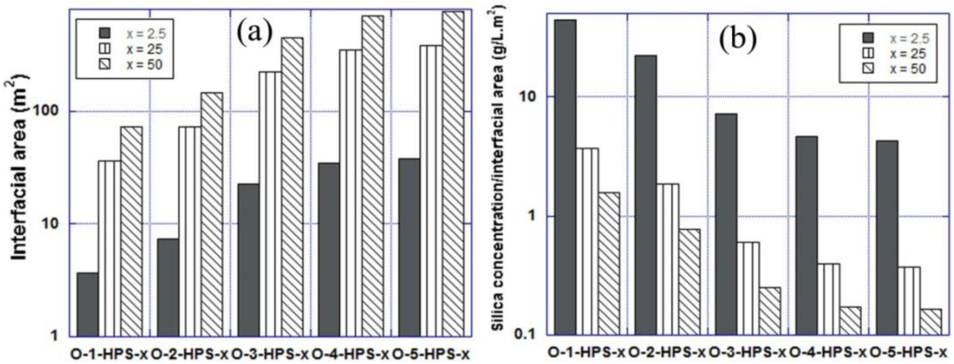

Figure 5.15: (a) calculated oil/water interfacial area for O-*y*-HPS-*x* and (b) calculated silica concentration/interfacial area.

5.4.5 Macroporosity

The mercury porosimetry is a method that can probe using about six orders of magnitude in order to access pore sizes ranging from about 400 mm down to a few Angstroms. Samples O-1-HPS-x, O-2-HPS-x, and O-3-HPS-x were analyzed with the use of this technique. Mercury intrusion curves plotted for one of the samples as a function of applied pressure and calculated pore size are represented in Figure C.2 (Appendix C).

The pore size distribution results shown in Figure 5.17 are surprising because no macropores can be observed; only mesopores peaking in the range between 8 nm - 14 nm can be seen. These results may be attributable to a number of causes, including the fact that the silica is too fragile to withstand the pressure and thus collapses, resulting in the manifestation of the mesoporosity but the absence of macropores. Some discrepancy in the absorption and desorption curves (Figure C.2, Appendix C)) may support this hypothesis, but it cannot explain every discrepancy. Another possibility is that the macropores, which should be filled at low pressures, can be filled only once the penetration pressure allows the mercury to enter the mesoporous windows. However, the mercury remains blocked in the mesopores and unable to fill the macropores. Other techniques, such as thermoporometry, should also be used for the full characterization of hierarchical porous structures.

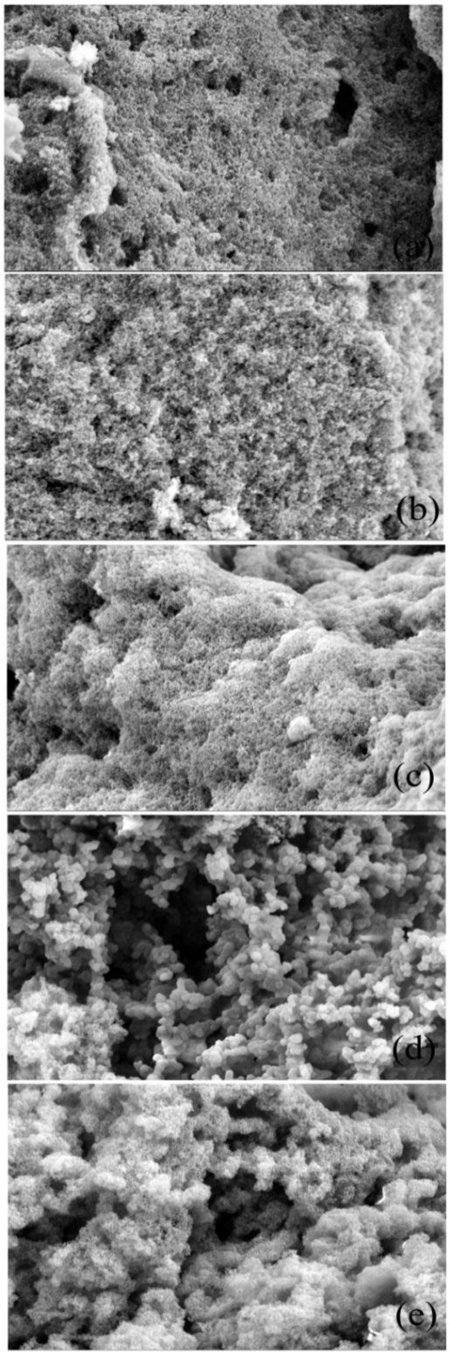

Figure 5.16:Silica concentration/ interfacial area (a) 22, (b) 7.2, (c) 0.7, (d) 0.6 and (e) 0.16

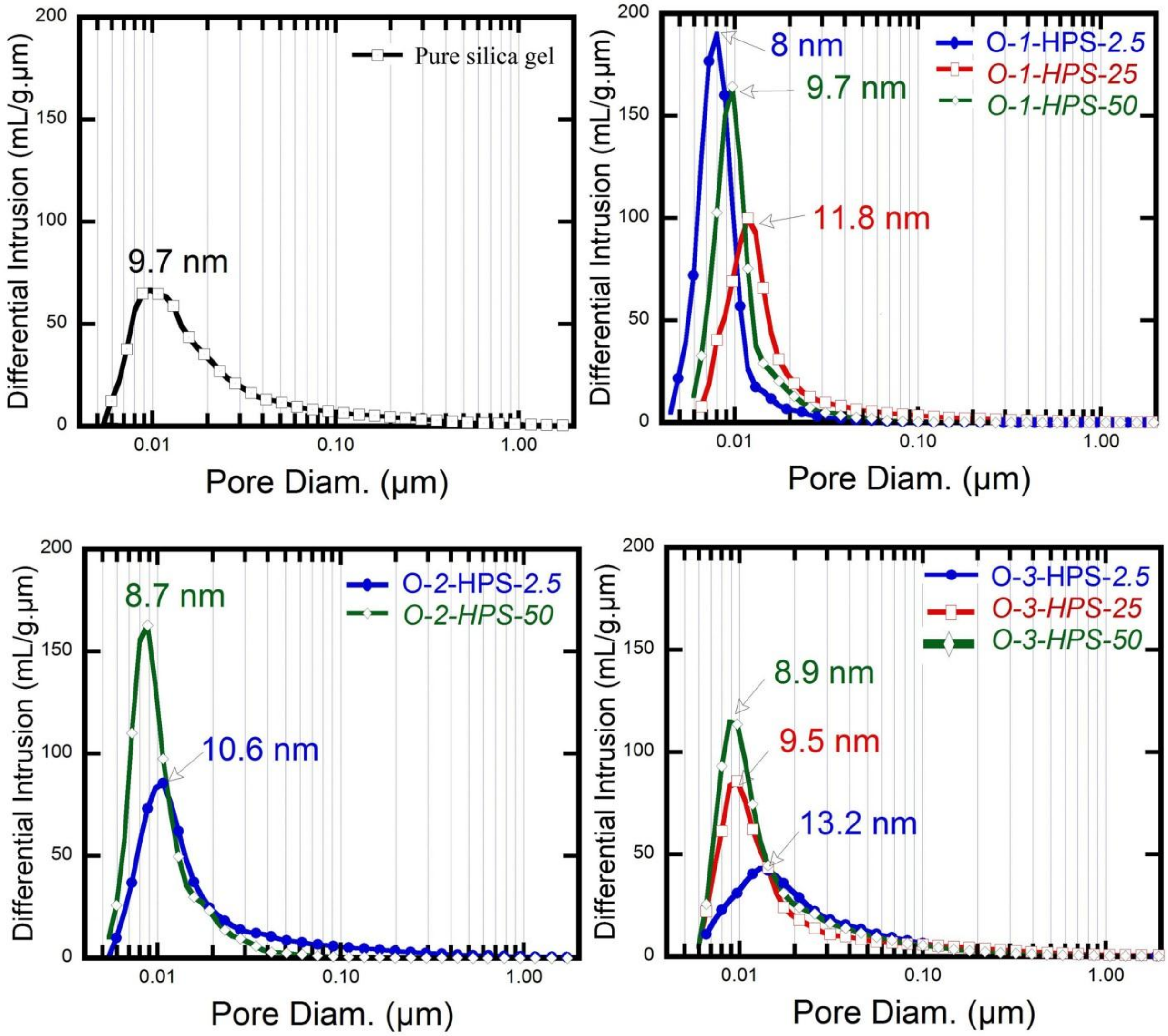

Figure 5.17: Pore size distribution of O-HPS-*x* measured by mercury porosimetry.

5.4.6 Structure of the Silica Framework

The FTIR spectra for (O-*y*-HPS-*x*) silica with different vol.% values of nanoemulsion: HSSS (*x*= 0, 2.5, 25, 100, and 200) are shown in Figure 5.18. The transmission peaks at 458 cm^{-1}, 802 cm^{-1}, 959 cm^{-1}, and 1,080 cm^{-1} are attributable to the bending vibration of the Si-O bond, the Si-O-Si asymmetric stretching vibration, the Si-OH symmetric stretching vibration, and the Si-O-Si symmetric stretching vibration, respectively.[15] The above peaks are found both in silica with no emulsion and in silica with different volumes of the nanoemulsion. The silica with the different volumes of the nanoemulsion typically exhibits the same structure as does the pure silica with no extra peaks. The addition of nanoemulsion has no effect on the local structure of the silica matrix when calcined in air, whatever the amount of nanoemulsion.

5.4.7 Mesoporous Structure of the Silica Framework

At that point, it is of importance to characterize the solidified walls porosity. First, when considering the emulsification process, a low amount of surfactants is used which should not generate mesoporosity through templating lyotropic mesophases. Figure 5.19.a displays a representative N_2 adsorption isotherm of silica with nanoemulsion vol. ratio = 2.5%, after calcination. The curves are in good agreement with type IV in the IUPAC classification for an H_{11} hysteresis loop, which is characteristic of a disordered mesoporous material.[16] The pore size distribution (Figure 5.19.b) shows two peaks with two little peaks at about 3 nm and 5 nm, and a much larger contribution at 18 nm. This analysis shows that the materials do exhibit mesoporosity in addition to the macroporosity observed by SEM (and not detectable by N_2 adsorption).

The origin of this type of mesoporosity needs to be identified, and see if the presence of the NE could modify this porosity, compared with that of a pure silica obtained with sodium silicate alone. The method employed was to condense a solution of hydrolyzed sodium silicate by adding ammonia until gelling. After freeze-drying, a xerogel was obtained which exhibits mesoporosity in a broad size range compared with that observed with templated mesostructured materials.

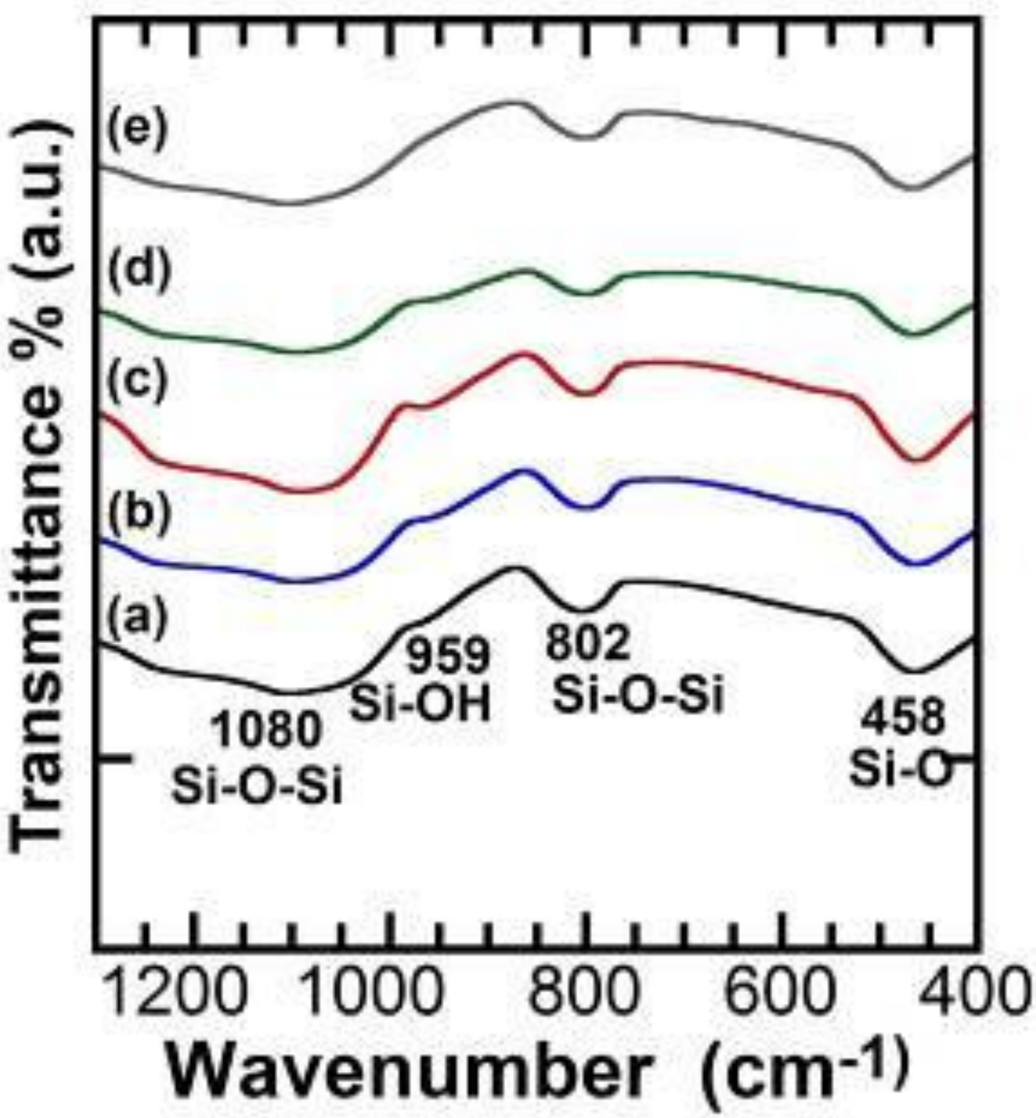

Figure 5.18: FTIR spectra of (HPS-*x*) silica with *x* = Vol.% of NE:HSSS: (a) 0, (b) 2.5, (c) 25, (d) 100, and (e) 200.

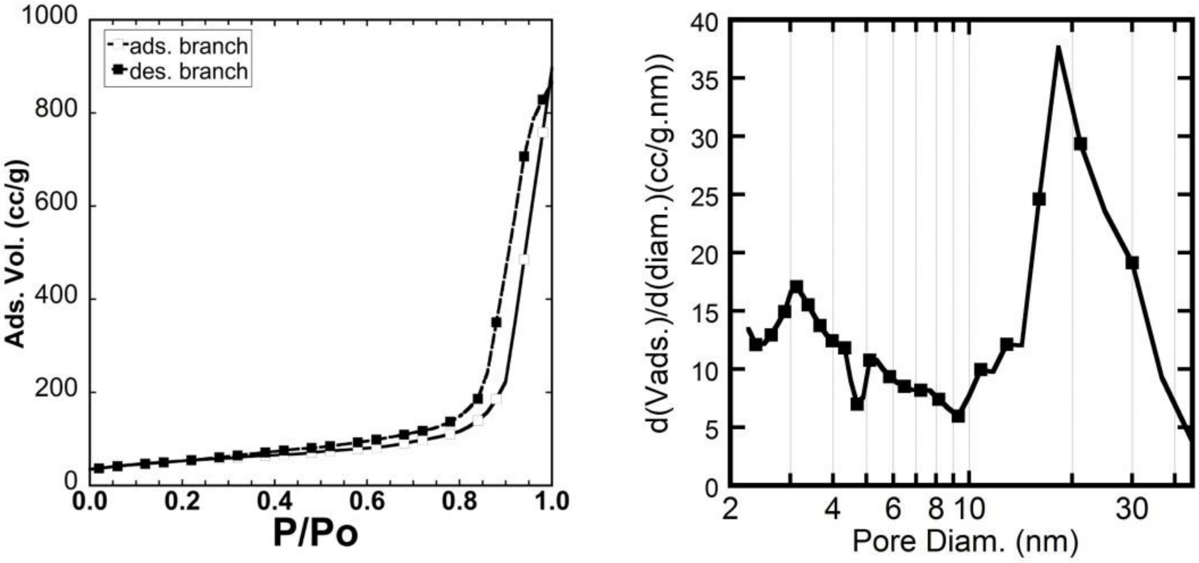

Figure 5.19: N_2 adsorption isotherm (a) and pore size distribution (b) for hierarchical porous silica O-*5*-HPS-*25*.

Silica gel is characterized by a microporous/mesoporous structure without the addition of any surfactant, which can be seen in sample (0) in Figures 5.20(a) and 5.20(b). Pure silica aerogel (sample (0)) has a BET surface area of 240 m^2/g, a pore volume of 2.2 cc/g at P/Po = 0.99, and an average pore width (4V/A) of 33 nm. Taking these initial values as starting points, the author examined how the addition of the nanoemulsion could modify the micro- and meso-porosity of the silica framework

A series of five samples were prepared by mixing different volumes of nanoemulsion with a constant volume of sodium silicate, with the nanoemulsion over sodium silicate vol.% equal to 2.5, 25, 50, 100, and 200, respectively. The isotherms of the calcined samples are shown in Figures 5.20.a and c, and the pore size distributions calculated for the samples are as shown in Figures 5.20.b and d. The N_2 isotherms of all the samples are of type IV but with different adsorption volumes at the highest partial pressure. The pore size distribution, deduced from the adsorption branch, reveals a significant porosity in the 2-5 nm range, and a clear additional contribution above 10 nm. If the small mesoporosity is similar to that observed with pure silica, and representative of the silica local coordination that remains unchanged and more affected by the chemical parameters (basic medium) than by the NE templating, the porosity in the 20 nm range is modified by the addition of the NE. This type of porosity is observed with pure silica (the NE cannot create such a small porosity), but it appears to be better defined when the nanoemulsion is added, at least up to a NE/HSSS vol.% of 50. Beyond, the structure is disturbed and the whole porosity is almost fully destroyed for the highest amount of NE (NE/HSSS = 200 vol.%). This last result proves that the nanoemulsion itself does not contribute to the formation of the mesoporosity in the 20 nm range, but that it results mostly from an optimization of the water content resulting from the addition of NE. Adding too much of the NE (above NE/HSSS = 50 vol.%) disturbs the spontaneous percolation of silicate species and the correct formation of the silica gel structure. This observation is in agreement with the previous results (Figure 5.8 & 5.9) that demonstrated that a too high dilution required a supplementary amount of ammonia to achieve the building of the silica framework.

This is also confirmed by the comparison between pore volumes and specific surface area. The adsorption volume at P/Po = 0.999 increases from 740 cc/g to 860 cc/g to 1,350 cc/g for NE/HSSS = 0.0, 2.5, and 25 vol.%, respectively. Then, it decreases to 945, 610, and 110 for silica with NE/HSSS = 50, 100, and 200 vol.%, respectively. These results indicate the absence of a direct relationship between the volume of the nanoemulsion and the pore volume, which can be attributed to the causal effect of the nanoemulsion with respect to the macroporosity that cannot be measured by the N_2 isotherm. This evolution describes mostly the influence of the increasing dilution of the silicate solution, upon the addition of increasing volumes of water, as a result of the addition of the nanoemulsion.

However, another question that arises is why the pore volume changes when the volume of the nanoemulsion is altered. The answer to this question is likely related to the concentration of the silicate. The nanoemulsion that is added to the sodium silicate solution contains oil, surfactant, and water. This water dilutes the silicate solution, and as the volume of the nanoemulsion increases, the additional water causes a decrease in the silicate concentration. This factor explains why, as the volume of the nanoemulsion increases from 0 to 2.5 to 25, the pore volume also increases because, as the silicate concentration decreases, the interaction distance between the silicate molecules increases, creating larger pores and higher surface areas. Additional increases in the volume of the nanoemulsion, with corresponding decreases in the silicate concentration, result in a weak silica framework, which collapses during the drying.

To confirm these observations, further hierarchical porous silica samples were characterized using N_2 isotherms in order to analyze how different nanoemulsions with different droplet size and different water ratios can affect the mesostructure of the silica. The surface area, pore volume, and surface roughness of these samples are summarized in Figure 5.21. Based on previous observations, the analysis is limited to the 0-50 domain in the NE over HSSS ratio. A uniform trend is observed with the parallel increase of both the specific surface area (Figure 5.21.a) and porous volume (Figure 5.21.b), which can be related to the previous analysis. To confirm this mechanism where the silica framework formation is not disturbed by the nanoemulsion, the silica surface roughness is deduced from the N_2 adsorption isotherms (Figure 5.21.c). Here again, and within the dilution range studied, the constant value of roughness (actually, the surface fractal dimension that must lie between 2 for a flat surface, and 3 for a theoretical infinitely rough surface) confirms an opened and rough surface that is not modified by the addition of the nanoemulsion. The porosity and bulk density are depicted in Figure 5.22. The porosity falls in the range of 58% to 93% and the bulk density is in the range of 0.1 to 0.9 g/cm^3. The highest porosity and lowest bulk density are assigned to sample O-*3*-HPS-*50* which has droplet size of 65 nm.

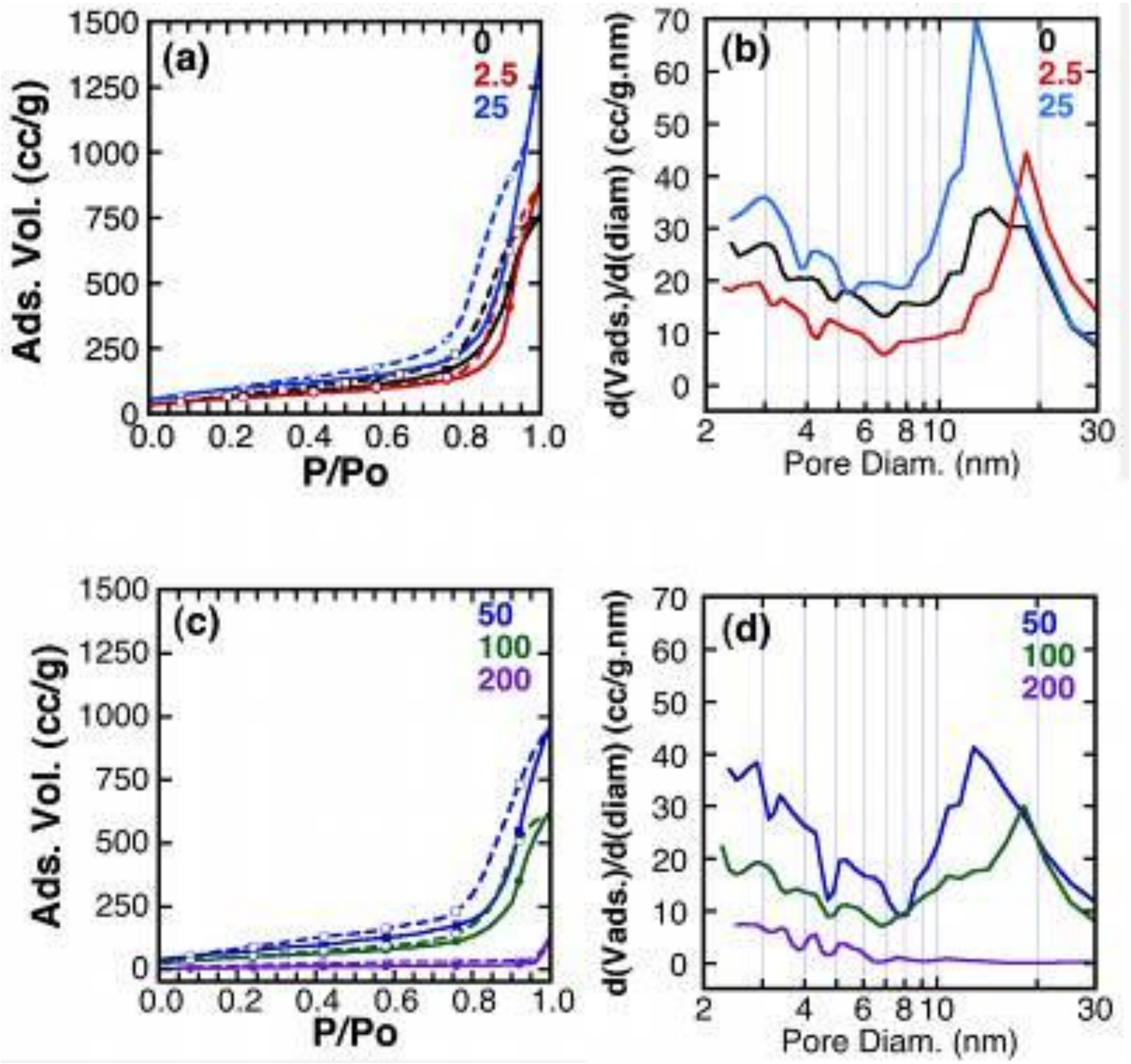

Figure 5.20: N_2 adsorption isotherm (a) and (c) and pore size distribution (b) and (d) for hierarchical porous silica HPS-*x*, where *x* = is the vol.% of NE to HSSS = 0, 2.5, 25, 50, 100 and 200.

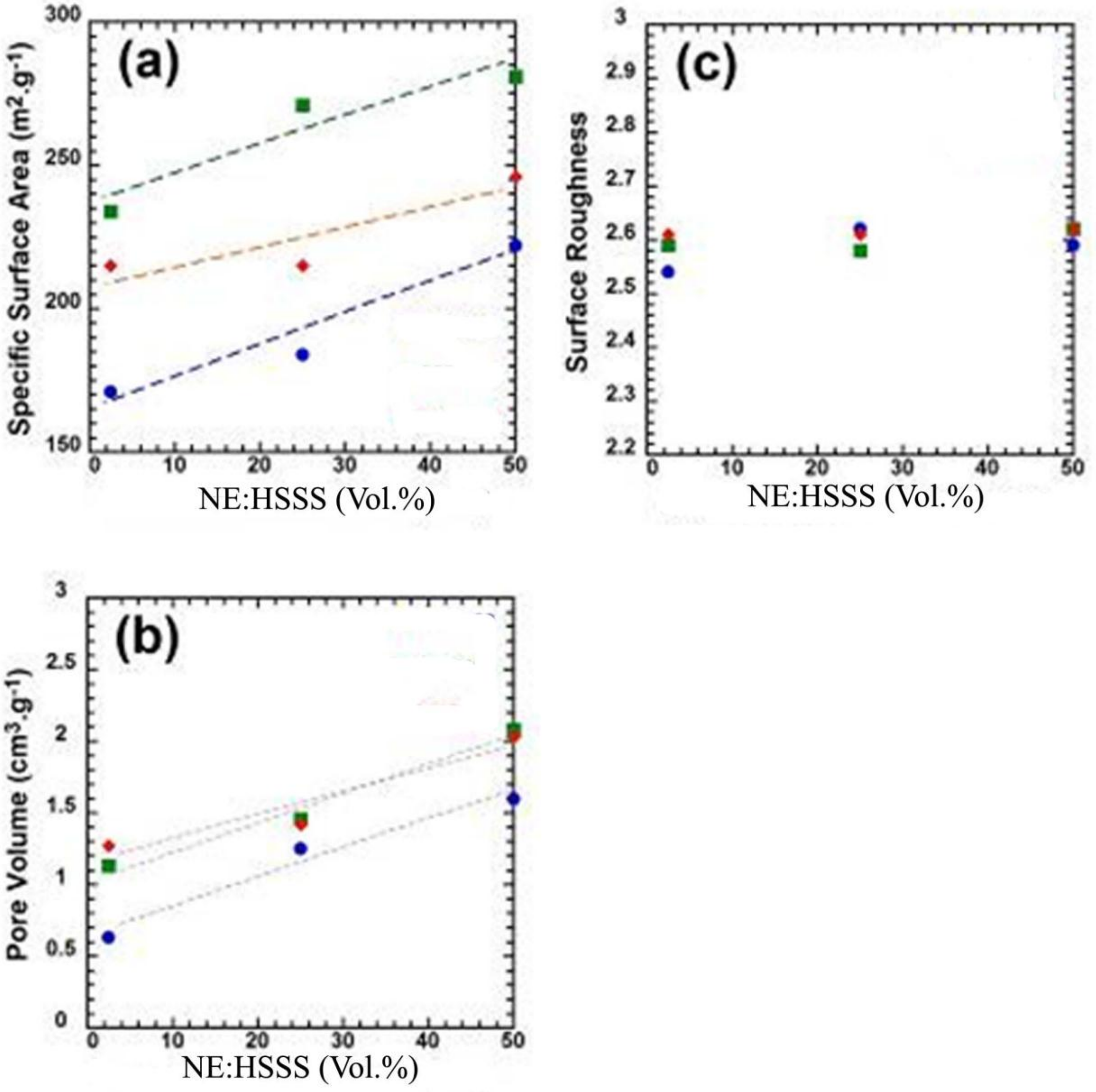

Figure 5.21: Surface area, pore volume, and surface roughness for hierarchical porous silica samples, blue for O-*1*-HPS-*x*, green for O-*4*-HPS-*x* and red for O-*5*-HPS-*x*.

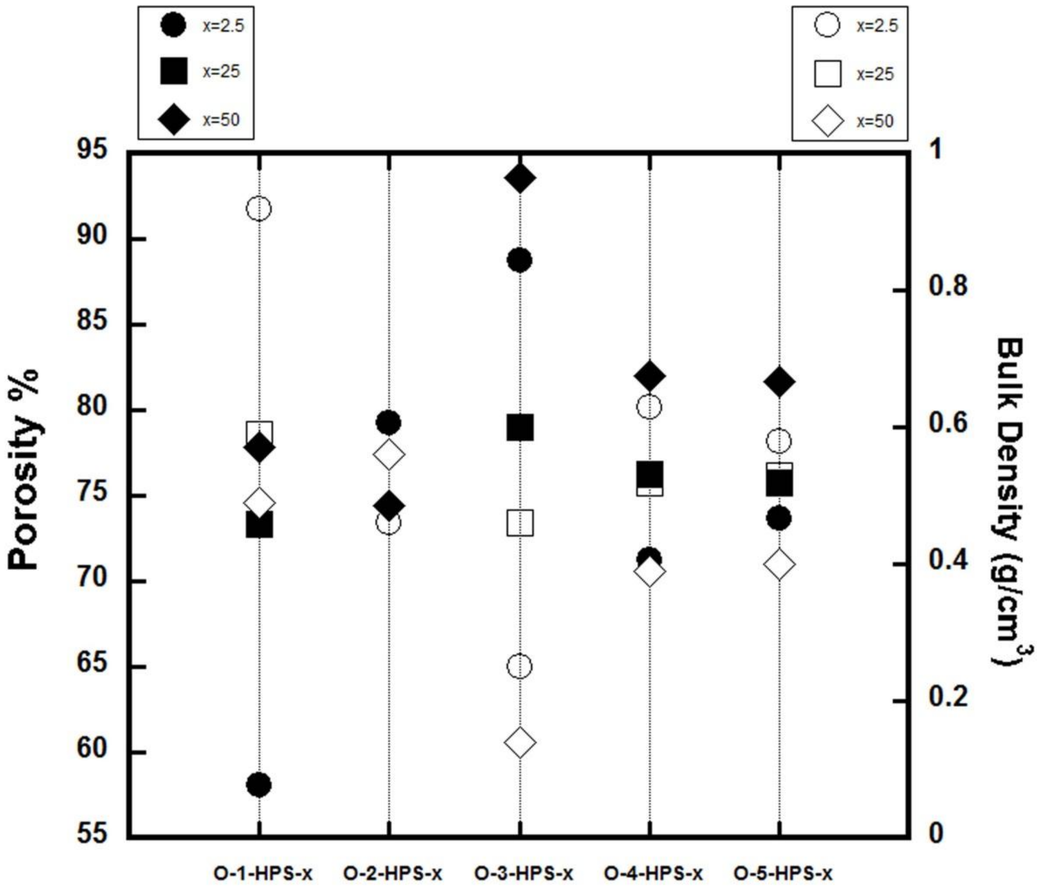

Figure 5.22: Porosity and bulk density as calculated from Nitrogen isotherm results for O-*y*-HPS-*x*, porosity (black symbols) and bulk density (white symbols).

5.4.8 Architecture of the Silica

The architecture of hierarchical porous silica was investigted by TEM and SAXS to probe the real structure of the prepared porous silica. The real-space morphology of the prepared hierarchical porous silica is examined by TEM and the resulting images for O-*1*-HPS-*2.5* and O-*5*-HPS-*50* are represented in Figure 5.23 (a,c) and (b,d), respectively. The dark regions correspond to the silica matrix and the bright regions are the pores. The pores are homogenously distributed in the silica matrix which is formed of tightly packed nanoclusters.

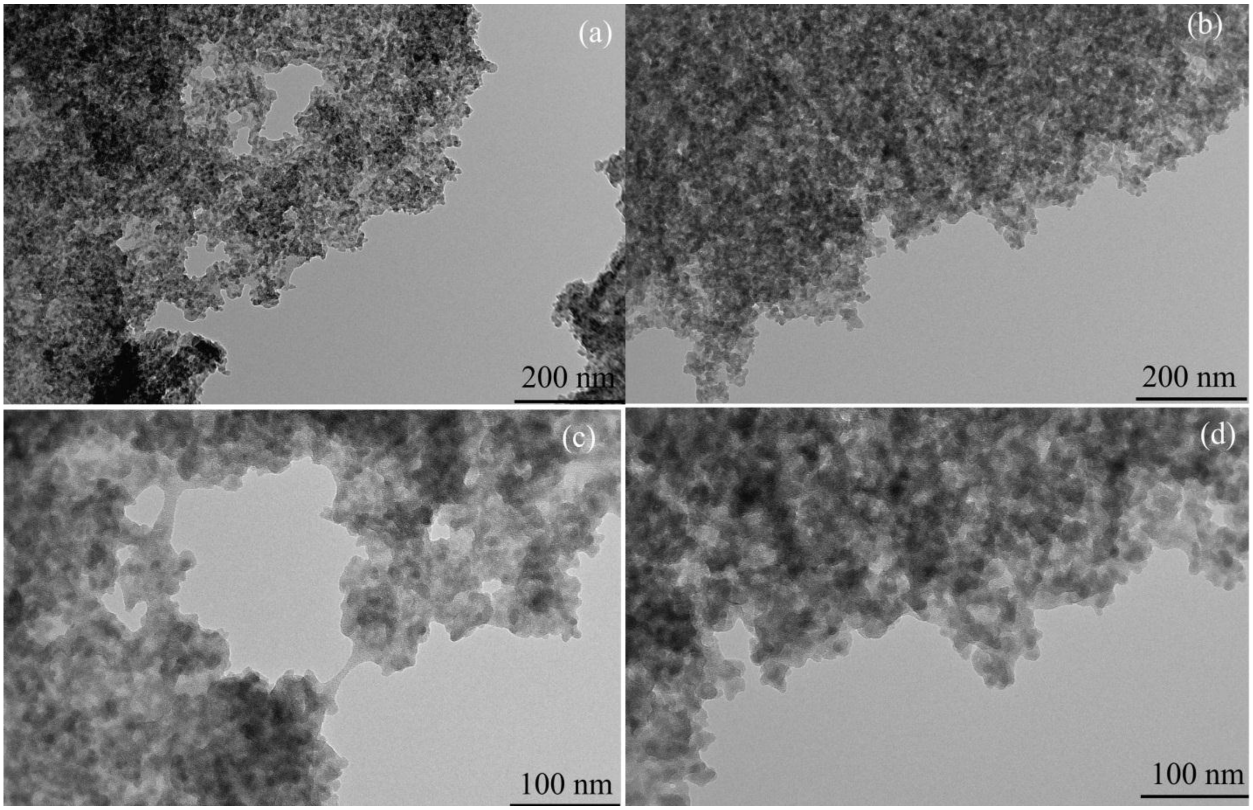

Figure 5.23: Representative TEM micrographs showing the real-space morphology of the O-*1*-HPS-*2.5* (a,c) and O-*5*-HPS-*50* (b,d).

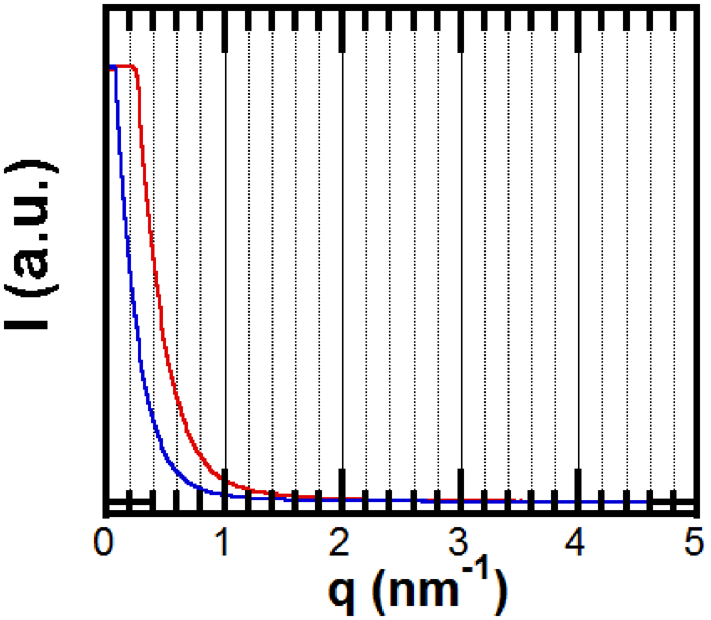

Figure 5.24: SAXS patterns for O-*1*-HPS-*2.5* (red) and O-*5*-HPS-*50* (blue).

Small Angle X-ray Scattering (SAXS) is a technique that allows for probing the existence of different levels of order (from simple correlation length to long range order) in the nanometric range. The SAXS pattern (Figure 5.24) for two hierarchical porous silica samples, with the absence of at least one single peak, indicates that the sample does not exhibit any long-range order in the pore arrangement. The description of the architecture of the silica gel networks is based on fractal geometry, which includes two types: surface and volume. Both types can be determined through SAXS analysis. Figure 5.25 displays the SAXS results for silica prepared with different volumes of a variety of nanoemulsions.

Figure 5.25 shows that the scattering profile plotted on the log(I)-log(q) scale is linear, with a change in the slope at low q. The linear behavior indicates that the SAXS profiles follow power law $I\ (q) \sim q^{-\alpha}$, where α is the fractal exponent. The value of α indicates which type of fractal is found: volume or surface. A volume fractal is found for $1 < -\alpha < 3$, and the mass fractal Dimension $D_v = -\alpha$, with a completely dense structure for $-\alpha = 3$. For a surface fractal, $3 < -\alpha < 4$, the surface fractal dimension $Ds = 6-(-\alpha)$, and a totally flat surface corresponds to $-\alpha =4$. The surface roughness can be assumed to be equal to the surface fractal dimension Ds

In an ideal case, the scattering curve, once plotted in the log-log way, should exhibit two linear parts, the first at lower q (corresponding to longer distances) that corresponds to the fractal distribution of porosity between particles, and the second one at higher q (corresponding to smaller distances) to the surface structure of the primary particles. However, it is important to remind that a fractal structure applies only to a self-similar structure, that is, a structure that exhibits the same geometry over a quite large range of dimensions. Therefore, the possible good fit of scattering curves with the fractal formalism has a real meaning only if this fit covers a minimum q range.

Figure 5.25 shows that for all of the curves, no linear part is observed in the q range, where the volume fractal should appear, but all of the figures display a rather linear evolution at a higher q range, which can be ascribed to the surface fractal. Figure 5.24 (a) represents curve for pure silica which when compared to other samples with nanoemulsion one can find that Guinier

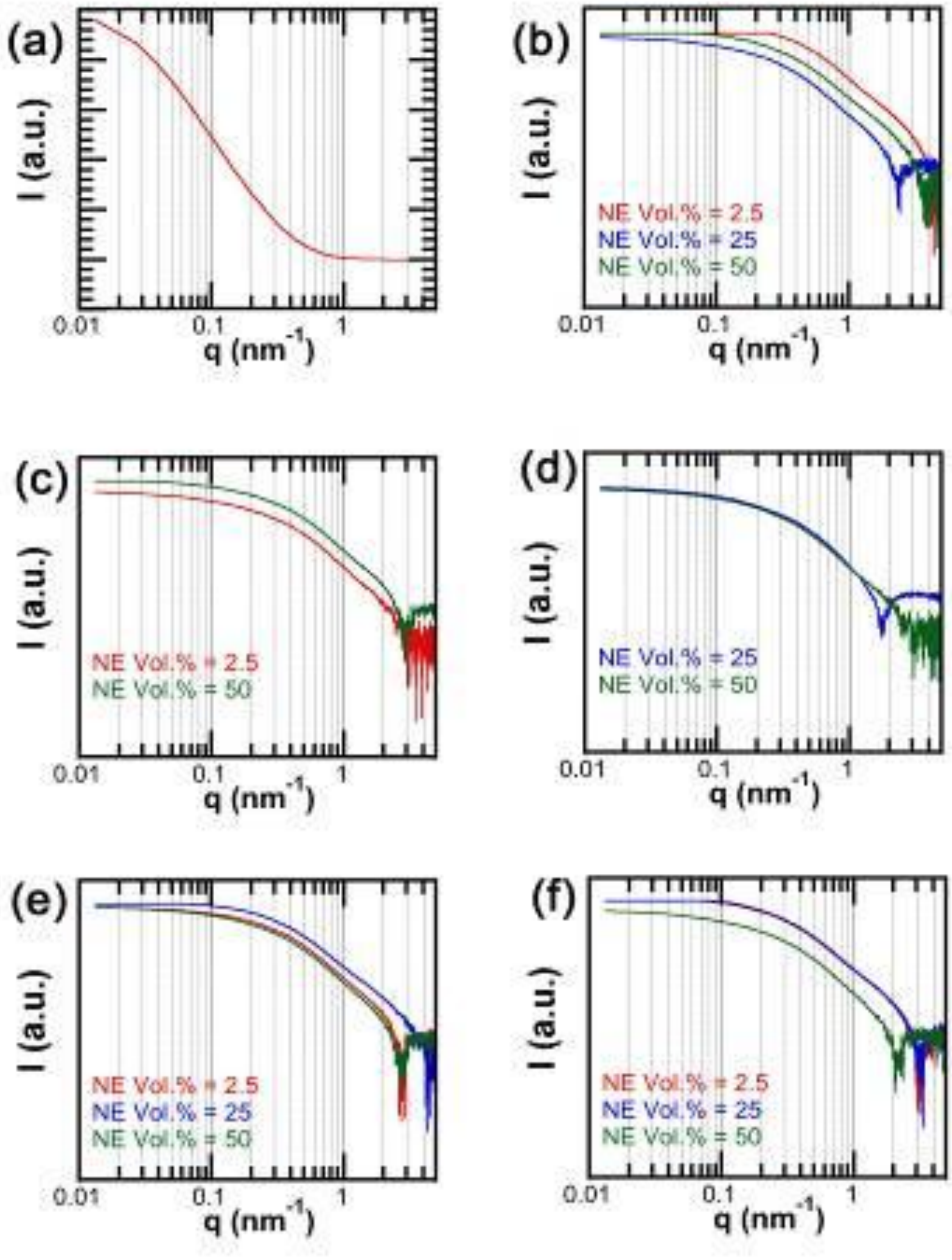

Figure 5.25: SAXS (a) pure silica with no nanoemulsion, (b) O-*1*-HPS-*x* silica (c) O-*2*-HPS-*x* silica (d) O-*3*-HPS-*x* silica (e) O-*4*-HPS-*x* silica and (f) O-*5*-HPS-*x* silica.

region is not found while it is long scale with other samples and show less scattering intensity. The surface roughness (surface fractal dimension), which can be calculated from surface fractal, are represented in Figure 5.25(Table C8, Appendix C). The overall average surface roughness is about 2.83 compared to 2.48 for pure silica which indicates an opened and rough surface.

In Figure 5.26, the cause behind change in surface roughness is not clear. To clarify the reason behind the change in surface fractal (surface roughness= 6-surface fractal), the surface fractal is depicted as a function in silica concentration. The surface fractal lies in the range of 3 to 4 with 4 is smooth surface and 3 is the fractal surface which has high roughness surface. In Figure 5.27, pure silica with highest silica concentration has highest surface fractal which in turn means that it is the smoothest surface in the series. By adding nanoemulsion to pure silica, silica concentration is diluted because of water coming from nanoemulsion which induces decreasing surface fractal by about 10%..

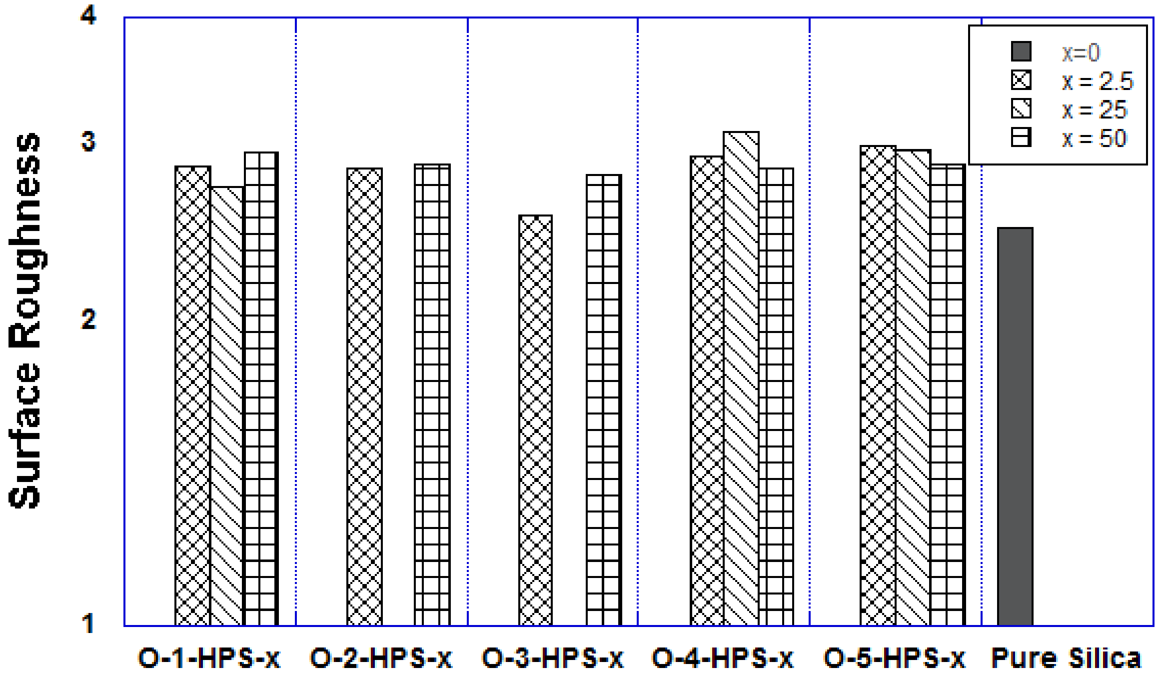

Figure 5.26: Representative demonstration for surface fractal dimension, *x* is the nanoemulsion volume%.

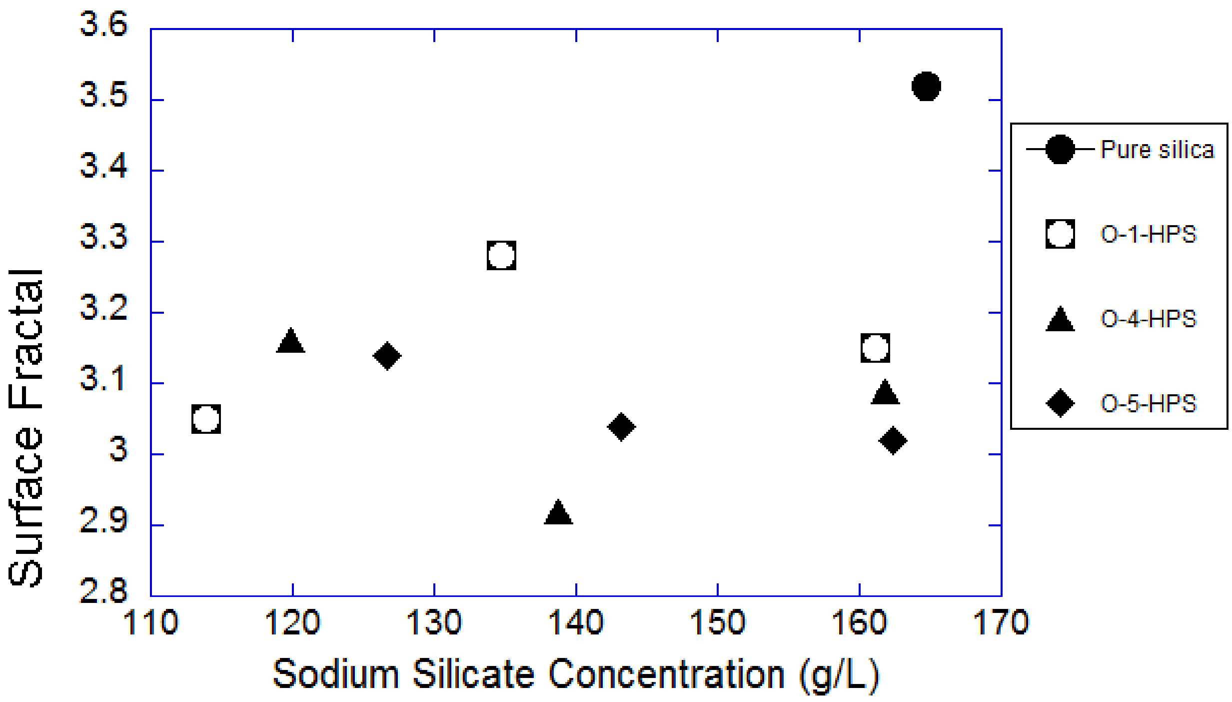

Figure 5.27: Surface fractal as a function in silica concentration.

5.4.9 Silica with Wax Nanoemulsion

Nanoemulsions proved to create macroporosity with a silica matrix as seen in SEM photos. However, the liquid state of paraffin oil droplets cannot allow them to fully withstand stress during condensation of silica. Thus, the possibility of preparing monodisperse oil droplets at higher temperature using a liquid state that could solidify as the system cools down at room temperature into solid particles is explored. Paraffin wax was used to partially replace paraffin oil in nanoemulsion and the melting temperature can be adapted along a whole range, depending on the proportions of oil and wax. Paraffin wax alone is solid at room temperature and has a melting point of 80 °C. Mixture of paraffin wax and oil are heated up so they are mixed well together then this mixture is used to prepare nanoemulsion by phase inversion composition (PIC) method. The oil:wax weight ratio was varied in order to adjust the temperature of solidification with the following oil:wax wt ratio: 5:15, 10:10, 15:5, 20:0 (in g). The novelty about this method is that the control of melting point is possible by changing the ratio between wax and oil as shown in Figure5.28. which opens the door to prepare thermostimulable materials. Details of compositions of wax nanoemulsion ((W-y-NE) and hierarchical porous silica prepared with wax nanoemulsion (W-y-HPS-x) are mentioned in Table C.4 and Table C.6 (Appendix C).

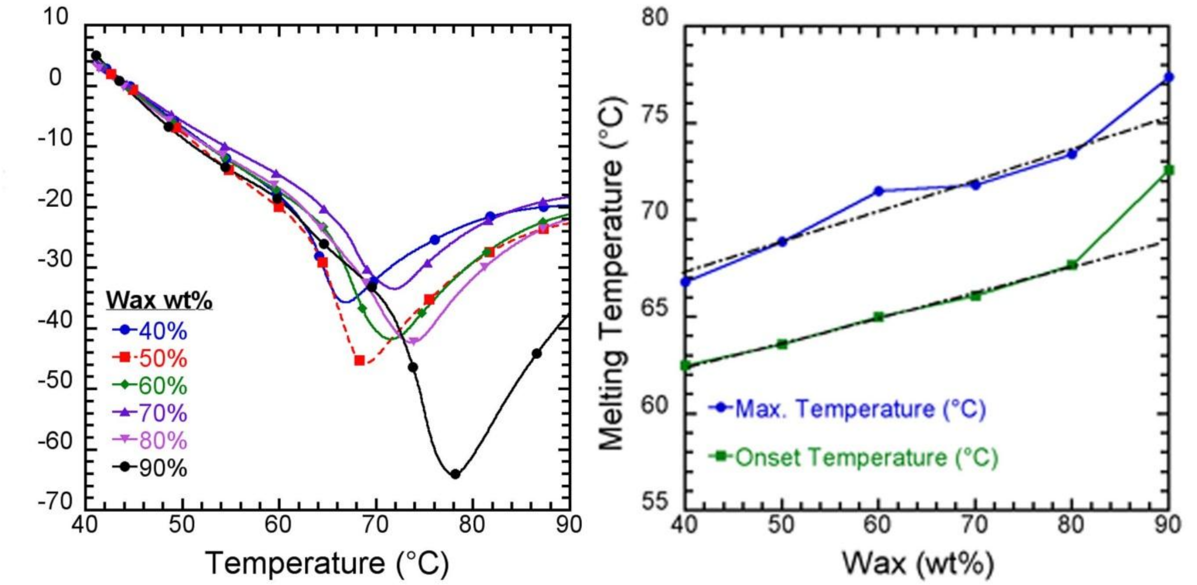

Figure 5.28: DTA curves for different mixtures of paraffin oil and paraffin wax, as a function of the wax weight content and relation between melting point and wax weight ratio.

SEM photos for (W-*y*-HPS-*x*) reveals good homogenous distribution for macropores within silica matrix as shown in Figure 5.29. It seems that these samples have monolithic structure more than observed in O-*y* -HPS-*x* as shown in SEM pictures in Appendix C (Figure C 3-C 6).

Nitrogen isotherms and pore size distributions of four series of (W-*y*-HPS-*x*) prepared using nanoemulsions with different ratios of wax and paraffin oil are shown in Figure C.7 and C.8 (Appendix C). The N_2 isotherms of all the samples show high different adsorption volumes at the highest partial pressure. The pore size distribution, deduced from the adsorption branch, reveals a significant porosity in the 2-5 nm range, and a clear additional contribution above 10 nm. If the small mesoporosity is similar to that observed with pure silica, and representative of the silica local coordination that remains unchanged and more affected by the chemical parameters (basic medium) than by the NE templating, the porosity in the 20 nm range is modified by the addition of the NE. Figure 5.30 shows BET surface area, pore volume and surface roughness as calculated from isotherm. Surface area for W-*y* -HPS-*x* samples has higher surface area range (230-300 m^2/g) compared to surface area for O-*y* -HPS-*x* samples which is in the range of 170-280 m^2/g. Surface roughness of W-*y* -HPS-*x* (2.58-2.68) is higher than O-*y* -HPS-*x* (2.54-2.63). The porosity and bulk density are depicted in Figure 5.31. The porosity falls in the range of 58% to 93% and the bulk density is in the range of 0.1 to 0.9 g/cm^3. The average porosity and the average bulk density are 80% and 0.45 g/cm^3. SAXS analysis for W-*y* -HPS-*x* is shown in Figure 5.32. Surface roughness is calculated from SAXS results as shown in Figure 5.33 and Table C.10 (Appendix C). Surface roughness for W-*y* -HPS-*x* (2.93) is higher than O-*y* -HPS-*x* (2.83).

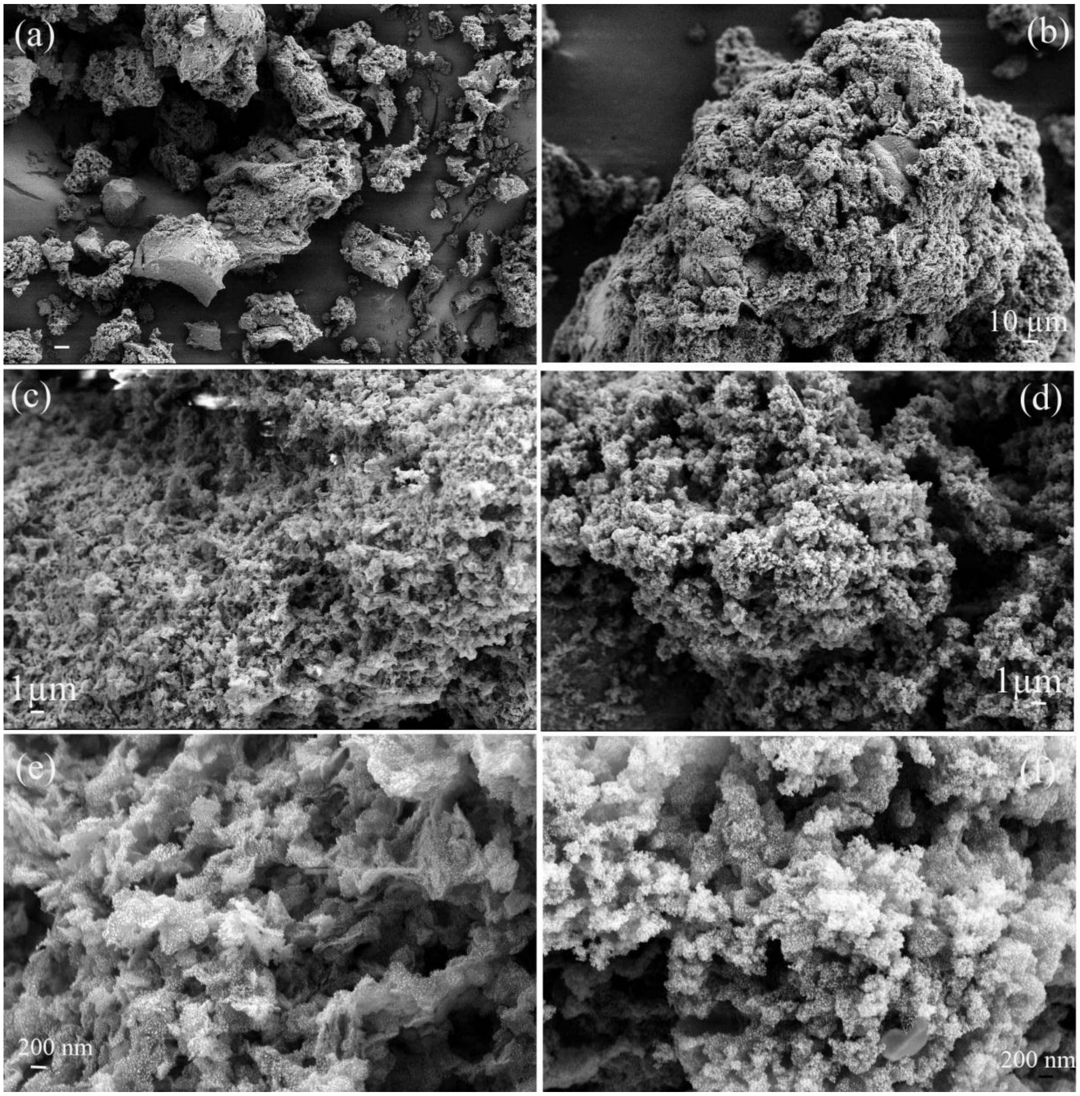

Figure 5.29: SEM photos for W-*2*-HPS-25 (a) , (c) and (e) and W-*4*-HPS-25 (b), (d) and (f).

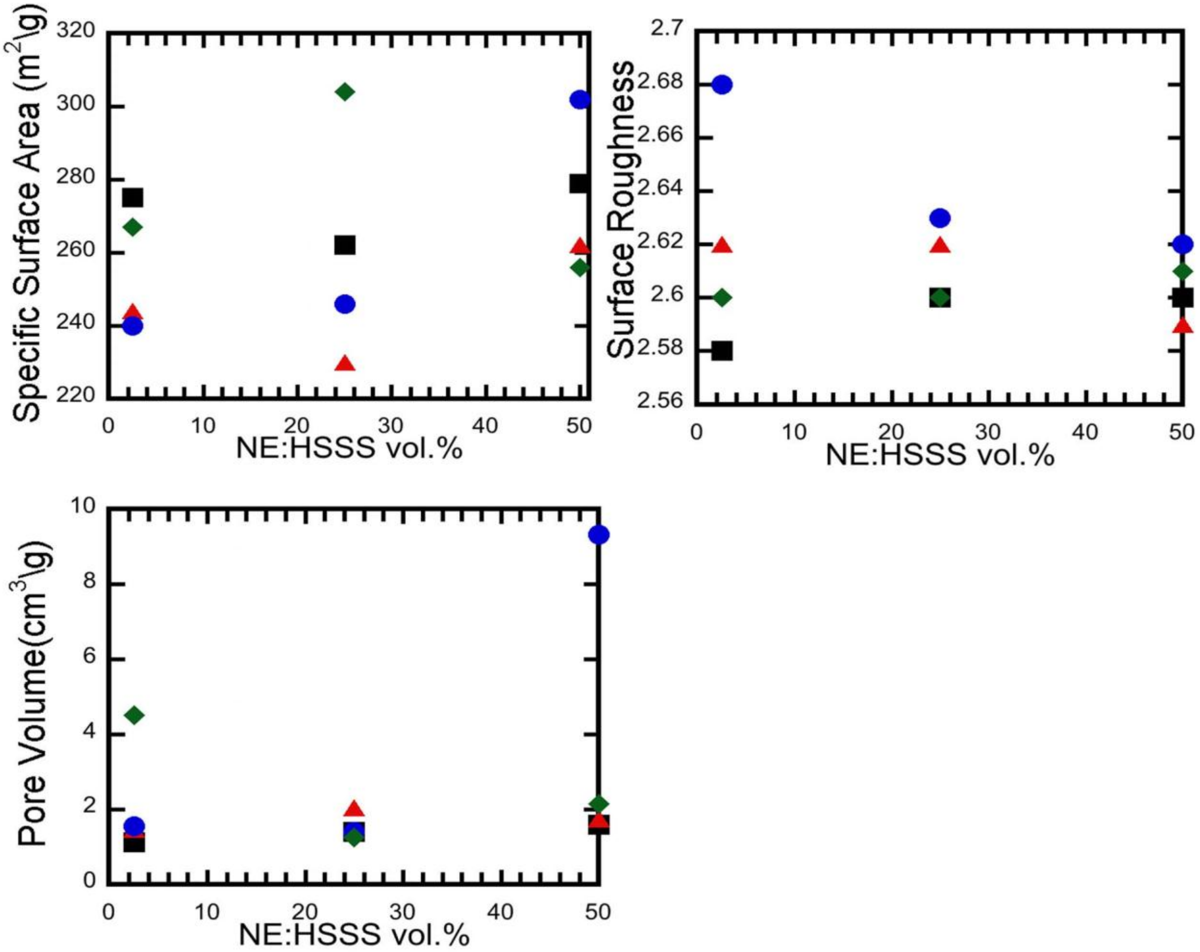

Figure 5.30: Surface area, pore volume and surface roughness of W-*y*-HPS-*x*: (♦) W-*1*-HPS-*x*, (●)W-*2*-HPS-*x*, (▲)W-*3*-HPS-*x* and (■)W-*4*-HPS-*x*

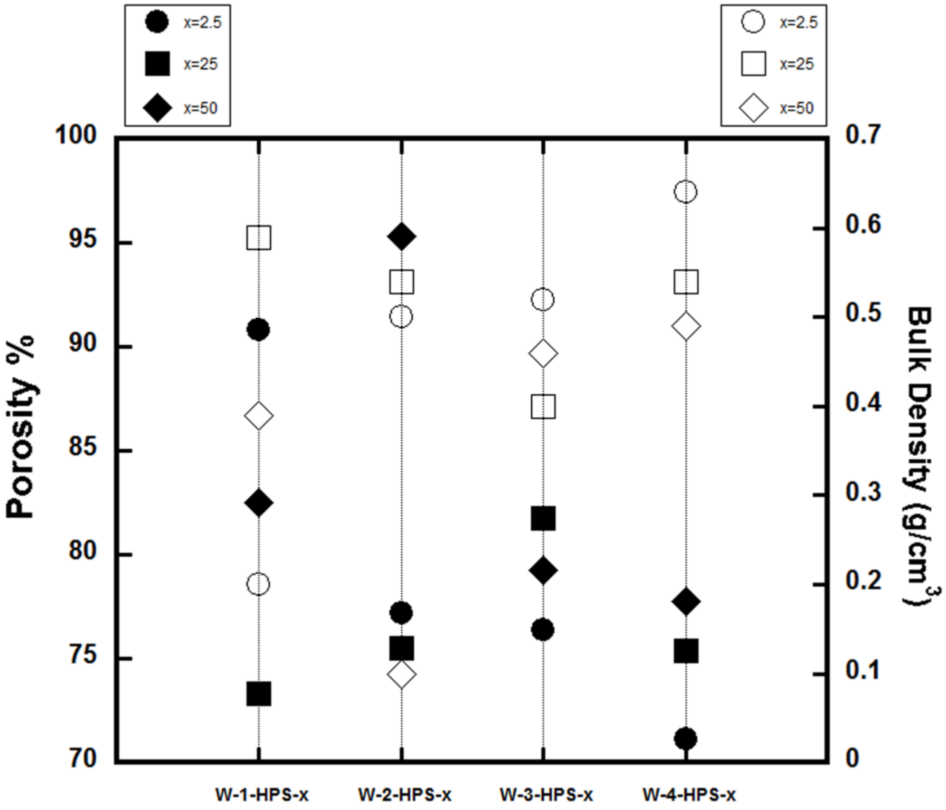

Figure 5.31: Porosity and bulk density as calculated from Nitrogen isotherm results for O-*y*-HPS-*x*, porosity (black symbols) and bulk density (white symbols).

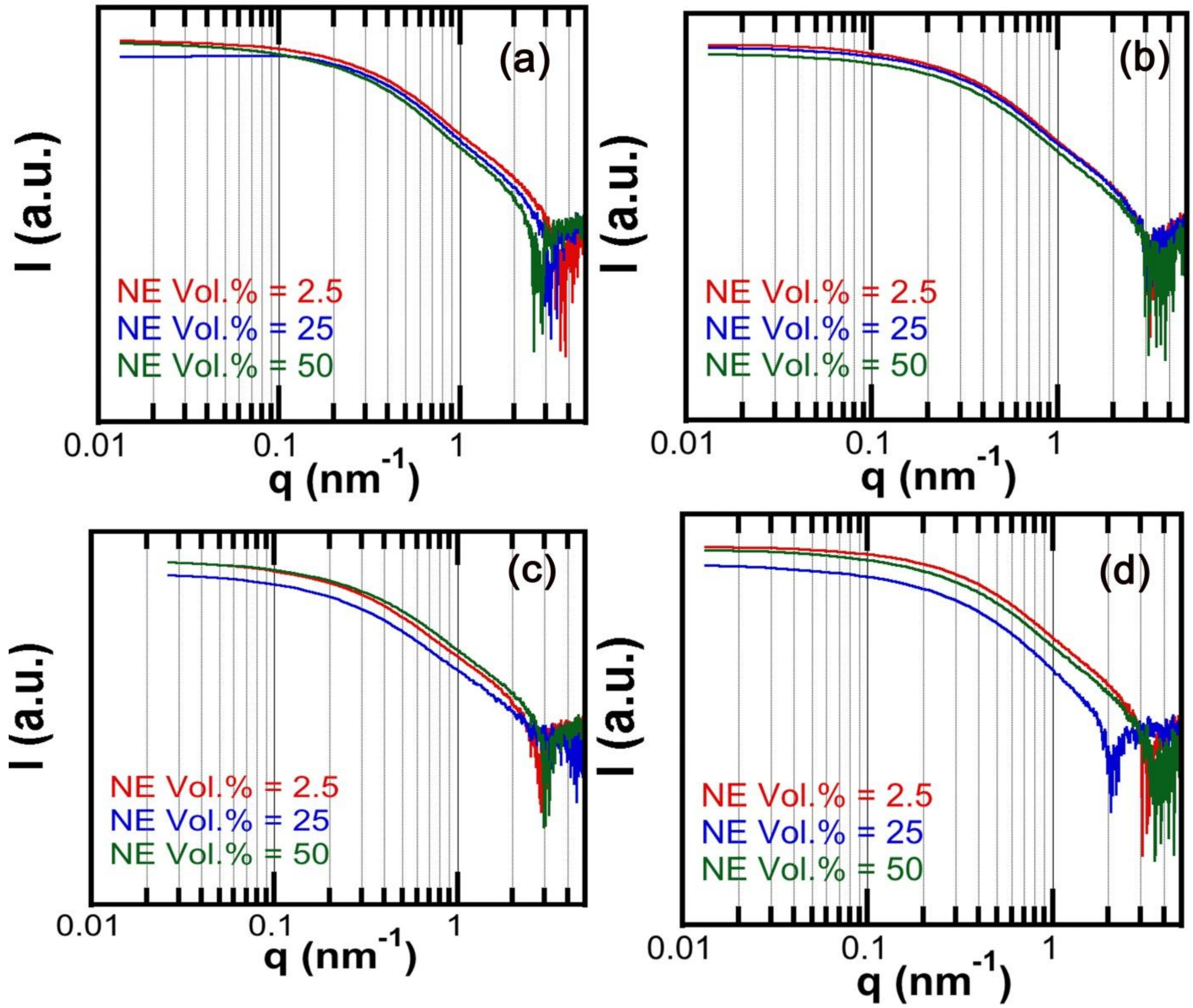

Figure 5.32: SAXS for (a) W-*1*-HPS-*x* (b) W-*2*-HPS-*x* (c) W-*3*-HPS-*x* and (d) W-*4*-HPS-*x*, with *x* =NE vol.%

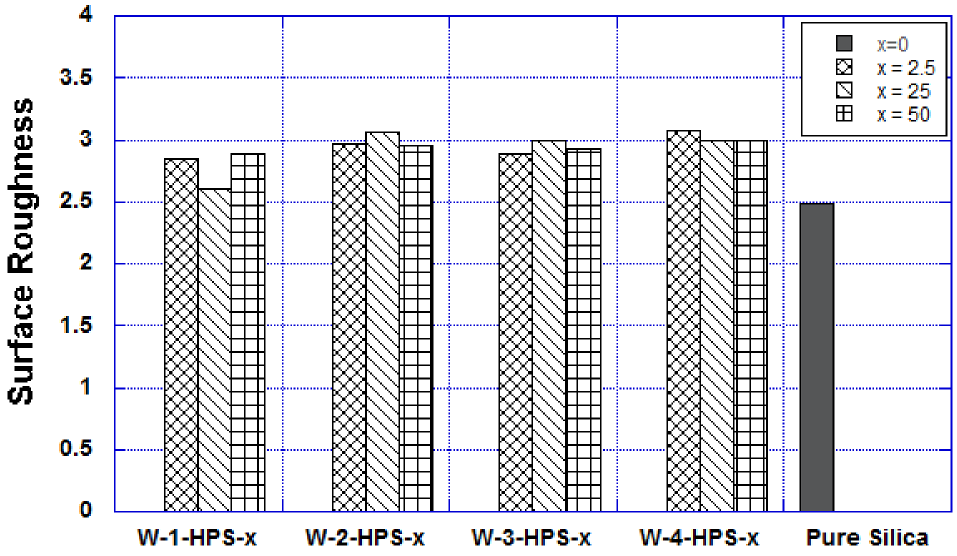

Figure 5.33: Representative demonstration for surface roughness, *x* is the nanoemulsion volume%.

5.5 Summary

In this chapter, it has been demonstrated that nanoemulsion prepared by low-energy methods can be integrated with sol-gel to prepare hierarchical porous silica in a facile way. Nanoemulsion templating provides an easy way to prepare macroporous silica with different pore sizes and different pore volumes by changing the nanoemulsion used. Moreover, changing the oil/water interfacial area results in changing the microstructure from macroporous materials into hollow spheres. In addition to macroporosity, the hierarchical porous silica has micro and mesoporosity, which cause together high surface area for materials of about 200-300 m^2/g. To increase the resistance of oil droplets to stresses of condensation, wax/oil nanoemulsion can be used. After the nanoemulsion proved its ability to be used as a template and this is the time to test the capability of nanoemulsion to template and functionalize silica in the same time.

Chapter 6

Metal Oxide-Hierarchical Porous Silica Nanocomposites*

6.1 Overview

The use of nanoemulsions as carriers for metal oleates as hydrophobic precursors for metal oxides and as nanoreactors has enabled the synthesis of metal oxide nanoparticles that remain trapped inside the large cavities delimited by porous silica, providing a "rattle-like" structure in the final material. This synthesis proceeds from a one-step formation of internal functionalized metal oxide-hierarchical porous silica (MHPS) nanocomposites. Using this strategy for synthesis gives control over type and concentration of functional materials, and prevents agglomeration.

6.2 Introduction

Silica is an inert material that must be functionalized in order for it to be useful in applications. Many methods are employed as a means of functionalizing silica, most of which involve post-treatment by wet techniques such as impregnation or chemical vapor deposition. Some methods are based on in-situ functionalization, which includes multi-step processes such as the initial impregnation of the latex with the functional material, followed by the formation of a matrix around the template.[1]

---

* Partially adapted from "Hessien, M.; Leone, P.; Suchaud, M.; Lebeau, B.; Nouali, H.; Guari, Y.; Prouzet, E., "Nanocrystalline iron oxide synthesised within Hierarchical Porous Silica prepared by nanoemulsion templating." *Chem Commun (Camb)* **2012,** *48* (80), 10022-4."

The work conducted for this thesis aimed to demonstrate the functionalization of hierarchical porous silica (HPS) in a one-pot synthesis through the double use of a functional nanoemulsion as a template for porous silica, and a carrier for hydrophobic precursors added to the silica matrix, as shown in Figure 6.1. The preparation of metal oxide nanoparticles inside porous silica, with the precursors being contained within the nanoemulsion droplets, required the initial preparation of hydrophobic precursors of metal oxides. Therefore, metal oleates were prepared and added to the oil phase in order to obtain a metal oleate nanoemulsion (MNE). This MNE was used as a template for the preparation of metal oxide-hierarchical porous silica (MHPS) nanocomposites. This type of synthesis is an example of a triple integrative synthesis, which integrates the aqueous sol-gel chemistry of sodium silicate (soft chemistry) with soft matter (nanoemulsion) and metal oxide preparation from metal oleate.

In this synthesis, the dispersed phase, or oil droplet, is used as a nanoreactor that contains the precursors of nanoparticles that will be generated directly into the porous silica matrix. To validate this new method, two types of metal oxides: iron oxide and cobalt oxide were tested. The choice of these metal oxides was based on the possibility to check how the initial oxidation degree (for Fe) "resist" to the synthesis, and above all, demonstrates that the original approach could be expanded to other metal oxides in the future. The method followed for this synthesis is very similar to that reported in the previous chapter: the aqueous phase of the NE is used to prepare the silica matrix from a hydrolyzed sodium silicate solution (HSSS), and the oil droplets of the NE, which contain metal oleate, are used as templates for the preparation of porous silica and nanoreactors for the synthesis of metal oxide and/or metal nanoparticles from the pristine metal oleate. With this method, after the MNE is mixed with the HSSS, an MNE-silica hydrogel is formed. The calcination of the MNE-silica hydrogel caused the transformation of the metal oleate into a metal oxide trapped in pores formed by the burning of paraffin oil, creating the metal oxide hierarchical-porous silica nanocomposite (M^z-y-HPS-x).

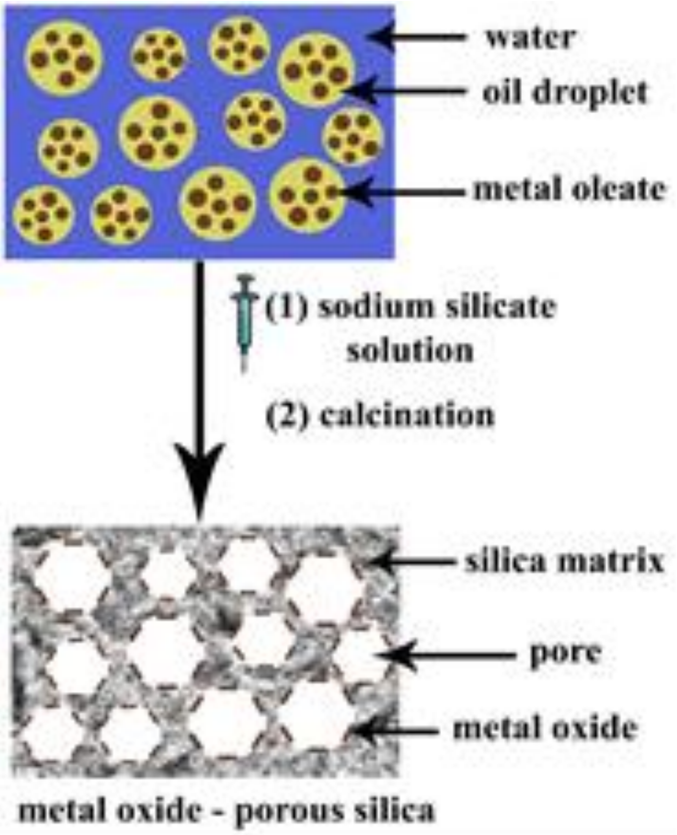

Figure 6.1: General scheme of the preparation of metal oxide-hierarchical porous silica (MHPS).

The advantages of this integrative synthesis include saving processing time because the porous silica is synthesized and functionalized at once, rather than in the conventional two-step method, known as the post-synthesis impregnation method.[2] This new method guarantees that a better homogeneity can be achieved. Watkins et al. functionalized mesoporous silica based on one-pot synthesis through the use of a block copolymer as a replica, and a solubilizing active nanoparticle as ferritin in the aqueous phase, with TEOS for the silica framework. Their method is an effective method of encapsulating nanoparticles in one step, but it fails to provide control of the porosity structure.[3]

6.3 Experimental Section

6.3.1 Materials

All chemicals were used as received, without further purification: paraffin oil (d = 0.86 g/cm^{-3}) (Fluka); Sorbitan monooleate (Span 80™, d=1.08, Mw = 428.6 g) (Across) and polyoxyethylene (20) sorbitan monooleate (Tween 80™, d = 0.994, Mw = 1,310 g) (Sigma); sodium silicate solution (reagent grade, ~10.6 Na_2O and ~26.5 SiO_2, d= 1.39) (Sigma-Aldrich); HCl (37 %, Sigma-Aldrich); ammonium hydroxide (28 %–30 % , d = 0.9); oleic acid (Technical grade, 90 %, $C_{18}H_{34}O_2$, FW= 282.47 g, Aldrich); sodium oleate ($C_{18}H_{33}NaO_2$,); ferric chloride hexahydrate ($Fe^{(III)}Cl_3\bullet 6H_2O$, EMD); ferrous chloride tetrahydrate ($Fe^{(II)}Cl_2\bullet 4H_2O$, Sigma Aldrich); and cobalt (II) chloride hexahydrate ($CoCl_2\bullet 6H_2O$, Sigma).

6.3.2 Synthesis

The work presented in this chapter entailed the synthesis of a number of materials, as described in these subsections.

6.3.2.1 Synthesis of Metal Oleate

The synthesis of the metal oleate was based on a method previously reported by Park et al.[4], with the reaction of metal chloride with sodium oleate. Three types of metal oleate were prepared: iron oleate (Fe^a-OL, Mw=900 g) prepared from ferric chloride, iron oleate (Fe^b-OL, Mw=2418.7g) prepared from a mixture of ferric and ferrous chloride with a ratio of 2:1, and cobalt oleate (Co-OL, Mw= 621g). For the typical synthesis of a metal oleate complex, 40 mmol of metal chloride and 120 mmol of sodium oleate (36.5 g) are dissolved in a homogeneous solution composed of ethanol (80 mL), water (60 mL), and n-hexane (140 mL). Details of the composition are presented in Table 6.1. The resulting solution was heated to 70 °C and kept at that temperature for 4 h. The metal oleate that resulted from the heating was recovered as a waxy layer on top of the solution and was then washed three times with 30 mL of distilled water in a separatory funnel.

Table 6.1: Composition of metal oleate.

Sample name	Metal chloride		Sodium oleate (g) (120 mmol)
	Type	Weight (g) (40 mmol)	
Iron Oleate (Fe^a-OL)	$Fe^{(III)}Cl_3 \bullet 6H_2O$	10.8	36.5
Iron Oleate (Fe^b-OL)	$Fe^{(II)}Cl_2 \bullet 4H_2O$	2.7	36.5
	$Fe^{(III)}Cl_3 \bullet 6H_2O$	7.2	
Cobalt Oleate (Co-OL)	$CoCl_2 \bullet 6H_2O$	14.2	36.5

6.3.2.2 Synthesis of (Metal Oleate/Paraffin Oil)-in-Water Nanoemulsion (MNE)

Metal oleate is hydrophobic, which means that it can be mixed easily with paraffin oil. Oleic acid was used as a means of controlling the growth of metal oxide from the metal oleate during the calcination of the metal oleate. To encapsulate the metal oleate in an oil-in-water nanoemulsion, the metal oleate/oleic acid was mixed with paraffin oil and a mixture of surfactants. The required amounts of metal oleate, oleic acid, paraffin oil, and surfactant mixture (Span and Tween) were mixed for 30 min. The solution was further heated in a thermostated bath at 70 °C for 30 min. The amount of water required, previously heated at 70 °C, was added drop by drop to the oily phase, with constant stirring during the addition. The resulting nanoemulsion was stored overnight, before being acidified at pH 2 with 70 mL HCl (0.7 M). Six metal oleate/paraffin oil nanoemulsions (M-*y*-NE) were prepared, in which M = Fe^a, Fe^b, Co, and *y*= *1* for low loading (20 g of metal oleate) or *2* for high loading (80 g of metal oleate). The compositions of the six metal nanoemulsions (MNE) used in this study are listed in Table 6.2.

Table 6.2: Composition of the (metal oleate/paraffin oil) in water nanoemulsion (MNE).

Sample	Span (g)	Tween (g)	Paraffin Oil (g)	Metal Oleate (g)	Oleic acid (g)	Water (g)	pH2 water (g)
Fe[a]NE-*1*	25.2	34.8	20	20	3.75	300	70
Fe[a]NE-*2*	18.6	41.4	80	80	15	180	70
Fe[b]NE-*1*	25.2	34.8	20	20	3.75	300	70
Fe[b]NE-*2*	18.6	41.4	80	80	15	180	70
CoNE-*1*	25.2	34.8	20	20	3.75	300	70
CoNE-*2*	18.6	41.4	80	80	15	180	70

6.3.2.3 Synthesis of Metal Oxide-Hierarchical Porous Silica (MHPS)

The general synthesis process is illustrated in Figure 6.2. Metal oxide-hierarchical porous silica (M-*y*-HPS-*x*) samples were prepared by adding different volumes of the acidified metal oleate nanoemulsion (MNE) to a constant volume of hydrolyzed sodium silicate solution (HSSS), *x* being the vol.% of the metal oleate nanoemulsion (MNE-*y*) to the hydrolyzed sodium silicate solution (HSSS), with *x* = 0 vol.%, 2.5 vol.%, 25 vol.%, 50 vol.%, 100 vol.%, and 200 vol.%. The resulting solution was mixed for 2 min., followed by the addition of ammonia (M) drop by drop until gelling occurred. The gels were left to age for one week before being freeze dried and then calcined at 500 °C under air for 2 h, in order to burn off the paraffin oil and surfactants, to open up the porosity, and to transform the initial metal oleate into metal oxide. The final amount of metal oxide encapsulated within the silica matrix was adjusted to between 0.29 wt. % and 63 wt. % (metal oxide:(metal oxide + silica) wt%). The amount of metal oxide was controlled through varying the initial amount of metal oleate (20 g or 80 g) added to the nanoemulsion and varying the amount of metal oleate nanoemulsion (2.5 mL, 25 mL, 50 mL, 100 mL, or 200 mL) added to the 100 mL sodium silicate solution. Sample calculations are included in Appendix D.

Details of the composition of the six series of samples that were prepared from the six MNEs listed in Table 6.1 are provided in Table D.1-D.3 in Appendix D. The term “M-*y*-HPS-*x*” denotes the metal oxide/hierarchical porous silica, where M indicates the source of the metal from the prepared metal oleates, *y* represents the metal oleate nanoemulsion and *x* represents the vol. % of the nanoemulsion to the sodium silicate solution.

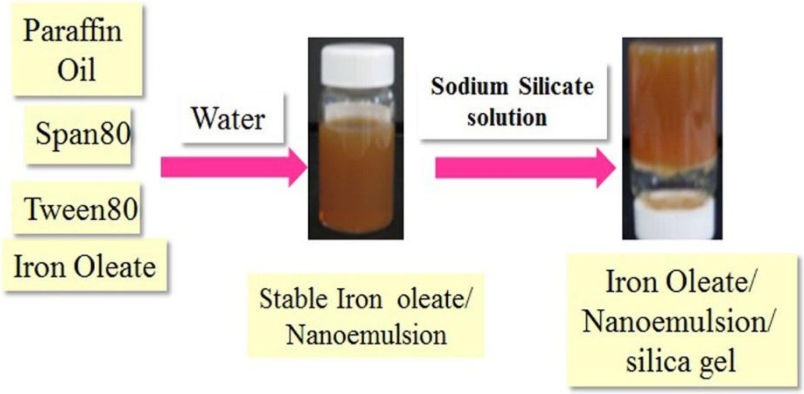

Figure 6.2: Preparation of the iron oleate nanoemulsion/silica gel.

6.3.3 Characterization Methods

The ^{57}Fe Mössbauer spectra were obtained in constant-acceleration mode and transmission geometry using a spectrometer. A room-temperature Co (Rh) source^{57} was employed. The velocity scale was calibrated using the absorption lines of iron foil, and isomer shifts were obtained relative to α−Fe. After folding, the spectra (256 channels) were computed based on a least-squares routine using Lorentzian lines. Spectra were acquired with a velocity scale of ±7,74 mm/s. The statistical rate for the base line spectra points was 7.4 10^6. , These measurements were conducted in collaboration with Philippe Léone and Michel Suchaud in université de Nantes.

AC magnetic susceptibility data were collected using a Quantum Design Physical Property Measurement System (PPMS), in ACMS mode with a helium cooling system. The overall magnetization levels were measured as a function of the applied magnetic field.

X-ray powder diffraction (XRD) patterns of the samples were obtained with the use of a Bruker D8-Advance powder diffractometer operating at 40 kV and CuKα radiation (λ =

0.154 nm). Other experiments based on nitrogen adsorption isotherms. Other techniques have been described in Chapter 5.

6.4 Results and Discussion

This section presents an analysis of the results of the experimental work together with a discussion of the significance of the findings.

6.4.1 Iron Oxide-Hierarchical Porous Silica (Fe^{a}-*y*-HPS-*x*) Nanocomposites

Figure 6.3 shows FTIR spectra for (a) pure hierarchical porous silica HPS-*200*), (b) iron oxide-hierarchical porous silica (Fe^{a}-*2*-HPS-*200)* nanocomposites, and (c) sample (Fe^{a}-*2*-HPS-*200)* nanocomposites after etching with HF. The spectrum for the pure hierarchical porous silica has transmission peaks at 458 cm^{-1}, 802 cm^{-1} , 959 cm^{-1} and 1080 cm^{-1}, which are associated with the bending vibration of the Si-O bond, the asymmetric stretching vibration of the Si-O-Si, the symmetric stretching vibration of the Si-OH, and the symmetric stretching vibration of the Si-O-Si, respectively.

The spectrum for the iron (III) oxide-silica nanocomposites show the same peaks as pure silica gel and two extra peaks at 575 cm^{-1} and 635 cm^{-1}. The peak at 575 cm^{-1} may be associated with Fe-O in the α-Fe_2O_3 (540 cm^{-1}) or in the Fe_3O_4 (570 cm^{-1}), and the peak at 635 cm^{-1} can be ascribed to Fe-O in the γ- Fe_2O_3 (620 cm^{-1}). The spectrum for the iron oxide remaining after the silica has been etched with HF shows three intense peaks at 478 cm^{-1}, 530 cm^{-1}, and 730 cm^{-1} as well as one broad peak at 620 cm^{-1}–660 cm^{-1}. The peak at 478 cm^{-1} can be attributed to Fe-O in the α-Fe_2O_3 rather than silica because the other strong peak for silica, around 1080 cm^{-1}, is not present, thus confirming the absence of silica in this sample. The peak at 530 cm^{-1} is ascribable to α-Fe_2O_3, and the peaks at 620–660 cm^{-1}and at 730 cm^{-1}can be attributed to γ- Fe_2O_3. The iron (III) oxide formed from the iron (III) oleate after calcination may be a mixture of γ- Fe_2O_3 and α-Fe_2O_3.[5]

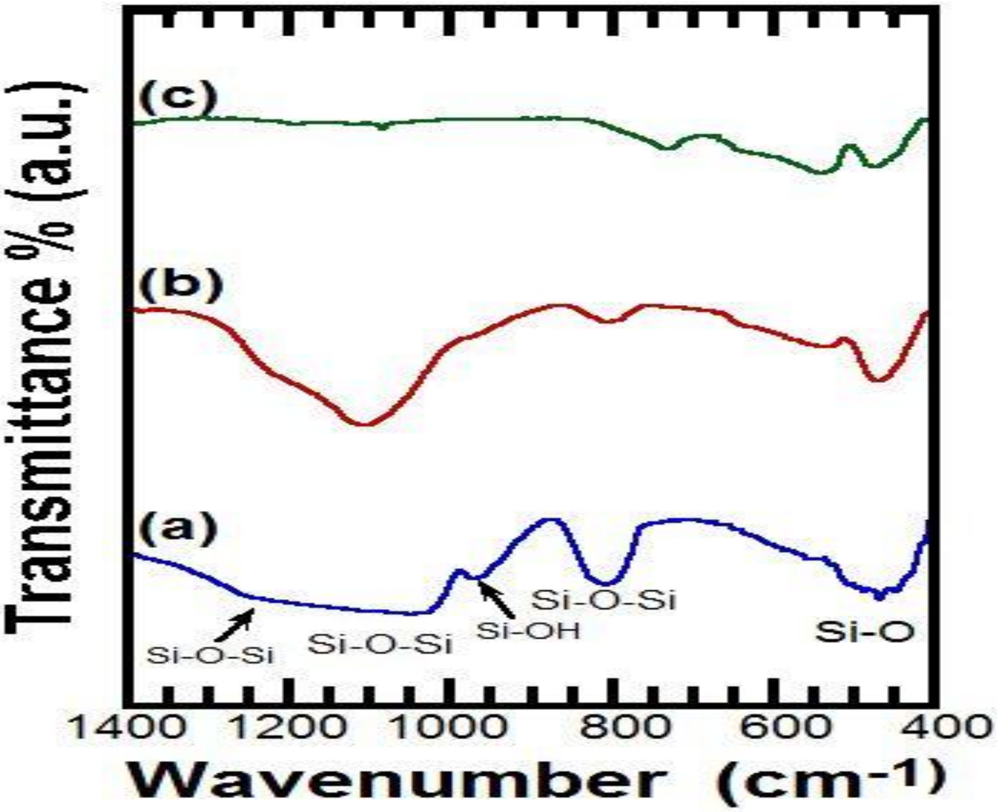

Figure 6.3: FTIR spectra for (a) hierarchical porous silica HPS-*200*, (b) iron oxide-hierarchical porous silica (Fe^a-*2*-HPS-*200)* nanocomposite, and (c) sample (Fe^a-*2*-HPS-*200)* nanocomposite after etching with HF.

Figure 6.4 shows the XRD pattern for the iron oxide-hierarchical porous silica (Fe^a-*2*-HPS-*200*) nanocomposite. The 2Θ peaks at 35.6°, 40.85°, 49.45°, and 62.4° closely match the (220), (311), (400), and (422) planes of the structure of the maghemite (γ Fe_2O_3) or magnetite (Fe_3O_4).[6] While the XRD peaks at 2Θ = 24.11°, 33.08°, and 55.44° are attributable to hematite (α Fe_2O_3). It worth noting that maghemite and magnetite are isostructural, which means that the XRD technique cannot clearly differentiate between them, especially in the nanophase state where the characteristic reflections are broad and appear almost at the same 2Θ positions (maghemite: JCPDS card number 00-039-1346 and magnetite: JCPDS card number 00-025-1402).[7 ,8] Based on the FTIR and XRD results, the presence of iron oxide within the silica is obvious, , with a high probability for the formation of iron(III) oxide (hematite α-Fe_2O_3 and maghemite γ-Fe_2O_3). From these results, the presence of a mixed valence Fe(III)/Fe(II) oxide like magnetite (Fe_3O_4) is highly questionable.

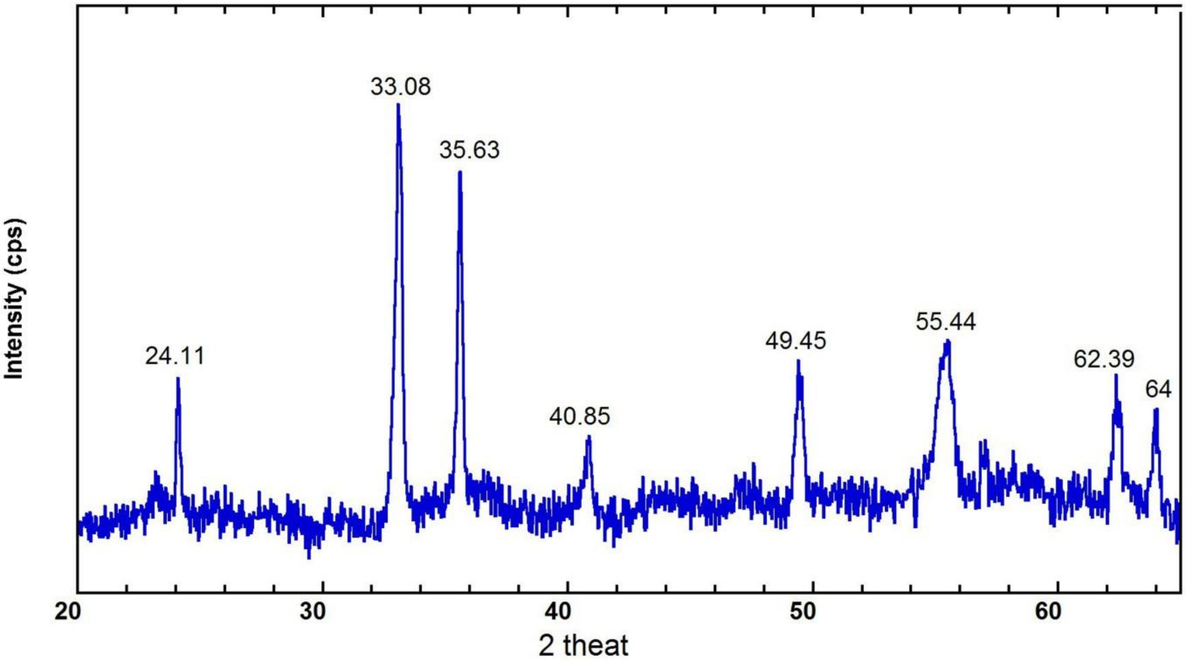

Figure 6.4: XRD pattern for iron oxide-hierarchical porous silica Fe^a-2-HPS-*200*.

Figure 6.5 shows the Mössbauer (MB) spectra of iron oxide-hierarchical porous silica Fe^a-*2*-HPS-*100* and Fe^a-*2*-HPS-*200*. The MB X-axis represents the velocity of moving the γ-ray source toward or away from the fixed sample, which is related to the energy of the γ-ray source. The Y-axis indicates the absorption of the γ-rays by the sample. The existence of γ-Fe_2O_3 nanoparticles is confirmed based on the MB spectroscopy, as shown in Figure 6.5. The spectrum displays a doublet (84 %) (isomer shift 0.32 mm/s; quadrupole splitting 0.85 mm/s) characteristic of Fe_2O_3 nanoparticles, and a sextuplet (16%) (isomer shift 0.41 mm/s; hyperfine field 447 kOe) that may be attributable to large size Fe_2O_3. This contribution could be assigned also to Fe(II), which could indicate the possible formation of some minor contribution of Fe_3O_4.as indicated by the FTIR and XRD results.[9-10]

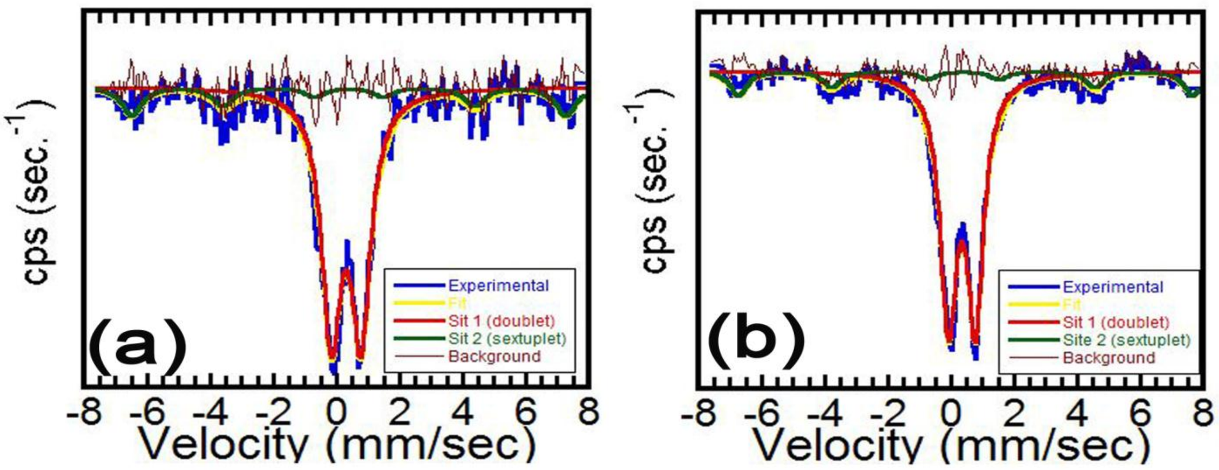

Figure 6.5: Mossbauer spectra of iron oxide-hierarchical porous silica (a) Fe^{a}-*2*-HPS-*100* and (b) Fe^{a}-*2*-HPS-*200*.

At this stage, it was confirmed that this integrative synthesis of metal oleate-nanoemulsion templating silica does form a crystalline iron oxide within the amorphous silica after calcination at 500 °C. SEM and TEM analyses were conducted in order to determine the distribution and position of the iron oxide within the silica matrix.

Figure 6.6 shows SEM photos for iron oxide-hierarchical porous silica Fe^{a}-*2*-HPS-*100* (Figure 6.6 (a), (c), (e)) and Fe^{a}-*2*-HPS-*200* (Figure 6.6 (b), (d), (f)). The samples are homogenous at both low magnification and high magnification, and no phase separation between iron oxide and silica phases can be observed. As well, macroporosity is still observable, with the macropores homogeneously distributed throughout the nanocomposite. A comparison of the two samples confirms that the nanocomposite retains its homogeneous structure with no separation between the iron oxide and the silica regardless of the volume of the nanoemulsion. Comparing Figure 6.6 (e) and (f), one can observe that Fe^{a}-*2*-HPS-*100* has macroporous silica while Fe^{a}-*2*-HPS-*200* has agglomerated spheres resulting from the difference in the oil/water interfacial area as discussed in Chapter 5. Figure D.1 in Appendix D shows the results of the EDAX analysis for Fe^{a}-*2*-HPS-*25*, which indicates that iron:silicon wt% $\underset{\sim}{}$ 17:83 wt.%.

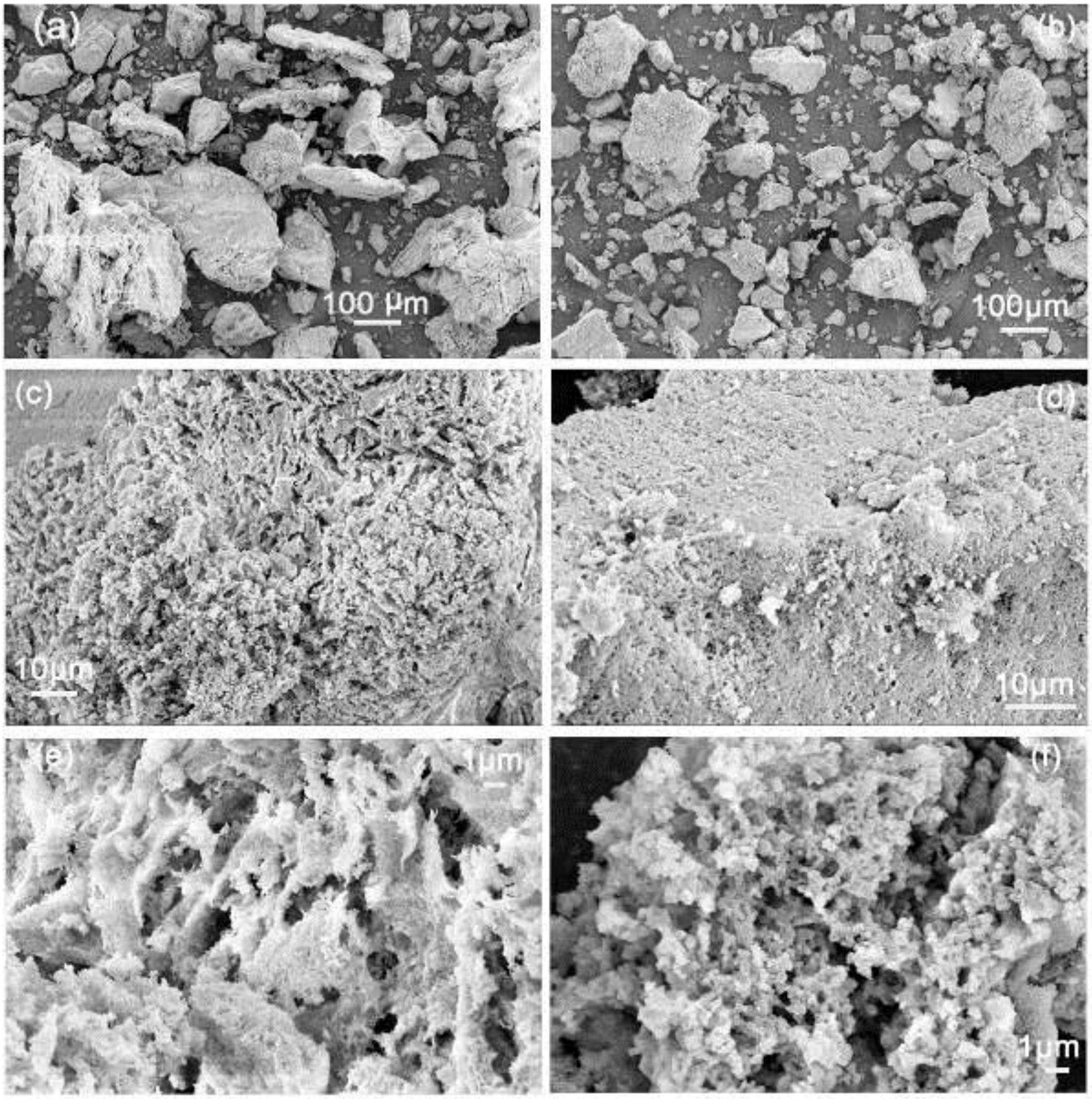

Figure 6.6: SEM photos of iron oxide-hierarchical porous silica: Fe^{a}-*2*-HPS-*100* ((a), (c), (e)) and Fe^{a}-*2*-HPS-*200* ((b), (d), (f)).

Figure 6.7 shows TEM photos for iron oxide-hierarchical porous silica with different concentrations of iron oxide. The photos indicate a homogeneous distribution of iron oxide within the silica matrix, and with increasing concentrations of iron oxide, no agglomeration or increased crystal growth can be observed. The inhibited agglomeration and crystal growth is one of the advantages of using nanoemulsion as a nanoreactor. Figure 6.7 (d) shows the size of the iron oxide nanoparticles to be about 50 nm. No agglomeration is evident between the iron oxide particles in spite of the high weight of iron oxide (1.56 g, 3.13 g, and 6.26 g iron oxide distributed in 3.7 g of silica matrix in Fe^a-*2*-HPS-*50*, Fe^a-*2*-HPS -*100*, and Fe^a-*2*-HPS -*200*, respectively), which confirms that the synthesis developed enables the preparation of a large quantity of small nanoparticles that can be embedded in the cavities of a mesoporous silica matrix without agglomeration of the particles.

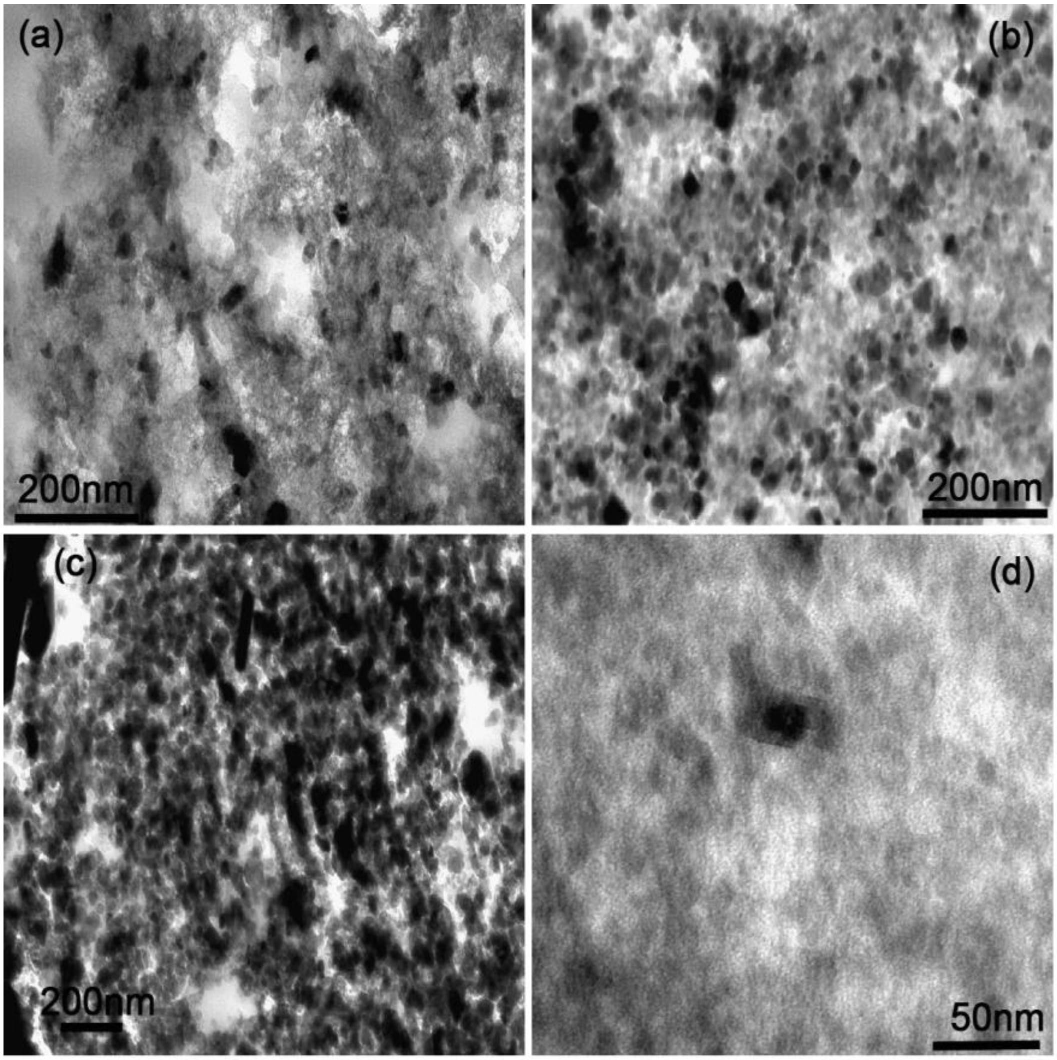

Figure 6.7: TEM for iron oxide-hierarchical porous silica: (a) Fe^a-*2*-HPS-*50*, (b) Fe^a-*2*-HPS-*100*, (c) Fe^a-*2*-HPS-*200*, and (d) Fe^a-*2*-HPS-*50*.

Park et al. [4] prepared iron oxide nanocrystals starting from iron oleate under reflux at 320 °C for 30 min and their nanoparticles had average size of 12 nm with perfect spherical shape. In the preparation conducted for this thesis, no reflux was used but calcination at 500 °C for 2 h to make sure that all the organics are burn out. Calcination at higher temperature for long time increases crystal growth which results in larger crystal size. Park et al. used $FeCl_3.6H_2O$ to prepare iron oleate and found that the XRD pattern of the 12-nm iron oxide nanocrystals revealed a cubic spinel structure of magnetite (Fe_3O_4). They found a relation between the crystal size and iron oxide phase formed which were confirmed by X-ray absorption spectroscopy (XAS) and X-ray Magnetic Circular Dichroism (XMCD). They compared iron oxide nanocrystals with diameters of 5 nm, 9 nm, 12 nm, 16 nm and 22 nm with two reference materials, bulk γ-Fe_2O_3 (maghemite) and bulk Fe_3O_4 (magnetite). Based on the results of the XAS and XMCD, Fe_3O_4 = 0.20, 0.57, 0.68, 0.86 and 1.00 for the 5, 9, 12, 16 and 22 nm nanocrystals, respectively. Therefore, γ- Fe_2O_3 is the dominant phase of the small 5-nm iron oxide nanocrystals, whereas the proportion of Fe_3O_4 component gradually increases on increasing the particle size. The size of iron oxide formed in this work of about 50 nm suggests that pure Fe_3O_4 should be formed. According to the Mossbauer results, the predominate phase is Fe_2O_3 (84%) and Fe_3O_4 (16%) which may be attributed to the deficiency of oxygen inside oil droplet.

Figure 6.8 shows the N_2 adsorption isotherm for iron oxide-hierarchical porous silica Fe^a-*2*-HPS-*25*. The N_2 adsorption isotherm exhibits a high N_2 gas uptake of about 800 cc/g and has the specific shape associated with a large hysteresis of the desorption curve. The absence of capillary condensation closure indicates that the pores are not saturated with N_2, which suggests a broad pore size distribution and/or the presence of macroporosity. This material has a BET surface area of (249 $m^2.g^{-1}$), similar to that of amorphous porous silica, but a larger pore volume (1.25 $cm^3.g^{-1}$). The hysteresis can be attributed to a delay in the desorption of globular pores, due to the necessity of reaching the partial pressure required for desorption within the silica matrix. A similar shape has already been reported for mesoporous silica that contains hollow structures.[11]

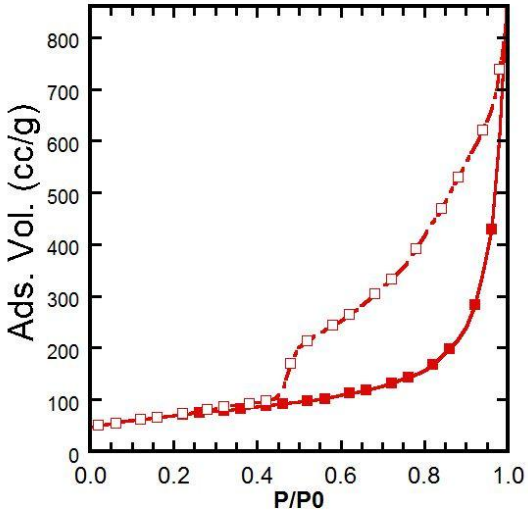

Figure 6.8: N_2 adsorption isotherm for iron oxide-hierarchical porous silica Fe^a*2*-HPS-*25*.

Figure 6.9 (a) and (b) show the N_2 adsorption isotherm for Fe^a-*1*-HPS-*x* and Fe^a-*2*-HPS-*x* nanocomposites, respectively, where *x* is the vol.% of nanoemulsion to the silicate solution and *x* = 2.5, 25, 50, 100, and 200. These samples are also characterized by a high N_2 uptake (from 800 to 1150 cc/g at STP), which implies a high pore volume in the range of 1 cc/g–2.5 cc/g. The pore size distribution (PSD) calculated based on the adsorption branch and using the Broekhoff and de Boer model is represented in Figure 6.9 (c) and (d).[12,13] All of the PSD representations have two peaks in the micoporosity range around 3 nm and 5 nm, and some of the samples have one or two peaks in the meso range at about 17 nm and/or 27 nm.

The effects of changing the (Fe^{a}NE/HSSS) vol.% on the mesoporous structure of the iron oxide-silica nanocomposite (Fe^a-HPS-*x*) were studied through an examination of the surface area (Figure 6.10), pore volume, and surface roughness (Figure D.2 in Appendix D) calculated based on the N_2 adsorption isotherm.

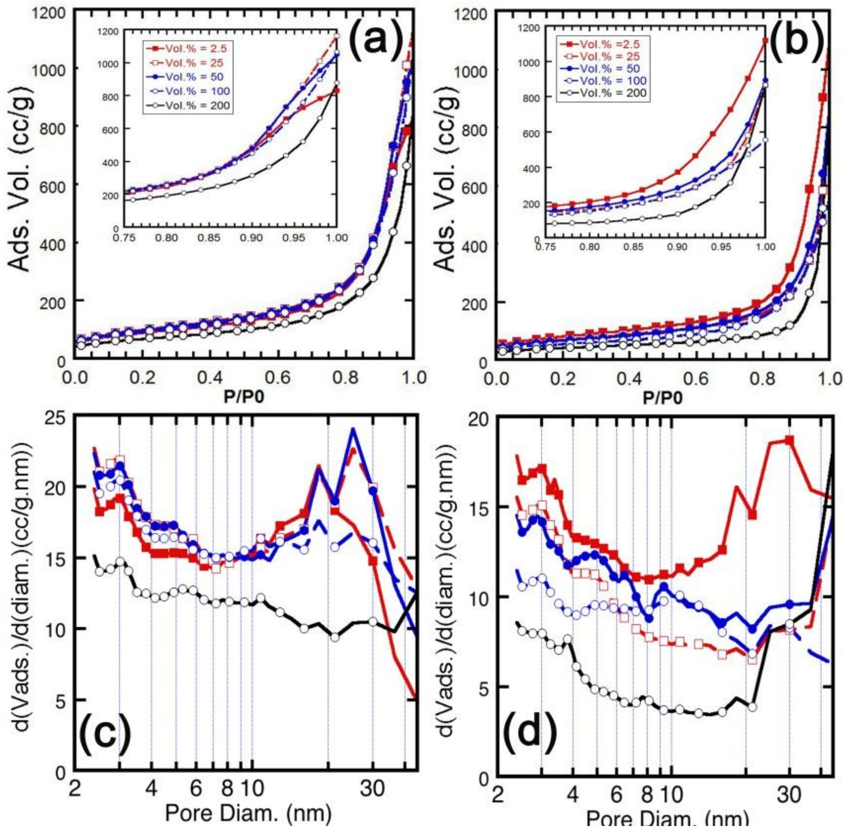

Figure 6.9: (a) and (b) show N_2 adsorption isotherm for Fe^a-*1*-HPS-*x* and Fe^a-*2*-HPS-*x* samples, respectively; (c) and (d) show the respective pore size distribution for the same samples.

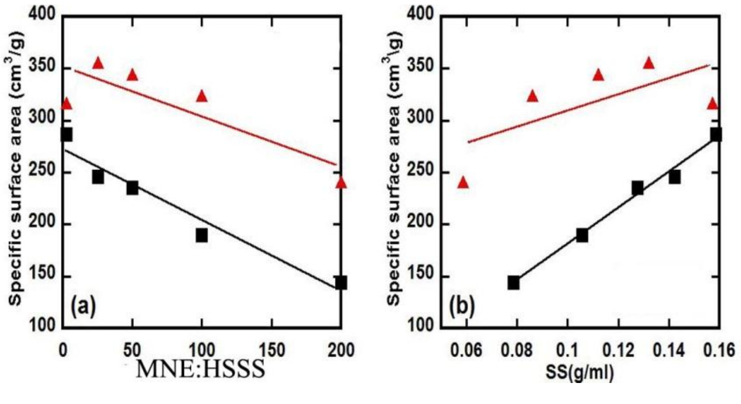

Figure 6.10: Surface area of Fe^a-*1*-HPS-*x* (▲) and Fe^a-*2*-HPS-*x* (■) as a function of the Fe^{a}NE/HSSS vol.% and the sodium silicate concentration.

Figure 6.10.a shows that the specific surface area decreases with increasing the (Fe^{a}NE/HSSS) vol.%, regardless of the type of nanoemulsion used (Fe^a-1-NE or Fe^a-2-NE). The surface area of the Fe^a-1-HPS-x nanocomposites is always higher than that of the Fe^a-2-HPS-x, irrespective of the volume of nanoemulsion used. Figure 6.10.b displays another view of these results, where the surface area is reported as a function of the concentration in sodium silicate. For all syntheses, the same initial amount of sodium silicate was used, but the final concentration depends on the amount of water added with the nanoemulsion. The values are in the range of values obtained for silica gels prepared with sodium silicate without templates. In our materials, the nanoemulsion templates do not modify the microstructure of silica that remains porous. As a result, no direct influence of the NE on the silica itself was observed. As illustrated in Figure 6.10.b, The origin of this variation in surface area may be attributed to change in the concentration of the sodium silicate precursor of the silica matrix. The concentration in sodium silicate is rather low and the silica resulting from the gelling, freeze-drying, and calcination procedure depends on the density of wet silica and its ability to resist to all stress created by drying and calcination. It is assumed that the smaller surface area observed for the lowest concentrations in sodium silicate is probably the result of a fragile silica framework that partially collapses during the synthesis. This first hypothesis will have to be confirmed by the preparation and study of silica gel with the same concentrations, but without the NE droplets.

Unlike the surface area that depends only on the silica framework, the pore volume results from the combination of silica and NE, and the same pore volume, around 1.5 cc/g, was obtained for both series (Figure D.2 in Appendix D). Average the surface roughness value of 2.6 was obtained (Figure D.2 in Appendix D). The direct comparison of surface area, porous volume, and surface roughness, leads to a contradictory vision of the material: if the porous volume remains constant, the evolution of the specific surface area should reflect an evolution in the surface, with more or less of roughness, which is not observed. These results confirm the need for additional analyses, as stated before.

Finally, the magnetic measurements (Figure 6.11), with the small coercive field of 130 Oe characteristic of nanoparticles, confirm the existence of small ferromagnetic nanoparticles of

Fe_2O_3, as deduced from TEM and Mössbauer spectroscopy. Moreover, the size of this small coercive field does not increase, even when the amount of Fe_2O_3 in the nanocomposites rises from 17 wt.% to 30 wt.% or 63 wt.%., which means that the average size of nanoparticles does not increase with the increasing concentration of iron oxide. The calculations are shown in Table D.1 in Appendix D.

These results confirm that the new synthesis technique enables the preparation of a large quantity of small nanoparticles that can be embedded in the cavities of a mesoporous silica matrix without any collapse of the particles. This property is very important for further development with respect to catalysis and magnetic properties.

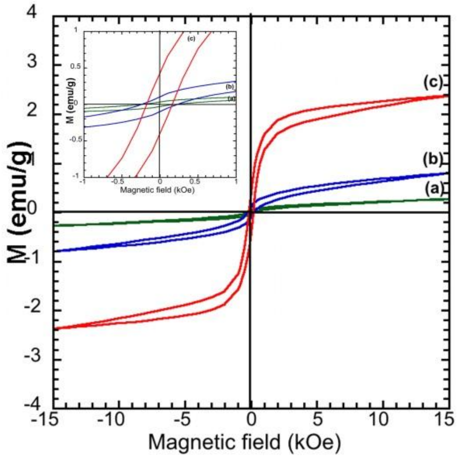

Figure 6.11: Magnetization of (a) Fe^a-2-HPS-25 (17 wt.%), (b) Fe^a-1-HPS-200 (30 wt.%), and (c) Fe^a-2-HPS-200 (63wt.%) iron oxide/nanocomposites (wt.%) measured at room temperature; inset: close-up view of the hysteresis.

6.4.2 Iron Oxide-Hierarchical Porous Silica (Fe^b-HPS-*x*) Nanocomposites

Iron (II/III) oleate was used in the same way as described in the experimental section of this chapter, with the intention of preparing magnetite as a means of validating the possibility of using this synthesis to prepare other metal oxide-hierarchical porous silica nanocomposites. The resulting iron oxide-hierarchical porous silica nanocomposites (Fe^b-HPS-*x*) were characterized in the same manner as the iron oxide-silica nanocomposites (Fe^a -HPS-*x*).

XRD analysis of the (Fe^b-2-HPS-*200*) nanocomposites (Figure 6.12) reveals the same pattern observed for the (Fe^a-HPS-*x*) nanocomposites. The FTIR results for Fe^b-2-HPS-*200* nanocomposite (Figure 6.13) show spectra that are slightly different from the ones observed for Fe^a-2-HPS-*200* nanocomposites, especially when the etching is incomplete and some silica can still be observed in the FTIR results. Hence, the formation of magnetite is not confirmed as the formed phase even though the Mössbauer spectrum shows that there is a mixture of iron (II) and iron (III), as shown in Figure 6.14. The SEM photo in Figure 6.15 indicates a homogenous structure of pores with a matrix of nanocomposites, and the EDAX analysis shows the Fe content to be about 14 wt.% (Figure D.7 in Appendix D).

The TEM photos for the iron oxide-hierarchical porous silica (Fe^b-2-HPS-*x*) nanocomposites that have a different concentration of iron oxide are presented in Figure 6.16. The TEM photos indicate a homogeneous distribution of iron oxide within the silica matrix, as shown in Figure 6.16 (a), but with an anisotropic structure. Nanoparticles of iron oxide are localized within the globular pores Figure 6.16 (b). An interesting observation is that increased concentrations of iron oxide do not produce observable agglomeration but do lead to noticeable increases in crystal growth (Figure 6.16 (c) and (d)). This result means that the larger crystals result from the initial higher concentration in metal oleate in the oil droplets, but not from the merging of iron oxide between oil droplets. Thus, the oil droplets of the nanoemulsion have perfectly accomplished the function of being nano-containers that evolve into nanoreactors.The effect of this anisotropic structure was observed with the use of magnetic measurement, which indicated increased magnetic saturation (Figure 6.17) compared with the levels in the isotropic structure observed in Fea-HPS-x nanocomposites.

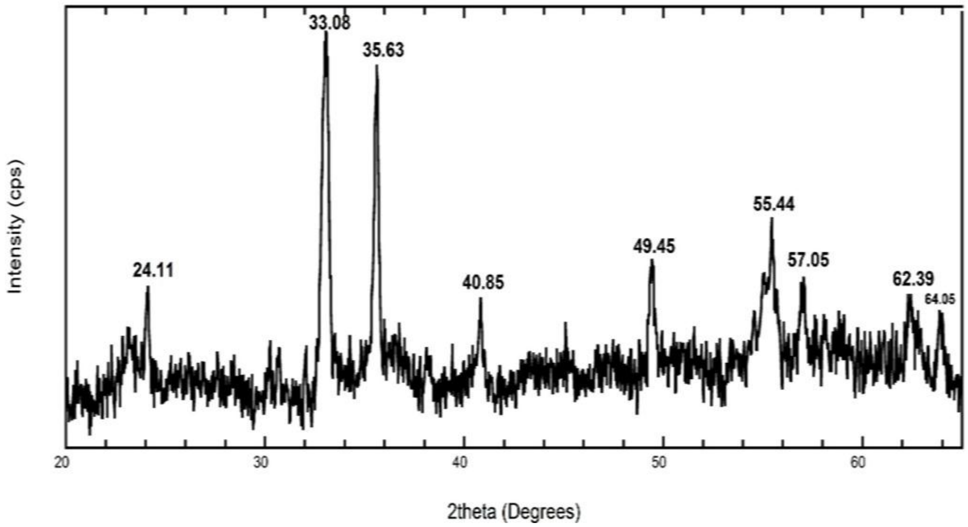

Figure 6.12: XRD of Iron oxide–Hierarchical porous silica Fe^{b}-2-HPS-200.

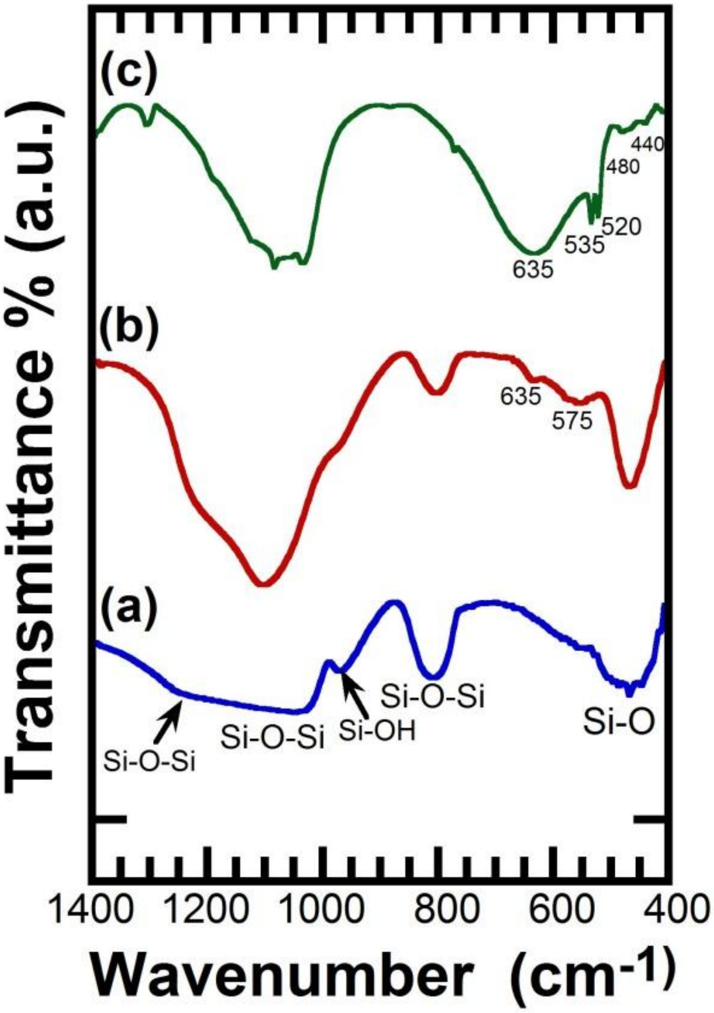

Figure 6.13: FTIR of (a) Hierarchical porous silica HPS-200 , (b) Iron oxide – Hierarchical porous silica Fe^{b}-2-HPS-200 and (c) Iron oxide remaining after etching Fe^{b}-2-HPS-200.

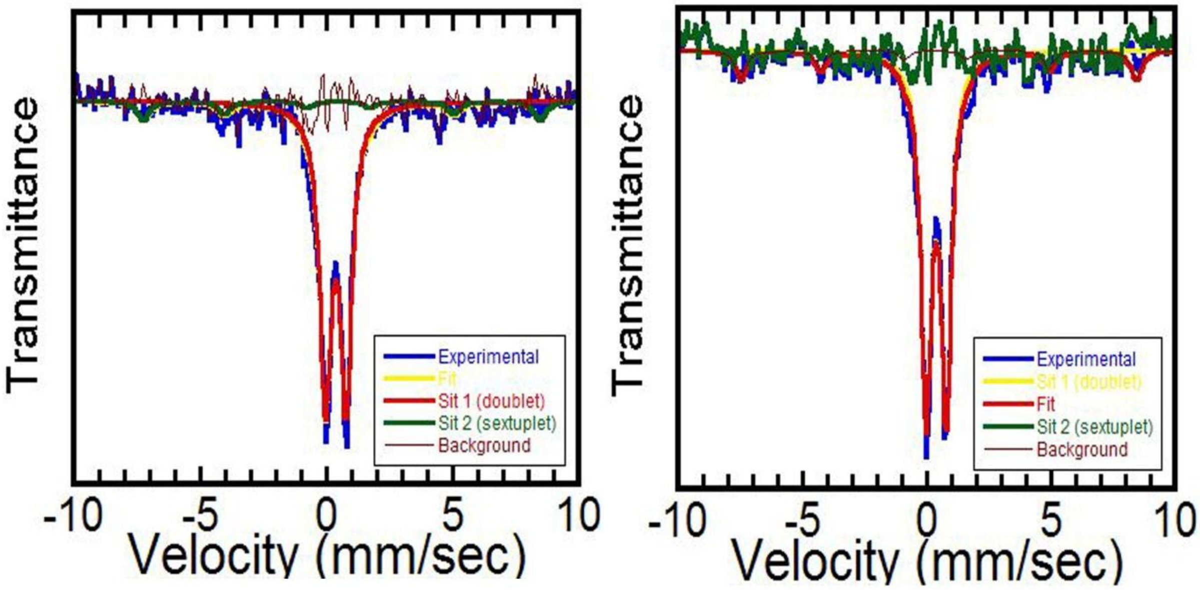

Figure 6.14: Mossbauer spectra of Iron oxide – Hierarchical porous silica (a) Fe^b-2-HPS-100 (b) Fe^b-2-HPS-200.

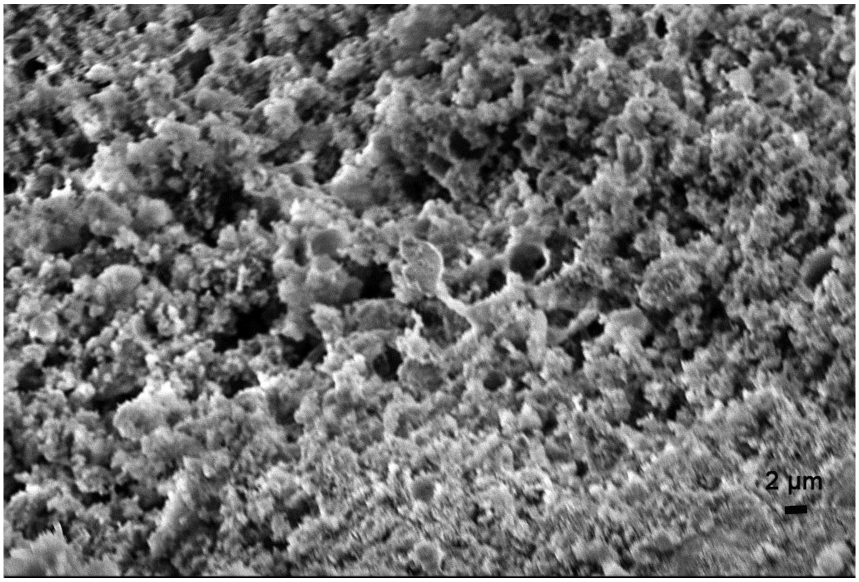

Figure 6.15: SEM photos of Fe^b-2-HPS-25.

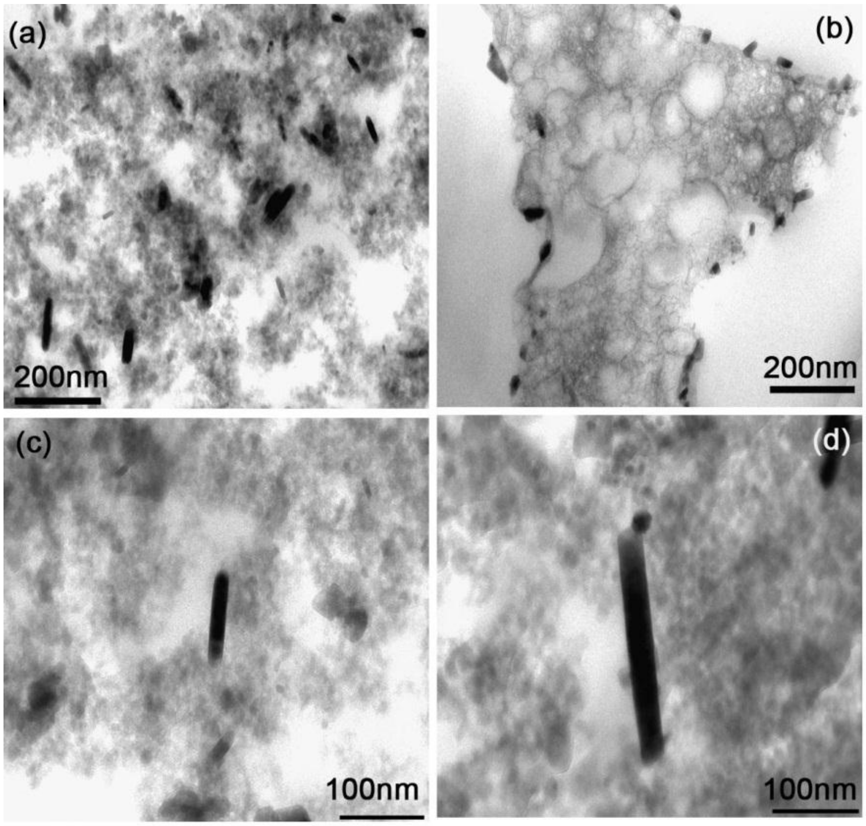

Figure 6.16: TEM for iron oxide-hierarchical porous silica (a) Fe^b-2-HPS-*2.5*, (b) Fe^b-*2*-HPS-*100*, (c) Fe^b-*2*-HPS -*2.5*and (d) Fe^b-*2*-HPS-HPS-*200*.

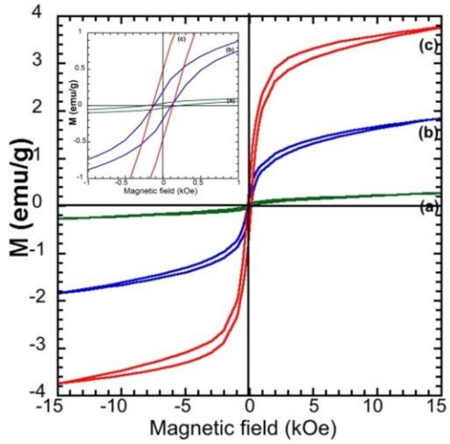

Figure 6.17: Magnetization of (a) Feb-2-HPS-25 (10.5wt.%), (b) Feb-1-HPS-200 (19.13wt.%), and (c) Feb-2-HPS-200 (48.6 wt.%) iron oxide/ nanocomposites (wt.%) measured at room temperature; inset: close-up view of the hysteresis.

6.4.3 Cobalt Oxide-Hierarchical Porous Silica (Co-HPS-*x*) Nanocomposites

The FTIR spectrum of cobalt oxide (Figure 6.18 (c)) shows two distinctive bands originating from the stretching vibrations of the cobalt-oxygen bond. The first band at 570 cm^{-1} is associated with the BOB3 vibrations in the spinel lattice, where B denotes theCo cations in an octahedral position, i.e., Co3+ ions. The second bands at 661 cm^{-1} can be attributed to the ABO3 vibrations, where A denotes the metal ions in a tetrahedral position.[14, 15] The form of cobalt oxide is cubic Co_3O_4, as confirmed through XRD, the results of which are shown in Figure 6.19 (JCPDS Card file No. 74-1656).

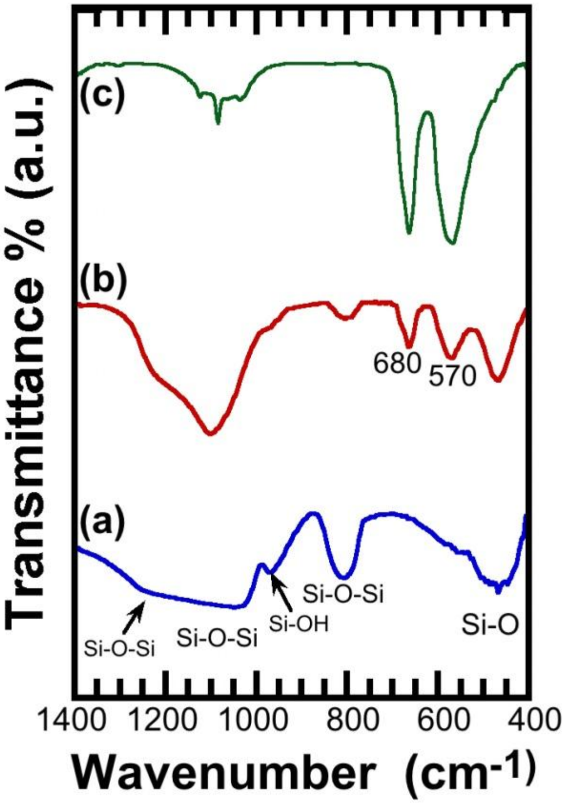

Figure 6.18: FTIR results for (a) hierarchical porous silica HPS-*200* , (b) cobalt oxide-hierarchical porous silica(Co-*2*-HPS-*200*) nanocomposite, and (c) cobalt oxide after etching of (Co-*2*-HPS-*200*) nanocomposite.

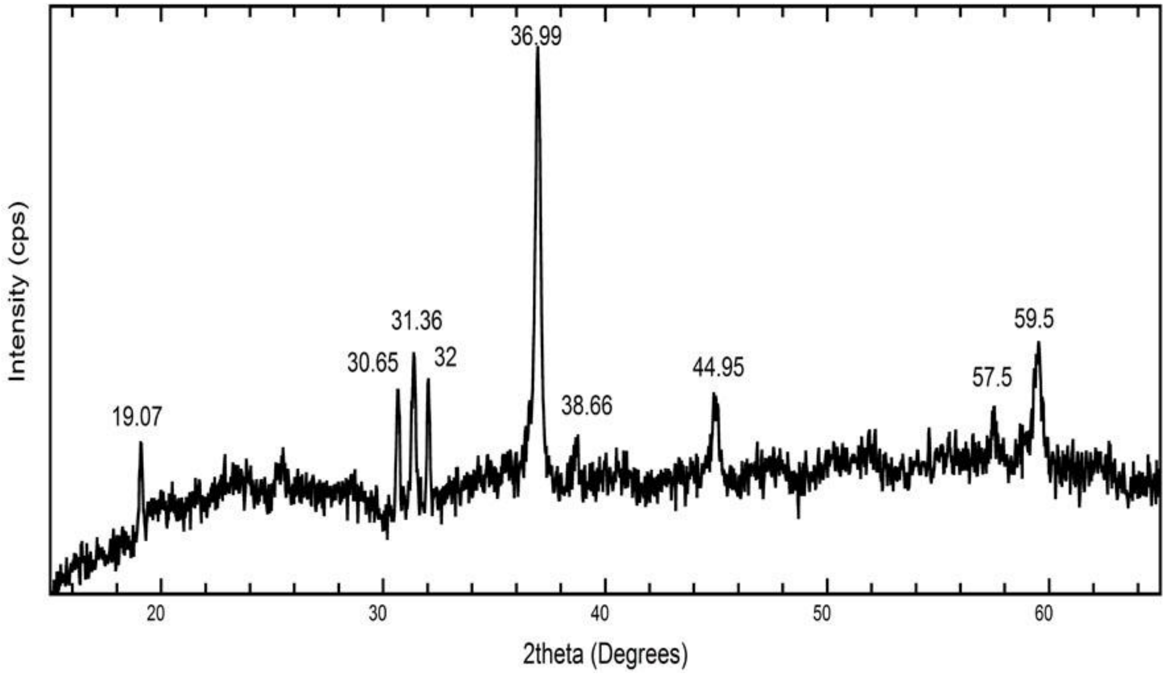

Figure 6.19: XRD pattern for cobalt oxide-hierarchical porous silica (Co-*2*-HPS-*200*) nanocomposite.

The SEM photos (Figure 6.20) show the formation of a homogenous nanocomposite with no phase separation between the cobalt oxide and the silica, and in spite of functionalization with high concentrations, an opened structure is still evident in the nanocomposites. The results of the EDAX analysis (Figure D.8 in Appendix D) reveal that cobalt 18 wt.%.

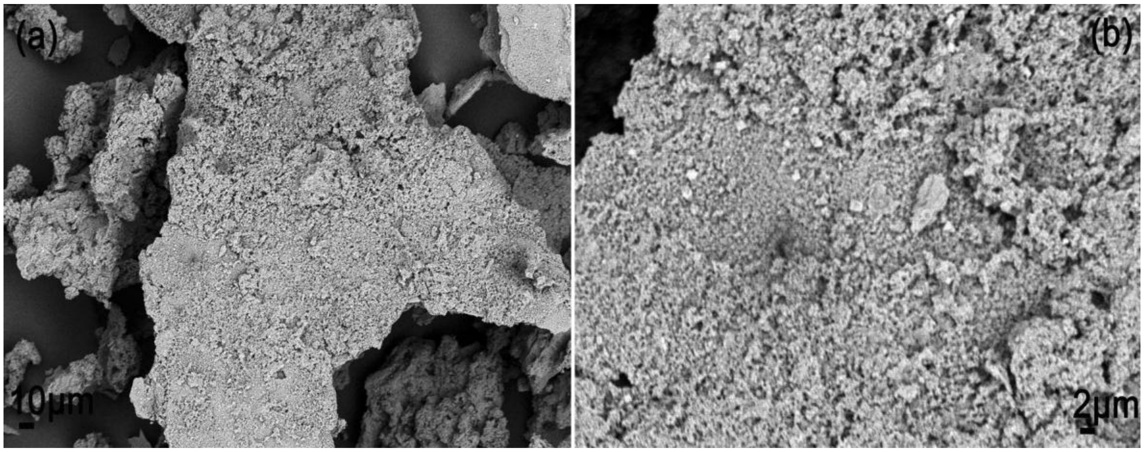

Figure 6.20: SEM analysis for cobalt oxide-hierarchical porous silica Co-*2*-HPS-*25*.

6.5 Summary

The results of the experimental testing have proven that the nanoemulsion can be used simultaneously as both a template and a nanoreactor in order to prepare metal oxide-hierarchical porous silica nanocomposites that have high surface areas up to 400 m^2/g, a high surface roughness value of about 2.56 on average, and a good range of pore volume of about 2 cc/g. This one-pot synthesis technique provides an efficient method for uploading the porous structure of silica with different types of metal oxides that can be applied to any hydrophobic precursors. Controlling the concentration of metal oxide within the nanocomposites was also demonstrated to be straightforward. The current state-of-the art for this new method has to go beyond the present validation and lead to more complete studies in order to investigate in details the parameters of the synthesis. For example, preparing mixed valence iron oxide and keeping the original (+II) oxidation degree of iron stable was not successful. The formation of metals by thermal treatment under a neutral atmosphere was not explored, but should be favoured by the carbonization of the organic components.

Chapter 7

Conclusions and Recommendations

7.1 Conclusions

Based on the research conducted for this thesis, the following conclusions can be drawn:

- Paraffin oil-in-water (O/W) nanoemulsions were prepared using the phase inversion composition (PIC) method. This system is based on environmental friendly materials that are both biocompatible and inexpensive. The preparation method is also energy efficient and can be used in drug and biomaterial applications without degradation. These advantages make this system suitable for use in the field of pharmacology.
- The O/W nanoemulsion prepared in this study proved to be stable for months and can also withstand the effects of dilution and temperature. These characteristics mean that once it is prepared, the nanoemulsion would be suitable for industrial use.
- The prepared nanoemulsions can incorporate a wide oil droplet sizes ranging from 65 nm to 400 nm and can also be fabricated from a wide variety of starting compositions, features that facilitate the selection of the required droplet size and meet the requirements for use in numerous chemical systems.
- Oil droplet size can be tuned: between180 nm and 60 nm by increasing S/O weight ratio from 0.25 to 1; between 115 nm and 60 nm by increasing temperature of preparation from 5 °C to 80 °C; and between 180 nm and 105 nm by decreasing HLB from 12 to 9.8.
- HLB effect on oil droplet size was found to be related to surface coverage of oil droplet with surfactant.
- The experimental design is a useful tool for the simultaneous study of intercrossing multifactors, leading to time and cost savings that result from the optimization of the determination of the experiments required.

- Sodium silicate is an inexpensive, environmental friendly precursor for silica gel, which yields micro-mesoporous silica when prepared under the appropriate conditions.
- Combining an O/W nanoemulsion with the sol-gel chemistry of sodium silicate and establishing the correct conditions for integration is a perfect example of integration synthesis.
- The integration synthesis developed for this work resulted in hierarchical porous silica with a wide spectrum of sample compositions. The successful integration of NE with sol-gel of sodium silicate depend on using the suitable conditions as pH of starting materials and amount of catalysis.
- Paraffin oil nanoemulsions proved to be a suitable soft template for macroporous materials, which fill the gap between mesoporous materials prepared with micelle templating and macroporous materials created with latex templating.
- The pore size and pore volume should be controllable through changes to the size of the oil droplet and the total volume of oil in the nanoemulsion, assuming a 1:1 correspondence between the template and the pore. However, this effect was not observed due to unsuccessful attempts to measure the macroporosity using mercury porosimetry. Based on SEM observations, the macroporosity was demonstrated but not with a strong correspondence to template size. This result may be attributable to the use of a soft template (oil), which is unable to withstand the stress related to the condensation of the silica.
- Paraffin wax/oil nanoemulsions were used as a template for the generation of macroporosity. This mixture of wax and oil provided an excellent opportunity for the preparation of a new template, which can be called a temperature-sensitive hard-soft template. A wax/oil mixture is liquid when heated and can be used in the preparation of the nanoemulsion while it is hot, but when it cools, it becomes solid.
- The nanoemulsion was used as a nanoreactor for the preparation of metal oxide from hydrophobic metal precursors and also as a carrier for the metal precursors that were occluded within the silica network during the templating.

- Functionalizing and templating silica through the exploitation of the dual nature of the nanoemulsion as a carrier for functional materials and as a template for pores opens the door to a simple new synthesis method for the creation of functionalized silica nanocomposites.

7.2 Recommendations

The work completed for this thesis could be explored further through the following suggestions for future research:

- Extend the study of the wax/oil nanoemulsion as a soft-hard template and as a carrier for functional materials.
- Further study the fabrication of hierarchical porous silica by experimenting with the use of supercritical drying and/or ambient temperature drying for its preparation in a monolithic form or in hollow spheres.
- Broaden the nanoemulsion templating process to include materials other than silica.
- Expand the use of the nanoemulsion as a carrier by applying this function in the study of large biological molecules, which may be beneficial in enzyme fuel cell applications.
- Investigate the thermal stability and mechanical properties of hierarchical porous silica and metal oxide hierarchical porous silica nanocomposites

Letters of copyright permission

Permission for Langmuir Paper used in Chapter 3 and chapter 4

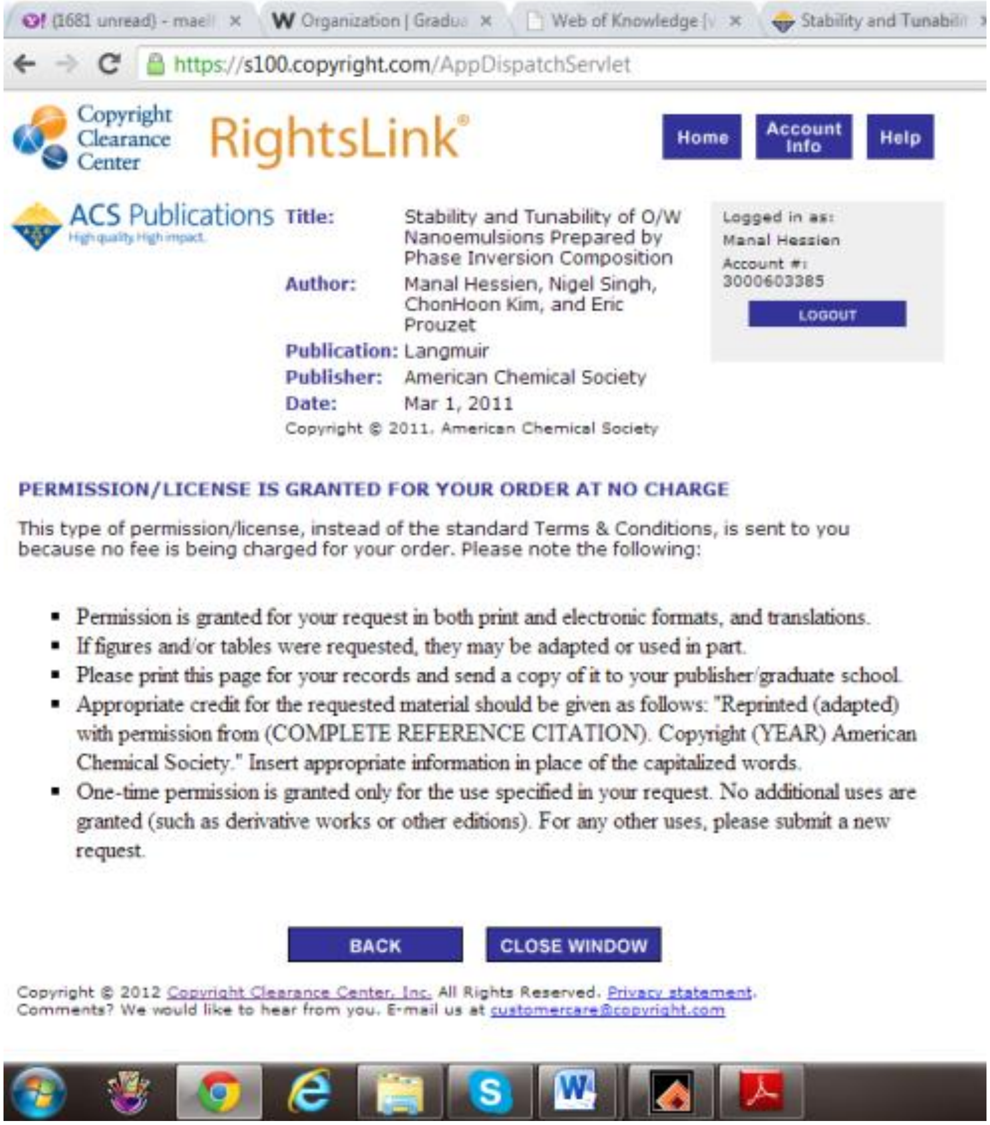

Title: Stability and Tunability of O/W Nanoemulsions Prepared by Phase Inversion Composition

Author: Manal Hessien, Nigel Singh, ChonHoon Kim, and Eric Prouzet

Publication: Langmuir

Publisher: American Chemical Society

Date: Mar 1, 2011

Copyright © 2011, American Chemical Society

Logged in as:
Manal Hessien
Account #:
3000603385

PERMISSION/LICENSE IS GRANTED FOR YOUR ORDER AT NO CHARGE

This type of permission/license, instead of the standard Terms & Conditions, is sent to you because no fee is being charged for your order. Please note the following:

- Permission is granted for your request in both print and electronic formats, and translations.
- If figures and/or tables were requested, they may be adapted or used in part.
- Please print this page for your records and send a copy of it to your publisher/graduate school.
- Appropriate credit for the requested material should be given as follows: "Reprinted (adapted) with permission from (COMPLETE REFERENCE CITATION). Copyright (YEAR) American Chemical Society." Insert appropriate information in place of the capitalized words.
- One-time permission is granted only for the use specified in your request. No additional uses are granted (such as derivative works or other editions). For any other uses, please submit a new request.

Copyright © 2012 Copyright Clearance Center, Inc. All Rights Reserved. Privacy statement.
Comments? We would like to hear from you. E-mail us at customercare@copyright.com

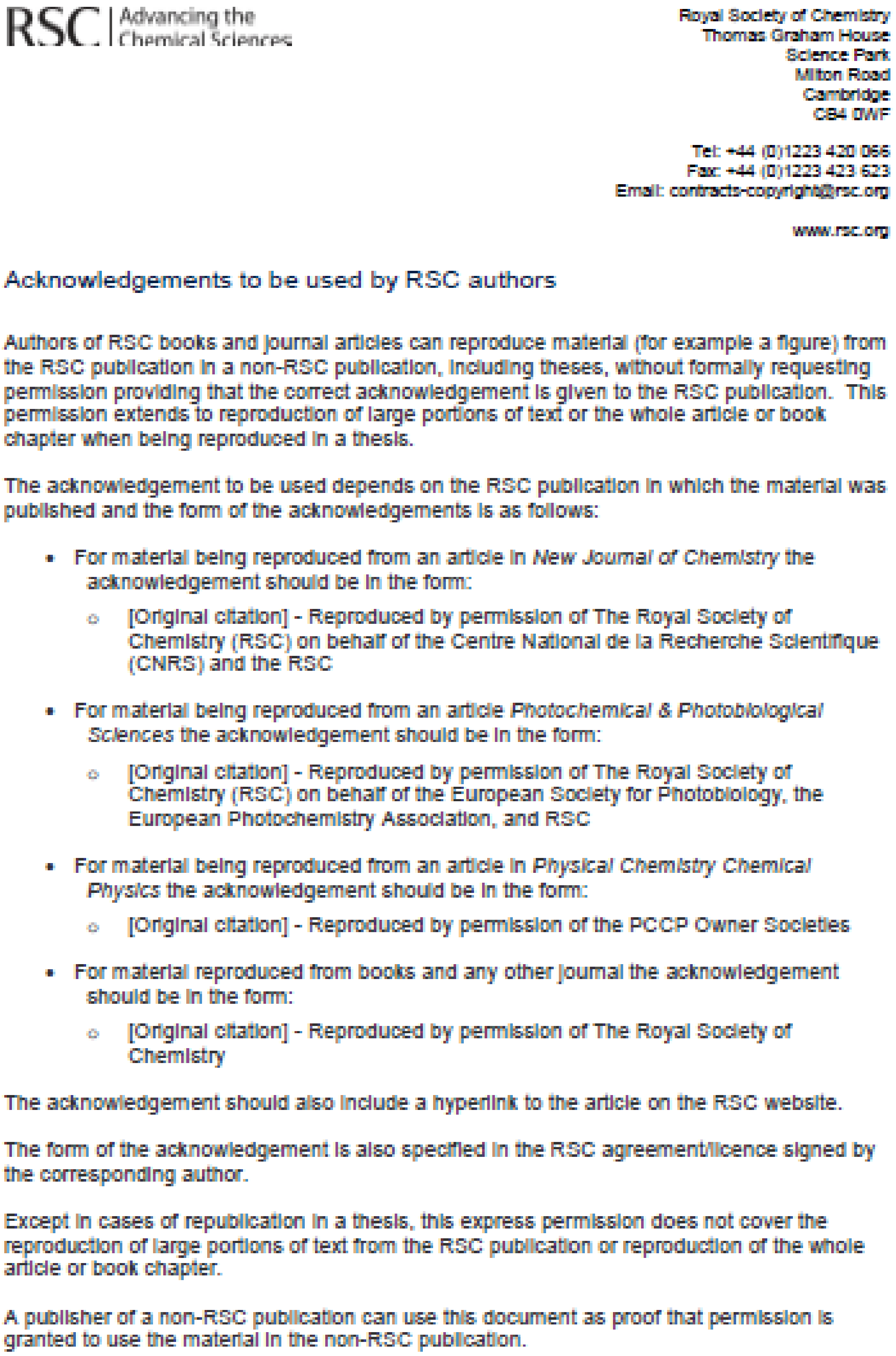

RSC | Advancing the Chemical Sciences

Royal Society of Chemistry
Thomas Graham House
Science Park
Milton Road
Cambridge
CB4 0WF

Tel: +44 (0)1223 420 066
Fax: +44 (0)1223 423 623
Email: contracts-copyright@rsc.org

www.rsc.org

Acknowledgements to be used by RSC authors

Authors of RSC books and journal articles can reproduce material (for example a figure) from the RSC publication in a non-RSC publication, including theses, without formally requesting permission providing that the correct acknowledgement is given to the RSC publication. This permission extends to reproduction of large portions of text or the whole article or book chapter when being reproduced in a thesis.

The acknowledgement to be used depends on the RSC publication in which the material was published and the form of the acknowledgements is as follows:

- For material being reproduced from an article in *New Journal of Chemistry* the acknowledgement should be in the form:
  - [Original citation] - Reproduced by permission of The Royal Society of Chemistry (RSC) on behalf of the Centre National de la Recherche Scientifique (CNRS) and the RSC
- For material being reproduced from an article *Photochemical & Photobiological Sciences* the acknowledgement should be in the form:
  - [Original citation] - Reproduced by permission of The Royal Society of Chemistry (RSC) on behalf of the European Society for Photobiology, the European Photochemistry Association, and RSC
- For material being reproduced from an article in *Physical Chemistry Chemical Physics* the acknowledgement should be in the form:
  - [Original citation] - Reproduced by permission of the PCCP Owner Societies
- For material reproduced from books and any other journal the acknowledgement should be in the form:
  - [Original citation] - Reproduced by permission of The Royal Society of Chemistry

The acknowledgement should also include a hyperlink to the article on the RSC website.

The form of the acknowledgement is also specified in the RSC agreement/licence signed by the corresponding author.

Except in cases of republication in a thesis, this express permission does not cover the reproduction of large portions of text from the RSC publication or reproduction of the whole article or book chapter.

A publisher of a non-RSC publication can use this document as proof that permission is granted to use the material in the non-RSC publication.

References

Chapter 1

1. Fournier, A. C.; Cumming, H.; McGrath, K. M., Assembly of two- and three-dimensionally patterned silicate materials using responsive soft templates. Dalton Trans 2010, 39 (28), 6524-31.

2. Zones, S. I.; Davis, M. E., Zeolite materials: Recent discoveries and future prospects. Current Opinion in Solid State & Material Science 1996, 1, 107-117.

3. Kresge, C. T.; Leonowicz, M. E.; Roth, W. J.; Vartuli, J. C.; Beck, J. S., Ordered mesoporous molecular sieves synthesized by a liquid-crystal template mechanism. Nature 1992, 359, 710-712.

4. Beck, J. S.; Vartuli, J. C.; Roth, W. J.; Leonowicz, M. E.; Kresge, C. T.; Schmitt, K. D.; Chu, C. T.-W.; Olson, D. H.; Sheppard, E. W.; McCullen, S. B.; Higgins, J. B.; Schlenker, J. L., A new family of mesoporous molecular sieves prepared with liquid crystal templates. Journal of the American Chemical Society 1992, 114, 10834-10843.

5. Inagaki, S.; Fukushima, Y.; Kuroda, K., Synthesis of highly ordered mesoporous materials from a layered polysilicate. Journal of the Chemical Society : Chemical Communication 1993, 680-682.

6. Behrens, P., Voids in variable chemical surroundings: Mesoporous metal oxides. Angewandte Chemie International Edition in English 1996, 35 (5), 515-518.

7. Gutiérrez, J. M.; González, C.; Maestro, A.; Solè, I.; Pey, C. M.; Nolla, J., Nano-emulsions: New applications and optimization of their preparation. Current Opinion in Colloid & Interface Science 2008, 13 (4), 245-251.

8. Maestro, A.; Sole, I.; Gonzalez, C.; Solans, C.; Gutierrez, J. M., Influence of the phase behavior on the properties of ionic nanoemulsions prepared by the phase inversion composition method. Journal of colloid and interface science 2008, 327 (2), 433-9.

9. Leong, T. S.; Wooster, T. J.; Kentish, S. E.; Ashokkumar, M., Minimising oil droplet size using ultrasonic emulsification. Ultrasonics sonochemistry 2009, 16 (6), 721-7.

10. Sole, I.; Pey, C. M.; Maestro, A.; Gonzalez, C.; Porras, M.; Solans, C.; Gutierrez, J. M., Nano-emulsions prepared by the phase inversion composition method: Preparation variables and scale up. Journal of colloid and interface science 2010, 344 (2), 417-23.

11. Prouzet, E.; Boissière, C., A review on the synthesis, structure and applications in separation processes of mesoporous msu-x silica obtained with the two-step process. Compte-Rendu de Chimie 2005, 8, 579-596.

12. Zhang, H.; Cooper, A. I., Synthesis and applications of emulsion-templated porous materials. Soft Matter 2005, 1 (2), 107.

Chapter 2

1. Yang, X. Y.; Leonard, A.; Lemaire, A.; Tian, G.; Su, B. L., Self-formation phenomenon to hierarchically structured porous materials: Design, synthesis, formation mechanism and applications. Chem Commun (Camb) 2011, 47 (10), 2763-86.

2. Ishizaki, K.; Komarneni, S.; Nanko, M., In Porous materials: Process technology and application, 1998; pp 1-11.

3. Giesche, H., Mercury porosimetry: A general (practical) overview. Particle & Particle Systems Characterization 2006, 23 (1), 9-19.

4. Sanchez, C.; Rozes, L.; Ribot, F.; Laberty-Robert, C.; Grosso, D.; Sassoye, C.; Boissiere, C.; Nicole, L., “Chimie douce”: A land of opportunities for the designed construction of functional inorganic and hybrid organic-inorganic nanomaterials. Comptes Rendus Chimie 2010, 13 (1-2), 3-39.

5. Prouzet, E.; Ravaine, S.; Sanchez, C.; Backov, R., Bio-inspired synthetic pathways and beyond: Integrative chemistry. New Journal of Chemistry 2008, 32 (8), 1284.

6. Mann, S., The chemistry of form. Angewandte Chemie International Edition in English 2000, 39, 3392-3406.

7. Yang, H.; Coombs, N.; Ozin, G. A., Morphogenesis of shapes and surface patterns in mesoporous silica. Nature 1997, 386, 692-695.

8. Ozin, S. M. a. G., Synthesis of inorganic materials with complex form. Nature 1996, 382, 313-318.

9. Soten, I.; Ozin, G. A., New directions in self-assembly: Materials synthesis over 'all' length scales. Current Opinion in Colloid & Interface Science 1999, 4, 325-337.

10. Soft chemistry routes to new materials. Trans Tech Publications: 1994; Vol. 152-153.

11. Prouzet, E.; Boissière, C., A review on the synthesis, structure and applications in separation processes of mesoporous msu-x silica obtained with the two-step process. Compte-Rendu de Chimie 2005, 8, 579-596.

12. Martines, M. A. U.; Yeong, E.; Larbot, A.; Prouzet, E., Temperature dependence in the synthesis of hexagonal msu-3 type mesoporous silica synthesized with pluronic p123 block copolymer. Microporous and Mesoporous Materials 2004, 74, 213-220.

13. Boissière, C.; Martines, M. A. U.; Tokomuto, M.; Larbot, A.; Prouzet, E., Mechanisms of pore size control in msu-x mesoporous silica. Chemistry of Materials 2003, 15, 509-515.

14. Prouzet, E.; Cot, F.; Boissière, C.; Kooyman, P. J.; Larbot, A., Nanometric hollow spheres made of msu-x type mesoporous silica. Journal of Materials Chemistry 2002, 12, 1553-1556.

15. Boissière, C.; van der Lee, A.; El Mansouri, A.; Larbot, A.; Prouzet, E., A double step synthesis of mesoporous micrometric spherical msu silica particles. Journal of the Chemical Society : Chemical Communication 1999, 20, 2047-2048.

16. Hammond, W.; Prouzet, E.; Mahanti, S. D.; Pinnavaia, T. J., Structure factor for the periodic walls of mesoporous mcm-41 molecular sieves. Microporous and Mesoporous Materials 1999, 27, 19-25.

17. A. Venkateswara Rao, G. M. P., Uzma K. H. Bangi,; A. Parvathy Rao, a. M. M. K., Sodium silicate based aerogels via ambient pressure drying. In Aerogels handbook, advances in sol-gel derived materials and technologies, Aegerter, M. A.; Prassas, M., Eds. 2011.

18. Gurav, J. L.; Rao, A. V.; Rao, A. P.; Nadargi, D. Y.; Bhagat, S. D., Physical properties of sodium silicate based silica aerogels prepared by single step sol–gel process dried at ambient pressure. Journal of Alloys and Compounds 2009, 476 (1-2), 397-402.

19. Sierra, L.; Guth, J. L., Synthesis of mesoporous silica with tunable pore size from sodium silicate solutions and a polyethylene oxide surfactant. Microporous and Mesoporous Materials 1999, 27, 243-253.

20. Rigacci, A. C. P. a. A., Sio2 aerogels. In Advances in sol-gel derived materials and technologies, Aegerter, M. A.; Prassas, M., Eds. 2011.

21. Schuth, F., Endo- and exotemplating to create high-surface-area inorganic materials. Angew Chem Int Ed Engl 2003, 42 (31), 3604-22.

22. Taguchi, A.; Schüth, F., Ordered mesoporous materials in catalysis. Microporous and Mesoporous Materials 2005, 77 (1), 1-45.

23. Wan, Y.; Zhao, D., On the controllable soft-templating approach to mesoporous silicates. Chemical Review 2007, 107 (7), 2821-2860.

24. Schacht, S.; Huo, Q.; Voigt-Martin, I.; Stucky, G. D.; Schüth, F., Oil-water interface templating of mesoporous macroscale structures. Science 1996, 273, 768-771.

25. Zoldesi, C. I.; Steegstra, P.; Imhof, A., Encapsulation of emulsion droplets by organo-silica shells. Journal of colloid and interface science 2007, 308 (1), 121-9.

26. C. Zoldesi, C. W., A. Imhof, Deformable hollow hybrid silica/siloxane colloids by emulsion templating. Langmuir : the ACS journal of surfaces and colloids 2006, 22, 4343-4352.

27. C. Zoldesi, A. I., Synthesis of monodisperse colloidal spheres, capsules, and microballons by emulsion templating. Advanced Materials 2005, 17 (7), 924-928.

28. V. Manoharan, A. I., J. Thorne, D. Pine, Photonic crystals from emulsion templates. Advanced Materials 2001, 13 (6), 447-450.

29. A. Imhof, D. P., Uniform macroporous ceramics and plastics by emulsion templating. Advanced Materials 1998, 10 (9), 697-700.

30. Imhof, A.; Pine, D. J., Ordered macroporous materials by emulsion templating. Nature 1997, 389, 948-951.

31. Pine, A. I. D. J., Ordered macroporous materials by emulsion templating. Nature 1997, 389, 948-951.

32. Destribats, M.; Faure, B.; Birot, M.; Babot, O.; Schmitt, V.; Backov, R., Tailored silica macrocellular foams: Combining limited coalescence-based pickering emulsion and sol-gel process. Advanced Functional Materials 2012, 22 (12), 2642-2654.

33. Destribats, M.; Schmitt, V.; Backov, R., Thermostimulable wax@sio2 core-shell particles. Langmuir : the ACS journal of surfaces and colloids 2010, 26 (3), 1734-42.

34. Carn, F.; Colin, A.; Achard, M.-F.; Deleuze, H.; Sellier, E.; Birot, M.; Backov, R., Inorganic monoliths hierarchically textured via concentrated direct emulsion and micellar templates. Journal of Materials Chemistry 2004, 14, 1370-1376.

35. Patrick Schmidt-Winkel, ‡ Charles J. Glinka,§ and Galen D. Stucky, Microemulsion templates for mesoporous silica. Langmuir : the ACS journal of surfaces and colloids 2000, 16, 6.

36. Schmidt-Winkel, P.; Lukens, W. W. J.; Yang, P.; Margolese, D. I.; Lettow, J. S.; Ying, J. Y.; Stucky, G. D., Microemulsion templating of siliceous mesostructured cellular foams with well-defined ultralarge mesopores. Chemistry of Materials 2000, 12, 686-696.

37. Phadke, S.; Ho, J.; Birnie, D. P., Emulsion templating to obtain dual-size-scale mesoporous titania coatings. Materials Letters 2009, 63 (30), 2619-2621.

38. P.Binks, Macroporous silica from solid stabilized emulsion templates. Advanced Materials 2002, 14, 1824-1827.

39. Blin, J. L.; Bleta, R.; Ghanbaja, J.; Stébé, M. J., Fluorinated emulsions: Templates for the direct preparation of macroporous–mesoporous silica with a highly ordered array of large mesopores. Microporous and Mesoporous Materials 2006, 94 (1-3), 74-80.

40. Schiller, R.; Weiss, C. K.; Geserick, J.; Hüsing, N.; Landfester, K., Synthesis of mesoporous silica particles and capsules by miniemulsion technique. Chemistry of Materials 2009, 21 (21), 5088-5098.

41. Fournier, A. C.; Cumming, H.; McGrath, K. M., Assembly of two- and three-dimensionally patterned silicate materials using responsive soft templates. Dalton Trans 2010, 39 (28), 6524-31.

42. Bean, K.; Black, C. F.; Govan, N.; Reynolds, P.; Sambrook, M. R., Preparation of aqueous core/silica shell microcapsules. Journal of colloid and interface science 2012, 366 (1), 16-22.

43. Yuan, Z.-Y.; Su, B.-L., Insights into hierarchically meso–macroporous structured materials. Journal of Materials Chemistry 2006, 16 (7), 663.

44. McClements, D. J., Nanoemulsions versus microemulsions: Terminology, differences, and similarities. Soft Matter 2012, 8 (6), 1719.

45. Mason, T. G.; Wilking, J. N.; Meleson, K.; Chang, C. B.; Graves, S. M., Nanoemulsions: Formation, structure, and physical properties. Journal of Physics: Condensed Matter 2006, 18 (41), R635-R666.

46. Anton, N.; Benoit, J. P.; Saulnier, P., Design and production of nanoparticles formulated from nano-emulsion templates-a review. Journal of controlled release : official journal of the Controlled Release Society 2008, 128 (3), 185-99.

47. Izquierdo, P.; Feng, J.; Esquena, J.; Tadros, T. F.; Dederen, J. C.; Garcia, M. J.; Azemar, N.; Solans, C., The influence of surfactant mixing ratio on nano-emulsion formation by the pit method. Journal of colloid and interface science 2005, 285 (1), 388-94.

48. Fernandez, P.; André, V.; Rieger, J.; Kühnle, A., Nano-emulsion formation by emulsion phase inversion. Colloids and Surfaces A: Physicochemical and Engineering Aspects 2004, 251 (1-3), 53-58.

49. Solans, C.; Solé, I., Nano-emulsions: Formation by low-energy methods. Current Opinion in Colloid & Interface Science 2012, 17 (5), 246-254.

50. Ungureanu, S.; Birot, M.; Laurent, G.; Deleuze, H.; Babot, O.; Julian-Lopez, B.; Achard, M.-F.; Ionel Popa, M.; Sanchez, C.; Backov, R., One-pot syntheses of the first series of emulsion based hierarchical hybrid organic-inorganic open-cell monoliths possessing tunable functionality (organo-si(hipe) series). Chemistry of Materials 2007, 19, 5786-5796.

51. Abdelhamid Sayari, a. S. H., Periodic mesoporous silica-based organic-inorganic nanocomposite materials. Chem. Mater 2001, 13, 3151-3168.

52. Sachse, A.; Galarneau, A.; Fajula, F.; Di Renzo, F.; Creux, P.; Coq, B., Functional silica monoliths with hierarchical uniform porosity as continuous flow catalytic reactors. Microporous and Mesoporous Materials 2011, 140 (1-3), 58-68.

53. Hu, J.; Chen, M.; Fang, X.; Wu, L., Fabrication and application of inorganic hollow spheres. Chemical Society reviews 2011, 40 (11), 5472-91.

54. Zhang, H.; Hussain, I.; Brust, M.; Cooper, A. I., Synthesis of hierarchically porous inorganic-metal site-isolated nanocomposites. Chem Commun (Camb) 2006, (24), 2539-41.

55. Dhainaut, J.; Dacquin, J.-P.; Lee, A. F.; Wilson, K., Hierarchical macroporous–mesoporous sba-15 sulfonic acid catalysts for biodiesel synthesis. Green Chemistry 2010, 12 (2), 296.

56. Crippa, M.; Callone, E.; D'Arienzo, M.; Müller, K.; Polizzi, S.; Wahba, L.; Morazzoni, F.; Scotti, R., Tio2 nanocrystals grafted on macroporous silica: A novel hybrid organic–inorganic sol–gel approach for the synthesis of highly photoactive composite material. Applied Catalysis B: Environmental 2011, 104 (3-4), 282-290.

57. Park, S. S.; Ha, C. S., Organic-inorganic hybrid mesoporous silicas: Functionalization, pore size, and morphology control. Chem Rec 2006, 6 (1), 32-42.

58. Markus Antonietti, K. L., Polyreactions in miniemulsions. Prog. Polym. Sci 2002, 27.

59. Han, Z. H.; Yang, B.; Qi, Y.; Cumings, J., Synthesis of low-melting-point metallic nanoparticles with an ultrasonic nanoemulsion method. Ultrasonics 2011, 51 (4), 485-8.

60. Park, J.; An, K.; Hwang, Y.; Park, J. G.; Noh, H. J.; Kim, J. Y.; Park, J. H.; Hwang, N. M.; Hyeon, T., Ultra-large-scale syntheses of monodisperse nanocrystals. Nature materials 2004, 3 (12), 891-5.

61. Rafael Muñoz-Espí, C. K. W., Katharina Landfester, Inorganic nanoparticles prepared in miniemulsion. Current Opinion in Colloid & Interface Science 2012, 17, 212-224.

Chapter 3

1. McClements, D. J., Nanoemulsions versus microemulsions: Terminology, differences, and similarities. Soft Matter 2012, 8 (6), 1719.

2. Klang, V.; Matsko, N. B.; Valenta, C.; Hofer, F., Electron microscopy of nanoemulsions: An essential tool for characterisation and stability assessment. Micron 2012, 43 (2-3), 85-103.

3. Hessien, M.; Leone, P.; Suchaud, M.; Lebeau, B.; Nouali, H.; Guari, Y.; Prouzet, E., Nanocrystalline iron oxide synthesised within hierarchical porous silica prepared by nanoemulsion templating. Chem Commun (Camb) 2012, 48 (80), 10022-4.

4. Han, Z. H.; Yang, B.; Qi, Y.; Cumings, J., Synthesis of low-melting-point metallic nanoparticles with an ultrasonic nanoemulsion method. Ultrasonics 2011, 51 (4), 485-8.

5. Edmund, A. R.; Kambalapally, S.; Wilson, T. A.; Nicolosi, R. J., Encapsulation of cadmium selenide quantum dots using a self-assembling nanoemulsion (sane) reduces their in vitro toxicity. Toxicology in vitro : an international journal published in association with BIBRA 2011, 25 (1), 185-90.

6. Spernath, L.; Magdassi, S., Formation of silica nanocapsules from nanoemulsions obtained by the phase inversion temperature method. Micro & Nano Letters 2010, 5 (1), 28.

7. Nam, Y. S.; Kim, J. W.; Shim, J.; Han, S. H.; Kim, H. K., Nanosized emulsions stabilized by semisolid polymer interphase. Langmuir : the ACS journal of surfaces and colloids 2010, 26 (16), 13038-43.

8. Kawada, H.; Kume, T.; Matsunaga, T.; Iwai, H.; Sano, T.; Shibayama, M., Structure and rheology of a self-standing nanoemulsion. Langmuir : the ACS journal of surfaces and colloids 2010, 26 (4), 2430-7.

9. Zhao, Y.; Zhang, J.; Li, W.; Zhang, C.; Han, B., Synthesis of uniform hollow silica spheres with ordered mesoporous shells in a co2 induced nanoemulsion. Chem Commun (Camb) 2009, (17), 2365-7.

10. Leong, T. S.; Wooster, T. J.; Kentish, S. E.; Ashokkumar, M., Minimising oil droplet size using ultrasonic emulsification. Ultrasonics sonochemistry 2009, 16 (6), 721-7.

11. Maestro, A.; Sole, I.; Gonzalez, C.; Solans, C.; Gutierrez, J. M., Influence of the phase behavior on the properties of ionic nanoemulsions prepared by the phase inversion composition method. Journal of colloid and interface science 2008, 327 (2), 433-9.

12. Mason, T. G.; Wilking, J. N.; Meleson, K.; Chang, C. B.; Graves, S. M., Nanoemulsions: Formation, structure, and physical properties. Journal of Physics: Condensed Matter 2006, 18 (41), R635-R666.

13. Liu, W.; Sun, D.; Li, C.; Liu, Q.; Xu, J., Formation and stability of paraffin oil-in-water nano-emulsions prepared by the emulsion inversion point method. Journal of colloid and interface science 2006, 303 (2), 557-63.

14. Pey, C. M.; Maestro, A.; Solé, I.; González, C.; Solans, C.; Gutiérrez, J. M., Optimization of nano-emulsions prepared by low-energy emulsification methods at constant temperature using a factorial design study. Colloids and Surfaces A: Physicochemical and Engineering Aspects 2006, 288 (1-3), 144-150.

15. Fernandez, P.; André, V.; Rieger, J.; Kühnle, A., Nano-emulsion formation by emulsion phase inversion. Colloids and Surfaces A: Physicochemical and Engineering Aspects 2004, 251 (1-3), 53-58.

16. Marszall, L., Hlb of nonionic surfactants: Pit and eip methods. In Nonionic surfactants, physical chemistry, Schick, M. J., Ed. Dekker, Marcel Inc.: New York, 1987; Vol. 23, pp 549-600.

17. Aubard, J.; Levoir, P.; Denis, A.; Claverie, P., Direct analysis of chemical relaxation signals by a method based on the combination of laplace transform and padé approximants. Computational Chemistry 1987, 11 (3), 163-178.

18. Bajzer, Z.; Myers, A. C.; Sedarous, S. S.; Prendergast, F. G., Pade-laplace method for analysis of fluorescence intensity decay. Biophysics Journal 1989, 56, 79-93.

19. Gutiérrez, J. M.; González, C.; Maestro, A.; Solè, I.; Pey, C. M.; Nolla, J., Nano-emulsions: New applications and optimization of their preparation. Current Opinion in Colloid & Interface Science 2008, 13 (4), 245-251.

20. Sole, I.; Pey, C. M.; Maestro, A.; Gonzalez, C.; Porras, M.; Solans, C.; Gutierrez, J. M., Nano-emulsions prepared by the phase inversion composition method: Preparation variables and scale up. Journal of colloid and interface science 2010, 344 (2), 417-23.

21. Solans, C.; Izquierdo, P.; Nolla, J.; Azemar, N.; Garciacelma, M., Nano-emulsions. Current Opinion in Colloid & Interface Science 2005, 10 (3-4), 102-110.

Chapter 4

1. Sole, I.; Pey, C. M.; Maestro, A.; Gonzalez, C.; Porras, M.; Solans, C.; Gutierrez, J. M., Nano-emulsions prepared by the phase inversion composition method: Preparation variables and scale up. Journal of colloid and interface science 2010, 344 (2), 417-23.

2. Liu, W.; Sun, D.; Li, C.; Liu, Q.; Xu, J., Formation and stability of paraffin oil-in-water nano-emulsions prepared by the emulsion inversion point method. Journal of colloid and interface science 2006, 303 (2), 557-63.

3. Pey, C. M.; Maestro, A.; Solé, I.; González, C.; Solans, C.; Gutiérrez, J. M., Optimization of nano-emulsions prepared by low-energy emulsification methods at constant temperature using a factorial design study. Colloids and Surfaces A: Physicochemical and Engineering Aspects 2006, 288 (1-3), 144-150.

4. Bendjaballah, M.; Canselier, J. P.; Oumeddour, R., Optimization of oil-in-water emulsion stability: Experimental design, multiple light scattering, and acoustic attenuation spectroscopy. Journal of Dispersion Science and Technology 2010, 31 (9), 1260-1272.

5. Nielloud, F.; Mestres, J. P.; Fortune, R.; Draussin, S.; Marti-Mestres, G., Formulation of oil-in-water submicron emulsions in the dermatological field using experimental design. Polymer International 2003, 52 (4), 610-613.

6. Fatoni, R. Product design of wheat straw polypropylene composite. University of Waterloo, Waterloo, ON, 2012.

7. Marszall, L., Hlb of nonionic surfactants: Pit and eip methods. In Nonionic surfactants, physical chemistry, Schick, M. J., Ed. Dekker, Marcel Inc.: New York, 1987; Vol. 23, pp 549-600.

8. Fernandez, P.; André, V.; Rieger, J.; Kühnle, A., Nano-emulsion formation by emulsion phase inversion. Colloids and Surfaces A: Physicochemical and Engineering Aspects 2004, 251 (1-3), 53-58.

Chapter 5

1. Beck, J. S.; Vartuli, J. C.; Roth, W. J.; Leonowicz, M. E.; Kresge, C. T.; Schmitt, K. D.; Chu, C. T.-W.; Olson, D. H.; Sheppard, E. W.; McCullen, S. B.; Higgins, J. B.; Schlenker, J. L., A new family of mesoporous molecular sieves prepared with liquid crystal templates. Journal of the American Chemical Society 1992, 114, 10834-10843.

2. Inagaki, S.; Fukushima, Y.; Kuroda, K., Synthesis of highly ordered mesoporous materials from a layered polysilicate. Journal of the Chemical Society : Chemical Communication 1993, 680-682.

3. Beck, J. S.; Vartuli, J. C., Recent advances in the synthesis, characterization and applications of mesoporous molecular sieves. Current Opinion in Solid State & Material Science 1996, 1, 76-87.

4. Zhao, D.; Feng, J.; Huo, Q.; Melosh, N.; Fredrickson, G. H.; Chmelka, B. F.; Stucky, G. D., Triblock copolymer syntheses of mesoporous silica with periodic 50 to 300 ångstrom pores. Science 1998, 279, 548-552.

5. Boissière, C.; Larbot, A.; van der Lee, A.; Kooyman, P. J.; Prouzet, E., A new synthesis of mesoporous msu-x silica controlled by a two-step pathway. Chemistry of Materials 2000, 12, 2902-2913.

6. McClements, D. J., Nanoemulsions versus microemulsions: Terminology, differences, and similarities. Soft Matter 2012, 8 (6), 1719.

7. Solans, C.; Izquierdo, P.; Nolla, J.; Azemar, N.; Garciacelma, M., Nano-emulsions. Current Opinion in Colloid & Interface Science 2005, 10 (3-4), 102-110.

8. Liu, W.; Sun, D.; Li, C.; Liu, Q.; Xu, J., Formation and stability of paraffin oil-in-water nano-emulsions prepared by the emulsion inversion point method. Journal of colloid and interface science 2006, 303 (2), 557-63.

9. M. Hessien, N. S., C. Kim and E. Prouzet,, Stability and tunability of o/w nan-emulsions prepared by phase inversion composition. Langmuir 2011, 27, 2299-2307.

10. Zoldesi, C. I.; Steegstra, P.; Imhof, A., Encapsulation of emulsion droplets by organo-silica shells. Journal of colloid and interface science 2007, 308 (1), 121-9.

11. C. Zoldesi, C. W., A. Imhof, Deformable hollow hybrid silica/siloxane colloids by emulsion templating. Langmuir : the ACS journal of surfaces and colloids 2006, 22, 4343-4352.

12. C. Zoldesi, A. I., Synthesis of monodisperse colloidal spheres, capsules, and microballons by emulsion templating. Advanced Materials 2005, 17 (7), 924-928.

13. V. Manoharan, A. I., J. Thorne, D. Pine, Photonic crystals from emulsion templates. Advanced Materials 2001, 13 (6), 447-450.

14. A. Imhof, D. P., Uniform macroporous ceramics and plastics by emulsion templating. Advanced Materials 1998, 10 (9), 697-700.

15. Imhof, A.; Pine, D. J., Ordered macroporous materials by emulsion templating. Nature 1997, 389, 948-951.

16. Blin, J. L.; Bleta, R.; Ghanbaja, J.; Stébé, M. J., Fluorinated emulsions: Templates for the direct preparation of macroporous–mesoporous silica with a highly ordered array of large mesopores. Microporous and Mesoporous Materials 2006, 94 (1-3), 74-80.

17. Zhao, Y.; Zhang, J.; Li, W.; Zhang, C.; Han, B., Synthesis of uniform hollow silica spheres with ordered mesoporous shells in a co2 induced nanoemulsion. Chem Commun (Camb) 2009, (17), 2365-7.

18. Phadke, S.; Ho, J.; Birnie, D. P., Emulsion templating to obtain dual-size-scale mesoporous titania coatings. Materials Letters 2009, 63 (30), 2619-2621.

19. Sébastien Abramsona, W. S., Bernard Malezieux , Vincent Dupuis,; Stephan Borensztajn, E. B., Agnès Bée, An eco-friendly route to magnetic silica microspheres and nanospheres. Journal of colloid and interface science 2011, 364, 324-332.

20. Sarvi, M. N.; Stevens, G. W.; Gee, M. L.; O'Connor, A. J., The co-micelle/emulsion templating route to tailor nano-engineered hierarchically porous macrospheres. Microporous and Mesoporous Materials 2012, 149 (1), 101-105.

21. Spernath, L.; Magdassi, S., Formation of silica nanocapsules from nanoemulsions obtained by the phase inversion temperature method. Micro & Nano Letters 2010, 5 (1), 28.

22. Washburn, E. W., Phys. Rev. 1921, 17 (273).

23. S. Schacht, Q. H., I. G. Voigt-Martin, G. D. Stucky , F. Schüth, Oil-water interface templating of mesoporous macroscale structures. Science 1996, 273 (5276), 4.

24. Fournier, A. C.; Cumming, H.; McGrath, K. M., Assembly of two- and three-dimensionally patterned silicate materials using responsive soft templates. Dalton Trans 2010, 39 (28), 6524-31.

25. Stein, J. C. L. a. A., Recent progress in syntheses and applications of inverse opals and related macroporous materials prepared by colloidal crystal templating In Annual reviews of nano research, G. CAO, C. J. B., Ed. 2006; Vol. 1, pp 1-79.

26. Destribats, M.; Faure, B.; Birot, M.; Babot, O.; Schmitt, V.; Backov, R., Tailored silica macrocellular foams: Combining limited coalescence-based pickering emulsion and sol-gel process. Advanced Functional Materials 2012, 22 (12), 2642-2654.

27. Destribats, M.; Schmitt, V.; Backov, R., Thermostimulable wax@sio2 core-shell particles. Langmuir : the ACS journal of surfaces and colloids 2010, 26 (3), 1734-42.

28. Carn, F.; Colin, A.; Achard, M.-F.; Deleuze, H.; Sellier, E.; Birot, M.; Backov, R., Inorganic monoliths hierarchically textured via concentrated direct emulsion and micellar templates. Journal of Materials Chemistry 2004, 14, 1370-1376.

Chapter 6

1. Zhang, H.; Hussain, I.; Brust, M.; Cooper, A. I., Synthesis of hierarchically porous inorganic-metal site-isolated nanocomposites. Chem Commun (Camb) 2006, (24), 2539-41.

2. Dhainaut, J.; Dacquin, J.-P.; Lee, A. F.; Wilson, K., Hierarchical macroporous–mesoporous sba-15 sulfonic acid catalysts for biodiesel synthesis. Green Chemistry 2010, 12 (2), 296.

3. David M. Hess, R. R. N., Carlos Rinaldi, Melanie M. Tomczak, and; Watkins, J. J., Fabrication of ordered mesoporous silica films with encapsulated iron oxide nanoparticles using ferritin-doped block copolymer templates. Chem. Mater 2009, 21, 2125-2129.

4. Park, J.; An, K.; Hwang, Y.; Park, J. G.; Noh, H. J.; Kim, J. Y.; Park, J. H.; Hwang, N. M.; Hyeon, T., Ultra-large-scale syntheses of monodisperse nanocrystals. Nature materials 2004, 3 (12), 891-5.

5. Nasrazadani, S., Corrosion science 2008, 50, 2493-97.

6. Palchoudhury, S.; Xu, Y.; Goodwin, J.; Bao, Y., Synthesis of iron oxide nanoworms. Journal of Applied Physics 2011, 109 (7), 07E314.

7. Ortega, D., Structure and magnetism in magnetic nanoparticles. In Magnetic nanoparticles from fabrication to clinical applications, Thanh, N. T. K., Ed. 2012; pp 3-44.

8. B. ZHAO, Y. W., H. GUO, J. WANG, Y. HE, Z. JIAO, M. WU, Iron oxide(iii) nanoparticles fabricated by electron beam irradiation method. Materials Science-Poland 2007, 25 (4), 6.

9. Dallas, P.; Bourlinos, A. B.; Niarchos, D.; Petridis, D., Synthesis of tunable sized capped magnetic iron oxide nanoparticles highly soluble in organic solvents. Journal of Materials Science 2007, 42 (13), 4996-5002.

10. T. Nakamura, T. S., Y. Endoh, N. Yamamoto, M. Shiga and Y.Nakamura, Physics Letters 1964, 12, 178-179.

11. Prouzet, E.; Cot, F.; Boissière, C.; Kooyman, P. J.; Larbot, A., Nanometric hollow spheres made of msu-x type mesoporous silica. Journal of Materials Chemistry 2002, 12, 1553-1556.

12. Broekhoff, J. C. P.; de Boer, J. H., Studies on pore systems in catalysts. Xii. Pore distributions from the desorption branch of a nitrogen sorption isotherm in the case of cylindrical pores. A. An analysis of the capillary evaporation process. Journal of Catalysis 1968, 10, 368-374.

13. Prouzet, E.; Pinnavaia, T. J., Assembly of mesoporous molecular sieves containing wormhole motifs by a nonionic surfactant pathway: Control of pore size by synthesis temperature. Angewandte Chemie International Edition in English 1997, 36 (5), 516-518.

14. Brankovic, D.; Jokanovic, V.; Babic-Stojic, B.; Jaglicic, Z.; Lisjak, D.; Kojic, D., Interference effect between superparamagnetic and spin glass correlated moments in a system of dispersed co3o4 nanocrystallites. J. Phys.-Condes. Matter 2009, 21 (9).

15. Salavati-Niasari, M.; Mir, N.; Davar, F., Synthesis and characterization of co3o4 nanorods by thermal decomposition of cobalt oxalate. Journal of Physics and Chemistry of Solids 2009, 70 (5), 847-852.

Appendix A

Nanoemulsion: A Single-Parameter Study

Relationship between the S/O ratio and the diameter of the oil droplets

The total volume of oil V_T is distributed among all droplets of the nanoemulsion, with a volume that can be assigned to the oil alone, the contribution of surfactants being neglected:

$V_T = n_i (\pi D_i^3/6)$

where V_T is the total volume of oil, D_i is the droplet diameter, and n_i is the number of droplets.

The total surface of the droplets S_T is

$S_T = n_i \pi D_i^2$

For the same total volume of oil V_T, the diameter of the droplets can change from D_1 to D_2, if the surfactant/oil ratio changes, according to

$V_T = n_1 (\pi D_1^3/ 6) = n_2 (\pi D_2^3/6) = n_1/ n_2 = (D_2/ D_1)^3$

This change in the droplet size induces a parallel change in the total droplet surface S_i, which must be adjusted by a modification in the surfactant/oil ratio:

$S_1 = n_1 \pi D_1^2$

and

$S_2 = n_2 \pi D_2^2$

leading to

$$S_1 / S_2 = Q_1/ Q_2 = (n_1 / n_2) (D_1/D_2)^2 = D_2 / D_1 \qquad (4)$$

Table A. 1: Composition of nanoemulsions prepared with a low concentration in water and a constant HLB = 11.6 (D_h: hydrodynamic diameter deduced from the DLS diffusion coefficient; D: diffusion coefficient calculated from the DLS autocorrelation curve). The water content is normalized to the total mass taken as 1.

Span 80 (g)	Tween 80 (g)	Paraffin Oil (g)	Water content (wt)	Surf./Oil	Wt% Surfactant
1.28	2.72	20	0.76	0.2	4
1.60	3.4	20	0.75	0.25	5
1.92	4.08	20	0.74	0.3	6
2.56	5.44	20	0.72	0.4	8
2.88	6.12	20	0.71	0.45	9
3.20	6.80	20	0.70	0.5	10

Table A.2: Composition of nanoemulsions prepared with different surfactant/oil weight ratios and a constant HLB = 11.6.

Span 80 (g)	Tween 80 (g)	Paraffin Oil (g)	Water content (wt)	Surf./Oil	Wt% Surfactant
1.28	2.72	20	0.76	0.2	4
1.60	3.4	20	0.75	0.25	5
1.92	4.08	20	0.74	0.3	6
2.56	5.44	20	0.72	0.4	8
2.88	6.12	20	0.71	0.45	9
3.20	6.80	20	0.70	0.5	10

Table A.3: Composition of nanoemulsions prepared with different surfactant/oil weight ratios and varied HLBs.

Span 80 (g)	Tween 80 (g)	Paraffin Oil (g)	Water (g)	Surf./Oil	Wt% Surfactant	HLB	Dh (nm)
7.95	7.05	20	65	0.75	15	9.36	152
7.28	6.72	20	66	0.70	14	9.43	125
4.8	5.2	20	70	0.50	10	9.84	104
3.6	4.4	20	72	0.40	8	10.2	107
2.34	3.66	20	74	0.30	6	10.8	125
1.75	3.25	20	75	0.25	5	11.3	150
1.12	2.88	20	76	0.20	4	12	175

Table A.4: Composition of nanoemulsions prepared with different surfactant/oil weight ratios and preparation temperatures.

Span 80 (g)	Tween80 (g)	Paraffin Oil (g)	Water (g)	Temperature (°C)	Surfactant:oil (wt ratio)	D_h (nm)
2.21	4.92	28.57	35.7	5	0.25	200
3.05	4.83	28.74	35.7	10	0.25	153
2.23	4.82	28.58	35.7	20	0.25	185
2.23	4.84	28.73	35.7	30	0.25	181
2.23	4.84	28.6	35.7	40	0.25	179
2.22	4.88	28.42	35.7	50	0.25	175
2.51	4.83	28.66	35.7	60	0.25	171
2.42	5.01	28.72	35.7	70	0.25	183
2.24	4.83	28.57	35.7	80	0.25	194
2.48	4.82	14.31	35.7	2	0.5	164
2.28	5.35	14.29	35.7	5	0.5	130
2.3	4.86	14.31	35.7	10	0.5	158
2.4	4.88	14.25	35.7	30	0.5	148
2.33	4.86	14.29	35.7	40	0.5	162
2.22	4.83	14.27	35.7	50	0.5	130
2.29	4.75	14.23	35.7	60	0.5	119
2.27	4.82	14.29	35.7	70	0.5	96
2.26	4.82	14.27	35.7	80	0.5	95

Table A.5: Composition of nanoemulsions prepared with different surfactant/oil weight ratios and preparation temperatures.

Span 80 (g)	Tween80 (g)	Paraffin Oil (g)	Water (g)	Temperature (°C)	Surfactant:oil (wt ratio)	D_h (nm)
2.25	4.83	7.14	35.7	5	1.0	115
2.22	4.84	7.16	35.7	10	1.0	117
2.3	4.83	7.42	35.7	20	1.0	105
2.44	4.88	7.15	35.7	30	1.0	114
2.28	4.85	7.15	35.7	40	1.0	92
2.28	4.85	7.14	35.7	50	1.0	79
2.3	4.89	7.17	35.7	60	1.0	57
2.26	4.85	7.15	35.7	70	1.0	60
2.31	4.82	7.24	35.7	80	1.0	57

Table A.6: Composition of the nanoemulsion after dilution (Span 80: 2.25g; Tween 80: 4.77g; paraffin oil: 20.0g; water: 73.0g). The water content is normalized to the total mass taken as 1.

Dilution	Water content (wt)	D_h (nm)	D ($cm^2.s^{-1}$)
1:1	0.809	700	7.0 10^{-9}
1:1.5	0.892	601	8.2 10^{-9}
1:2	0.91	466	1.1 10^{-8}
1:3	0.932	455	1.1 10^{-8}
1:4	0.946	437	1.1 10^{-8}
1:5	0.955	497	1.2 10^{-8}
1:6	0.961	388	1.3 10^{-8}
1:7	0.966	422	1.2 10^{-8}
1:8	0.97	352	1.4 10^{-8}
1:9	0.973	372	1.3 10^{-8}
1:10	0.975	452	1.1 10^{-8}
1:20	0.987	392	1.2 10^{-8}
1:30	0.991	348	1.4 10^{-8}
1:40	0.993	335	1.5 10^{-8}
1:50	0.995	250	1.8 10^{-8}
1:100	0.997	239	2.1 10^{-8}
1:150	0.998	235	2.1 10^{-8}
1:200	0.9986	246	2.0 10^{-8}
1:300	0.9991	227	2.2 10^{-8}
1:400	0.9993	240	2.0 10^{-8}
1:500	0.9994	217	2.3 10^{-8}

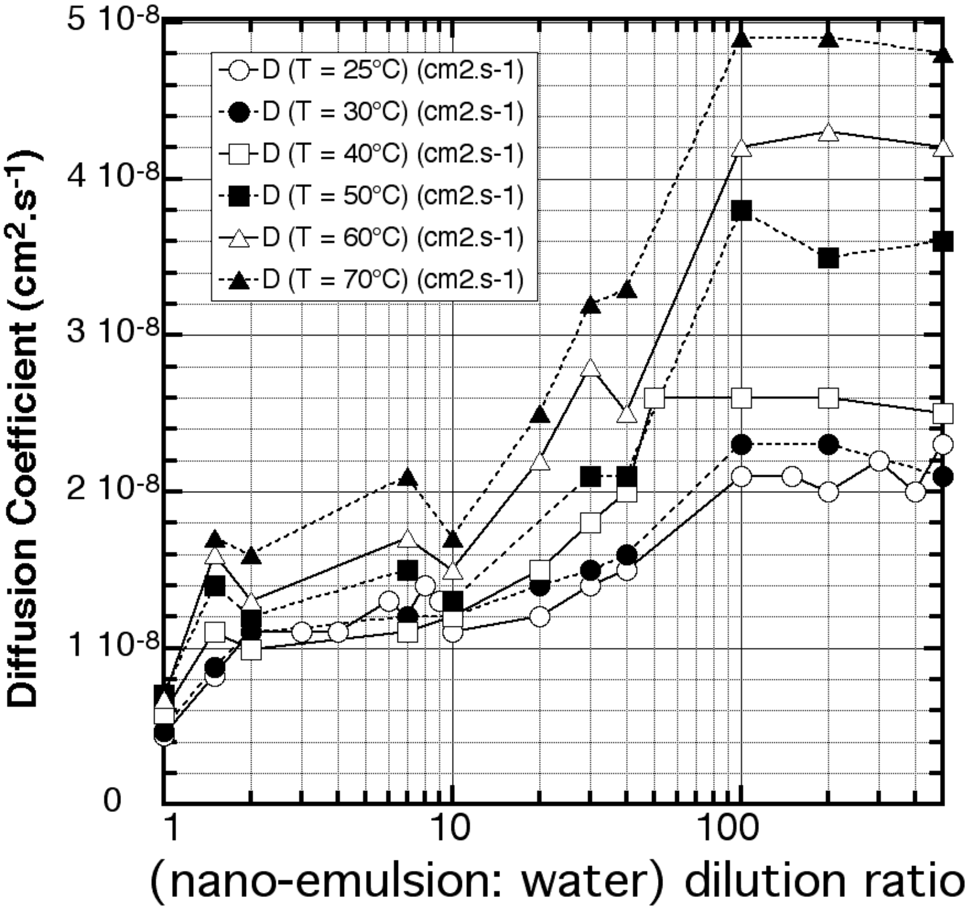

Figure A.1: For different analysis temperatures, the evolution of the diffusion coefficient of the nanoemulsion as a function of the dilution rate.

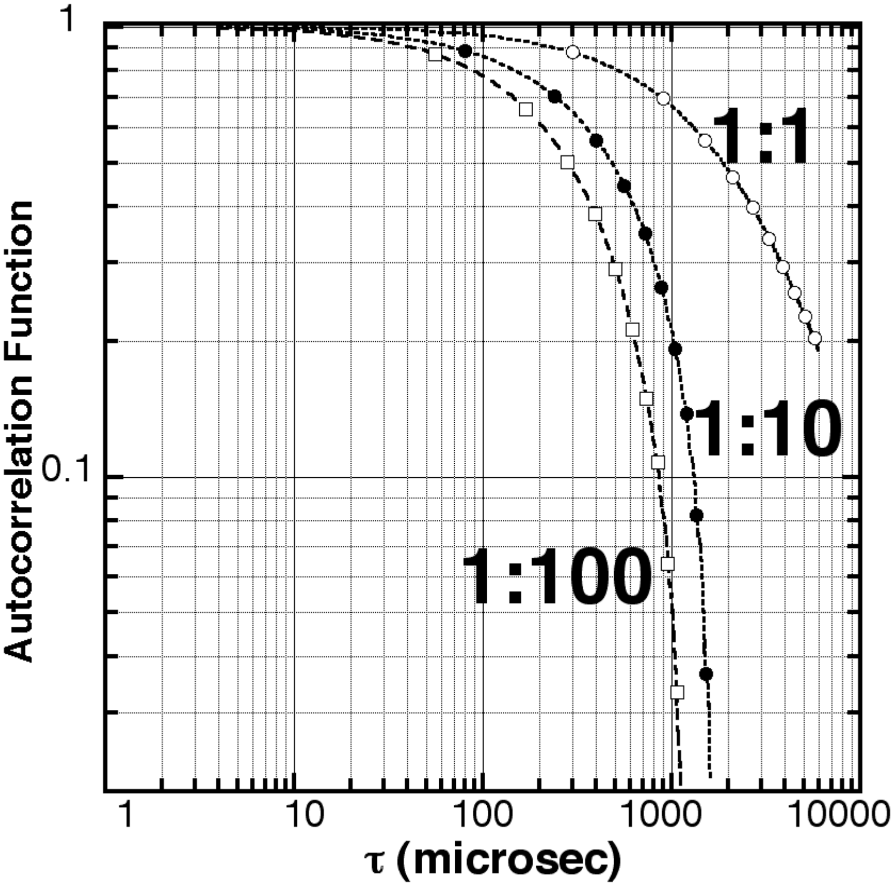

Figure A.2: Sample autocorrelation curves (dotted) and their single-size fit (dashed) for samples recorded at 25 °C, with different nanoemulsion:water dilution ratios (1:1, 1:10, 1:100).

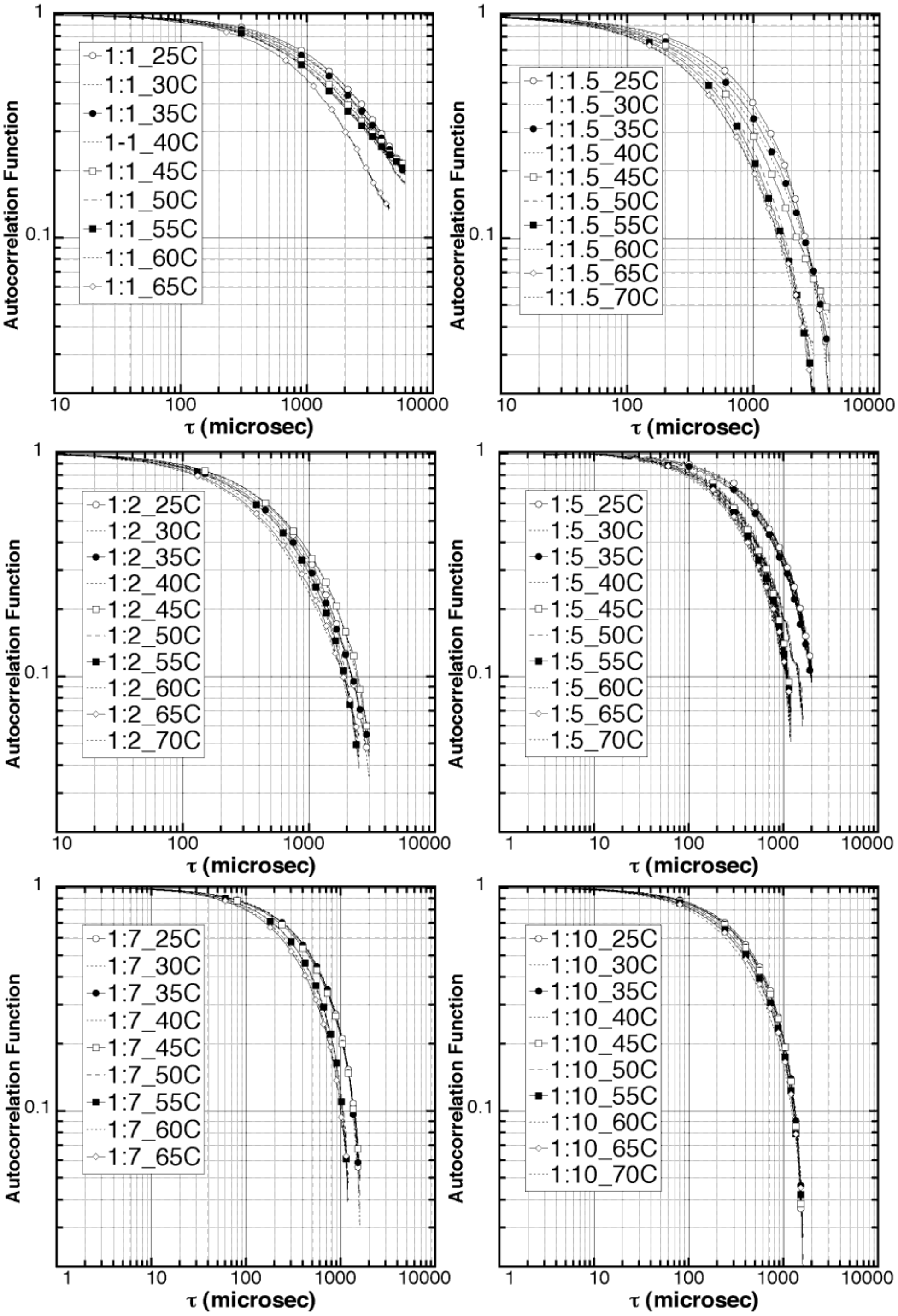

Figure A.3: Experimental autocorrelation curves for the nanoemulsion recorded at different temperatures with dilution ratios varying from 1:1 to 1:10.

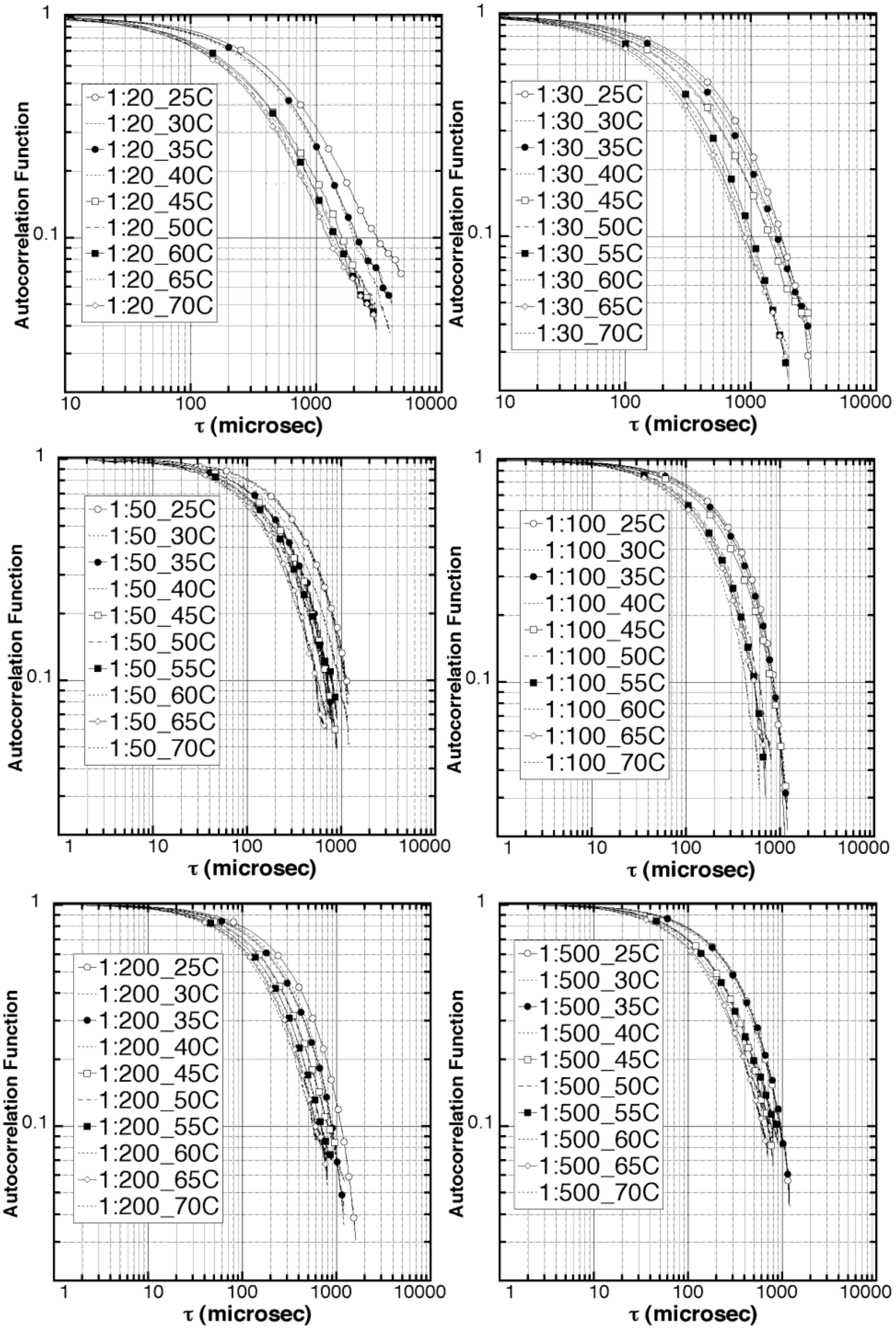

Figure A.4: Autocorrelation curves for the nanoemulsion recorded at different temperatures with dilution ratios varying from 1:20 to 1:500.

Appendix B

Nanoemulsion: Experimental Design Study

Table B. 1: Main features of the sample sets used for the experimental design based on the water/ surfactant/oil phase diagram shown in Figure 4.1.

Set	**HLB**	**Preparation Temperature (°C)**
Set 1	9.6	50
Set 2	9.6	70
Set 3	10.5	60
Set 4	11.7	50
Set 5	11.7	70

Table B. 2: Sample compositions (wt%) used in the experimental design modeling.

Samples	**Component A: Surfactant**	**Component B: Oil**	**Component C: Water**	**Surfactant/Oil Ratio**
1	15	10	75	1.5
2	15	40	45	0.375
3	10	25	65	0.4
4	15	25	60	0.6
5	10	25	65	0.4
6	5	10	85	0.5
7	5	25	70	0.2
8	10	25	65	0.4
9	5	40	55	0.125
10	10	25	65	0.4
11	10	40	50	0.25
12	10	10	80	1.0

Table B.3: Values of the hydrodynamic diameters (nm) for the different sets of measurements (T: preparation temperature).

Sample	Surf./Oil ratio	Set 1□T = 50°C□HLB = 9.65	Set 2□T = 70°C□HLB = 9.65	Set 3□T = 60°C□HLB = 10.5	Set 4□T = 50°C□HLB = 11.7	Set 5□T = 70°C□HLB = 11.7
9	0.125	196	185	-	290	252
7	0.2	190	-	262	-	180
11	0.25	156	-	176	248	166
2	0.375	152	171	138	192	154
3	0.4	170	161	161	151	156
5	0.4	149	128	157	164	146
8	0.4	116	118	157	128	136
10	0.4	109	-	131	114	121
6	0.5	135	-	153	146	136.5
4	0.6	136	136	166	-	105
12	1.0	148	191	191	170	75
1	1.5	174	220	412	192	65

Table B. 4: Models statistics

Set	Model type	Model Equation	R^2	Prob (F)^2
Set 1 **T = 50°C** **HLB = 9.6**	Special cubic	+34.27.S - 3.75.O + 0.27.W +0.34.(S*O) – 0.23.(S*W)+ 0.18.(O*W) - 0.02.(S*O*W)	0.67	0.29 (Not S^3)
Set 2 **T = 70°C** **HLB = 9.6**	Special Cubic	-13.4.S - 4.09.O - 0.59.W+ 1.33.(S*O)+ 0.48.(S*W)+ 0.19.(O*W) - 0.03.(S*O*W)	0.88	0.0339 (S)
Set 3 **T = 60°C** **HLB = 10.5**	Quadratic	+312.47.S + 32.95.O + 1.98.W -5.49.(S*O) – 3.35.(S*W) - 0.24.(O*W)	0.94	0.0036 (S)
Set 4 **T = 50°C** **HLB = 11.7**	Quadratic	-1.61.S + 26.78.O + 1.79.W - 0.67.(S*O) + 0.16.(S*W) - 0.35.(O*W)	0.94	0.003 (S)
Set 5 **T = 70°C** **HLB = 11.7**	Quadratic	80.03.S + 5.68.O + 2.58.W - 1.02.(S*O) – 1.09.(S*W) - 0.02.(O*W)	0.95	0.0001 (S)

Appendix C

Hierarchical Porous Silica

Expected pore volume and pore size and criteria for choosing the composition of the nanoemulsion

Because the oil droplet determines the creation of the pore, there should be a direct relationship between oil droplet size (D_h) and pore size (PS). In addition, the total pore volume (PV), which is the sum of all the pores within the silica, should exhibit a relation with the volume of oil in the nanoemulsion. Determining the total pore volume from macroporosity and the macropore size should enable the verification of this relationship.

Example for calculation of determining the total macropore volume

Taking the O-*1*-HPS-*2.5* sample as an example, it contains 2.5 ml of nanoemulsion (O-*1*-NE) and 100 ml of hydrolyzed sodium silicate solution. This amount of the sodium silicate solution has 14.05 g of pure sodium silicate, which is 26.5 % SiO2, which equals 3.72 g. The total weight of nanoemulsion O-*1*-NE is 117 g, and it contains 10 g of paraffin oil. As an example, in sample O-*1*-HPS-*2.5*, 2.5 g of nanoemulsion includes 0.21 g of paraffin oil, which equals 0.24 cm^3. This sample therefore has a total pore volume of 0.24 cm^3 in 3.7 g of silica, which equals 0.067 cm^3/g.

Example for calculation of determining interface area between oil and water

Taking the O-*1*-NE sample as an example, it contains 10 g of paraffin oil, with density of 0.86 g/cm^3, which results in volume of 11.63 cm^3 = $11.63x10^{21}$ nm^3. Diameter of oil droplet of this nanoemulsion equals to 400 nm and radius of 200 nm. Volume of one oil droplet is $33.5x10^6$ nm^3. Number of oil droplets equals to total oil volume divided by volume of one oil droplet. Number of oil droplets is 3.47×10^{14}. Surface area of one droplet is about $5x10^5$ nm^2 and total surface area of all oil droplets which is the total interface area between oil and water is equal to surface area of one droplet multiply by total number of droplets = 174 m^2. The detailed calculations are in Table C.1

Table C. 1: Calculation of interfacial area

NE sample	oil mass (g)	oil vol. (cm^3)	oil vol. nm^3	D_h (nm)	rh (nm)	droplet Vol (nm^3)	# of droplets	SA of one nm^2	SA of all drops nm^2	m^2
1	10	11.62790698	1.16E+22	400	200	3.35E+07	3.47E+14	5.02E+05	1.74E+20	174
2	10	11.62790698	1.16E+22	200	100	4.19E+06	2.78E+15	1.26E+05	3.49E+20	349
3	10	11.62790698	1.16E+22	65	32.5	1.44E+05	8.09E+16	1.33E+04	1.07E+21	1073
4	25	29.06976744	2.91E+22	105	52.5	6.06E+05	4.80E+16	3.46E+04	1.66E+21	1661
5	40	46.51162791	4.65E+22	154	77	1.91E+06	2.43E+16	7.45E+04	1.81E+21	1812

Table C.2: Composition of the O/W nanoemulsions (O-*y*-NE) used for preparing the hierarchical porous silica (O-*y*-HPS-*x*) samples.

Nanoemulsio name	Span (g)	Tween (g)	Oil (g)	Water (g)	Temperature of preparation (°C)	Hydrodynamic diameter (D_h) (nm)
O-*1*-NE	6.3	8.7	10	75	60	400
O-*2*-NE	4.65	10.35	10	75	50	200
O-*3*-NE	4.65	10.35	10	75	70	65
O-*4*-NE	4.65	10.35	25	60	70	105
O-*5*-NE	4.65	10.35	40	45	70	154

Table C. 3: Calculated pore volume and total interfacial area.

Nanoemulsion Name	Expected total macropore Volume (PV)	Expected Pore Size (PS)	Expected total interface area between oil and water (m^2)
O-*1*-NE	1PV	400 PS	174.41
O-*2*-NE	1PV	200 PS	348.84
O-*3*-NE	1PV	65 PS	1073.35
O-*4*-NE	2.5PV	105 PS	1661.13
O-*5*-NE	4PV	154 PS	1812.141

Table C.4: Compositions of wax/oil-in-water nanoemulsions (W-*y*-NE) used to prepare hierarchical porous silica (W-*y*-HPS-*x*).

Nanoemulsio name	Span (g)	Tween (g)	Oil (g)	Wax (g)	Water (g)	Temperature of preparation (°C)
W-*1*-NE	4.65	5.35	20	0	70	80
W-*2*-NE	4.65	5.35	15	5	70	80
W-*3*-NE	4.65	5.35	10	10	70	80
W-*4*-NE	4.65	5.35	5	15	70	80

Table C. 5: Composition of the hierarchical porous silica (O-*y*-HPS-*x*) samples.

Sample Name	Nanoemulsion Volume (ml)	Hydrolyzed Sodium Silicate Solution (ml)	Expected Macropore Size (nm)	Expected Total Volume of Macropores (cc/gm)
O-*1*-HPS-*2.5*	2.5	100	< 400	0.067
O-*1*-HPS-*25*	25	100	< 400	0.67
O-*1*-HPS-*50*	50	100	< 400	1.34
O-*2*-HPS-*2.5*	2.5	100	< 200	0.067
O-*2*-HPS-*25*	25	100	< 200	0.67
O-*2*-HPS-*50*	50	100	< 200	1.34
O-*3*-HPS-*2.5*	2.5	100	< 65	0.067
O-*3*-HPS-*25*	25	100	< 65	0.67
O-*3*-HPS-*50*	50	100	< 65	1.34
O-*4*-HPS-*2.5*	2.5	100	< 105	0.17
O-*4*-HPS-*25*	25	100	< 105	1.68
O-*4*-HPS-*50*	50	100	< 105	3.35
O-*5*-HPS-*2.5*	2.5	100	< 154	0.27
O-*5*-HPS-*25*	25	100	< 154	2.7
O-*5*-HPS-*50*	50	100	< 154	5.4

Table C. 6: Composition of the hierarchical porous silica (W-*y*-HPS-*x*) sample.

Sample Name	Nanoemulsion Volume (ml)	Hydrolysed Sodium Silicate Solution (ml)
W-*1*-HPS-*2.5*	2.5	100
W-*1*-HPS-*25*	25	100
W-*1*-HPS-*50*	50	100
W-*2*-HPS-*2.5*	2.5	100
W-*2*-HPS-*25*	25	100
W-*2*-HPS-*50*	50	100
W-*3*-HPS-*2.5*	2.5	100
W-*3*-HPS-*25*	25	100
W-*3*-HPS-*50*	50	100
W-*4*-HPS-*2.5*	2.5	100
W-*4*-HPS-*25*	25	100
W-*4*-HPS-*50*	50	100

Table C.7: Compositions of samples mentioned in Figure 5.5.

Nanoemulsion composition

Span (g)	Tween (g)	Oil (g)	Water (g)
1.86	2.14	16	60

Porous silica composition

NE/HSSS vol.%	Nanoemulsion (ml)	HSSS (ml)	Samples in Figure 5.5
18	7.5	42.5	(a, c, e)
50	16.67	33.33	(b, d, f)

Table C. 8: Fractal characterization of silica prepared with different oil nanoemulsion vol.% amounts.

Sample name	**Surface fractal exponent (α)**	**Surface roughness (D_s=6-α)**
Pure silica	3.52	2.48
O-*1*-HPS-*2.5*	3.15	2.85
O-*1*-HPS-*25*	3.28	2.72
O-*1*-HPS-*50*	3.05	2.95
O-*2*-HPS-*2.5*	3.16	2.84
O-*2*-HPS-*50*	3.14	2.86
O-*3*-HPS-25	3.45	2.55
O-*3*-HPS-*50*	3.21	2.79
O-*4*-HPS-*2.5*	3.09	2.91
O-*4*-HPS-*25*	2.92	3.08
O-*4*-HPS-*50*	3.16	2.84
O-*5*-HPS-*25*	3.02	2.98
O-*5*-HPS-*25*	3.04	2.96
O-*5*-HPS-*50*	3.14	2.86

Table C. 9: Data used in Figure 5.14

HSSS/Water	Oil/Water
0.11	4.3
0.15	0.22

Table C. 10: Fractal characterization of silica prepared with different volume of wax nanoemulsion.

Sample Name	**Surface fractal exponent (α)**	**Surface roughness** **($D_s=6-\alpha$)**
W-*1*-HPS-*2.5*	3.15	2.85
W-*1*-HPS-*25*	3.39	2.61
W-*1*-HPS-*50*	3.12	2.88
W-*2*-HPS-*2.5*	3.03	2.97
W-*2*-HPS-*25*	2.94	3.06
W-*2*-HPS-*50*	3.05	2.95
W-*3*-HPS-*2.5*	3.11	2.89
W-*3*-HPS-*25*	3.01	2.99
W-*3*-HPS-*50*	3.07	2.93
W-*4*-HPS-*2.5*	2.92	3.08
W-*4*-HPS-*25*	3.01	2.99
W-*4*-HPS-*50*	3.01	2.99

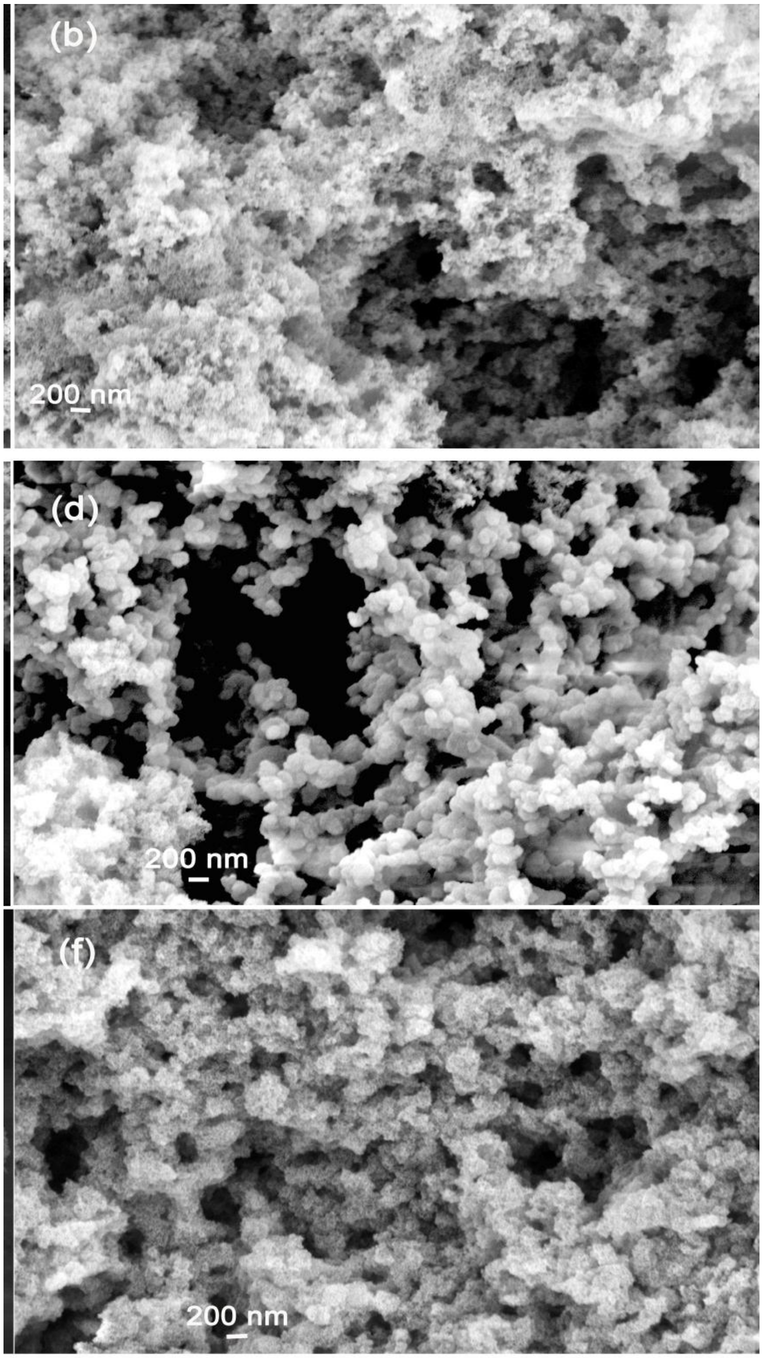

FigureC.1: SEM images of hierarchical porous silica (O-*3*-HPS-*x*) samples prepared with *x* = 2.5 (a), 25 (b) , and 50 (c).

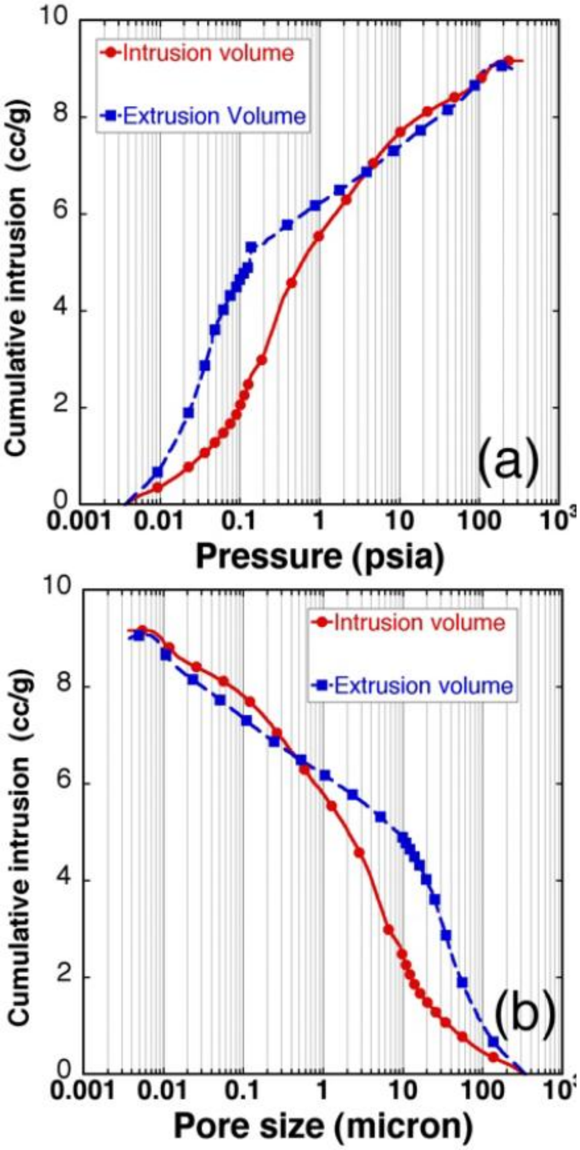

Figure C. 2: Mercury intrusion curves as a function of the applied pressure (a) and as a function of pore size (b).

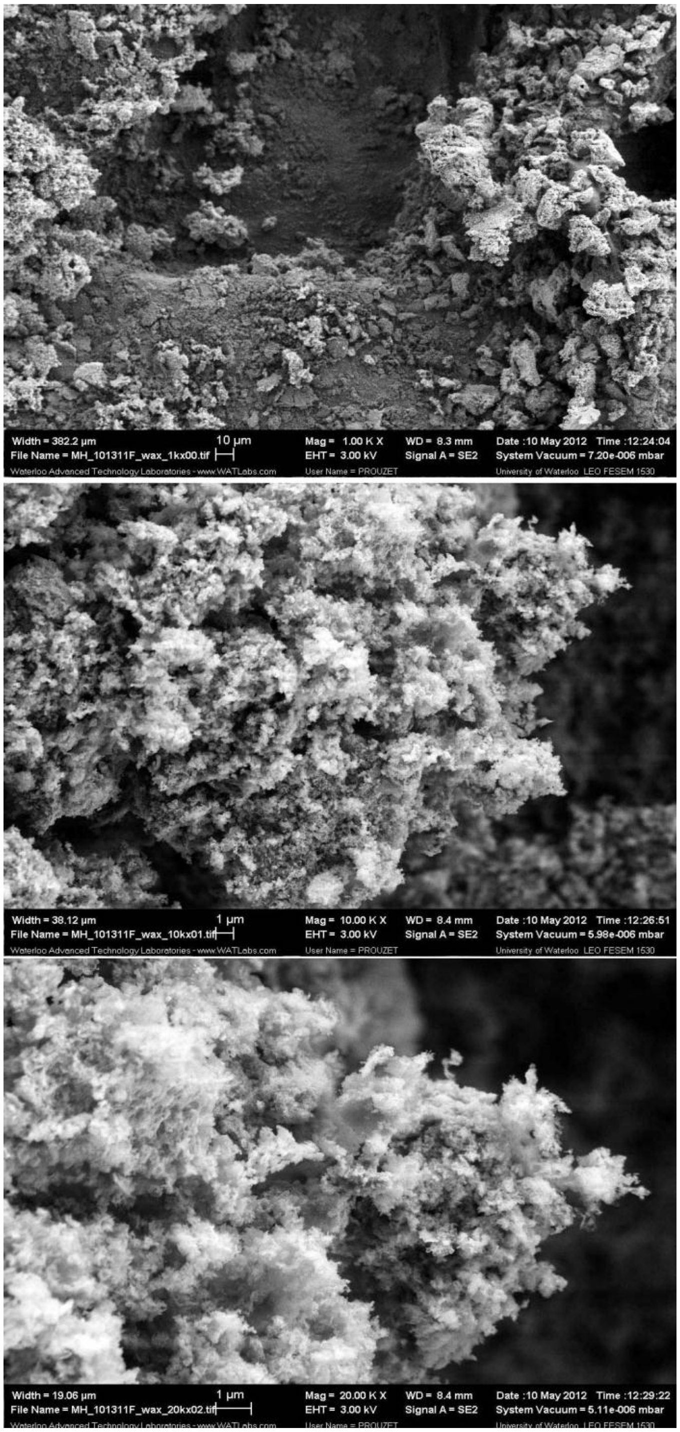

Figure C. 3: SEM photos for W-*4*-HPS-*2.5* sample.

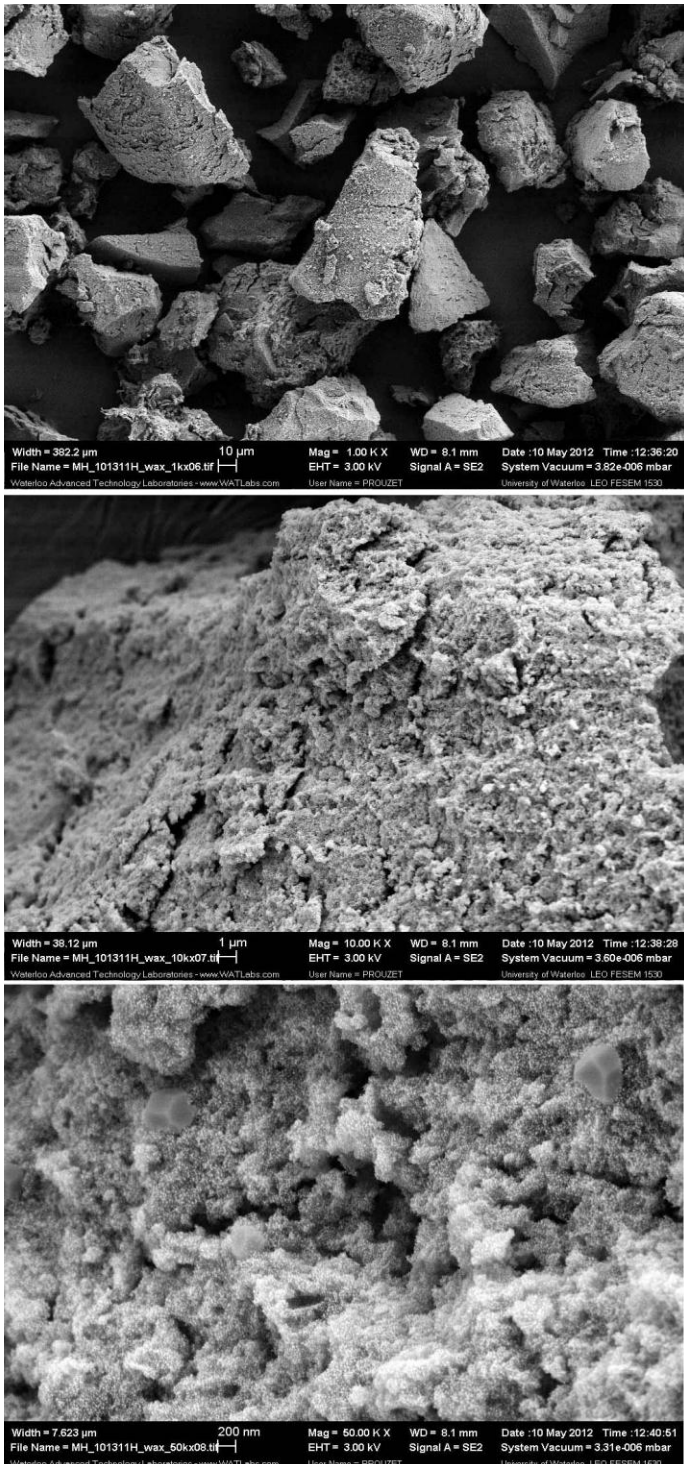

Figure C. 4: SEM photos for W-*4*-HPS-*50* sample.

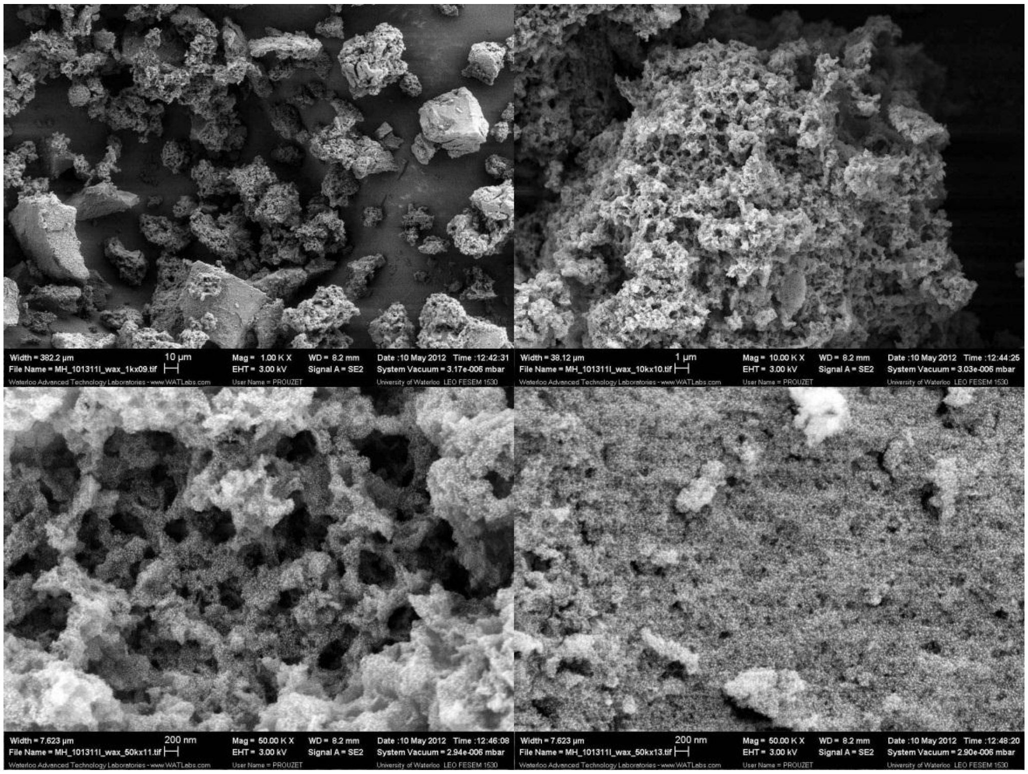

Figure C. 5: SEM photos for W-*2*-HPS-*2.5* sample.

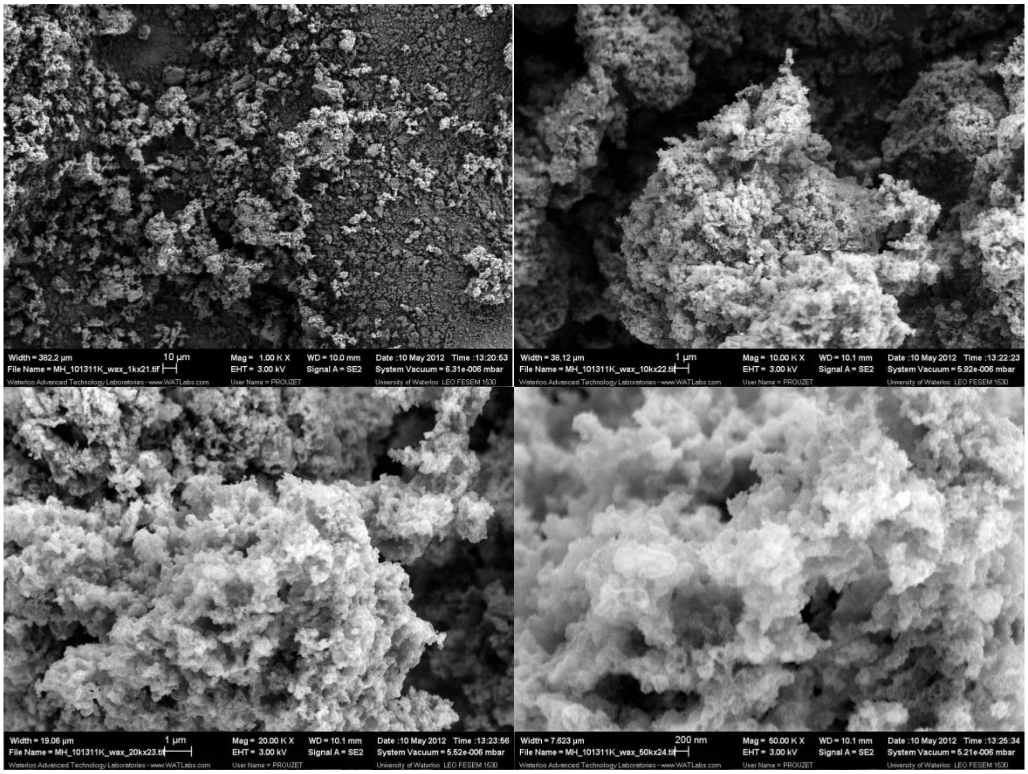

Figure C. 6: SEM photos for W-*2*-HPS-*50* sample.

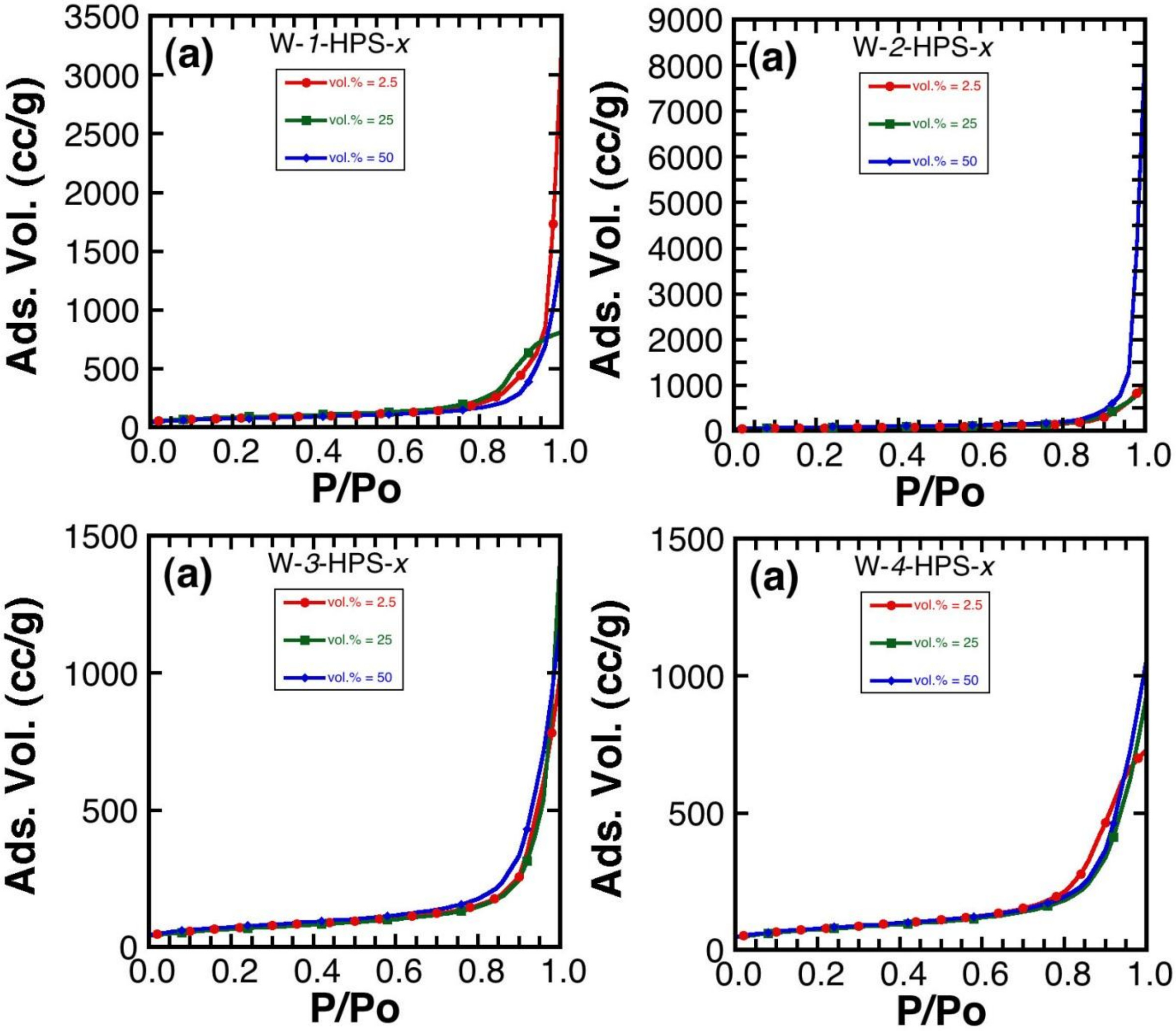

Figure C. 7: N_2 adsorption isotherm for hierarchical porous silica W- y-HPS-*x*, where *x* = is the vol.% of NE to HSSS = 2.5, 25, and 50.

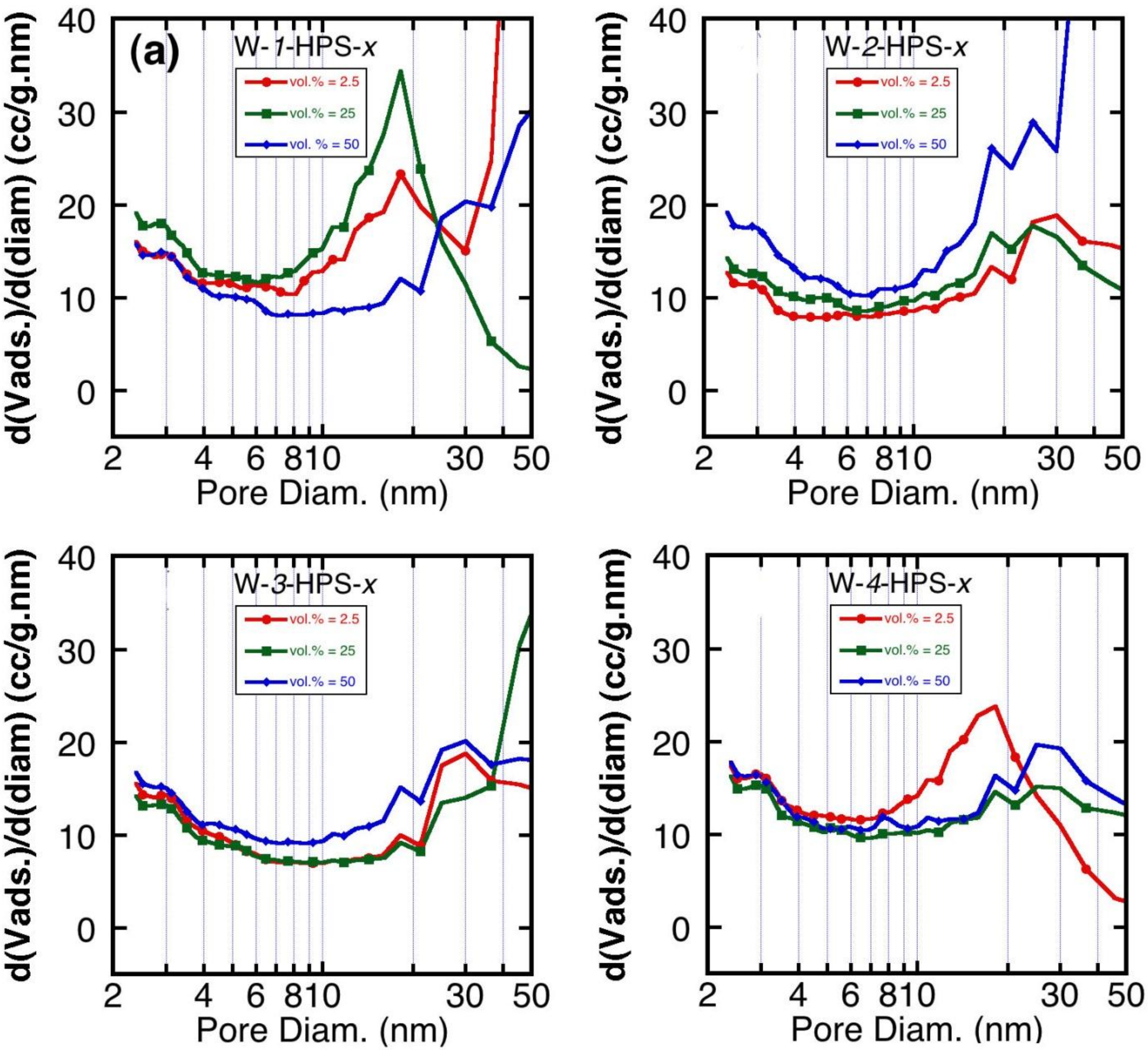

Figure C.8: Pore size distriobution for hierarchical porous silica W- y-HPS-*x*, where *x* = is the vol.% of NE to HSSS = 2.5, 25, and 50.

Appendix D

Metal Oxide-Hierarchical Porous Silica Nanocomposites

Table D. 1: Compositions of iron oxide-hierarchical porous silica (Fe^a-y-HPS-x) prepared from iron oleate (Fe^a-OL) nanoemulsion Fe^{a}NE-1 or Fe^{a}NE-2.

Sample Name	Fe^{a}NE-*y* (ml)*	HSSS (ml)*	Fe_2O_3 (g)**	SiO_2 (g)**	$Fe_2O_3/(Fe_2O_3+SiO_2)$ (wt.%)
Fe^a-*1*-HPS-*2.5*	2.5	100	0.019	3.72	0.508
Fe^a-*1*-HPS-*25*	25	100	0.196	3.72	5.01
Fe^a-*1*-HPS-*50*	50	100	0.391	3.72	9.51
Fe^a-*1*-HPS-*100*	100	100	0.782	3.72	17.37
Fe^a-*1*-HPS-*200*	200	100	1.564	3.72	29.59
Fe^a-*2*-HPS-*2.5*	2.5	100	0.078	3.72	2.05
Fe^a-*2*-HPS-*25*	25	100	0.782	3.72	17.37
Fe^a-*2*-HPS-*50*	50	100	1.564	3.72	29.60
Fe^a-*2*-HPS-*100*	100	100	3.128	3.72	45.68
Fe^a-*2*-HPS-*200*	200	100	6.256	3.72	62.71

* Experimental value, ** Calculated value

Example of calculation of iron oxide with silica

Total weight of nanoemulsion Fe^{a}NE-*1* is 470 (g) contains 20 (g) of iron oleate (Fe^a-OL). Fe_2O_3 (M.wt. = 160 g) is formed upon calcination of iron oleate (Fe^a-OL) (M.wt. = 900 g). In sample Fe^a-*1*-HPS-*2.5* ,as an example, 2.5(g) of nanoemulsion has 0.11 (g) iron oleate which form 0.019 (g) of Fe_2O_3 after calcination.

One hundred grams of sodium silicate solution has 14.05 (g) of pure sodium silicate which has 26.5% SiO_2 which equals 3.72 (g)

Table D. 2: Compositions of iron oxideb -hierarchical porous silica (Fe^b-y-HPS-x) prepared from iron oleate (Fe^b-OL) nanoemulsion Fe^bNE-1 or Fe^bNE-2.

Sample Name	Fe^bNE-*y* (ml)[*]	HSSS (ml)[*]	Fe_3O_4 (g)[**]	SiO_2 (g)[**]	$Fe_3O_4/(Fe_3O_4+SiO_2)$ (wt.%)
Fe^b-*1*-HPS-*2.5*	2.5	100	0.011	3.72	0.29
Fe^b-*1*-HPS-25	25	100	0.11	3.72	2.87
Fe^b-*1*-HPS-50	50	100	0.22	3.72	5.58
Fe^b-*1*-HPS-100	100	100	0.44	3.72	10.58
Fe^b-*1*-HPS-200	200	100	0.88	3.72	19.13
Fe^b-*2*-HPS-*2.5*	2.5	100	0.044	3.72	1.17
Fe^b-*2*-HPS-25	25	100	o.44	3.72	10.58
Fe^b-*2*-HPS-50	50	100	o.88	3.72	19.13
Fe^b-*2*-HPS-100	100	100	1.76	3.72	32.12
Fe^b-*2*-HPS-200	200	100	3.52	3.72	48.62

[*] Experimental value, [**] Calculated value

Example of calculation iron oxide with silica

Total weight of nanoemulsion Fe^aNE-*1* is 470 (g) contains 20 (g) of iron oleate (Fe^b-OL). Fe_3O_4 (M.wt. = 232 g) is formed upon calcination of iron oleate (Fe^b-OL) (M.wt. = 2418.7 g). In sample Fe^b-*1*-HPS-*2.5* ,as an example, 2.5(g) of nanoemulsion has 0.11 (g) iron oleate which form 0.011 (g) of Fe_3O_4 after calcination.

One hundred grams of sodium silicate solution has 14.05 (g) of pure sodium silicate which has 26.5% SiO_2 which equals 3.72 (g)

Table D. 3: Compositions of cobalt oxide-hierarchical porous silica (Co-y-HPS-x) prepared from cobalt oleate (Co-OL) nanoemulsion CoNE-1 or CoNE-2.

Sample Name	CoNE-*y* (ml)*	HSSS (ml)*	CoO (g)**	SiO_2 (g)**	CoO/(CoO +SiO_2) (wt.%)
Co-*1*-HPS-*2.5*	2.5	100	0.013	3.72	0.35
Co-*1*-HPS-25	25	100	0.133	3.72	3.45
Co-*1*-HPS-50	50	100	0.266	3.72	6.67
Co-*1*-HPS-100	100	100	0.531	3.72	12.49
Co-*1*-HPS-200	200	100	1.06	3.72	22.18
Co-*2*-HPS-*2.5*	2.5	100	0.052	3.72	1.38
Co-*2*-HPS-25	25	100	0.52	3.72	12.26
Co-*2*-HPS-50	50	100	1.04	3.72	21.85
Co-*2*-HPS-100	100	100	2.08	3.72	35.86
Co-*2*-HPS-200	200	100	4.16	3.72	52.79

Experimental value, ** Calculated value

Example of calculation cobalt oxide with silica

Total weight of nanoemulsion CoNE-*1* is 470 (g) contains 20 (g) of iron oleate (Co-OL). CoO (M.wt. = 75 g) is formed upon calcination of iron oleate (Co-OL) (M.wt. = 621 g). In sample Co-*1*-HPS-*2.5* ,as an example, 2.5(g) of nanoemulsion has 0.11 (g) iron oleate which form 0.013 (g) of CoO after calcination.

One hundred grams of sodium silicate solution has 14.05 (g) of pure sodium silicate which has 26.5% SiO_2 which equals 3.72 (g)

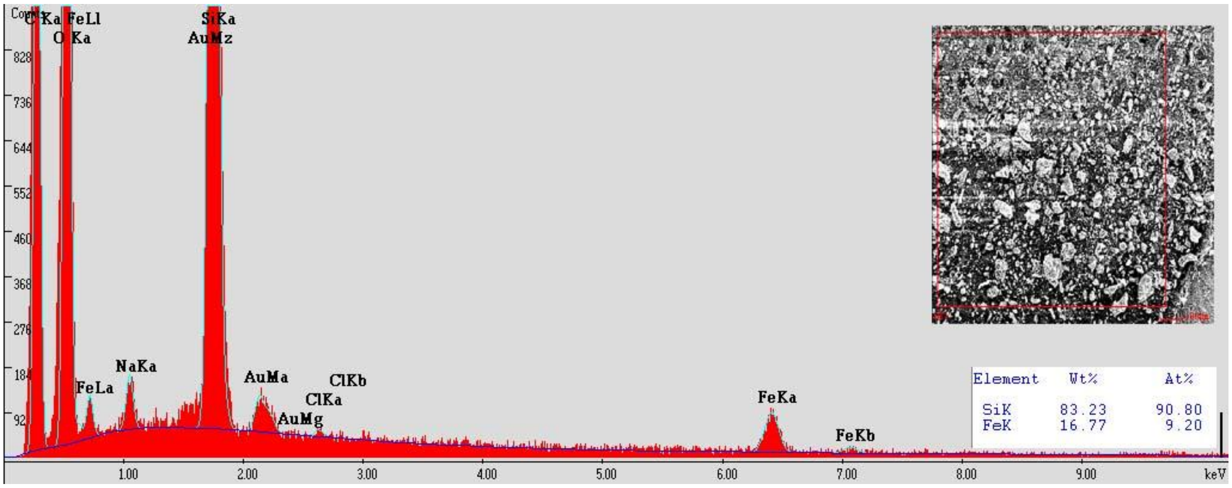

Element	Wt%	At%
SiK	83.23	90.80
FeK	16.77	9.20

Figure D. 1: EDAX analysis for Iron oxide-hierarchical porous silica Fe^{a}-*2*-HPS-*25*.

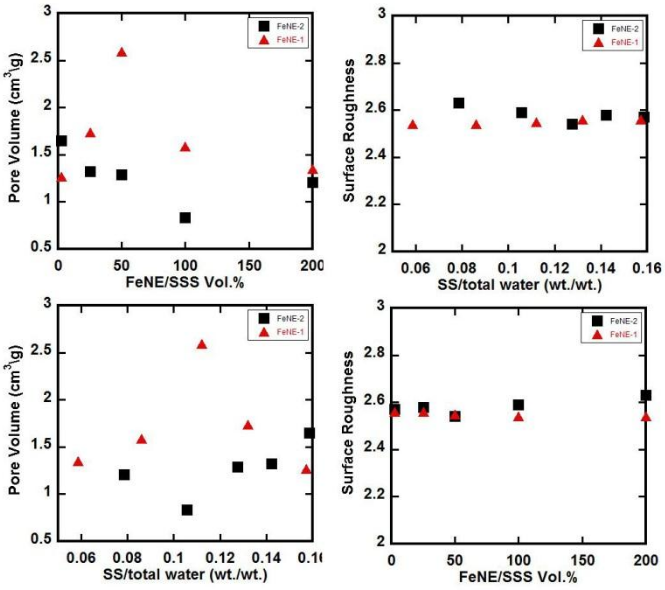

Figure D. 2: Pore volume and surface roughness of Fe^{a}-*2*-HPS -*x* and Fe^{a}-*2*-HPS -*x* as a function of Fe^{a}NE/HSSS and concentration of sodium silicate (g/ml).

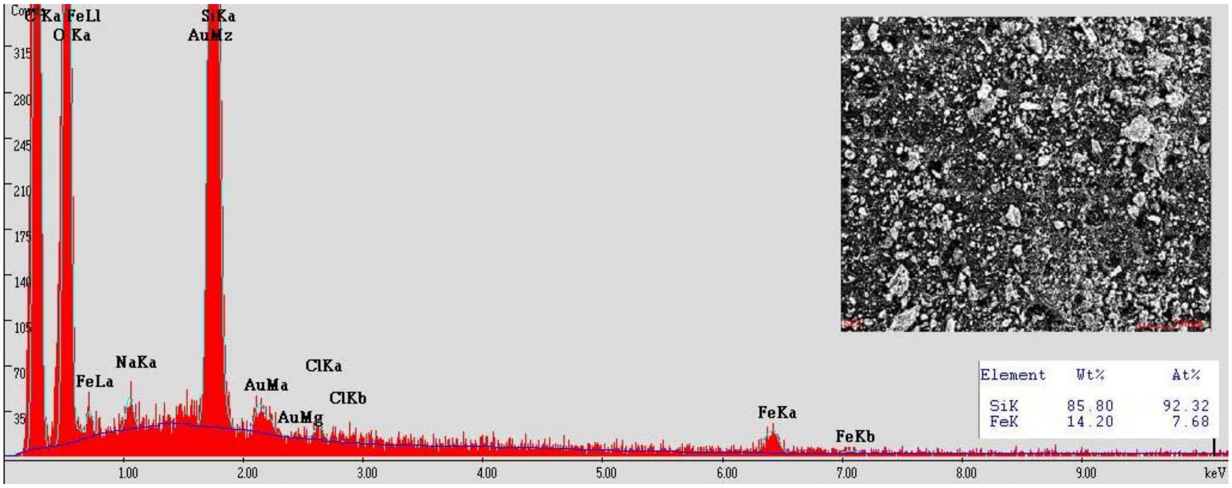

Element	Wt%	At%
SiK	85.80	92.32
FeK	14.20	7.68

Figure D. 3: EDAX analysis for Iron oxide- hierarchical porous silica Fe^b-*2*-HPS-*25*.

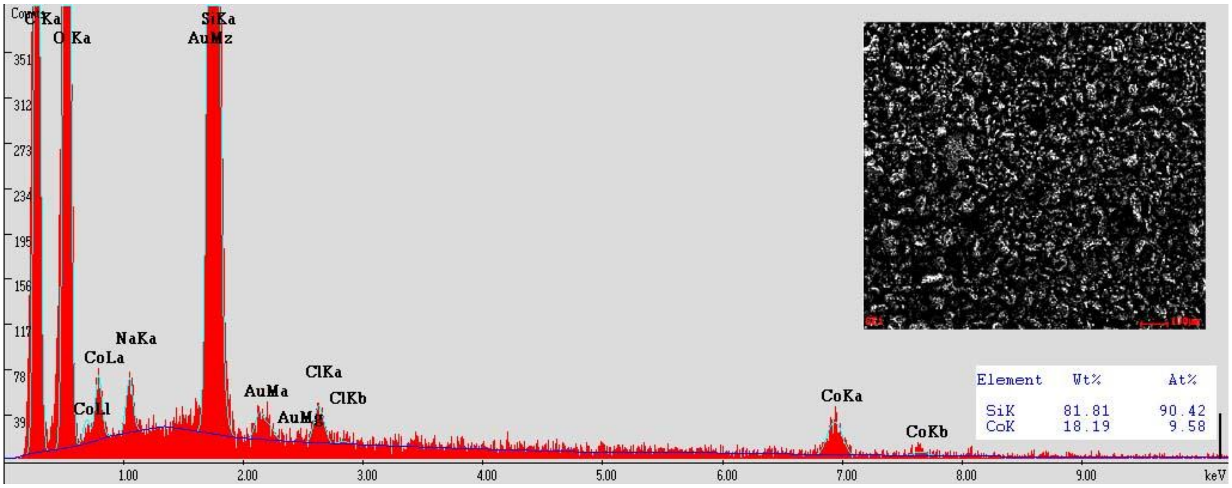

Element	Wt%	At%
SiK	81.81	90.42
CoK	18.19	9.58

Figure D. 4: EDAX analysis for Cobalt oxide- hierarchical porous silica (Co-*2*-HPS-*25*).